Towards *a priori* models for differential diffusion in turbulent non-premixed flames

Thesis by
Nicholas Burali

In Partial Fulfillment of the Requirements for the
Degree of
Doctor of Philosophy

CALIFORNIA INSTITUTE OF TECHNOLOGY
Pasadena, California

2018
Defended May 22, 2018

Nicholas Burali

ORCID: http://orcid.org/0000-0002-0733-0577

To my family.

ACKNOWLEDGEMENTS

First and foremost, I would like to thank the people that introduced me to the world of Computational Fluid Dynamics, starting with my master's thesis advisor, Professor Sergio Pirozzoli. I am very grateful to Professor Tim Colonius, for hosting me in his lab for a few months, and giving me a first taste of graduate research at Caltech. Finally, I express my gratitude to my thesis advisor, Professor Guillaume Blanquart, for his constant support, patience, guidance, and unwavering devotion to his job.

I also thank Professors Melany Hunt and Dan Meiron, for reading this thesis, and for providing comments and suggestions to improve its quality.

I wish to thank all past and present members of my research group, The FORCE. Many friends have made my experience at Caltech amazing. I am especially thankful to my roommates, Phillipe Tosi and Damian Hirsch, and to my beer buddy Nikola Georgiev.

At Caltech I've had the opportunity to practice Shotokan karate with the Caltech Karate Club. Not many know that this club holds the distinction of being the first university karate club in the US. Its first instructor, Tsutomu Oshima, is the founder of Shotokan Karate of America. I am especially grateful to Chris and David for their devotion and patience.

I am grateful for generous funding from the National Defense Science and Engineering Graduate (NDSEG) Fellowship (FA9550-11-C-0028) and from the Josephine de Kármán Fellowship Trust. Funding from the U.S. Department of Energy-Basic Energy Sciences (DE-SC0006591) under the supervision of Dr. Wade Sisk is gratefully acknowledged. This work used the Extreme Science and Engineering Discovery Environment (XSEDE), which is supported by National Science Foundation grant number ACI-1053575, and resources from the National Energy Research Scientific Computing Center (NERSC), a DOE Office of Science User Facility supported by the Office of Science of the US Department of Energy under Contract No. DE-AC02-05CH11231.

I wish to thank Dr. Barlow at Sandia National Laboratories for the experimental data, and Prof. Mueller from Princeton University for sharing the LES data.

Last but not least, I am grateful to my family for their constant support and encouragement throughout my life.

ABSTRACT

In this work, progress is made towards modeling of differential molecular diffusion for resolved simulations with detailed transport, and for flamelet-based reduced-order combustion models.

For resolved simulations with detailed transport, the validity and the limitations of the constant non-unity Lewis number approach in the description of molecular mixing in laminar and turbulent flames is studied. Three test cases are selected, including a lean, highly unstable, premixed hydrogen/air flame, a lean turbulent premixed n-heptane/air flame, and a laminar ethylene/air coflow diffusion flame. For the hydrogen flame, both a laminar and a turbulent configuration are considered. The three flames are characterized by Lewis numbers which are less than unity, greater than unity, and close to unity, respectively. For each flame, mixture-averaged transport simulations are carried out and used as reference data. The analysis suggests that, for numerous combustion configurations, the constant non-unity Lewis number approximation leads to small errors when the set of Lewis numbers is chosen properly. For the selected test cases and our numerical framework, the reduction of computational cost is found to be minimal. Two different methods of evaluating the Lewis numbers are tested, with both performing well, and neither consistently better than the other.

Next, modeling of differential molecular diffusion for reduced-order combustion models is analyzed. The flamelet-based chemistry tabulation technique is a popular reduced-order chemical model for non-premixed turbulent flames. In this approach, the correct choice of the species Lewis numbers in the flamelet equations plays an important role. Experimental results have highlighted that, in turbulent non-premixed jet flames, turbulent transport becomes gradually dominant over molecular mixing with (i) increasing axial distance from the burner exit plane, and (ii) increasing jet Reynolds number. In the current work, this transition is characterized and *a priori* models for the *effective* species Lewis numbers in turbulent non-premixed flames are assessed.

First, a flamelet-based methodology is proposed to extract these effective Lewis numbers from data sets of turbulent non-premixed flames. For each flame and each downstream station, two flamelet parameters are extracted, including an optimal stoichiometric scalar dissipation rate, χ_{st}^{opt}, and the parameter γ^{opt}, which is related

to the effective species Lewis numbers through $\mathrm{Le}_{i,\mathrm{eff}} \equiv (1 + \gamma^{opt})/(1/\mathrm{Le}_i + \gamma^{opt})$. This methodology is then applied to the Sandia methane/air jet flames B, C, D, and E (R. Barlow, Int. Work. Meas. Comput. Turb. Non-Prem. Flames, 2003). The effective Lewis numbers are found to transition from their laminar values, close to the burner exit plane, to unity further downstream. Previously-suggested scalings for γ^{opt} are then assessed. The limitations associated with the experimental data, including large uncertainties, limited spatial resolution, and relatively few measured quantities, prevent a conclusive assessment of the models for γ^{opt}, and suggest that Direct Numerical Simulation (DNS) data should be used.

To overcome these limitations, a campaign of DNS of Sandia flame B is carried out. A baseline grid is carefully designed, and grid independence is assessed through simulations using refined grids in the axial, radial and azimuthal directions. Radiation and differential diffusion effects are systematically isolated by considering radiating and unity Lewis number cases, respectively. The DNS database is then validated using available measured statistics for flame B, and comparisons to the higher Reynolds number flames are carried out. The effective Lewis numbers extracted from the DNS data are found to transition towards unity with increasing downstream distance. Finally, flame and turbulence parameters are recomputed from the DNS data, and scalings for the parameter γ^{opt} are assessed.

PUBLISHED CONTENT AND CONTRIBUTIONS

- Ch. 3 is based on: N. Burali *et al.* "Assessment of the constant non-unity Lewis number assumption in chemically-reacting flows". *Combust. Theor. Model.* Vol. 20, No. 4 (2016), pp. 632-657, doi:10.1080/13647830.2016.1164344.

  N.B. performed the majority of the simulations, analyzed the data, made most of the figures, and was the primary author of the article.

- Ch. 4 is based on: N. Burali and G. Blanquart "Modeling turbulent Lewis numbers in non premixed flames: insights from DNS data of Sandia flame B", *10th U.S. National Combustion Meeting*, April 2017, University of Maryland at College Park, College Park, MD.

  N.B. performed the data analysis, made all the figures, and was the primary author of the article.

CONTENTS

LIST OF FIGURES

LIST OF TABLES

Chapter 1

INTRODUCTION

1.1 Background

Most of the world's energetic needs are met through the combustion of fossil fuels, which account for about 80% of global energy production [1]. Recent projections from the U.S. Energy Information Administration suggest that they will still account for 77% of global energy use by 2040 [2]. Unfortunately, the combustion of fossil fuels has several negative implications, such as the emission of green-house gases, nitrogen oxides, sulfur dioxide, unburnt hydrocarbon compounds, and soot, which have been shown to affect both the environment [3] and human health [4–6]. The uneven distribution of these resources is also a cause of geo-political tensions [7]. For all these reasons, efficiency improvements to combustion processes are of great importance.

While combustion devices exist in a wide range of configurations, most share the same fundamental complexities. In these systems, the combustion of practical fuels may be represented by hundreds of species and thousands of reactions [8], and typically takes place under turbulent conditions [9]. Turbulent combustion is divided into three fundamental modes, including premixed, non-premixed, and partially-premixed [10]. In premixed turbulent flames, the fuel and the oxidizer are completely mixed before they are consumed through combustion. Typical applications include spark-ignition engines, lean-burn gas turbines, and household burners. In non-premixed turbulent combustion, the fuel and the oxidizer are initially separated, and mixing must occur to have chemical reactions. Turbulent non-premixed flames are also known as diffusion flames, since diffusion is the rate-controlling process. They are typically found in furnaces, diesel engines, and gas turbines. In partially-premixed combustion, the fuel and the oxidizer are partially mixed before the combustion takes place. Common applications include aircraft gas turbines and gasoline engines with direct injection.

1.2 Challenges in turbulent combustion

In turbulent combustion, mixing plays a central role and a close interaction of turbulence and combustion takes place. A schematic diagram is shown in Fig. 1.1. The largest eddying motions are controlled by the size of the combustion device,

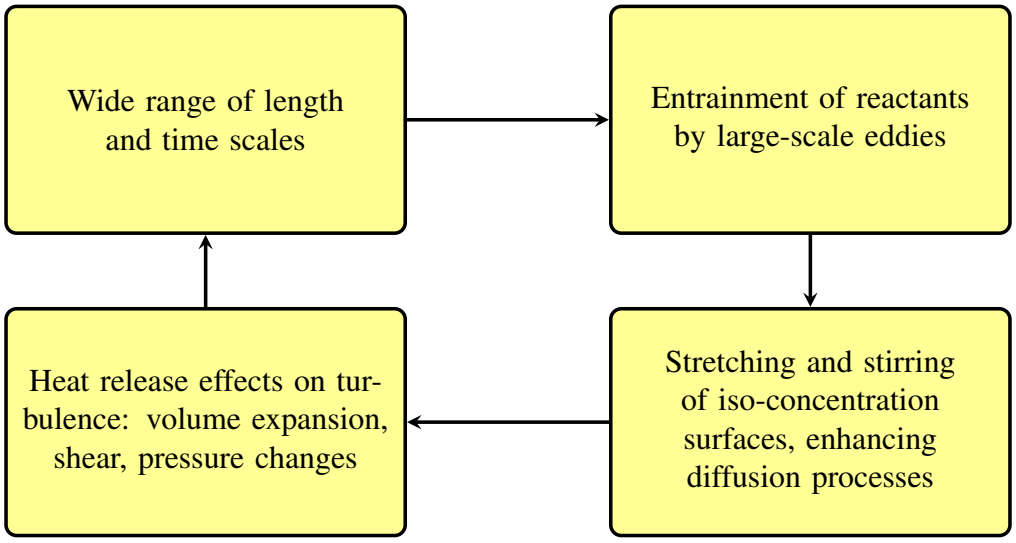

Figure 1.1: Diagram illustrating turbulence-chemistry interactions (adapted from Bray [9].)

while the smallest scales are determined by the dissipation of turbulent energy by viscosity. The largest scales, which contain most of the kinetic energy, entrain and bring into contact the reactant species. Turbulent motion at intermediate scales is then responsible for stirring the iso-concentration surfaces, which greatly enhances molecular diffusion processes. This increases the rate of depletion of the reactants, the production of product species, and the attendant heat release. The heat release then strongly affects the turbulence through dilatation, shear and pressure changes. Thus, from this simple diagram it is clear that an accurate description of turbulent flames requires a simultaneous understanding of turbulent mixing and combustion [11]. That is why modeling of these systems has proven to be a major challenge, and the subject of many studies over the past few decades (see for example the reviews of Bilger [12, 13] and Peters [14]).

1.2.1 Differential diffusion effects and soot formation

An important parameter when considering the transport of species in mixtures is the Lewis number, defined as

$$Le_i = \frac{\lambda}{\rho c_p D_{i,m}}, \tag{1.1}$$

where λ is the mixture thermal conductivity, ρ is the density, c_p is the mixture specific heat, and $D_{i,m}$ is the mass diffusivity of species i with respect to the mixture. In practical combustion devices, heavy hydrocarbons such as gasoline, diesel, and kerosene are typically used [15]. The combustion of these fuels is characterized by a wide range of species Lewis numbers, and significant *differential diffusion* effects

are observed [16]. The Lewis numbers for large hydrocarbon species are typically much larger than one. For example, in Ch. 3 a turbulent *n*-heptane/air flame is considered, where the fuel Lewis number is 2.9.

Representing differential diffusion effects accurately when a large number of species is considered, such as for the combustion of large hydrocarbon fuels, can be a challenging task. More specifically, molecular diffusion processes occur at the smallest scales, and either these scales must be fully resolved, or some reduced-order model must be used. In Direct Numerical Simulation (DNS), where all scales of motion are represented on the computational grid, the diffusion fluxes must be computed for each species in the mixture, at each spatial location, and at each time step. The computational cost of this type of simulation is prohibitive for all but the simplest configurations. For these simulation, neglecting differential diffusion effects represents a crude, yet effective cost-reduction approach [17]. A practical alternative to DNS is to resolve only the large scales of turbulent motion. For these simulations, chemical reactions, molecular diffusion processes, as well as their interaction with the turbulence are not resolved, and reduced-order models must be used. Unfortunately, physics-consistent models for differential diffusion are either crude, or have yet to be developed [18], and these effects are often neglected altogether by considering all species diffusivities to be equal [19–25].

However, while neglecting differential diffusion typically only has a small impact on major combustion products, such as H_2O and CO_2, it can more seriously affect the concentration of species with Lewis numbers significantly far from unity [26]. That is important for a variety of phenomena that present a high sensitivity to differential diffusion, such as soot formation [27]. Soot is made of black carbon particles formed during the incomplete combustion of hydrocarbon fuels [28], and its nucleation rate is known to present a quadratic dependence on the concentration of so-called soot precursor species [29, 30]. Unfortunately, the yield of these species (such as acetylene and polycyclic aromatic hydrocarbons, or PAH) is strongly affected by differential diffusion.

1.2.2 Computational cost of detailed species transport

Great strides have been made towards the simulation of reacting flows of ever increasing complexity, which have extended the realm of problems that can be tackled [31–33]. Nonetheless, the computational cost of simulating practical configurations often remains beyond the reach of available resources, and approximations

must be accommodated within reacting flow codes. In other terms, large scale simulations represent a constant trade-off between relevance to engineering problems (high Reynolds number, large domain, etc.) and fidelity to the physical processes simulated (combustion, radiation, turbulence, etc.). Within this framework, using an accurate but overly expensive model comes at the cost of more realistic simulations. An essential question arises: what level of fidelity is sufficient?

In simulations of multicomponent mixtures, a large fraction of the computational cost is associated with the evaluation of the species mass diffusion fluxes, $\boldsymbol{j_i}$ [34]. These appear in the species transport equations, which read

$$\frac{\partial}{\partial t}(\rho Y_i) + \nabla \cdot (\rho \boldsymbol{u} Y_i) = -\nabla \cdot \boldsymbol{j_i} + \dot{\omega}_i, \tag{1.2}$$

where $\boldsymbol{u}$ is the velocity, Y_i and $\dot{\omega}_i$ are the ith species mass fraction and chemical source term, respectively, and in the energy conservation equation. The most accurate formulation to compute the diffusion fluxes $\boldsymbol{j_i}$ for gas mixtures, involves the solution of the so-called multicomponent diffusion equations, which require the inversion of linear systems at each computational node and each time step. Efficient implementations have been proposed, such as EGLIB, a Fortran library for cost-effective and accurate evaluation of multicomponent transport coefficients in gas mixtures, developed by Ern and Giovangigli [35]. The multicomponent approach remains, however, an expensive choice, and the benefits stemming from the greater accuracy do not always justify the high computational cost. That is why multicomponent mixture computations have been used mostly for one- and two-dimensional simulations [34, 36–38], and its extension to three-dimensional flames remains currently impractical.

For typical hydrocarbon flames, the use of mixture-averaged diffusion coefficients represents an effective approximation to the full multicomponent transport model [39]. In this formulation, the transport coefficients, including the dynamic viscosity, the heat conductivity, and the mixture-averaged diffusion coefficients, are computed using an averaging procedure [40]. This approach represents the first-order approximation to the full multicomponent transport equations [34]. The resulting species diffusion mass fluxes are computed using the Curtiss-Hirschfelder approximation [41]

$$\boldsymbol{j_i} = -\rho D_{i,m} \frac{Y_i}{X_i} \nabla X_i - \rho Y_i \boldsymbol{u_c}, \tag{1.3}$$

where

$$\boldsymbol{u_c} = -\sum_i D_{i,m} \frac{Y_i}{X_i} \nabla X_i \tag{1.4}$$

is the correction velocity, which ensures zero net mass diffusion flux, *i.e.*, $\sum_i \boldsymbol{j_i} = 0$. Y_i and X_i are the ith species mass and mole fractions, respectively, and the diffusivities $D_{i,m}$ are computed by summing over all other species

$$D_{i,m} = \frac{1 - Y_i}{\sum_{k \neq i} \frac{X_k}{\mathcal{D}_{k,i}}}. \tag{1.5}$$

In Eq. (1.5), $\mathcal{D}_{k,i}$ is the binary diffusion coefficient of the kth specie relative to the ith species.

Despite the great simplification introduced by the mixture-average framework over the full multicomponent transport model, the associated computational cost can be significant when large chemical models are used. More precisely, the cost associated with the computation of the N_s mixture mass diffusion coefficients scales as $\mathcal{O}(N_s^2)$, as all other species must be considered in the computation of each species diffusion coefficient, and this operation must be repeated at each node and at each time step. In comparison, both the mixture conductivity and viscosity may be evaluated accurately with $\mathcal{O}(N_s)$ expressions [42, 43]. This quadratic cost represents a computational bottleneck, especially when large chemical models with hundreds of species are used [15, 44, 45]. Moreover, the effort required to compute the diffusion fluxes at a greater accuracy may be nullified in turbulent combustion, where enhanced mixing through turbulent transport reduces the influence of the molecular diffusion coefficients on the physics of the flame [10, 46–48]. Hence, many applications require a further reduction in the computational cost.

A common strategy to reduce the computational cost is to use reduced chemical kinetics, *i.e.*, to reduce the number of species [49, 50]. This can be done with either a pre-reduced chemical model, or with the use of dynamic reduction [32, 51, 52]. Nevertheless, to capture all the relevant chemical timescales, the number of species remains typically large (20-40 species), with only a modest cost reduction. To overcome this limitation, one could pursue an adaptive chemistry (AC) strategy, whereby the mechanism is chosen from a library of pre-generated mechanisms depending on the local properties of the mixture [53]. Unfortunately, the use of AC is limited by the ability of the pre-chosen mechanisms to span the domain of possible reacting flow conditions. A more recent approach to bypass this issue is the use of dynamic adaptive chemistry (DAC) [54].

Independently of whether or not chemical models may be reduced, a practical technique to reduce significantly the computational cost associated with evaluating species diffusivity coefficients is to take advantage of the small variation of the

Lewis numbers [55], by approximating them with constant values. It is common practice to prescribe the mass diffusion coefficients through a set of constant Lewis numbers [55–58]. For example, Hawkes and Chen [59] performed calculations of laminar strained premixed methane-air twin flames, showing that the mixture-averaged calculations were well reproduced by constant-Lewis number simulations over a wide range of strain rates. In many applications, using constant Lewis numbers can provide significant savings of computational cost, releasing resources that can be used to tackle more complex problems [60]. These Lewis numbers are usually extracted from one-dimensional simulations with multicomponent or mixture-averaged properties, following some criterion such as selecting the values corresponding to the maximum temperature.

Yet, the validity of the constant non-unity Lewis number approach should be investigated systematically for a wide range of configurations, including laminar and turbulent, premixed and non-premixed flames. Further, criteria to pre-compute these constant Lewis numbers should be assessed. That is the subject of Ch. 3.

1.2.3 Reduced-order modeling of turbulence-chemistry interaction

Turbulent combustion is characterized by a wide range of length and time scales, which results in complex interactions. The cost of performing DNS of these flows, for which even the smallest scales must be resolved, remains prohibitive for all but the simplest configurations. That is why reduced-order turbulence and combustion models must be used when configurations of practical relevance are considered.

An effective alternative to DNS, is Large Eddy Simulation (LES) [61]. In LES, the spectrum of turbulent scales is divided into large-scale resolved motions and unresolved small-scale fluctuations through a filtering operation. While this greatly reduces the computational cost, closure must be provided for the sub-filter processes [62–64], such as the chemical source terms and the turbulence-chemistry interactions. In this work, an emphasis is placed on reduced-order modeling of the effects of turbulent mixing on the flame structure, as will be explained in the following sections.

Flamelet-based chemistry tabulation

One popular reduced-order chemical model for non-premixed turbulent flames is the flamelet-based chemistry tabulation technique [61]. In this approach, the one-dimensional flamelet equations [65, 66] are solved, and the fluid and flame proper-

ties (such as density, viscosity, heat diffusivity and temperature), are tabulated with respect to the mixture fraction, Z, and either its scalar dissipation rate, χ, or the progress variable, C [20, 67]. The mixture fraction variable is a non-reactive scalar that describes the rate of mixing of fuel and oxidizer [10]. In a two-feed system, Z is 0 in the oxidizer stream and 1 in the fuel stream, and satisfies the following conservation equation

$$\frac{\partial \rho Z}{\partial t} + \nabla \cdot (\rho Z \boldsymbol{u}) = \nabla \cdot (\rho D \nabla Z), \tag{1.6}$$

where D is the diffusivity of mixture fraction. In this work, D is taken to be equal to the mixture heat diffusivity, α. The scalar dissipation rate is defined as

$$\chi \equiv 2D|\nabla Z|^2, \tag{1.7}$$

and the progress variable is typically defined as a linear combination of the mass fractions of major intermediate and product species [68], such as

$$\mathrm{C} = \mathrm{Y_{CO_2}} + \mathrm{Y_{CO}} + \mathrm{Y_{H_2O}} + \mathrm{Y_{H_2}}. \tag{1.8}$$

In generating the individual flamelets to populate the chemical table, the choice of the species Lewis numbers plays an important role [55]. Yet, a popular assumption in LES of turbulent combustion is to set all Lewis numbers to unity when generating the individual flamelets [20–25].

Differential diffusion and turbulence-chemistry interaction

In turbulent non-premixed flames, differential diffusion effects on the flame structure are observed to transition from a laminar, molecular diffusion-controlled regime, to a turbulence-dominated one. This transition is well illustrated in the work of Drake *et al.* [69, 70], for experiments involving H_2/air turbulent diffusion flames, and Barlow *et al.* [46, 71, 72], for a set of piloted CH_4/air flames of increasing jet Reynolds numbers. In these studies, species measurements show a decrease of differential diffusion effects with (*i*) increasing axial distance from the issuing nozzle and (*ii*) increasing jet Reynolds number. The extremes of this transition are exemplified in Fig. 1.2, taken from Barlow *et al.* [46], where it is shown that flamelets can be well representative of the flame structure at both limiting regimes. More specifically, the figure on the left shows conditional mean species measurements at 15 diameters downstream of the burner exit plane of a low Reynolds number jet flame ($\mathrm{Re_{jet}} \approx 8200$). The figure on the right represents measurements at 45 diameters downstream of the burner exit plane, for a jet flame at a much higher Reynolds

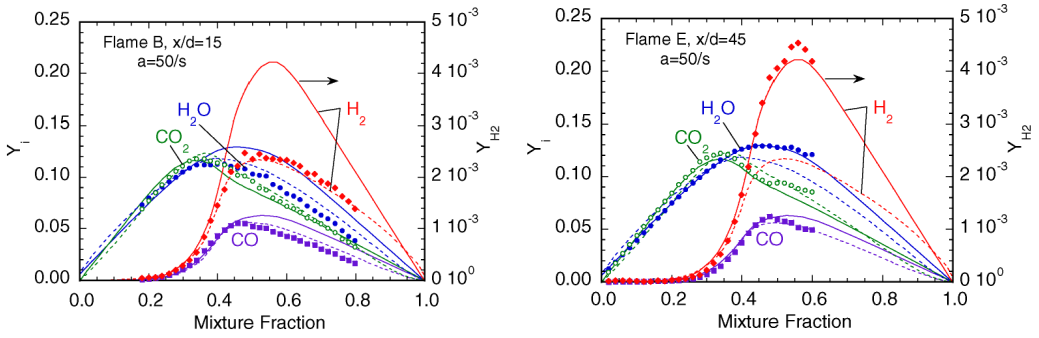

Figure 1.2: Comparison of measured conditional mean species mass fractions [72] (symbols), and laminar opposed-flow flame simulations, with either full molecular transport (dashed lines) or unity Lewis numbers (solid lines). Left: Sandia flame B ($\mathrm{Re_{jet}} \approx 8200$) at $x/d = 15$; right: Sandia flame E ($\mathrm{Re_{jet}} \approx 33600$) at $x/d = 45$. Reprinted from Barlow *et al.* [73], with permission from Elsevier.

number ($\mathrm{Re_{jet}} \approx 33600$). For the former, species profiles are found to be in excellent agreement with a flamelet calculation with full differential diffusion. For the latter, a unity-Lewis number flamelet calculation was found to be representative of the flame structure. These examples can be considered to be at the extremes of the transitioning behavior of the flame structure. However, a continuous transition between these cases is expected to occur. While these well-known experiments shed light on the role of differential diffusion in turbulent non-premixed flames, several questions remain unanswered. First, what are the flame and turbulence parameters that control the transition between these two limiting regimes? Second, can flamelets be used to represent the state space between the limiting cases? If that is the case, then for which parameters can flamelets achieve this goal, and what is their correct *a priori* modeling? In this work, progress is made towards answering these questions. That will be the subject of Chs. 4 and 7 of this thesis.

Modeling differential diffusion with effective Lewis numbers

While several reasons have been suggested for the strong jet near-field differential diffusion effects [19], including (*i*) the presence of a laminar mixing layer, (*ii*) the possibility that for certain species the turbulent diffusivity is comparable with the molecular diffusivities, and (*iii*) that the thickness of the mixing layer may be smaller than the Kolmogorov scale, the mechanisms involved with the transition remain elusive, and relatively few models are available from the literature. Pitsch [19] modeled this transition with a Lagrangian flamelet model [66], using laminar Lewis numbers for the initial laminar mixing layer, and then switching to unity Lewis

numbers past the end of the potential core. While an improvement over the use of a single unity-Lewis number flamelet, this approach assumes that the local mixing steady-state is described by either a laminar flamelet, or an equal diffusivity model, and requires *a priori* knowledge of the transition point.

An alternative approach to account for turbulent mixing can be found in the theoretical work of Peters [10]. There, chemical reactions are assumed to occur in a narrow layer embedded within two, non-reacting, turbulent mixing layers. By filtering the transport equations for the reactive scalars and mixture fraction and performing a two-scale asymptotic expansion, a filtered form of the flamelet equations was derived. These equations are formally identical to their non-filtered counterpart, except for the replacement of the Lewis number by an *apparent* Lewis number [10]

$$\hat{\mathrm{Le}}_i = \frac{D_T}{D_T + D_i}, \tag{1.9}$$

where the turbulent diffusivity D_T comes from the gradient transport assumption. For increasing turbulence intensities, Eq. (1.9) tends to unity, justifying the equal diffusivity assumption. Unfortunately, this method requires the solution of these separate flamelet equations (lean region, rich region, and the reaction zone) and is impractical for arbitrary chemistry [10].

Inspired by Eq. (1.9), Savard & Blanquart [47] found that the average chemical structure of a turbulent *premixed* flame can be mapped onto that of a laminar flame with the appropriate choice of *effective* Lewis numbers

$$\mathrm{Le}_{i,\mathrm{eff}} = \frac{\alpha + \alpha_T}{D_i + D_T}, \tag{1.10}$$

where α_T is the eddy heat diffusivity (assumed to be equal to D_T). With this assumption, Eq. (1.10) can be rewritten as

$$\mathrm{Le}_{i,\mathrm{eff}} = \frac{1 + \gamma}{\frac{1}{\mathrm{Le}_i} + \gamma}, \tag{1.11}$$

where γ is the ratio α_T/α. The general form of γ is unknown, and requires modeling. Savard & Blanquart [47] extracted γ from DNS data of lean H_2/air and n-C_7H_{16}/air [74] turbulent *premixed* flames, and *a posteriori* models for γ as a function of the local Reynolds and Karlovitz numbers were proposed.

Recently, Wang [75] proposed a modeling framework for differential diffusion in turbulent non-premixed flames. In his Nonlinear Differential Diffusion (NDD)

model, Wang [75] introduced a *modified* Lewis number, which is equivalent to Eq. (1.11), and obtained this expression through a simplified flamelet analysis of a turbulent mixing layer. The quantity D_T was estimated *a priori* by using a k-ε model, and does not include any flame-relevant parameter.

While Eqs. (1.10) and (1.11) are used uniformly in past studies [10, 47, 74, 75], the exact value of D_T (and α_T) and its physical meaning remain unknown. Furthermore, it is important to recognize that not all scales of turbulent motion may contribute to mixing at flame length and time scales [76], and a physically-consistent model for γ must be representative of this.

These previous studies suggest that the parameter γ in Eq. (1.11) may be expressed as a function of the turbulent Reynolds number (Savard & Blanquart [47], Wang [75]), the Karlovitz number Ka, (Savard & Blanquart [47]) or the Damkhöler number Da, (Han *et al.* [77]). These dimensionless numbers are representative of different effects, and are defined using different quantities. More specifically, Savard & Blanquart [47] investigated effective Lewis numbers for lean premixed turbulent H_2 flames at different turbulent Reynolds numbers

$$Re_T \equiv \frac{u' l}{\nu}, \tag{1.12}$$

where u' is the rms velocity, l is the integral length scale, and ν is the kinematic viscosity, and different Karlovitz numbers

$$Ka \equiv \left(\frac{l_F}{\eta}\right)^2, \tag{1.13}$$

where l_F is the flame thickness and η is the Kolmogorov length scale (additional definitions for the Karlovitz number will be discussed in the following chapters). It should be noted that, for the simulations analyzed in their work, the turbulent Reynolds number and Karlovitz number were related by the scaling $\mathrm{Re_T} \propto \mathrm{Ka}^{2/3}$. Han *et al.* [77] investigated the dependence of differential diffusion on the Damkhöler number

$$Da \equiv \frac{\tau_F}{\tau_C}, \tag{1.14}$$

where τ_F is a flame time scale, taken to be $\tau_F \propto \chi_{st}^{-1}$, and τ_c is a chemical time scale, taken to be $\tau_c \propto \chi_{st,q}^{-1}$, where $\chi_{st,q}$ is the extinction scalar dissipation rate.

From this lack of consensus, it is clear that a more quantitative description of the transition from molecular, diffusion-controlled mixing to turbulence-dominated transport is warranted.

1.3 Objectives and outline

The specific goals of this thesis can be identified as follows:

1. to systematically investigate the validity of the constant non-unity Lewis number assumption, and to quantify the associated computational savings;
2. to propose and evaluate two methods to select these constant Lewis numbers;
3. to propose a methodology to extract effective Lewis numbers from experimental and numerical data sets of turbulent non-premixed flames;
4. to characterize the transition from a molecular-diffusion controlled mixing, to turbulence dominated transport in turbulent non-premixed jet flames using effective Lewis numbers;
5. to assess previously-suggested models for these effective Lewis numbers;
6. to carry out a well-documented DNS of a canonical, laboratory-scale turbulent non-premixed flame, with extensive validation using experimental data;
7. to extract effective Lewis numbers from the DNS data, and assess models for the effective species Lewis numbers.

This manuscript is organized as follows. Chapter 2 provides a description of the governing equations, the numerical approach, and an overview of the flamelet model. Chapter 3 presents a discussion of the validity of the constant Lewis number assumption for chemically reacting flows. In Ch. 4, a flamelet-based methodology to extract effective Lewis numbers from data sets of turbulent diffusion flames is proposed; this methodology is then applied to the Sandia piloted CH_4/air flames [72]; finally, the validity of previously-suggested models for these effective Lewis numbers is assessed. In Ch. 5, a campaign of DNS of Sandia flame B is carried out. More specifically, a detailed *a priori* analysis of the grid resolution is carried out, followed by an analysis of grid independence. Chapter 6 provides detailed comparisons of the DNS with available measurements. In Ch. 7, effective Lewis numbers are extracted from the DNS data base, and the results are compared to the observations from Ch. 4. Major conclusions from the present work and future research directions are summarized in Ch. 8.

1.4 Summary of contributions

First, the validity and the limitations of the constant non-unity Lewis number approach in the description of molecular mixing in laminar and turbulent flames is systematically assessed for a wide range of configurations of practical interest. To carry out this analysis, three test cases are selected, including a lean, highly unstable, premixed hydrogen/air flame, a lean turbulent premixed *n*-heptane/air flame, and a laminar ethylene/air coflow diffusion flame. For the hydrogen flame, both a laminar and a turbulent configuration are considered. The three flames are characterized by fuel Lewis numbers which are less than unity, greater than unity, and close to unity, respectively. For each flame, mixture-averaged transport simulations are carried out and used as reference data. The results of this analysis suggest that, for numerous combustion configurations, the constant non-unity Lewis number approximation leads to small errors when the set of Lewis numbers is chosen properly. The two constant Lewis number-extraction criteria are found to perform well, with neither consistently better than the other. For the selected test cases and our numerical framework, the reduction of computational cost is found to be minimal. This work is the subject of Ch. 3.

Second, the transition in the flame structure of turbulent non-premixed flames from a molecular diffusion-controlled regime to a turbulent transport-dominated one is characterized, and *a priori* models for the effective species Lewis numbers are assessed. More precisely, (i) a flamelet-based methodology is proposed to extract the effective species Lewis numbers from data sets of turbulent non-premixed flames; (ii) this methodology is applied to the Sandia non-premixed methane/air jet flames B, C, D, and E; (iii) and previously-suggested scalings for the effective Lewis numbers are assessed using the same experimental data set. This work is discussed in Ch. 4. For each flame and each downstream measurement station, two flamelet parameters are extracted, including an optimal γ value, "γ^{opt}", and an optimal stoichiometric scalar dissipation rate, "χ_{st}^{opt}". For the four turbulent flames considered, the evaluated effective Lewis numbers are found to transition from their laminar values close to the burner exit plane ($\gamma^{opt} \to 0$), towards unity further downstream ($\gamma^{opt} \to \infty$). Previously-suggested correlations for the parameter γ with both Reynolds and Karlovitz numbers are compared to the extracted γ^{opt} values. Large experimental uncertainties and the limited number of measured quantities prevent a conclusive assessment of these models.

Next, a campaign of DNS of Sandia flame B is carried out. Several simulations are considered, including a baseline case (BL), three refined cases, where the baseline grid is refined twice in the axial (Res-x), radial (Res-r) and azimuthal (Res-z) directions, a unity Lewis number case (UL), and a radiating case (RAD). A careful *a priori* description of the grid design process is carried out. This is followed by a detailed *a posteriori* assessment, including (i) a comparison of the chosen grid resolution with the smallest turbulence and chemistry scales, (ii) an assessment of grid independence though comparisons with refined cases, and (iii) an extensive validation with available experimental data. This work is the subject of Chs. 5 and 6.

Optimal flamelet parameters are extracted from the DNS data base. For case RAD, which is used for comparisons with the experimental data base, the χ_{st}^{opt} and γ^{opt} values are found to follow the same trends observed for the parameters extracted from experimental data for flames B-E. However, χ_{st}^{opt} and γ^{opt} from case RAD are found to under-estimate the corresponding values extracted from the experimental data of flame B.

The radial flame location, r_F, and the jet half-width, r_{12}, are analyzed for case RAD, and compared to the measurements for all flames. The comparison suggests that the r_F and r_{12} profiles from flame B are approximately equal to those from the higher Reynolds number flames only after normalization with respect to the stoichiometric flame tip. Significant differences are found for u'/U_{jet} and l/r_{12} at r_F from case RAD, when compared to the fits used in Ch. 4. Given these differences, the local Reynolds number is re-computed for flame B using case RAD. The γ^{opt} values from case RAD are then plotted with the Re_T values, at the radial flame location r_F. The slope found for case RAD is lower than that of flames C-E. Similarly to flames C-E, these values are found to not fall within the range estimated from the k-ε model coefficients.

Three expressions to compute the flame length scale, l_F, are tested. An optimal expression is selected to compute the flame Karlovitz number. It is shown that the flame thickness estimates used for the experimental data, l_F^{exp}, under-predict l_F. It is observed that when the l_F^{exp} values are used to compute the Karlovitz number, the evolution of γ^{opt} from case RAD has a similar trend to the γ^{opt} values extracted from the experiments. However, when correcting for the flame thickness, a significantly different slope is found. This slope was observed to be close to the predicted flame length scale-based scaling for γ, *i.e.*, $\gamma \propto Ka^{2/3}$.

Chapter 2

THEORETICAL FRAMEWORK AND COMPUTATIONAL METHODOLOGY

All two- and three-dimensional simulations considered in this work were carried out using the low-Mach number code NGA [78], while the one-dimensional simulations were carried out using the FlameMaster code [79]. The governing equations and the numerical approach are presented in this chapter.

2.1 Direct Numerical Simulations

2.1.1 Governing equations

The flows considered in this work are governed by the Navier-Stokes and scalar transport equations. The low-Mach number approximation is considered [80, 81]. This is a valid assumption for a wide range of combustion systems, and allows large density variations while removing acoustic effects. For example, Mach numbers found in laminar and turbulent non-premixed flames are typically well below 0.1 [82].

Conservation of mass and momentum read

$$\frac{\partial \rho}{\partial t} + \nabla \cdot (\rho \boldsymbol{u}) = 0, \tag{2.1}$$

$$\frac{\partial}{\partial t}(\rho \boldsymbol{u}) + \nabla \cdot (\rho \boldsymbol{u} \otimes \boldsymbol{u}) = -\nabla p + \nabla \cdot \boldsymbol{\sigma} + \boldsymbol{f}, \tag{2.2}$$

respectively, where p is the hydrodynamic pressure, $\boldsymbol{u}$ is the velocity, $\boldsymbol{\sigma}$ is the stress tensor

$$\boldsymbol{\sigma} = \mu(\nabla \boldsymbol{u} + \nabla \boldsymbol{u}^T) - \frac{2}{3}\mu(\nabla \cdot \boldsymbol{u})\boldsymbol{I}, \tag{2.3}$$

where μ is the dynamic viscosity of the mixture, and $\boldsymbol{f}$ represents all volumetric forces, including a gravitational term. The viscosity μ is computed as [43]

$$\mu = \frac{1}{2}\left(\sum_{i=1} X_i \mu_i + \left[\sum_{i=1} \frac{X_i}{\mu_i}\right]^{-1}\right), \tag{2.4}$$

where the ith species viscosity is computed using its kinetic theory definition [83]. The transport equation for the ith species, which was introduced in Ch. 1, and is repeated here for clarity, reads

$$\frac{\partial}{\partial t}(\rho Y_i) + \nabla \cdot (\rho \boldsymbol{u} Y_i) = -\nabla \cdot \boldsymbol{j_i} + \dot{\omega}_i, \tag{2.5}$$

The mixture-averaged diffusion coefficients of species i, $D_{i,m}$, are calculated either by supplying a set of Lewis numbers, Eq. (1.1), or by using a mixture-averaged formulation, *i*.e., using Eq. (1.5). The binary diffusion coefficients $\mathcal{D}_{ki}$ are computed using classical molecular gas theory [40]. In this work, Soret and Dufour effects are not considered. The energy equation reads

$$\frac{\partial}{\partial t}(\rho T) + \nabla \cdot (\rho \boldsymbol{u} T) = \nabla \cdot (\rho \alpha \nabla T) + \dot{\omega}_T - \frac{1}{c_p} \sum_i c_{p,i} \boldsymbol{j_i} \cdot \nabla T + \frac{\rho \alpha}{c_p} \nabla c_p \cdot \nabla T, \quad (2.6)$$

where T is the temperature, $c_{p,i}$ is ith species specific heat at constant pressure, and $\dot{\omega}_T = -c_p^{-1} \sum_i h_i(T) \dot{\omega}_i$ is the temperature source term; $h_i(T)$ are the species specific enthalpies at temperature T. The heat diffusivity α is computed as

$$\alpha = \frac{\lambda}{\rho c_p}, \quad (2.7)$$

where λ is computed using [42]

$$\lambda = \frac{1}{2} \left(\sum_{i=1} X_i \lambda_i + \left[\sum_{i=1} \frac{X_i}{\lambda_i} \right]^{-1} \right). \quad (2.8)$$

In Eq. (2.8), the species thermal conductivities λ_i are computed using the modified Eucken formulation [83]. The equation of state is given by the perfect gas law

$$\rho = \frac{W P_0}{RT}, \quad (2.9)$$

where W is the mixture molecular weight, P_0 is the thermodynamic pressure, and R is the universal gas constant.

2.1.2 Radiation model

For some simulations, radiation heat transfer is considered. This is done by means of a radiation source term added to the energy equation, *i*.e., $\dot{q}_{\text{rad}}/c_p$, where $\dot{q}_{\text{rad}}$ is modeled according to the RADCAL model of Grosshandler [84]

$$\dot{q}_{\text{rad}} = -4\sigma \sum_i p_i a_{p,i} (T^4 - T_\infty^4), \quad (2.10)$$

where $\sigma = 5.669\text{e-}08$ W/m^{2}K^4 is the Stefan-Boltzmann constant, p_i and $a_{p,i}$ are the partial pressure and the Planck mean absorption coefficient of the ith species, respectively, and T_∞ is the background temperature. The $a_{p,i}$ coefficients are fitted as functions of the temperature for CO_2, H_2O, CH_4, and CO, which account for most of the radiation heat losses. This model assumes that the gas is optically thin, and all radiation heat transfer is dispersed to the background.

In this work, radiation heat losses are included for two flames. The first, which is discussed in Ch. 3, is a laminar N_2-diluted C_2H_4/air-coflow pressurized diffusion flame, which is one of the target flames of the International Sooting Flame (ISF) Workshops [27, 85, 86]. The purpose of Ch. 3, is to assess the validity of the constant non-unity Lewis number assumption over a wide range of combustion configurations. While the optically-thin RADCAL model may not be the ultimate choice for the laminar C_2H_4/air flame, it is used consistently across all four cases, and does not impact the outcome of that analysis.

The second is Sandia flame B, a CH_4/air, partially premixed, turbulent jet flame, discussed in Chs. 5, 6, and 7, which is one of the target flames of the International Workshop on Measurement and Computation of Turbulent Nonpremixed Flames (TNF) [72]. While RADCAL is the suggested radiation model for both flames [72, 86], enabling a computationally-inexpensive treatment of radiation, the optically-thin assumption is known to overpredict the radiant fraction for hydrocarbon flames [87]. Frank *et al.* [87] performed radiant fraction and multiscalar measurements for Sandia flames C-F. In their work, radiation calculations using RADCAL were coupled with temperature and species mean profiles, and it was found that, for Sandia flame D, the total radiant power for the emission-only case was 39% greater than emission/absorption computations. It is suggested that this over-prediction of radiative heat losses is due to the strong absorption by CO_2 at the 4.3 μm wavelength [87–89]. However, the emphasis of the work of Frank *et al.* [87] is on the prediction of nitric oxide (NO) formation, which is known to be highly sensitive to the radiation model [90–93]. For the simulation of Sandia flame B discussed in Chs. 5, 6, and 7, the NO chemistry is not considered in the chemistry model. While not the primary goal of those chapters, radiation heat loss is considered to assess if a good agreement with experiments can be achieved. Further, in Ch. 7 it is shown that including radiation heat loss does not affect the analysis carried out in that chapter. For all these reasons, the RADCAL model is a valid, practical choice for the present work.

Scalar transport is controlled by a balance of three main contributions, including convection, diffusion, and the scalar source term. For the flames considered in this work, the radiation source term, $\dot{q}_{\text{rad}}/c_p$, is expected to be small compared to the dominant terms in Eq. (2.6). For instance, the radiant fraction, f_{rad}, values measured for the Sandia flames C-F by Frank *et al.* [87], were found to vary from 6.4% for flame C, to 3.0% for flame F. In their work, the radiant fraction was defined

as the ratio of the total radiated power, $\dot{S}_{\text{rad}}$, to the power released in the combustion reaction

$$f_{\text{rad}} \equiv \frac{\dot{S}_{\text{rad}}}{\dot{m}_{\text{fuel}}\Delta H_{\text{comb}}}, \tag{2.11}$$

where $\dot{m}_{\text{fuel}}$ and ΔH are the mass flow rate of the fuel and the heat of combustion, respectively. The reduction of f_{rad} with increasing jet Reynolds number was primarily ascribed to the reduced residence time [87]. For Sandia flame B, f_{rad} should be higher, yet close to the measured value for flame C, which is relatively small. For reference, the reported energy release of the pilot flame in flames C-F is only approximately 6% of the main jet [72]. It will be shown in Ch. 6 that the maximum temperature for the radiating simulation is about 70K less than the adiabatic case (which is approximately a 3% reduction).

2.1.3 Numerical approach

The governing equations are solved using the finite differences, discretely energy-conserving code NGA, designed for the simulation of variable density laminar and turbulent flows [78]. The low-Mach Navier-Stokes equations are solved using a fractional step approach [94], whereby the momentum, scalar, and density fields are staggered in time. Time marching is carried out using a semi-implicit Crank-Nicolson scheme, where the integration of the chemical source terms is carried out using the preconditioned iterative method of Savard *et al.* [95] (four subiterations are used). With this semi-implicit time-stepping, the time step is constrained by the stiffness of the chemical source terms in laminar flames, while for the turbulent flames the convective CFL becomes more restrictive. Conservation of mass is then enforced through a pressure Poisson equation. For most simulations, the Lawrence Livermore National Laboratories HYPRE libraries are used for the pressure solver [96]. In the present work, the scheme used for the Navier-Stokes equations is second-order accurate both in space and in time. The scalars (Y_i, T) are transported using the third-order accurate Bounded QUICK (BQUICK) scheme [97], which ensures boundedness of the transported scalars. The one-dimensional flames are solved using the FlameMaster code [79]. NGA and FlameMaster give the same simulation results in one-dimensional calculations.

The NGA code has been extensively tested to verify the order of accuracy of the numerical methods. Desjardin *et al.* [78] simulated a range of canonical, constant density flows, to assess the influence of the order of the spatial numerical schemes on the solution. Savard *et al.* [95] considered one-dimensional premixed flames to

assess the order of accuracy of the preconditioned iterative method for the integration of the chemical source terms. The BQUICK scheme has been tested considering constant density canonical problems [98]. Tests involving laminar diffusion flames have not been performed, and should be the subject of future work. One promising configuration is the one-dimensional counterflow diffusion flame, which is already implemented in several benchmark codes, such as FlameMaster [79], CHEMKIN [99], and Cantera [100].

For each flame considered in this thesis, a description of the computational domain and the boundary conditions is provided in the respective chapter.

2.2 The flamelet model

In this section, the flamelet model is reviewed. Here, only the species flamelet equations will be discussed, but an analogous equation for the temperature can be derived. Detailed derivations may be found in the work of Xuan [82] and Xuan & Blanquart [101]. For simplicity, constant non-unity Lewis numbers are assumed.

2.2.1 Generalized coordinate transformation

As a first step towards deriving the flamelet equations, the following coordinate transformation is considered

$$(x_1, x_2, x_3, t) \rightarrow (Z(x_1, x_2, x_3, t), Z_2(x_1, x_2, x_3, t), Z_3(x_1, x_2, x_3, t), \tau), \tag{2.12}$$

where Z_2 and Z_3 are curvilinear coordinates chosen such that

$$\nabla Z \cdot \nabla Z_2 = 0 \quad \text{and} \quad \nabla Z \cdot \nabla Z_3 = 0 \tag{2.13}$$

everywhere in the domain. Equation (2.13) ensures that Z_2 and Z_3 lie within the isosurface of mixture fraction Z. A two-dimensional sketch of this coordinate transformation is shown in Fig. 2.1.

2.2.2 Transformed species transport equations

Using the coordinate transformation given by Eq. (2.12), as well as the transport equation for the mixture fraction given by Eq. (1.6), the species transport equations given by Eq. (2.5) can be written in the local (Z, Z_2, Z_3) reference frame

$$\rho \frac{\partial Y_i}{\partial \tau} + \underbrace{\rho \sum_{k=2}^{3} \left[\frac{\partial Y_i}{\partial Z_k} \left(\frac{\partial Z_k}{\partial t} + \boldsymbol{u} \cdot \boldsymbol{\nabla} Z_k \right) \right]}_{\text{Lagrangian transport } L_t} +$$

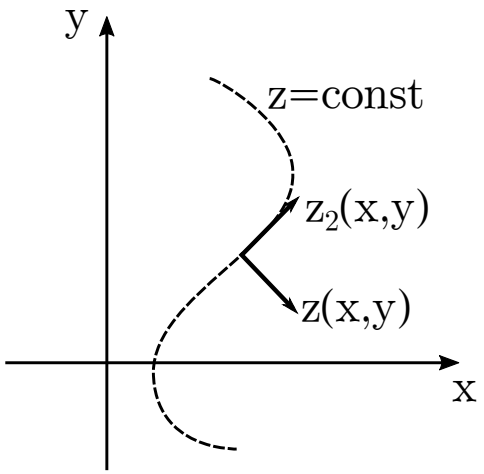

Figure 2.1: Two-dimensional schematic of the coordinate transformation (adapted from Xuan & Blanquart [82]).

$$\underbrace{\left(1-\frac{1}{\mathrm{Le}_i}\right)\nabla\cdot(\rho\alpha\nabla Z)\,\frac{\partial Y_i}{\partial Z}}_{\text{convection in mixture fraction } C_Z} \tag{2.14}$$

$$\begin{aligned}
&= \underbrace{\frac{\rho\chi}{2\mathrm{Le}_i}\frac{\partial^2 Y_i}{\partial Z^2}}_{\text{normal diffusion } D_Z} + \underbrace{\dot{\omega}_i}_{\text{source } S} + \\
&+ \underbrace{\sum_{k=2}^{3}\frac{\rho\chi_k}{2\mathrm{Le}_i}\frac{\partial^2 Y_i}{\partial Z_k^2} + \frac{2\rho\alpha}{\mathrm{Le}_i}\left(\boldsymbol{\nabla}Z_2\cdot\boldsymbol{\nabla}Z_3\right)\frac{\partial^2 Y_i}{\partial Z_2\partial Z_3}}_{\text{tangential diffusion } D_t} + \\
&+ \underbrace{\frac{1}{\mathrm{Le}_i}\sum_{k=2}^{3}\boldsymbol{\nabla}\cdot(\rho\alpha\boldsymbol{\nabla}Z_k)\frac{\partial Y_i}{\partial Z_k}}_{\text{tangential convection } C_t} + \\
&+ \underbrace{\boldsymbol{\nabla}\cdot(\rho Y_i\boldsymbol{u}_{c,i})}_{\text{correction terms R}},
\end{aligned} \tag{2.15}$$

where

$$\chi \equiv 2D|\nabla Z|^2, \tag{2.16}$$

and

$$\chi_k \equiv 2D|\nabla Z_k|^2, \text{ for } k = 2, 3. \tag{2.17}$$

In Eq. (2.15), the second and third terms on the left hand side (LHS) represent the Lagrangian transport of the flamelet in the Z_2 and Z_3 directions, and the convection in mixture fraction, respectively. The first term on the right hand side (RHS) represents normal diffusion in mixture fraction. The second term on the RHS is the

source term of species i. The third and fourth terms on the RHS represent tangential diffusion and convection along the iso-surfaces of mixture fraction. The fifth term represents convection in mixture fraction. The last term on the RHS is the unprocessed correction terms from Eq. (2.5).

2.2.3 Convection in mixture fraction

The convection in mixture fraction term C_Z is present only with non-unity Lewis numbers. Following Xuan [82], the normalized velocity in mixture fraction space can be split in the sum of two contributions

$$\nabla \cdot (\rho\alpha\nabla Z) = \boldsymbol{n} \cdot \nabla(\rho\alpha|\nabla Z|) + \rho\alpha|\nabla Z|\nabla \cdot \boldsymbol{n}, \tag{2.18}$$

where the normal unity vector to the mixture fraction iso-surface $\boldsymbol{n}$ is

$$\boldsymbol{n} = \frac{\nabla Z}{|\nabla Z|}. \tag{2.19}$$

The first term on the RHS of Eq. (2.18) can be expressed as

$$\boldsymbol{n} \cdot \nabla(\rho\alpha|\nabla Z|) = |\nabla Z|\frac{\partial}{\partial Z}(\rho\alpha|\nabla Z|) \tag{2.20}$$

$$= \left(\frac{\chi}{2\alpha}\right)^{\frac{1}{2}} \frac{\partial}{\partial Z}\left[(\rho\alpha)^{\frac{1}{2}}\left(\frac{\rho\chi}{2}\right)\right] \tag{2.21}$$

$$= \frac{1}{4}\left(\frac{\partial\rho\chi}{\partial Z} + \frac{\chi}{\alpha}\frac{\partial\rho\alpha}{\partial Z}\right). \tag{2.22}$$

Considering the local curvature of the mixture fraction iso-surface

$$\kappa = \nabla \cdot \boldsymbol{n}, \tag{2.23}$$

the second term on the RHS of Eq. (2.18) can be written as

$$\rho\alpha|\nabla Z|\nabla \cdot \boldsymbol{n} = \rho\kappa\sqrt{\frac{\chi\alpha}{2}}. \tag{2.24}$$

Finally, the convection term in mixture fraction C_Z can be written as the sum of two contributions

$$\left(\frac{1}{Le_i} - 1\right)\nabla \cdot (\rho\alpha\nabla Z)\,\frac{dY_i}{dZ} = \underbrace{\left(\frac{1}{Le_i} - 1\right)\rho\kappa\sqrt{\frac{\chi\alpha}{2}}\frac{dY_i}{dZ}}_{\text{curvature } C_K} +$$

$$\underbrace{\left(\frac{1}{Le_i} - 1\right)\frac{1}{4}\left(\frac{\partial\rho\chi}{\partial Z} + \frac{\chi}{\alpha}\frac{\partial\rho\alpha}{\partial Z}\right)\frac{dY_i}{dZ}}_{\text{normal convection } C_1}. \tag{2.25}$$

In Eq. (2.25), the first term on the RHS represents normal convection, while the second term accounts for the effect of curvature on the flame.

2.2.4 One-dimensional curved flamelets

If all derivatives in Z_2 and Z_3 can be neglected, *i*.e., if one-dimensionality can be assumed in the new coordinate system (Z, Z_2, Z_3), then the exact flamelet equations given by Eq. (2.15) can be simplified to

$$\rho\frac{\partial Y_i}{\partial \tau} + \left(1 - \frac{1}{Le_i}\right)\left[\frac{1}{4}\left(\frac{\partial \rho\chi}{\partial Z} + \frac{\chi}{\alpha}\frac{\partial \rho\alpha}{\partial Z}\right) + \rho\kappa\sqrt{\frac{\chi\alpha}{2}}\right]\frac{\partial Y_i}{\partial Z} = \frac{\rho\chi}{2Le_i}\frac{\partial^2 Y_i}{\partial Z^2} + \dot{\omega}_i, \quad (2.26)$$

where the correction terms are not shown for clarity.

2.2.5 One-dimensional flat flamelets

If one further neglects the curvature effects from Eq. (2.26), then the flat flamelet model of Pitsch & Peters [66] is recovered (in their derivation the Lewis numbers were not considered to be constant in mixture fraction space)

$$\rho\frac{\partial Y_i}{\partial \tau} + \left(1 - \frac{1}{Le_i}\right)\left[\frac{1}{4}\left(\frac{\partial \rho\chi}{\partial Z} + \frac{\chi}{\alpha}\frac{\partial \rho\alpha}{\partial Z}\right)\right]\frac{\partial Y_i}{\partial Z} = \frac{\rho\chi}{2Le_i}\frac{\partial^2 Y_i}{\partial Z^2} + \dot{\omega}_i. \quad (2.27)$$

It should be reminded that the Lewis number of the mixture fraction, $Le_Z \equiv \alpha/D$ is set to 1 in the present work. A flamelet equation for the temperature analogous to Eq. (2.27), may also be written. In this thesis, steady-state solutions of Eq. (2.27), with unity, constant non-unity, or mixture-averaged Lewis numbers, are considered.

If one further assumes unity Lewis numbers, the original flamelet model of Peters [65, 102] is recovered

$$\rho\frac{\partial Y_i}{\partial \tau} = \frac{\rho\chi}{2}\frac{\partial^2 Y_i}{\partial Z^2} + \dot{\omega}_i, \quad (2.28)$$

where the correction terms are dropped for clarity. In other words, under unity Lewis number and thin flame, curvature does not affect the flamelet solution.

Unity Lewis number flamelets are a popular reduced-order model for chemistry tabulation in simulations of turbulent flames, due to their simplicity. The typical justification for this approach is that for large enough Reynolds numbers, differential diffusion effects have a small impact on the average flame structure, and can be neglected altogether [46, 103]. However, a large body of work over the past four decades has shown that differential diffusion effects cannot be neglected at moderate turbulence intensities (see for example Bilger and coworkers [13, 104, 105]), and may only disappear at very high Reynolds numbers [19, 56, 106, 107]. As discussed in Ch. 1, differential diffusion effects in turbulent non-premixed flames are observed to transition from a molecular, diffusion-controlled mixing regime, to a

turbulence-dominated one with (*i*) increasing axial distance from the issuing nozzle and (*ii*) increasing jet Reynolds number [46, 69–72]. Thus, while offering a significant simplification, the unity Lewis number flamelet model may represent a harsh approximation. This will be discussed in the following chapters.

2.2.6 Flamelet-based modeling of turbulent non-premixed combustion

The flamelet equations represent a popular reduced-order model in turbulent non-premixed combustion [10]. They provide a constitutive relationship between thermo-chemical quantities and a small number of scalars, including the mixture fraction, and either its scalar dissipation rate or a progress variable [20, 67]. More precisely, the reactive scalar profiles, $\boldsymbol{\psi}$, obtained from the solution of the steady-state flamelet equations [65], can be written as

$$\boldsymbol{\psi} = \boldsymbol{\psi}^{\mathrm{FM}}(Z, \chi_{st}), \tag{2.29}$$

Where the superscript "FM" stands for "Flamelet Model", and χ has been parameterized by its stoichiometric value,

$$\chi(Z) = \chi_{st} \frac{f(Z)}{f(Z_{st})}. \tag{2.30}$$

Several analytical expressions for $f(Z)$ are available from the literature [56, 65, 108]. In general, the parameter χ_{st} will change depending on the spatial location, $\boldsymbol{x}$, and time, t. In an LES formulation, which represents a popular application of the flamelet model [61], the resolved reactive scalars, $\widetilde{\boldsymbol{\psi}}$, can then be computed through a subfilter pdf approach

$$\widetilde{\boldsymbol{\psi}}(\boldsymbol{x}, t) = \iint \boldsymbol{\psi}^{\mathrm{FM}}(Z, \chi_{st}; \boldsymbol{x}, t) P(Z, \chi_{st}; \boldsymbol{x}, t) d\chi_{st} dZ, \tag{2.31}$$

where $P(Z, \chi_{st}; \boldsymbol{x}, t)$ is the joint filtered pdf of Z and χ_{st}, and quantifies the unresolved turbulence-chemistry interactions. It should be noted that the steady-state flamelet model is just one approach to provide a constitutive relationship between $\boldsymbol{\psi}$ and a limited number of scalars. In Eq. (2.31), the joint filtered pdf is un unknown, and is generally obtained through transported pdf methods [109], or through a presumed-pdf approach.

The focus of this work is on the flamelet closure given by Eq. (2.29). In Chs. 4 and 7, it will be shown that a single steady-state, non-unity Lewis number flamelet can be well representative of the conditional mean flame structure of a turbulent non-premixed jet flame. However, two flamelet parameters must be chosen properly, including an *optimal* χ_{st} value, χ_{st}^{opt}, and an *optimal* γ value, γ^{opt}. The γ^{opt}

values determine the effective species Lewis numbers (Eq. (1.11)) used to solve the flamelet equations.

Chapter 3

ASSESSMENT OF THE CONSTANT NON-UNITY LEWIS NUMBER ASSUMPTION

Chapter 3 has been adapted from:

- N. Burali *et al.* "Assessment of the constant non-unity Lewis number assumption in chemically-reacting flows". *Combust. Theor. Model.* Vol. 20, No. 4 (2016), pp. 632-657, doi:10.1080/13647830.2016.1164344.

3.1 Introduction

In many practical combustion systems the correct representation of differential diffusion effects is of crucial importance. In this chapter, the validity of two common assumptions, namely constant unity and constant non-unity Lewis numbers, is systematically assessed for several configurations, spanning a wide range of operating conditions.

The objectives of this work include (a) understanding how much the Lewis numbers fluctuate, (b) investigating in which circumstances these fluctuations are relevant, and (c) comparing two constant Lewis number extraction methodologies. In addressing these questions, one should be mindful of the full spectrum of combustion configurations, including (but not limited to) differences between premixed and diffusion flames, laminar and turbulent flames, light fuels and heavy fuels. The study should consider not only major species, but also minor ones, especially soot precursors. The work presented herein is focused on multi-dimensional and unsteady flames, which present significant computational challenges. While some of the theoretical analysis will be done using one-dimensional flames, the objective is not to suggest changes to one-dimensional, steady-state codes (such as Chemkin, FlameMaster, and Cantera). Furthermore, the analysis presented in this chapter considers only ideal gases, and does not include trans-critical effects.

To carry out this analysis, three test cases are investigated, including a lean, highly unstable, premixed hydrogen/air flame, a lean turbulent premixed n-heptane/air flame, and a laminar ethylene/air coflow diffusion flame.

This chapter is organized as follows. Section 3.2 presents a description of the chosen flames. These include a lean premixed H_2/air flame (Sec. 3.3), a lean *n*-heptane/air flame (Sec. 3.4), and a pressurized, laminar, C_2H_4/air-coflow diffusion flame (Sec. 3.5). For each flame, a one-dimensional analysis is performed to estimate the variation of the Lewis numbers and to show a comparison of two Lewis number extraction methodologies against both a mixture-averaged transport benchmark and a unity Lewis number simulation. The one-dimensional analysis is followed by multi-dimensional simulations. Section 3.6 provides a discussion of the computational cost of constant Lewis number simulations compared to their mixture-averaged counterparts. Finally, a summary of the observations will be discussed in Sec. 3.7.

3.2 Test cases and chemical models

3.2.1 Selected flames

To explore the validity of the constant non-unity Lewis number approach, three flames have been investigated, which are representative of common engineering configurations, but at the same time present strong differential diffusion effects.

First, a premixed H_2/air flame has been selected, with an equivalence ratio of 0.4, close to the extinction limit. The small molecular weight of the fuel translates into a Lewis number close to 0.3, and, consequently, strong differential diffusion effects. This flame corresponds to a highly unstable configuration, albeit with a simple chemistry, which is ideal to study the effect of the choice of the diffusion coefficients on the evolution of the flame. Two freely propagating configurations have been considered: a two-dimensional laminar flame, and a three-dimensional moderately turbulent case. More details will be provided in the following sections.

The second test case is a turbulent premixed, slightly lean ($\phi = 0.9$), *n*-heptane/air flame, which is considered to study the interaction between intense turbulent transport and differential diffusion. This flame is characterized by a fuel Lewis number larger than unity (about 2.9) and a high unburnt Karlovitz number of $Ka = (l_F/S_L)(\varepsilon/\nu)^{\frac{1}{2}} = 220$, where l_F and S_L are the laminar unstretched flame thickness and flame speed, respectively, ε is the dissipation of turbulent kinetic energy, k, and ν is the kinematic viscosity. In this work ε is defined as u'^3/l, where u' is the root mean square (rms) velocity, and l is the integral length scale.

The third flame is a pressurized, laminar, C_2H_4/air-coflow diffusion flame. This configuration was chosen as it is one of the target configurations of the 2014/2016

International Sooting Flame (ISF) Workshops [27, 85] (Target Flame 3), and experimental data is available for comparisons. Under the given conditions, this flame does not produce significant amounts of soot, which is not considered in this work. The radiative heat loss associated with strong soot production would significantly impact the temperature field and, hence, the transport properties. The large Lewis numbers of typical soot precursors are expected to play an important role (for example, the Lewis number of naphthalene for this flame is around 3.0), and the focus is placed on the formation of these soot precursors.

In summary, with these three cases, we have covered both laminar and turbulent flames, light, medium, and heavy fuels, and finally, major and trace species. Given the large range of conditions considered, the conclusions to be drawn should be general. It should also be noted that the three configurations were selected to exaggerate the effects due to differential diffusion. However, it should be noted that they all contain a large fraction of N_2 as a diluent.

3.2.2 Lewis numbers

For each of the selected flames presented in Sec. 3.2.1, four different test cases are compared: one using mixture-averaged transport properties (i), which is used as a benchmark, two simulations with constant Lewis numbers (test cases (ii) and (iii)), and a fourth simulation with unity Lewis numbers (iv). The two sets of constant Lewis numbers (test cases (ii) and (iii)) are extracted from one-dimensional FlameMaster simulations.

Evaluating Lewis numbers from one-dimensional flames requires particular attention. In test case (ii), the Lewis numbers are taken at the maximum temperature. In test case (iii), the Lewis numbers of intermediates are taken at their peak mass fractions, while the maximum temperature criterion is used for the reactant/product species. The two Lewis number-extraction criteria of cases (ii) and (iii) are suggested on the basis that (ii) most of the chemistry occurs at higher temperatures, and that (iii) mass diffusion fluxes are expected to be the strongest where the species mass fractions are close to their peak values. As intermediate species present a peak close to the flame front, the two methods are expected to yield similar results.

As an example of the quality of the two test cases (ii) and (iii) at predicting global quantities, Fig. 3.1 shows a comparison of the relative change of S_L and l_F, with respect to the benchmark (i), against equivalence ratio for one-dimensional hydro-

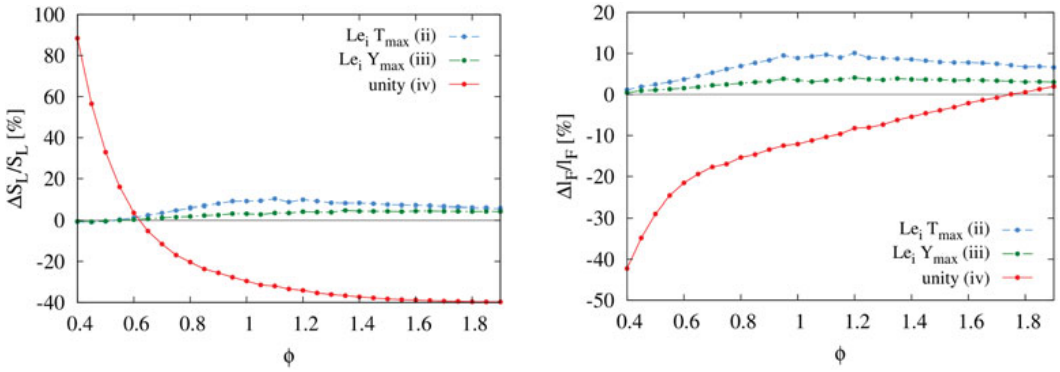

(a) Relative change of S_L. **(b)** Relative change of l_F.

Figure 3.1: Relative change of laminar flame speed (a) and laminar flame thickness (b) with respect to the benchmark test case (i). Test cases (ii)-(iv) correspond to the blue, green, and red lines, respectively.

gen/air premixed flames. While not being the optimal, test case (iii) predicts S_L and l_F with about half the errors of test case (ii).

3.2.3 Chemical mechanisms

For the simulations considered in this chapter, three chemical models are used. The combustion of hydrogen uses the 9-species, 52-reaction mechanism of Hong *et al.* [110], without argon. The mechanism for the ethylene flame is the full CaltechMech version 2.0 [111], which contains 171 species and 1835 reactions (forward and backward reactions counted separately). Finally, the heptane flame uses a 35-species, 217 reaction (forward and backward reactions counted separately) reduced version of the mechanism of Bisetti *et al.* [16] (aromatic species have been removed).

3.3 Premixed hydrogen/air flame

The first configuration corresponds to a thermo-diffusively unstable lean hydrogen/air flame. The selected equivalence ratio of $\phi = 0.4$ is characteristic of conditions investigated in low swirl burners [112, 113]. Before presenting the two- and three-dimensional simulations, a one-dimensional analysis of this configuration is discussed in the following section.

3.3.1 One-dimensional preliminary analysis

Figure 3.2a shows the Lewis numbers against temperature obtained from a one-dimensional mixture-averaged calculation. As can be seen, the Lewis numbers have a limited variation between the unburnt mixture and the burnt products (the species

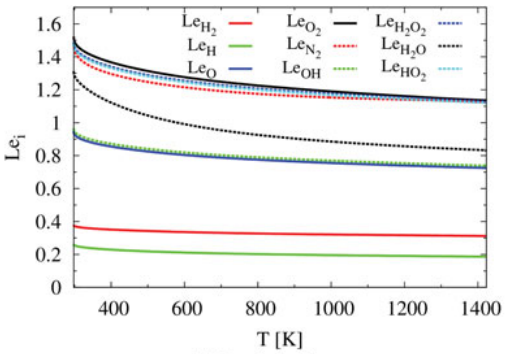

(a) Lewis numbers.

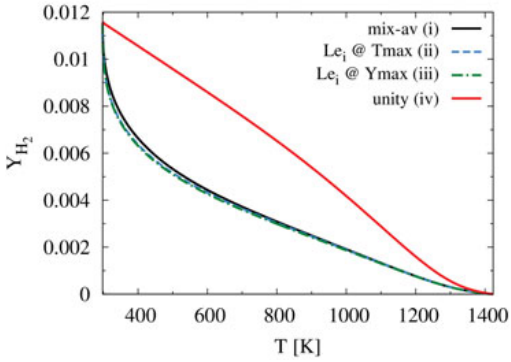

(b) Fuel mass fraction.

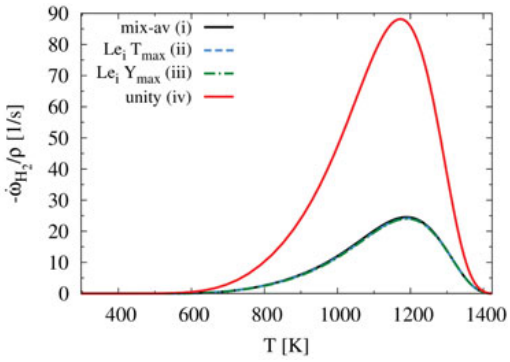

(c) Fuel source term.

Figure 3.2: Variation of the Lewis numbers through the lean laminar premixed H_2/air flame (a), fuel mass fraction (b) and its source term (c) against temperature for mixture-average transport (black), unity Lewis numbers (red), and Lewis numbers corresponding to T max (blue) and Y_i, max (green). The blue and green lines are overlapping in both plots. These data were obtained from one-dimensional flame calculations.

presenting the greatest change is H, with an excursion of about 35%). This is in part a consequence of the large fraction of molecular nitrogen (inherently present in air)

Figures 3.2b and 3.2c show a comparison of the mass fraction of the fuel and its source term obtained from one-dimensional simulations corresponding to test cases (i)–(iv). Cases (ii) and (iii) are in excellent agreement with the benchmark (i), while the simulation with unity Lewis numbers (iv) predicts a radically different profile. The results are not surprising, as Fig. 3.2b shows that the Lewis numbers present limited excursion through the flame (10-20%). From these results, it would seem that the location (in the flame) where the Lewis numbers are evaluated has little influence on the results.

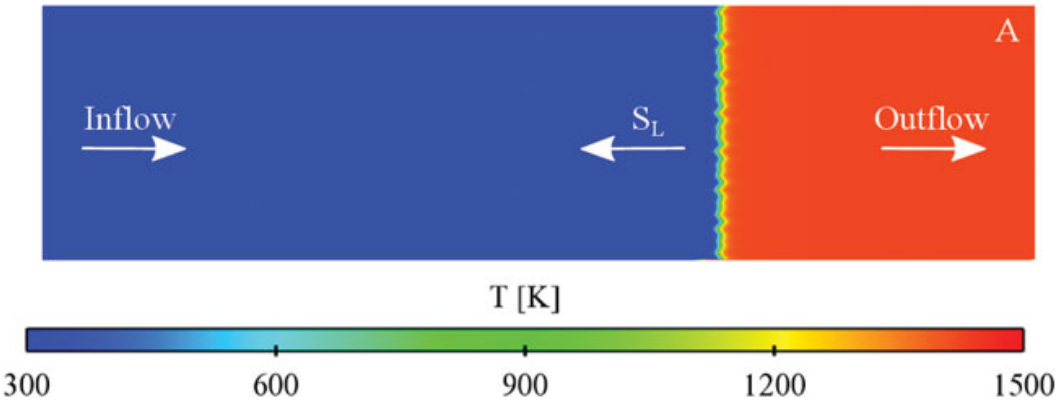

Figure 3.3: Sketch of the computational domain for the two-dimensional H_2/air flame simulation.

T_u (K)	P (atm)	ϕ	l_F (mm)	$n_x \times n_y$	$\Delta x = \Delta y$ (mm)	l_F/S_L (ms)
298	1	0.4	0.65	1888 × 472	0.0424	3

Figure 3.4: Parameters for the two-dimensional H_2/air flame simulation.

3.3.2 Two-dimensional simulations

Configuration

The laminar H_2/air flame is simulated using the two-dimensional domain shown in Fig. 3.3, with the numerical parameters given in Table 1. The initial two-dimensional data file is generated from a one-dimensional unstretched flame, obtained using the FlameMaster code with mixture-averaged transport properties. The one-dimensional solution is then interpolated to build the two-dimensional initial data file. The two-dimensional grid is uniform in both directions, and the ratio of the laminar flame thickness to the spacing between nodes is approximately 15, which was found to be sufficient to represent the flame. Figure 3.5 shows the dimensionless source term of OH along the centerline of a data file corresponding to a two-dimensional simulation with mixture-average properties, at 10 ms. As can be seen, the grid spacing is such that there are about 20 grid points per OH layer, as suggested by Hawkes *et al.* [114].

The initial flame front is perturbed according to

$$x_{f,0} = E + A \sum_{i=1,2} \cos\left(\frac{2\pi k_i y}{H}\right), \tag{3.1}$$

where $x_{f,0}$ is the initial flame position, E is the average flame position, k_1 and k_2 are two coprime modes, y is the vertical coordinate, and H is the height of the

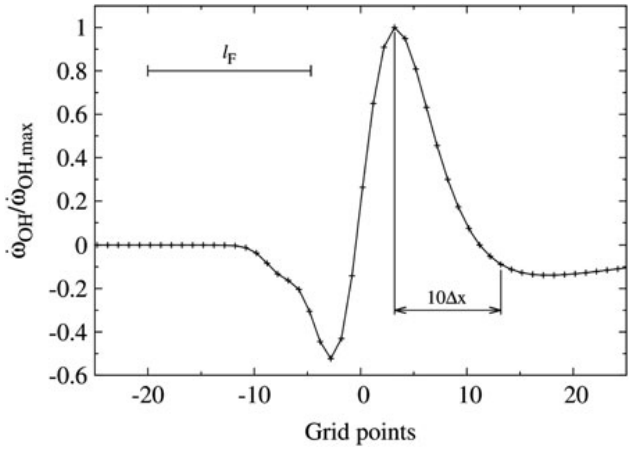

Figure 3.5: Normalized OH production term against grid spacing.

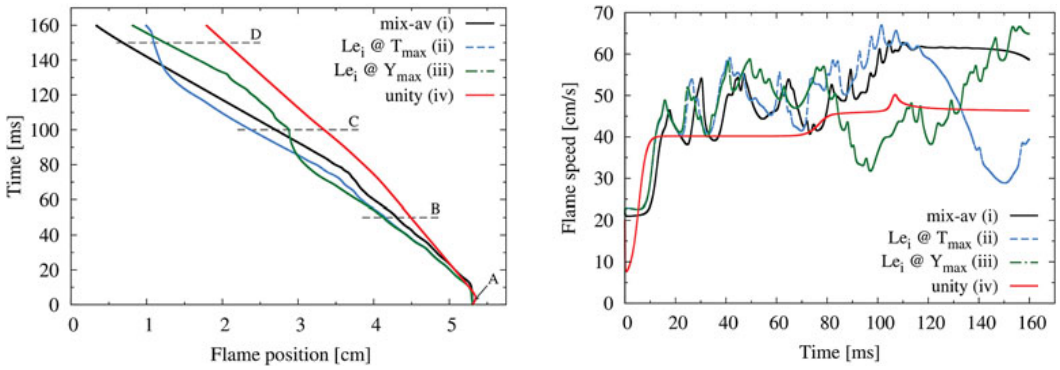

(a) Average flame position. **(b)** Consumption-based flame speed.

Figure 3.6: Average flame position (a) and fuel consumption-based flame speed (b) for the four simulations of the two-dimensional lean H_2/air flame. Snapshots corresponding to times B, C, and D are shown in Fig. 3.7, while time A was shown in Fig. 3.3.

domain. A is set to 10^{-4}m, and k_1 and k_2 are 20 and 13, respectively. The two modes produce an asymmetric initial perturbation, which is intended to trigger the thermo-diffusive and Darrieus-Landau instabilities quickly. This flame was selected as its evolution is strongly dependent on the choice of the initial perturbation [115], and any deviations (even due to minute differences between the four cases) will undoubtedly lead to different flame evolutions.

An inflow velocity is provided to match the unstretched laminar flame speed of the benchmark case (i). However, due to the development of cellular structures, the flame burns faster and, hence, propagates to the left. Yet the length of the domain is sufficient for the simulation time. A convective outflow condition is used for the right boundary, while periodic boundary conditions are used in the vertical direction.

Results

In this section, the four two-dimensional simulations corresponding to the four cases (i)-(iv) are compared. All four simulations start from the same initial flow field (shown in Fig. 3.3), and share the same grid.

Figure 3.6a shows the average flame position for the four simulations, which is calculated by averaging a progress variable in the vertical direction, and selecting the horizontal coordinate corresponding to a predetermined value. The progress variable is Y_{H_2O}, and the value corresponding to the flame is set to 0.04. Figure 3.6b shows the corresponding consumption-based flame speed, $S_{\dot{\omega}_{H_2}}(t)$, defined as

$$S_{\dot{\omega}_{H_2}} = \frac{1}{\rho_u Y_{H_2,u} A} \int_V -\dot{\omega}_{H_2}(t) dV, \tag{3.2}$$

where $\dot{\omega}_{H_2}$ is the H_2 source term, V is the volume of the computational domain, A is the cross section, and ρ_u and $Y_{H_2,u}$ are the unburnt density and fuel mass fraction, respectively. Figure 3.7 shows the snapshots marked B through D, which correspond to 50, 100, and 150 ms, respectively. The initial snapshot, A, was shown in Fig. 3.3.

In all cases, the initial perturbations disappear, leading to an almost smooth flame front. This initial transient (represented by the vertical section of the lines in Fig. 3.6b) lasts for about 10 ms, after which test cases (i)-(iii) rapidly develop instabilities, and accelerate towards the inflow at a flame speed greater than the respective S_L (Fig. 3.6b). After about 5 ms, the unity Lewis number test case propagates towards the inlet with a flat flame front (up to about 70 ms), and at the unstretched laminar flame speed (Fig. 3.6b). At 70 ms, there is a change of slope in Fig. 3.6a of the unity Lewis number test case, corresponding to the appearance of the Darrieus-Landau instabilities, and a consequent increase of the average burning velocity. As can be seen from Fig. 3.6b, despite the initial shift of about 4 ms, both cases (ii) and (iii) remain qualitatively and quantitatively very close to the mixture-averaged case (i) up to 40 ms. After that, the three cases deviate from each other, as is expected in very sensitive unstable dynamical systems. As expected, the unity Lewis number test case (iv), shows smaller fluctuations than the non-unity Lewis number cases.

In summary, while cases (ii) and (iii) are in reasonable agreement (both qualitatively and quantitatively) with the benchmark (i), the unity Lewis number simulation (iv) displays a radically different behavior, resulting from the absence of the thermo-diffusive instabilities.

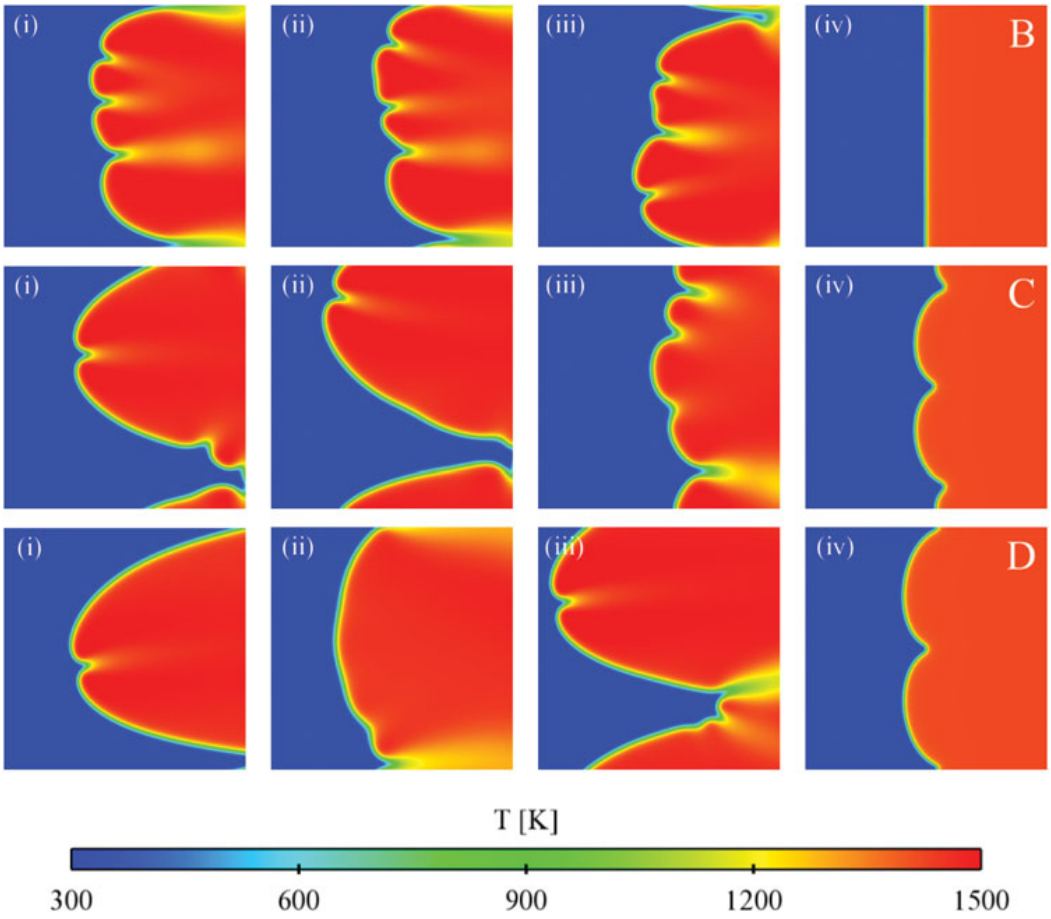

Figure 3.7: Snapshots of the temperature field corresponding to $t = 50$ ms (B), $t = 100$ ms (C), and $t = 150$ ms (D). The initial field is the same for all simulations (Fig. 3.3), while B, C, and D, show a comparison of the four test cases (i)-(iv).

3.3.3 Three-dimensional simulations

Hydrogen flames under moderate levels of turbulence have been shown to present a stronger sensitivity to differential diffusion [116]. For this reason, the constant Lewis number assumption is also tested in a three-dimensional configuration with low-intensity turbulent conditions.

Configuration

A schematic of the three-dimensional configuration is shown in Fig. 3.8. The reader is referred to Savard *et al.* [47, 48, 95, 117] for more details on the configuration. Only a brief overview is given here. The domain has a square cross-section, where depth and width are of size $L = 8.35$mm. The total length is 8L. The grid is uniform, with a cell size of 0.0424 mm, which is the same as that used for the previous

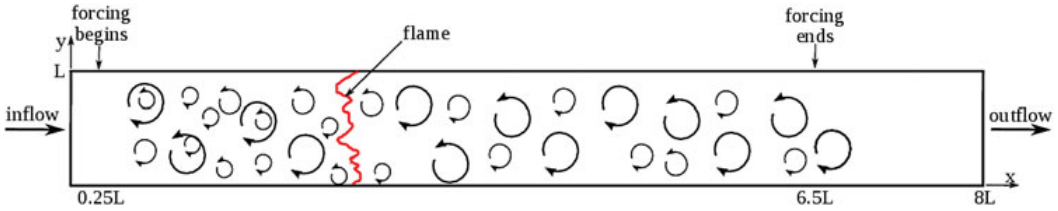

Figure 3.8: Schematic of the three-dimensional H_2/air simulation configuration (sketch adapted from Savard *et al.* [48]).

two-dimensional laminar flames. The unburnt gas is injected with a low turbulent kinetic energy, and is generated through a separate homogeneous isotropic turbulence simulation. A velocity forcing is used to reach the desired level of turbulence intensity for each streamwise location between 0.25L and 6.5L from the inlet [117–119]. The average inflow velocity is set to a value close to the turbulent burning velocity, so that the statistically-planar flame is almost stationary. The unburnt Karlovitz number for the benchmark test case is $\mathrm{Ka} = 149$. The unburnt turbulent Reynolds number is $\mathrm{Re}_t = u'l/\nu = 289$. The ratios l/l_F and u'/S_L are 2 and 18, respectively, and the eddy turnover time, $\tau = k/\varepsilon$, is about $500\mu s$. The integral length scale, l, is computed as 16% of the domain width [119]. These conditions are close to case C from Aspden *et al.* [116]. It should be noted that the definition of the Karlovitz number used in the current work differs from the definition used by Aspden *et al.* [116] (in their work, $\mathrm{Ka} = (u'/S_{L,fp})^{3/2}(l_{F,fp}/l)^{1/2}$, where the subscript '$fp$' stands for 'freely-propagating').

Results

Four three-dimensional DNS corresponding to cases (i)-(iv) are carried out. Each simulation is advanced for about 30 eddy turnover times. The statistics shown in this section correspond to the last 20, after any transient effects are gone. As was done for the two-dimensional case, two global parameters are shown: the average flame position (Fig. 3.9a) and the normalized fuel consumption-based turbulent flame speed, S_T (Fig. 3.9b), which are shown against the number of eddy turnover times. As can be seen, both flame position and flame speed of test cases (i)-(iii) remain close for about 3τ. After this initial phase, the three test cases can be seen gradually drifting apart (Fig. 3.9a), and the respective turbulent flame speeds fluctuate differently (Fig. 3.9b). Table 3.10 shows that test cases (ii) and (iii) have a slightly larger mean and RMS S_T fluctuation than the benchmark (i), while test case

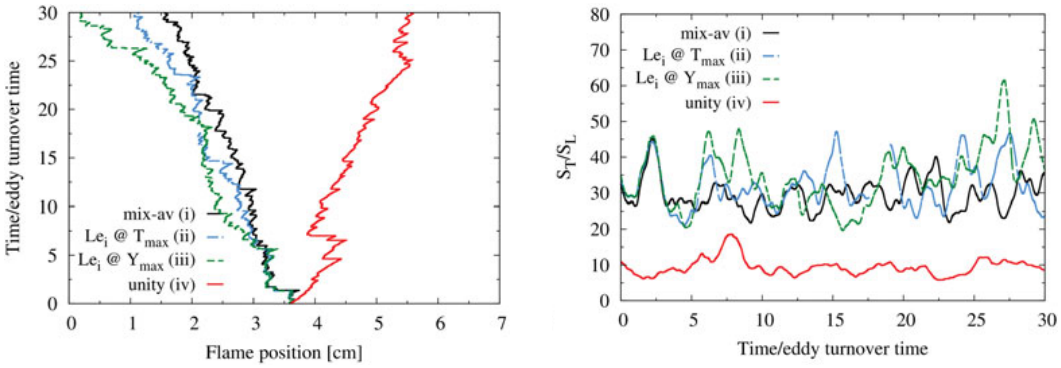

(a) Average flame position. **(b)** Consumption-based flame speed.

Figure 3.9: Average flame position (a) and fuel consumption-based flame speed normalized by the respective laminar unstretched flame speed (b), for the four simulations (i)–(iv) of the three-dimensional lean H_2/air flame.

Test case	S_L (m/s)	$\overline{S_T}$ (m/s)	$\overline{S_T}/S_L$	S'_T (m/s)
Mix.-av. (i)	0.22	6.5	29.5	1.0
Le$_i$ @ T_{max} (ii)	0.22	7.2	32.7	1.3
Le$_i$ @ Y_{max} (iii)	0.21	7.7	36.7	1.8
Unity (iv)	0.41	4.0	9.8	1.2

Figure 3.10: Laminar unstretched flame speed, S_L, mean and normalized mean turbulent flame speed, denoted by S_T and S_T/S_L, respectively (where each test case is normalized by the respective S_L), and RMS turbulent flame speed, S_T, for test cases (i)-(iv).

(iv) has a much reduced mean and RMS S_T. The unity Lewis number test case (iv) presents an instantaneous drop, which reduces S_T/S_L by a factor of about three.

A more quantitative comparison of the four test cases (i)-(iv) is made in Fig. 3.11, which shows various turbulence statistics of the fuel mass fraction, and its (normalized) source term. Figures 3.11a and 3.11b show a comparison of the area-weighted conditional means of the fuel mass fraction and its normalized source term, respectively, for the four cases (i)-(iv) (the reader is referred to Lapointe *et al.* [43] for a description of the averaging procedure). These conditional means reveal that test cases (ii) and (iii) are both in good agreement with the benchmark. Test cases (ii) and (iii) have some minor differences with respect to the benchmark (i) in regions of high curvature, corresponding to the hot spots ($T > 1400K$). As expected, the conditional mean fuel mass fraction and source term of the unity Lewis number test case are zero above 1400 K.

Finally, as predicting mean quantities is often not enough, Fig. 3.11c and 3.11d show a comparison of the probability density functions (PDFs) of the normalized fuel mass fraction and of its normalized source term, respectively, taken at the tem-

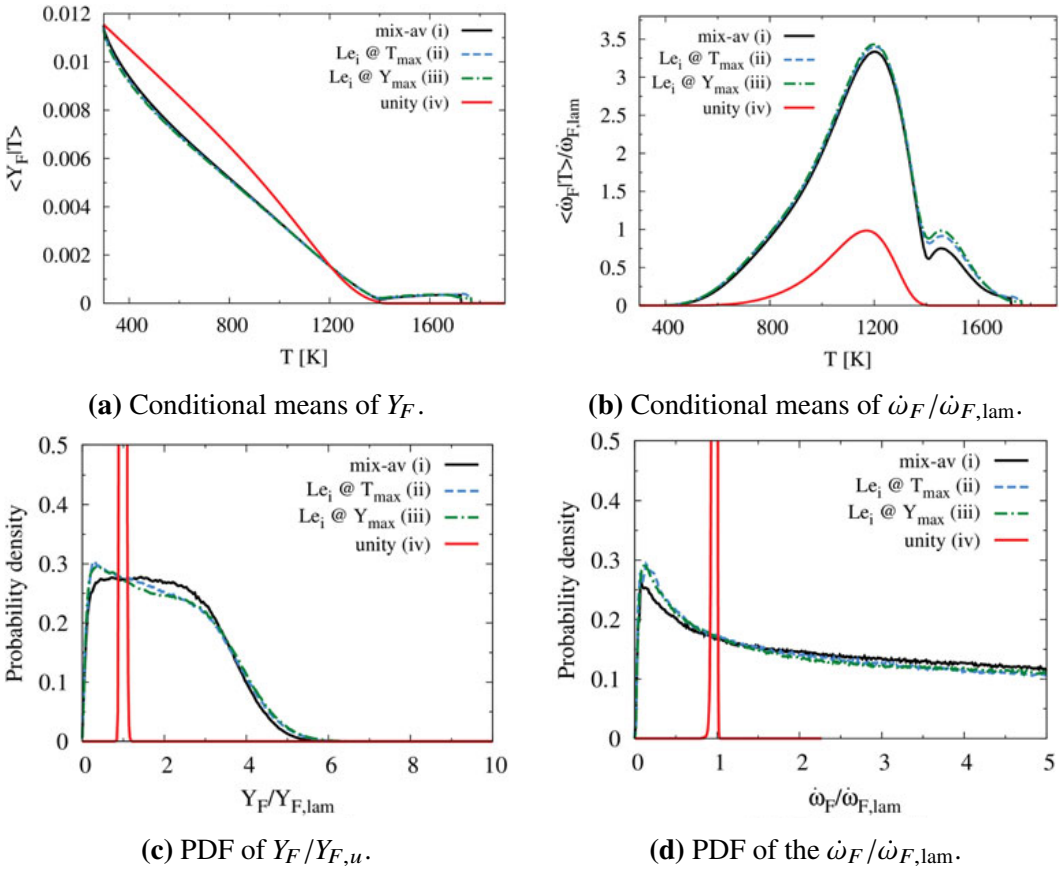

(a) Conditional means of Y_F.

(b) Conditional means of $\dot{\omega}_F/\dot{\omega}_{F,\text{lam}}$.

(c) PDF of $Y_F/Y_{F,u}$.

(d) PDF of the $\dot{\omega}_F/\dot{\omega}_{F,\text{lam}}$.

Figure 3.11: Turbulence statistics of the four three-dimensional hydrogen-air flames corresponding to test cases (i)-(iv). The top row shows the area-weighted conditional means of the fuel mass fraction (a) and its normalized source term (b); the bottom row shows the PDF of the fuel mass fraction (c), and its normalized source term (d) at the temperature of the maximum mixture-averaged fuel source term (1191 K). The black line corresponds to case (i), while cases (i)-(iv) are shown by the blue, green, and red lines, respectively.

perature of peak laminar source term (1191 K). Once again, test cases (ii) and (iii) provide good agreement with the mixture-averaged benchmark, with only minor differences in the shape of the PDF. On the other hand, the unity Lewis number simulation has a completely different profile, with the mean centered around unity.

3.4 Turbulent premixed n-C_7H_{16}/air flame

Under high turbulent conditions, the assumption of unity Lewis numbers has often proven adequate [46, 120]. It is important, however, to shed light on the transition occurring from a molecular diffusion controlled process to one where turbulent transport dominates. In Sec. 3.3, a hydrogen/air turbulent flame was studied. In this section, the effect of the constant Lewis number assumption is evaluated in a

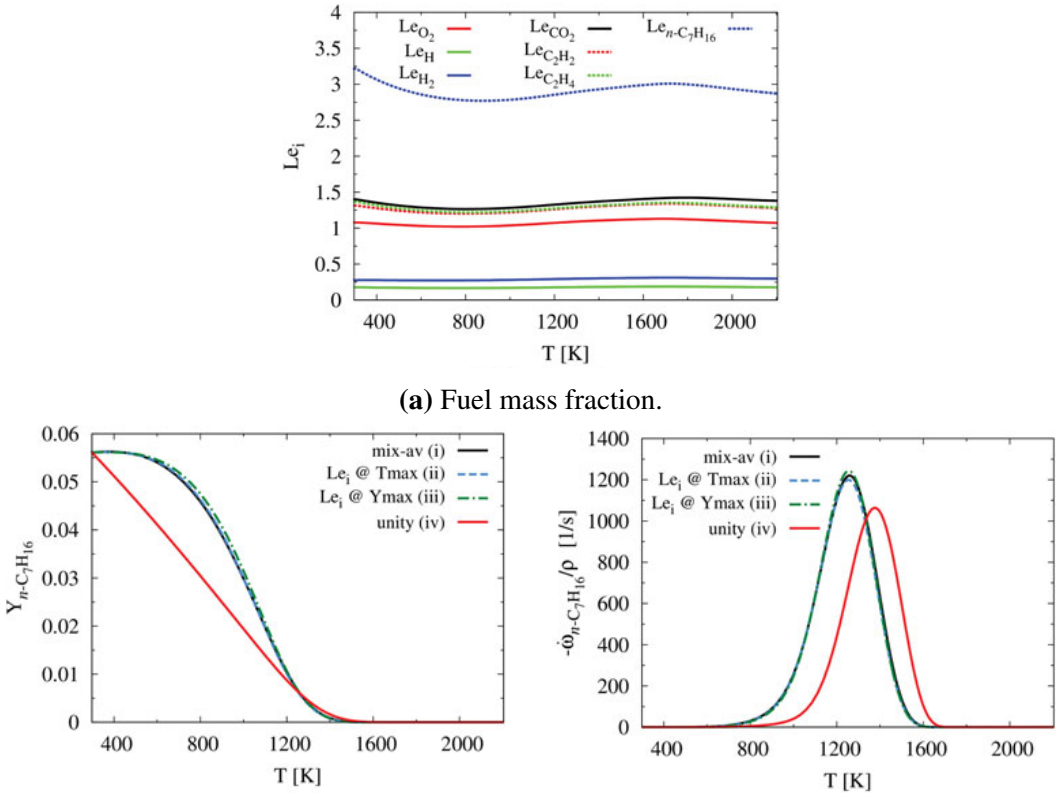

(a) Fuel mass fraction.

(b) Fuel source term.

(c) Fuel source term.

Figure 3.12: Lewis numbers for the n-C_7H_{16}/air flame, obtained from a mixture-averaged one- dimensional flame (a), fuel mass fraction (b) and its source term (c) against temperature, for the four cases (i)-(iv) using one-dimensional flames with an equivalence ratio of 0.9.

turbulent, premixed, slightly lean (ϕ =0.9), n-C_7H_{16}/air flame, where the fuel Lewis number is greater than one.

3.4.1 One-dimensional preliminary analysis

Once again, before analyzing the results of the three-dimensional simulations, an analysis of one-dimensional flames is performed.

Figure 3.12a shows the Lewis numbers of selected species in temperature space, obtained from the simulation of a one-dimensional flame with mixture-averaged properties. Despite the wide range of Lewis numbers, which is expected given the variety of molecular weights involved, the fluctuations for each species are limited. The species presenting the largest variation is the fuel, with a Lewis number falling in the range 2.77-3.22.

T_u (K)	P (atm)	ϕ	l_F (mm)	$n_x \times n_y \times n_z$	$\Delta x = \Delta y = \Delta z$ (mm)	l_F/S_L (ms)
298	1	0.9	0.39	1408 × 128 × 128	0.018	1.08

Figure 3.13: Parameters for the turbulent premixed n-C_7H_{16}/air flame of Savard *et al.* [48].

Figures 3.12b and 3.12c show a comparison of four one-dimensional simulations corresponding to test cases (i)-(iv), showing the fuel mass fraction, and its chemical source term, respectively. Both sets of constant non-unity Lewis numbers (ii) and (iii), lead to excellent agreement with the benchmark (with case (ii) performing better than (iii)). As expected, the unity Lewis number test case leads to a linear profile for the fuel mass fraction in the preheat zone, and to a shifted flame position, as can be seen in Fig. 3.12c.

The one-dimensional analysis suggests once again that a suitable choice of the Lewis numbers might provide an excellent approximation to the mixture-averaged benchmark.

3.4.2 Three-dimensional simulations

The configuration is similar to the one shown in Fig. 3.8, and a summary of the parameters used in the simulations is given in Table 3.13. Once again, more details can be found in [47, 48, 95, 117], and only a brief overview is provided here. The unburnt Karlovitz number is $\mathrm{Ka} = 220$, and the unburnt turbulent Reynolds number is $\mathrm{Re}_t = u' l / \nu = 190$. A discussion of the grid resolution may be found in [43].

As for the previous configurations, four three-dimensional direct numerical simulations corresponding to cases (i)-(iv) are carried out. Each simulation is run for about 50 eddy turnover times. The statistics shown in this section correspond to the last 35, after any transient effects are gone.

Figure 3.14 shows various turbulence statistics of the fuel mass fraction, and its (normalized) source term. Figures 3.14a and 3.14b show a comparison of the area-weighted conditional means of the fuel mass fraction and its normalized source term, respectively, for the four cases (i)-(iv). Both conditional means reveal that test cases (ii) and (iii) are both in excellent agreement with the benchmark. The unity Lewis number case (iv) is close to the benchmark case at low temperatures, where the turbulence is strong, but leads to large relative errors in high temperature regions, especially close to the flame front.

Finally, Figs. 3.14c and 3.14d show a comparison of the PDFs of the normalized fuel mass fraction and of its normalized source term, respectively. The PDFs are taken at the temperature of peak mixture-averaged laminar source term (1240 K). The analysis of the PDFs further corroborates the quality of the approximation introduced by test cases (ii) and (iii). The unity Lewis number simulation in Fig. 3.14d has a profile closer to a log normal centered around unity, completely missing the high probability of extinction shown by the benchmark simulation. This, in turn, leads to a much higher fuel consumption rate in test case (iv), as can be seen in Fig. 3.14b.

From the analysis of Fig. 3.14, it can be concluded that while the conditional means of the species mass fractions tend to collapse onto one another, their source terms retain strong differential diffusion effects, even at high unburnt Karlovitz numbers [43]. That being said, the use of mixture-averaged properties is not warranted for the present flame, as using constant non-unity Lewis numbers is capable of producing the same statistics (both conditional means and fluctuations).

3.5 Laminar diffusion ethylene/air flame

The last test case is a four-atmosphere, N_2-diluted, C_2H_4/air-coflow diffusion flame, which is one of the target flames selected for the International Sooting Flame (ISF) Workshops [27, 85, 86].

3.5.1 One-dimensional preliminary analysis

To estimate the fluctuations of the Lewis numbers, the diffusion flamelet equations are first solved [66]. Figure 3.15a shows the Lewis numbers of selected species against mixture fraction, for a stoichiometric scalar dissipation rate, χ_{st}, of 0.1 (though the observations hold for other values of χ_{st} as well). As in the previous case, the Lewis numbers have a limited variation, which is largely a consequence of the large fraction of N_2 (mass fractions of N_2 range from 82.4% in the fuel stream to 76.8% in the oxidizer stream). Figure 3.15b shows the Lewis number of benzene and its mole fraction in mixture fraction space. As can be seen, a variation of $\mathrm{Le}_{C_6H_6}$ of at most 10% occurs within the region of formation of benzene. This observation is also common to other aromatic species.

An appropriate choice of the Lewis numbers is capable of producing results in good agreement with the benchmark. This can be seen in Figs. 3.15c and 3.15d, which show a comparison in mixture fraction space of the temperature and the benzene mass fraction profiles, respectively, for the four simulations (i)-(iv). The two plots

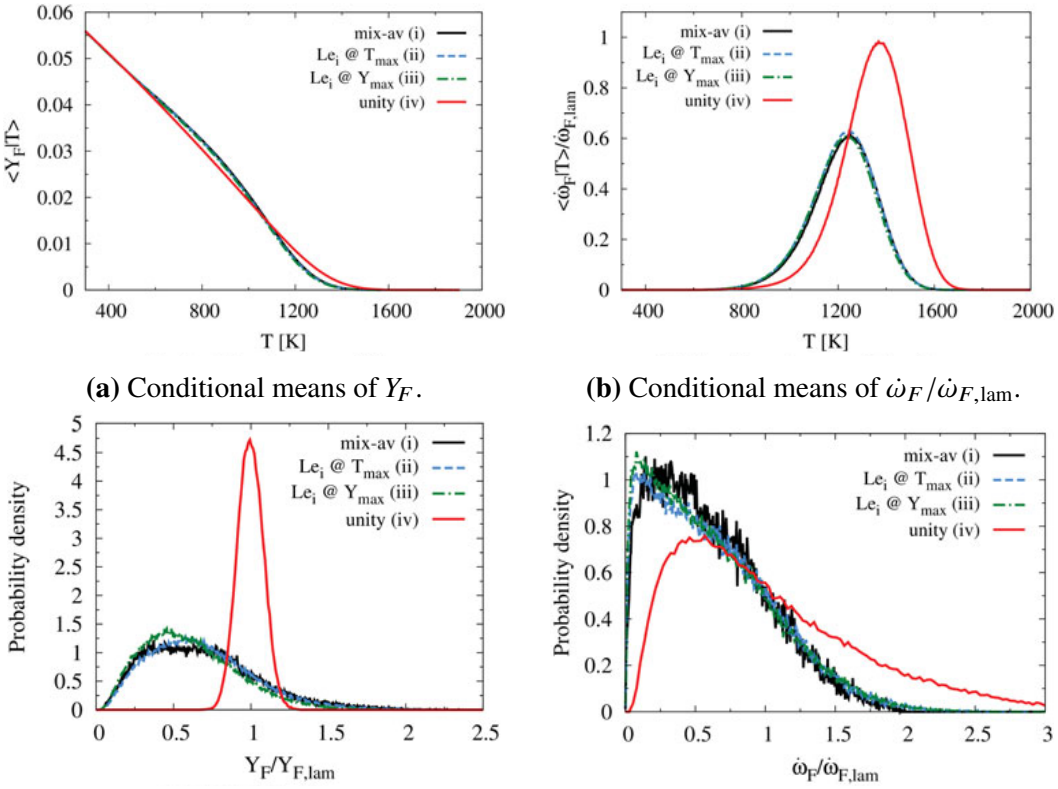

(a) Conditional means of Y_F.

(b) Conditional means of $\dot{\omega}_F/\dot{\omega}_{F,\text{lam}}$.

(c) PDF of $Y_F/Y_{F,\text{lam}}$.

(d) PDF of the $\dot{\omega}_F/\dot{\omega}_{F,\text{lam}}$.

Figure 3.14: Turbulence statistics of the four three-dimensional heptane-air flames corresponding to test cases (i)-(iv). The top row shows the area-weighted conditional means of the fuel mass fraction (a) and its normalized source term (b); the bottom row shows the PDF of the fuel mass fraction (c), and its normalized source term (d) at the temperature of maximum mixture-averaged fuel source term (1240 K). The black line corresponds to case (i), while cases (ii)-(iv) are shown by the blue, green, and red lines, respectively.

were obtained from one-dimensional computations with a χ_{st} of 10, as at high strain rates the diffusivities have a stronger effect on the structure of the flame. As can be seen, test cases (ii) and (iii) are in good agreement with the benchmark (i), with test case (iii) performing better. The test case with unity Lewis numbers leads to large differences in the structure of the flame.

3.5.2 Description of the configuration

A sketch of the set-up is shown in Fig. 3.16, while a summary of the numerical parameters used in the simulations is given in Table 3.17. More details on the experimental set-up may be found in Kailasanathan *et al.* [121]. The two-dimensional governing equations are solved on a cylindrical mesh, with 420×192 cells. The flame region is within a uniform unstretched "core" made of 360×120 cells, and

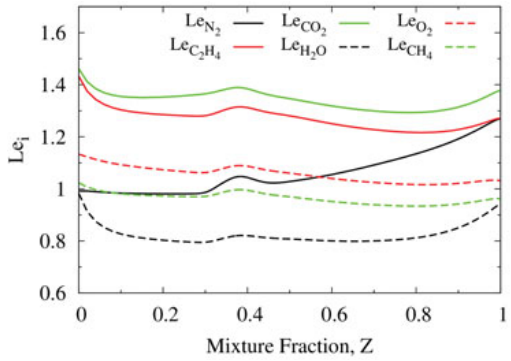

(a) Species Lewis numbers.

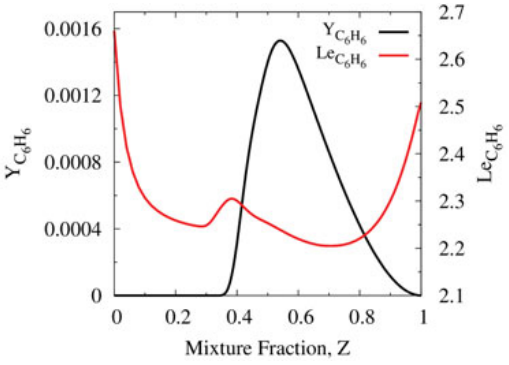

(b) Benzene Lewis number (red) and mass fraction (black).

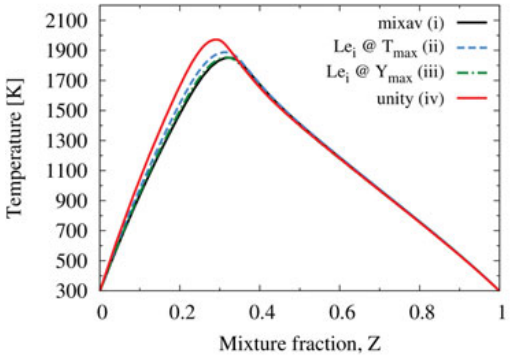

(c) Temperature.

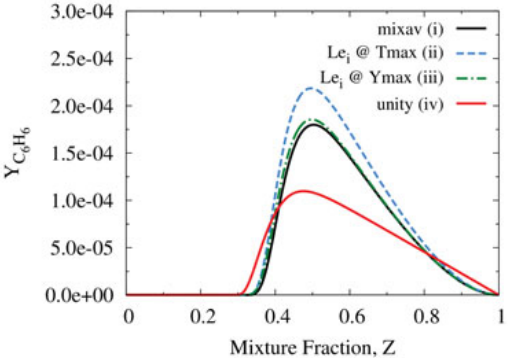

(d) Benzene mass fraction.

Figure 3.15: Lewis numbers in mixture fraction space (a), and $\mathrm{Le}_{\mathrm{C_6H_6}}$ and $\mathrm{Y}_{\mathrm{C_6H_6}}$ from a one-dimensional mixture-averaged simulation (b); comparison of temperature profiles for the four test cases (i)-(iv) (c), and comparison of $\mathrm{Y}_{\mathrm{C_6H_6}}$ for the four test cases (i)-(iv) (d).

linear stretching with a factor of 1.02 is used in both the axial and radial directions outside of the core region. The inflow velocity profiles are flat.

The fuel stream (fuel and diluent) and the air-coflow have the same inlet velocities [121]. The remaining boundaries are modeled through a convective boundary condition for the outflow, a Neumann boundary condition for the unperturbed free-stream coflow, and a symmetry condition is imposed along the centerline axis. Standard no-slip and no-penetration conditions are used for the fuel pipe. Heat loss through conduction to the fuel pipe is included. A temperature of 298 K was used for the walls of the fuel pipe.

For the sake of comparison with available experimental data [121, 122] (see Sec. 3.5.3, radiation heat transfer is considered for this flame. This is done by means of a radiation source term added to the energy equation, *i*.e., $\dot{q}_{\mathrm{rad}}/c_p$, where

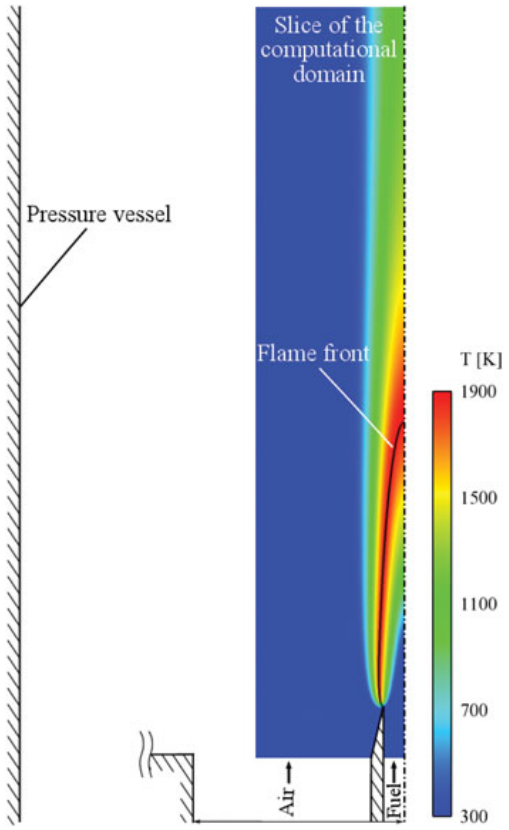

Figure 3.16: Sketch of the computational domain for the C_2H_4/air flame simulation.

$\dot{q}_{\text{rad}}$ is modeled according to the RADCAL model of Barlow *et al.* [123] (see Ch. 2). Soot formation and soot radiation are not considered.

3.5.3 Two-dimensional simulations

In this section, the four two-dimensional direct numerical simulations corresponding to the four cases (i)-(iv) are discussed.

Two-dimensional temperature and benzene mole fraction contour plots for test cases (i)-(iv) are shown in Fig. 3.16. As can be seen, the only visual difference is the length of the flame, with test cases (ii) and (iii) in good agreement with the benchmark, and test case (iv) presenting a slightly more pronounced change. De-

Inflow velocity (cm/s)				$n_x \times n_y$		Unstretched	
Fuel feed	Air-coflow	P (atm)	T_{fuel}, T_{Air} (K)	Unstretched	Total	Δx (cm)	Δy (cm)
13.5	13.5	4	298	360 × 120	420 × 192	0.01	0.005

Figure 3.17: Parameters for the laminar C_2H_4 diffusion flame of Kailasanathan *et al.* [121].

	Case				
	Exp.	Mix.-av. (i)	$\mathrm{Le_i}$ @ T_{max} (ii)	Le_i @ Y_{max} (iii)	Unity (iv)
Length (mm)	25.0	28.2	27.3	28.0	26.2

Figure 3.18: Experimental and computational flame heights for the C_2H_4/air flame. The heights are defined as the centerline location of the peak temperature.

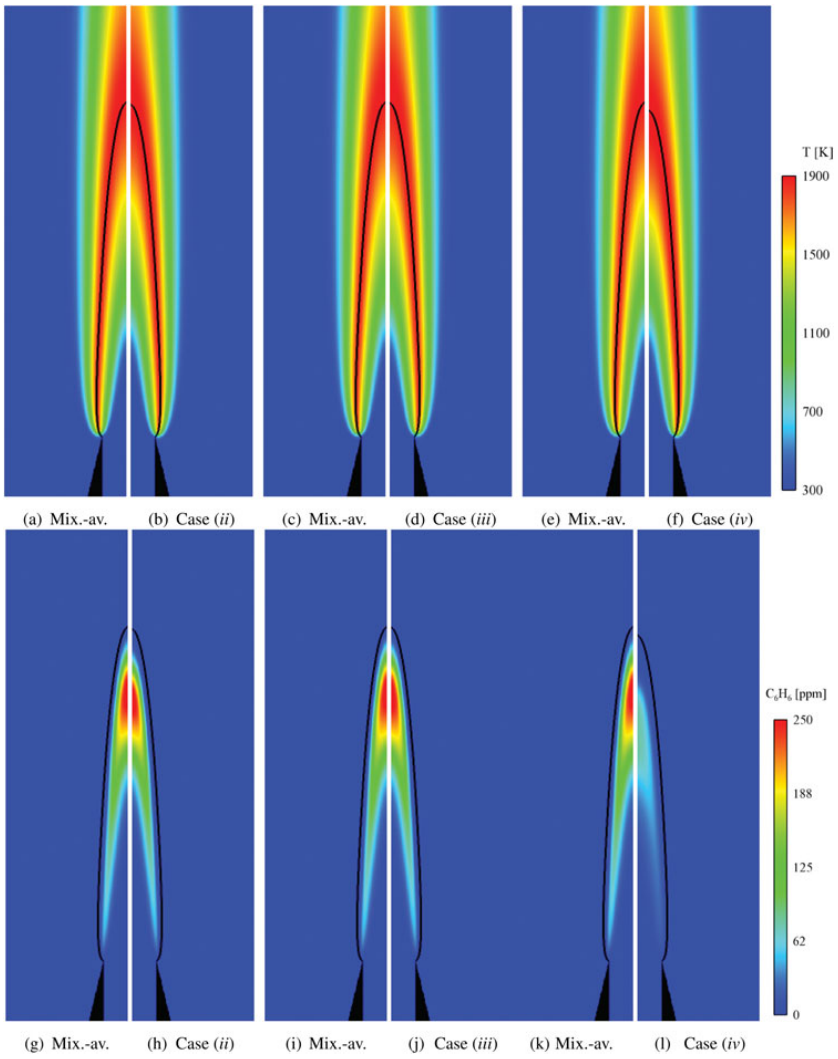

Figure 3.19: Comparison of temperature ((a)-(f)), and benzene mole fraction ((g)-(l)). The left halves represent the mixture-average benchmark, while the right halves represent test cases (ii)-(iv), respectively. In all plots, the solid black line represents the stoichiometric mixture fraction, *i*.e., $Z_{st} = 0.278$. The size of the snapshots is 4 cm in height, and 1 cm in radius.

spite these differences, the four test cases (i)–(iv) predict a similar temperature field. An analysis of the benzene two-dimensional plots reveals that test case (iv) under-

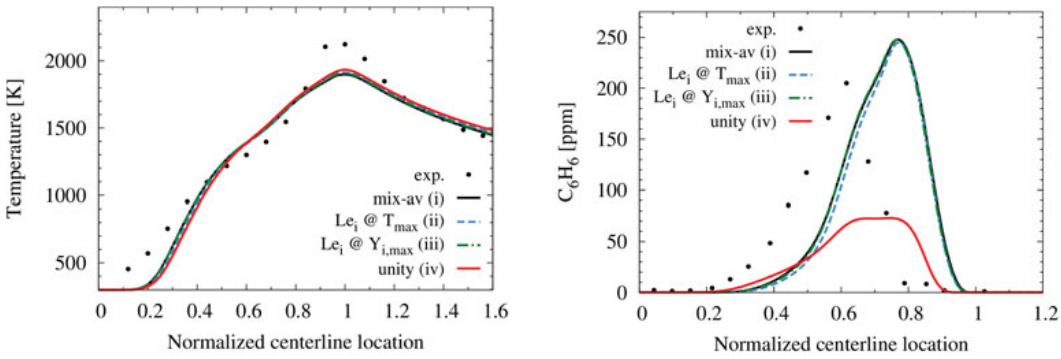

(a) Centerline temperature profile.

(b) Centerline benzene mole fraction.

Figure 3.20: Comparison of centerline temperature (a) and benzene mole fraction (b) profiles for the four simulations (i)-(iv) and the experimental data of Kailasanathan *et al.* [121]. The centerline location is normalized by the position of the maximum temperature, which is slightly different in each test case and in the experimental measurements.

predicts the formation of benzene, whereas the results for cases (i), (ii), and (iii) are very similar.

Figure 3.20 compares the centerline temperature and the benzene mole fraction profiles for the four simulations (i)-(iv) against the experimental data of Kailasanathan *et al.* [121, 122]. Both the temperature and the benzene mole fraction profiles are plotted with respect to the normalized flame height. The normalization is intended to separate any differences specific to benzene transport from differences in the overall flow field. The flame heights for the experimental data and test cases (i)-(iv) are shown in Table 3.18. Figure 3.20a shows that the shape of the temperature profiles does not change significantly. On the other hand, the use of unity Lewis numbers does lead to significant changes in the structure of the flame. In contrast, both test cases (ii) and (iii) perform well, when compared to the benchmark.

There are large differences with the experimental temperature measurements, especially in the region close to the burner exit, and further downstream, in the flame-tip region. The former is common to measurements carried out with thermocouples [124], and the cause is likely to be found in the heating of the thermocouple through radiation from the flame. Heavy soot deposition may be responsible for the peak shown around the flame tip. The shift in the centerline profile of benzene is another significant difference and may be the consequence of probe effects. The recent work of Gururajan *et al.* [125] highlights very clearly that the perturbation introduced by the sampling probe and the supporting flange can introduce significant

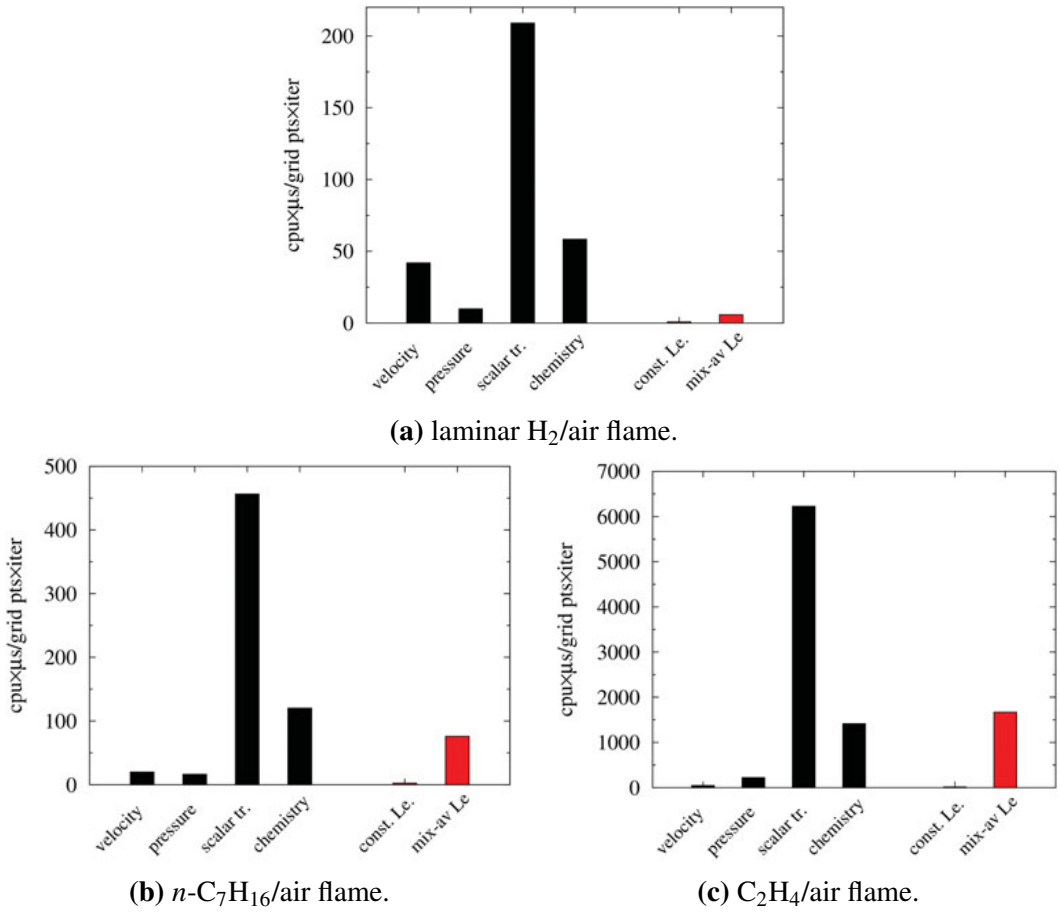

(a) laminar H_2/air flame.

(b) n-C_7H_{16}/air flame.

(c) C_2H_4/air flame.

Figure 3.21: Computational cost (cpu×μs/grid pts×iter) of the different parts of the NGA code for the three flames considered in this work. The first four bars from the left represent the cost that does not change with the choice of the mass diffusion model, while the last two bars on the right represent the cost associated with constant Lewis numbers and mixture-averaged transport.

deviations in the flame structure. The main conclusion to draw from these comparisons is that the uncertainties introduced by the constant Lewis number approach are significantly smaller than the differences between experiments and simulations.

3.6 Computational cost

While not a primary objective of the present work, it remains important to assess the computational cost savings associated with using fixed Lewis numbers. Of course, these savings over the mixture-averaged approach depend on the relative size of the computational domain, the number of scalars in the chemical model, and the numerical algorithm.

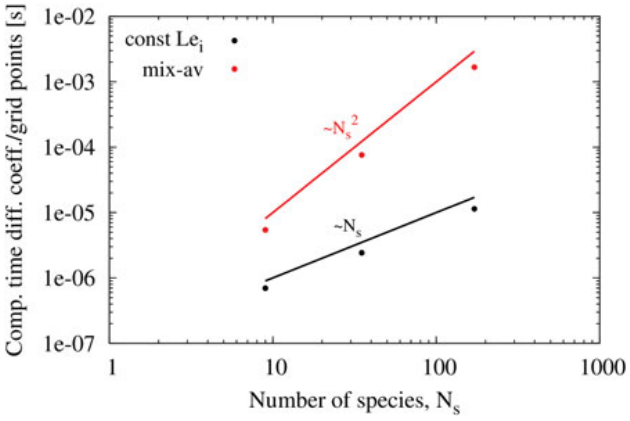

Figure 3.22: Scaling of the time required to compute the diffusion coefficients with the number of species. The red and black points correspond to the mixture-averaged and constant Lewis number calculations, respectively.

Figure 3.21 shows a comparison of the CPU time (in μs) per time step, normalized by the number of grid points, for the various parts of the NGA code, and for the three flames considered in the present work. For the sake of comparison, the numbers given in Fig. 3.21 are obtained by running all flames on the same cluster (an Intel-based cluster with QDR Infiniband interconnect). Most parts of the code (e.g. velocity solver, scalar transport) scale linearly with the number of grid points. The only exception is the pressure solver which scales between linearly and quadratically depending on the configurations. The costs of 'velocity' and 'pressure' are independent of the number of species, while 'scalar transport' and 'chemistry' (which does not include the computation of the mass diffusivities) scale linearly. As described in Savard *et al.* [117], the cost of the semi-implicit time integration scheme was designed to be linear with the number of species. This is important, as other more expensive time integration methods are available in the literature (the reader is referred to the introduction of Savard *et al.* [117] for a review of other methods). In the present numerical framework, the mixture transport properties (viscosity, conductivity, and diffusivities) are computed once per time step. A more accurate formulation would require their computation at each of the four subiterations of the iterative procedure, and this would increase the relative cost of the red bars in Fig. 3.21 by a factor of four.

Figure 3.22 shows the computational time required to compute the mass diffusion coefficients divided by the number of grid points, shown as a function of the number of species in the chemical model. As can be seen, the mixture-averaged approach leads to a greater cost, which grows rapidly as the number of species in the chem-

ical model is increased ($O(N_s^2)$ versus $O(N_s)$). The cost of computing the mass diffusion coefficients follows the $O(N_s)$ or $O(N_s^2)$ scaling, but, as explained above, the ratio of the total time per grid point and per time step depends on the combined effect of the transport model and the choice of the numerical algorithms.

For the hydrogen flame, the small number of species translates into limited cost savings of the constant Lewis number simulations, when compared to the mixture-averaged benchmark. More precisely, using 96 CPUs, the total time per iteration of the mixture-averaged simulation is about 2% greater than that of the constant Lewis number simulation. The time required to evaluate the mass diffusion coefficients using mixture-averaged properties is almost eight times that of using constant Lewis numbers. On the other hand, larger chemical models lead to more significant cost savings when precomputing the Lewis numbers. Using 144 CPUs for the heptane flame, the mixture-averaged simulations are about 12% slower than the constant Lewis number ones, and computing the mass diffusion coefficients is about 30 times more expensive. Finally, for the ethylene flame, with 96 CPUs, using constant Lewis numbers is about 21% faster than using the mixture-averaged formulation. For this flame, the cost of computing the coefficients $D_{i,m}$ from a set of constant Lewis numbers is 136 times smaller than the mixture-averaged approach.

3.7 Summary

In this work, we explored the validity of the constant non-unity Lewis number assumption in the simulation of chemically reacting flows. Towards this goal, three flames have been selected, which are representative of common engineering configurations, and display strong differential diffusion effects.

First, a premixed H_2/air flame with an equivalence ratio of 0.4 was selected to study the effect of the choice of the Lewis numbers on the evolution of a thermo-diffusively unstable flame. For this flame, both a laminar two-dimensional, and a moderately turbulent three-dimensional configuration were considered. Second, a highly turbulent premixed n-C_7H_{16}/air flame was simulated to investigate the effect of the choice of the Lewis numbers in a turbulent flame burning a fuel with a Lewis number greater than unity. Third, a laminar N_2-diluted C_2H_4/air-coflow pressurized diffusion flame was selected to investigate the effect on the formation and evolution of key soot precursors.

All of those simulations clearly show that it is possible to use a set of properly-chosen, constant, non-unity Lewis numbers while retaining good agreement with

mixture-averaged simulations. Two different methods of evaluating the Lewis numbers were tested, with both performing well, and neither consistently better than the other.

For our numerical framework, the computational cost savings associated with the use of pre-computed constant Lewis numbers were found to be minimal for all configurations considered in this work. For larger chemical models, the computational cost savings may be more substantial.

In summary, if the number of species is relatively low, the mixture-averaged approach is only marginally more expensive than using constant non-unity Lewis numbers. That is why the more general mixture-averaged approach will be used for all but one of the DNS carried out in Chs. 5 and 6 (a unity Lewis number case is also considered to isolate differential diffusion effects). Yet the fact that the two approaches lead to practically the same results suggest that all the theoretical analysis for the effective Lewis numbers (given by Eq. (1.11)) can be carried out using constant Lewis numbers for each species. This will significantly simplify the analysis presented in Chs. 4 and 7.

Chapter 4

EFFECTIVE LEWIS NUMBERS IN TURBULENT NON-PREMIXED FLAMES: ANALYSIS OF THE "SANDIA FLAMES" EXPERIMENTAL DATA SET

Chapter 4 has been adapted from:

- N. Burali & G. Blanquart "Modeling turbulent Lewis numbers in non premixed flames: insights from DNS data of Sandia flame B", *10th U.S. National Combustion Meeting*, April 2017, University of Maryland at College Park, College Park, MD.

In this chapter, differential diffusion effects in turbulent non-premixed flames are described though the use of effective Lewis numbers. A methodology to extract these effective Lewis numbers is presented and subsequently applied to a well-characterized measurement database from turbulent non-premixed flames. Modeling for these effective Lewis numbers is then discussed.

4.1 Introduction

Neglecting differential diffusion effects is a common assumption in simulations of turbulent combustion [20–25]. A number of reasons motivate this choice. First, the equal diffusivities assumption may provide significant cost savings when three-dimensional DNS with large chemical models are considered (see Ch. 3). Second, there is limited work towards accommodating differential diffusion effects within simulations where turbulence-chemistry interactions are unresolved, such as in LES (see Ch. 1).

For turbulent non-premixed combustion, the average flame structure is observed to transition from molecular, diffusion-controlled mixing to turbulence-dominated transport. This transition has been described in detail by Drake *et al.* [69, 70] and Barlow *et al.* [46, 71, 72]. In their experiments, species measurements show a clear decrease of differential diffusion effects with (*i*) increasing axial distance from the issuing nozzle and (*ii*) increasing jet Reynolds number.

The mechanisms involved with the stream-wise transition remain not well characterized, and a deeper understanding is needed. It is the objective of this chapter to perform an analysis similar to the work of Savard & Blanquart [47] for turbulent non-premixed flames. More precisely, the present work has three goals: (*i*) to propose a flamelet-based methodology to extract effective Lewis numbers from data sets of turbulent diffusion flames, (*ii*) to apply the proposed methodology to the Sandia piloted CH_4/air flames [72], and (*iii*) to assess the validity of previously-suggested models for γ based on relevant turbulence/flame parameters. This analysis is carried out using the well-documented experimental database of Barlow *et al.* [72].

This chapter is organized as follows: Sec. 4.2 provides an overview of the experimental data that is used in this work. Section 4.3 outlines the procedure to extract effective Lewis numbers from the experimental data. Section 4.4 provides a discussion of potential biases to the present analysis. In Sec. 4.5, a k-ε model used in other studies to model γ, is applied to the present analysis. Section 4.6 presents a discussion of additional modeling attempts for γ, based on the Karlovitz number. Finally, a summary of the observations is provided in Sec. 4.7.

4.2 Review of experimental data

The data considered for this work is composed of four of the six Sandia non-premixed methane/air jet flames, made available from the TNF workshop [72]. The same burner [126, 127] is used for all jet flames, which differ only by their jet Reynolds number (see Table 4.1). Flame B is described as transitional [46], while flames C, D, and E are all turbulent. Further, flame E presents localized extinction in the jet near-field [71]. The main jet is composed of a mixture of CH_4 and air, respectively 25% and 75% by volume. The equivalence ratio of the main jet is above the burning limit. A pilot flame is used to anchor the main jet to the burner exit. The pilot is composed of a lean mixture of C_2H_2, H_2, air, CO_2, and N_2, whose burnt products are the same as those of a methane/air flame at $\phi = 0.77$.

Mass fraction measurements used in this work include O_2, CH_4, CO, CO_2, H_2O, and H_2 for flames B through E, which are provided by Barlow *et al.* [46, 71, 72]. Table 4.2 shows the estimated uncertainties for the measured species [46]. NO is not considered in the present work, as the steady state flamelet model (see Sec. 4.3.2) is not well suited to represent slow processes such as NO_x evolution [67]. The radical

OH is not considered due to its high sensitivity on the choice of the chemistry model.

It should be noted that for some species, signal interferences may be significant. For example, as discussed in [123] and in the proceedings of the TNF Workshop [72], the Raman scattering measurements of CH_4 also include contributions from other hydrocarbon species, such that the CH_4 mass fraction approximates the total hydrocarbon mass fraction.

Barlow *et al.* [71] defined a measured mixture fraction, hereby denoted as Z_{TNF}, and given by

$$Z_{\mathrm{TNF}} = \frac{2\frac{Y_{\mathrm{C}}-Y_{\mathrm{C},2}}{W_{\mathrm{C}}} + \frac{Y_{\mathrm{H}}-Y_{\mathrm{H},2}}{2W_{\mathrm{H}}}}{2\frac{Y_{\mathrm{C},1}-Y_{\mathrm{C},2}}{W_{\mathrm{C}}} + \frac{Y_{\mathrm{H},1}-Y_{\mathrm{H},2}}{2W_{\mathrm{H}}}}. \tag{4.1}$$

In Eq. (4.1), Y_{C} and Y_{H} are the experimentally-measured mean carbon and hydrogen mass fractions, respectively, and W_{C} and W_{H} are the molecular weights of carbon and hydrogen, respectively. The fuel stream has the label "2", and the oxidizer stream has the subscript "1". The measured mixture fraction, "$\mathrm{Z_{TNF}}$", represents an approximation of Bilger's definition of mixture fraction [71, 128].

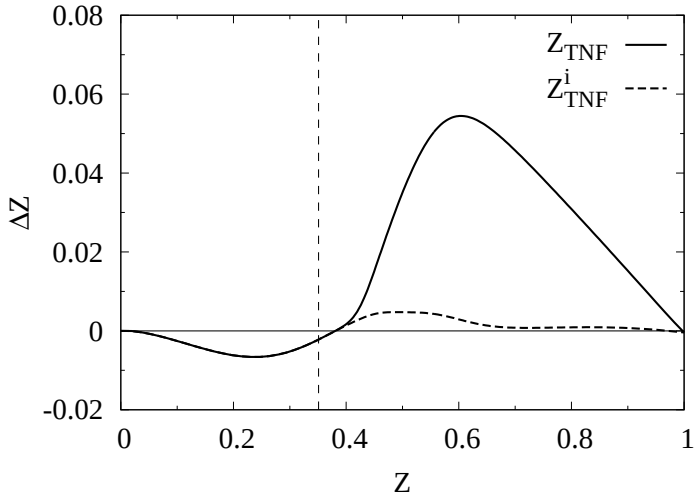

Figure 4.1: Comparison of mixture fraction definitions computed using the optimal flamelet (see Sec. 4.3) corresponding to flame C at $x/d = 30$. ΔZ is the difference between Peters' definition of the mixture fraction and $\mathrm{Z_{TNF}}$, computed using (*i*) only the measured species (solid line) and (*ii*) the measured species with $\mathrm{Y_{CH_4}}$ computed using Eq. (4.2) (dashed line). The vertical dashed line represents the stoichiometric mixture fraction ($\mathrm{Z}_{st} = 0.351$).

Flame	Re_{jet} [†]	U_{jet} [m/s]	U_{pilot} [m/s]	U_{coflow} [m/s]
B	8200	18.2	6.8	0.9
C	13400	29.7	6.8	0.9
D	22400	49.6	11.4	0.9
E	33600	74.4	17.1	0.9

Table 4.1: Flow parameters for the SANDIA flames used in this work. Data obtained from Table 1 in [46].

	Scalar	Systematic uncertainty	Scalar	Systematic uncertainty
used	Y_{O_2}	0.004	Y_{H_2}	6-12 %
	Y_{CH_4}	0.005	Y_{CO_2}	4 %
	Y_{H_2O}	4 %	Y_{CO}	10-20 %
not used	Y_{N_2}	3 %	Y_{NO}	10-20 %
	Y_{OH}	10 %		

Table 4.2: Estimated systematic uncertainties for the experimentally-measured species [46, 71, 123]. The uncertainties for Y_{O_2} and Y_{CH_4} are absolute values.

To take into account the interferences in the CH_4 signal, a modified form of Eq. (4.1) is considered, where the CH_4 mass fraction is computed as

$$Y^{i}_{CH_4} = Y_{CH_4} + Y_{C_2H_2} + Y_{C_2H_4} + Y_{C_2H_6}. \tag{4.2}$$

In Eq. (4.2), the "i" stands for "interference", and it is expected that $Y^{i}_{CH_4}$ approximates the total hydrocarbon mass fraction [123]. The measured mixture fraction computed using Eq. (4.2) is referred in this section as "Z^{i}_{TNF}".

Multiple definitions of the mixture fraction exist in the literature. In the present work, the definition of Peters is used (see Ch. 2). A comparison of Z, Z_{TNF} and Z^{i}_{TNF} is shown in Fig. 4.1 for the optimal flamelet (see Sec. 4.3) corresponding to flame C at $x/d = 30$. As can be seen, due to the missing contributions of species that are not directly measured (mainly C_2H_2, C_2H_4, and C_2H_6), Z_{TNF} deviates from Z mostly on the rich side of the mixture. The analysis presented in the following sections considers the mean species mass fraction measurements conditioned on Z^{i}_{TNF}, $\langle Y_i | Z^{i}_{TNF} \rangle$. Henceforth, the superscript "i" is dropped for simplicity.

[†] Re_{jet} is defined as $U_{jet}d/\nu$, where d is the fuel pipe's inner diameter, and ν is the kinematic viscosity.

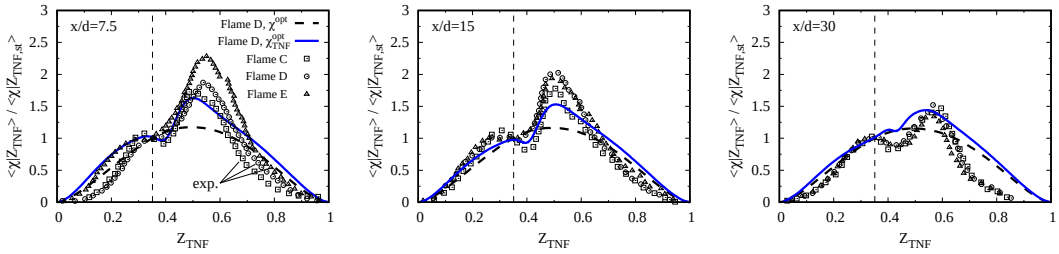

Figure 4.2: Comparison of the χ profile imposed in the FlameMaster code [79] (Eq. (4.6), dashed black lines) against experimental measurements (symbols) from Karpetis & Barlow [132], for flames C, D and E, and for $x/d = 7.5$, $x/d = 15$ and $x/d = 30$. The solid blue lines represent χ_{TNF}, which is computed using Eqs. (4.7) and (4.6). All profiles are normalized such that the stoichiometric value is unity. The vertical dashed line represents the stoichiometric mixture fraction.

Finally, Two-color laser Doppler velocimetry (LDV) measurements for flames D and E are provided by Schneider *et al.* [129].

4.3 Extracting effective Lewis numbers

In this section, a methodology to extract the effective Lewis numbers from the experimental data is outlined. The approach used by Savard & Blanquart [47] to develop a model for turbulent premixed flames is used as the basis for the current analysis.

4.3.1 Model for the effective Lewis numbers

In Ch. 1, the expression for the effective Lewis numbers was written as

$$\mathrm{Le}_{i,\mathrm{eff}} = \frac{1+\gamma}{\frac{1}{\mathrm{Le}_i}+\gamma}, \tag{4.3}$$

Equation (4.3) provides a simple and intuitive way to describe how the *effective* local mixing state varies between the laminar and the equal diffusivity regimes, and is used as a basis for the analysis presented in the following sections. In this work, and as a first step, any cross-stream variation of differential diffusion [46, 130, 131] is neglected, and γ is assumed to be constant in mixture fraction space, and only varies with downstream direction (*i.e.*, with x/d) for a given flame.

4.3.2 Flamelet equations

The first step of the analysis is to solve the steady-state flamelet equations [66] using the FlameMaster code [79]. The steady-state, one-dimensional, non-unity Lewis number flamelet equations for the species mass fractions take the form

$$-\frac{\rho\chi}{2}\frac{1}{\mathrm{Le}_{i,\mathrm{eff}}}\frac{\partial^2 Y_i}{\partial Z^2} - \dot{m}_i = \text{correction terms}. \tag{4.4}$$

In Eq. (4.4), the "correction terms" include diffusion, correction diffusion, and differential diffusion contributions. The reader is referred to Ch. 2 for the complete form of these equations.

Equation (4.4) requires user-supplied Lewis numbers, and scalar dissipation rate. The effective Lewis numbers in Eq. (4.4) are evaluated using Eq. (1.11), where the laminar Lewis numbers are computed from the flamelet equations for each χ_{st} at the mixture fraction location of maximum temperature (see Ch. 2).

In these flamelet equations, the effect of the flow-field on the flamelet structure, represented by the scalar dissipation, is unknown and must be modeled *a priori*. This is typically done by imposing an analytical function for χ, and scaling it by the stoichiometric value, χ_{st},

$$\chi(Z) = \chi_{st} \frac{f(Z)}{f(Z_{st})}, \tag{4.5}$$

where Z_{st} is the stoichiometric mixture fraction. The function $f(Z)$ is evaluated from the solution of the mixture fraction equation for counterflow diffusion flames [133, 134] and unsteady laminar mixing layers [65], and takes the form

$$f(Z) = \exp\left\{-2\left[\mathrm{erfc}^{-1}(2Z)\right]^2\right\}. \tag{4.6}$$

Figure 4.2 shows a comparison between the optimal χ profiles imposed in the FlameMaster code [79] using Eq. (4.6), and the experimentally-measured scalar dissipation rate, referred to as $\chi^{\mathrm{exp}}_{\mathrm{TNF}}$, for flames C, D and E at $7.5d$, $15d$ and $30d$ downstream of the burner lip (from Karpetis & Barlow [132]), normalized by the stoichiometric value. For the sake of clarity, only the imposed optimal χ profile for flame D is shown. To compare the imposed scalar dissipation profile with $\chi^{\mathrm{exp}}_{\mathrm{TNF}}$, a '$\chi_{\mathrm{TNF}}$' is computed from χ using

$$\chi_{\mathrm{TNF}} = 2\alpha|\nabla Z_{\mathrm{TNF}}|^2 = (\partial Z_{\mathrm{TNF}}/\partial Z)^2\,\chi, \tag{4.7}$$

and is shown in Fig. 4.2, normalized by the stoichiometric value. As mentioned in Sec. 4.2, Z_{TNF} is computed from the measured species, and is slightly different from Z. This is the reason for the shape difference between the χ and χ_{TNF} profiles in Fig. 4.2. As can be seen, the shape of the imposed χ_{TNF} profile is close to the experimentally-measured profiles.

Finally, the chemical model used in this work is GRIMech3.0 [135] without the nitrogen chemistry, with a total of 36 species. A comparison with Caltech-Mech2.4 [111] is discussed in Sec. 4.4.3.

4.3.3 Error maps

The flamelet equations are solved for a range of χ_{st} and γ values. The values for χ_{st} span the range [2, 260], to cover the relevant part of the stable burning branch of the S-shaped curve. The scalar dissipation rate at the extinction point is $260 s^{-1}$ for the laminar Lewis number limit, and $475 s^{-1}$ for the unity Lewis number limit. The Lewis numbers are computed from Eq. (1.11), where γ takes values in the range [0, 120], such that the effective Lewis numbers span the range $[\mathrm{Le}_i, 1]$ and $[1, \mathrm{Le}_i]$, for sub-unity and above-unity laminar Lewis numbers, respectively.

The solutions of the flamelet equations are then compared to the experimental data to obtain two-dimensional error maps, for which a total of 1598 flamelets is used. The error is defined as

$$L_2(\chi_{st}, \gamma) = \left\{ \frac{1}{N_s N_p} \sum_{j,i} \frac{\left| Y_i(\chi_{st}, \gamma, Z_{\mathrm{TNF},j}) - Y_i^{\mathrm{exp}}(Z_{\mathrm{TNF},j}) \right|^2}{\left[\max_j \{ Y_i^{\mathrm{exp}}(Z_{\mathrm{TNF},j}) \} \right]^2} \right\}^{\frac{1}{2}}, \tag{4.8}$$

where N_s and N_p are the number of species and the number of experimental data points, respectively. $Y_i(\chi_{st}, \gamma, Z_{\mathrm{TNF},j})$ is the ith species mass fraction obtained from the solution of the flamelet equations for given χ_{st} and γ, and interpolated onto the experimental mixture fraction point $Z_{\mathrm{TNF},j}$. $Y_i^{\mathrm{exp}}(Z_{\mathrm{TNF},j})$ is the ith species measured conditional mean mass fraction at $Z_{\mathrm{TNF},j}$. The use of different error norms is discussed in Sec. 4.4.4.

The *optimal* values of χ_{st} and γ , *i.e.*, $(\chi_{st}^{opt}, \gamma^{opt})$, are then estimated by solving

$$\begin{aligned} &\arg\min_{\chi_{st},\gamma} \{L_2(\chi_{st}, \gamma)\} \\ s.t. \quad &\chi_{st} \in [2, 260], \gamma \in [0, 120]. \end{aligned} \tag{4.9}$$

It should be noted that the approach described in this section provides a simple means of separating two different effects of increasing the jet Reynolds number: increased scalar dissipation rates [136] and decrease of differential diffusion [69, 71].

In Eq. (4.8), the temperature is not considered. The motivation for this choice is that radiation heat losses are not included in the flamelet model used to extract the optimal flamelet parameters. Doing so would significantly increase the complexity of the present approach. However, while the comparisons between the DNS and

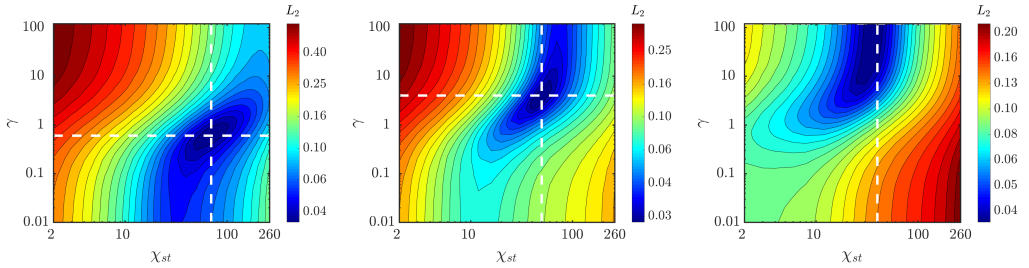

(a) Flame B, x/d=15. **(b)** Flame C, x/d=30. **(c)** Flame E, x/d=45.

Figure 4.3: Colormaps of L_2 error by Eq. (4.8) for flames B at $x/d = 15$ (left), C at $x/d = 30$ (center), and E at $x/d = 45$ (right). The white dashed lines intersect at the optimal flamelet (minimum L_2 error).

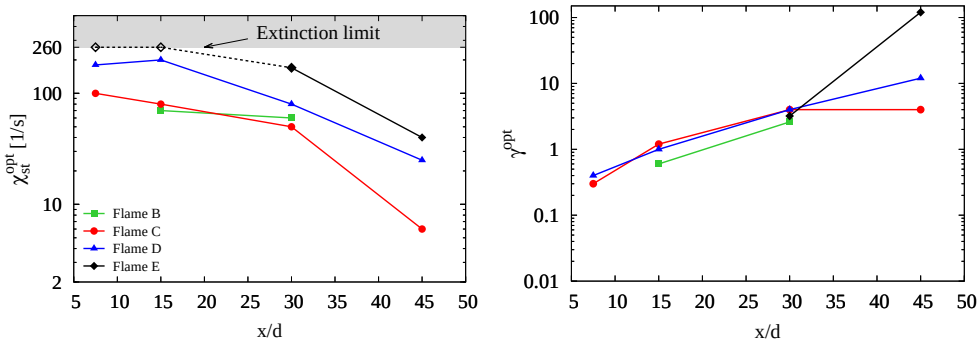

(a) χ_{st}^{opt} *vs.* x/d. **(b)** γ^{opt} *vs.* x/d.

Figure 4.4: Optimal scalar dissipation rate, χ_{st}^{opt} (left), and γ^{opt} (right) as a function of the downstream direction x/d for flames B, C, D, and E. In Fig. 4.4a, the shaded region corresponds to values of χ_{st} above the laminar Lewis number extinction limit. In Fig. 4.4b the values of γ^{opt} for Flame E and $x/d < 30$ are 0, and are not shown.

the measurements for Sandia flame B discussed in Ch. 6, suggest that radiation has a non-negligible impact on the global mixing field and on the flame structure, it will be shown in Ch. 7 that the optimal flamelet parameters extracted from DNS data with and without radiation, present only small differences. This suggests that radiation has a secondary effect on the optimal flamelet parameters.

Figure 4.3 shows the error given by Eq. (4.8) for flame B at $x/d = 15$, flame C at $x/d = 30$, and flame E at $x/d = 45$. The first and the third cases were shown in [46] as examples of laminar and turbulent limiting behavior. The white dashed lines intersect at the point of minimum error, *i.e.*, $(\chi_{st}^{opt}, \gamma^{opt})$. As expected, for flame B at $x/d = 15$, γ^{opt} is small, such that the effective Lewis number for H_2 is 0.4, close to its laminar value ($Le_{H_2} \approx 0.3$). However, with increasing jet Reynolds

number and streamwise distance from the burner exit, $\mathrm{Le}_{\mathrm{H_2,eff}}$ increases to 0.7 for flame C at $x/d = 30$, and to 1.0 in flame E at $x/d = 45$.

Figure 4.3 also shows that Eq. (1.11) has a high sensitivity on γ for $\gamma \approx 1$, but there is low sensitivity (or high error) for low γ ($\gamma < 0.1$) and high γ ($\gamma > 10$).

4.3.4 Optimal flamelet parameters

The optimal χ_{st} and γ for all x/d locations for flames B, C, D, and E, are shown in Figs. 4.4a and 4.4b, respectively. Only two measurement locations are available for flame B. The error maps are computed only up to $x/d = 45$, as the flame length (defined using the iso-surface of stoichiometric mixture fraction at the centerline) is located close to that measurement station for all four flames [72]. The stoichiometric flame length for flames C, D, and E, can be estimated through interpolation as 45.4, 48.1, and 49.9 diameters, respectively. Furthermore, due to the large uncertainties for the scalars immediately downstream of the burner exit, and the fact that for that region $\gamma^{opt} \approx 0$, only stations starting from $x/d = 7.5$ are shown.

Optimal χ_{st}

Figure 4.4a shows that, as expected, χ_{st}^{opt} generally decreases with axial distance from the burner exit. The regions of the flame with the highest strain rates are located close to the burner exit, and a progressive reduction of χ_{st}^{opt} takes place as the (average) strain rate decreases. Furthermore, as the jet Reynolds number is increased, the χ_{st}^{opt} shifts upwards, as greater strain rates are found in the jets. In fact, χ_{st}^{opt} scales almost linearly with the jet Reynolds number, consistent with observed scalings in self-similar regions of isothermal round turbulent jets [136, 137]. One notable exception is flame B, for which the χ_{st}^{opt} values are found to be greater than expected. It's important to consider that flame B is often described as transitional [46].

Figure 4.5 compares the optimal $\chi_{\mathrm{TNF},st}$ values, with the measurements of $\langle \chi | \mathrm{Z_{TNF}} \rangle$ at the stoichiometric mixture from Karpetis & Barlow [132]. Measurements are available for flames C, D, and E, and at $x/d = 7.5$, 15, and 30. The optimal $\chi_{\mathrm{TNF},st}$ values are found to be systematically larger than the measured $\langle \chi | \mathrm{Z_{TNF},}_{st} \rangle$. While multiple reasons could explain this difference, such as experimental uncertainties, it should be reminded that, in the present approach, a single, one-dimensional, steady-state flamelet is used to represent the conditional mean flame structure. Thus, it is expected that both optimal parameters χ_{st} and γ^{opt} are also representative of any

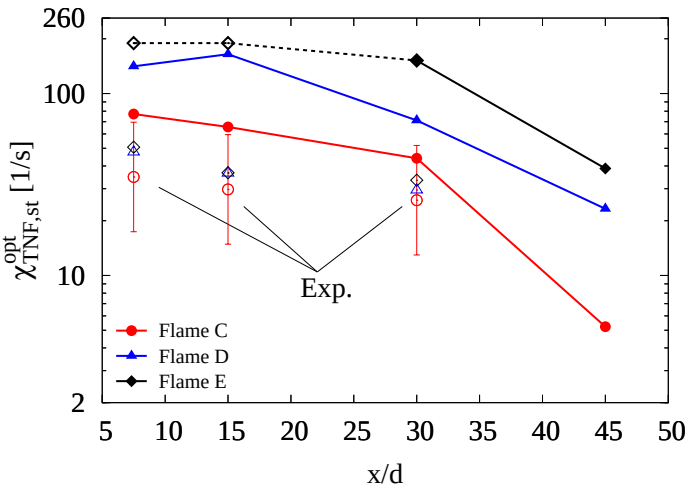

Figure 4.5: Comparison of the optimal scalar dissipation rate, $\chi^{opt}_{\mathrm{TNF},st}$ with the measured values $\langle \chi_{\mathrm{TNF},st} \rangle$ [132], as a function of the downstream direction x/d for flames C, D, and E. The vertical bars (shown only for flame C for clarity) represent the reported maximum uncertainty [132].

effect not adequately represented by this approximation. For instance, it is expected that multi-dimensional effects, including convective and diffusive transport along the mixture fraction iso-surfaces, are essentially lumped into the effective χ^{opt}. In the work of Sholtissek *et al.* [138], the analysis of a lifted turbulent hydrogen jet flame showed that multi-dimensional effects can be significant.

Optimal γ

Figure 4.4b shows that γ^{opt} generally increases with axial distance from the burner exit, which is consistent with turbulent transport being increasingly dominant over molecular mixing [46, 71]. It is not surprising that the only point which is not increasing is represented by flame C at $x/d = 45$, for which the estimated stoichiometric flame length is $x/d = 45.4$, as previously discussed. The values of γ^{opt} close to the burner exit are small (in fact, $\gamma^{opt} \approx 0$ for $x/d < 7.5$), as molecular diffusion dominates the mixing of the scalars, consistently with experimental observations [139–145]. Moving further downstream, turbulent transport becomes increasingly dominant, and the effective Lewis numbers become closer to unity.

It should be noted that the extracted γ^{opt} values are representative of two effects: as the jet Reynolds number is increased, the Kolmogorov length scale, η, decreases. At the same time, χ^{opt}_{st} increases (in fact the χ^{opt}_{st} profiles scale almost with U_{jet}/D, as shown later in Fig. 4.16), and hence the flame thickness decreases, *i.e.*, scalar gradients are increased. These competing effects explain why the profiles shown in

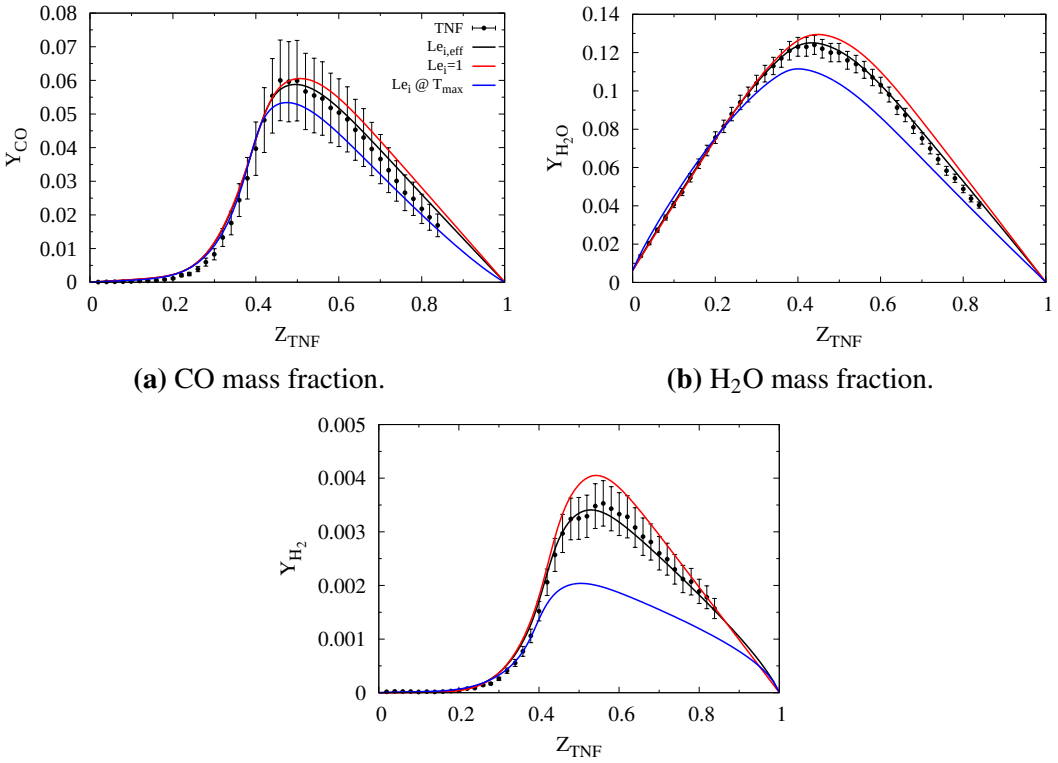

(a) CO mass fraction.

(b) H_2O mass fraction.

(c) H_2 mass fraction.

Figure 4.6: Comparison of measured species conditional mean mass fractions of Y_{CO} (left), Y_{H_2O} (center), and Y_{H_2} (right), for flame C at $x/d = 30$ [72], against the flamelet solutions corresponding to effective Lewis numbers (black line), unity Lewis numbers (red line), and laminar Lewis numbers (blue line).

Fig. 4.4b are close for the first three stations (once again, it should be noted that the fourth measurement station is close to the stoichiometric flame tip). Possible correlations of γ^{opt} with the local Reynolds and Karlovitz numbers will be discussed in Secs. 4.5 and 4.6, respectively.

Extinction in flame E

Flame E is characterized by significant local extinction for $x/d < 30$ [71], which may explain the low values of γ^{opt} found in this region. Under these conditions, a single flamelet is not expected to reproduce the average thermo-chemical state. It should be noted that the χ_{st}^{opt} values for flame E at $x/d = 7.5$ and 15 are at the flamelet extinction limit.

4.4 Discussion

In this section, potential biases of the present error map analysis are discussed.

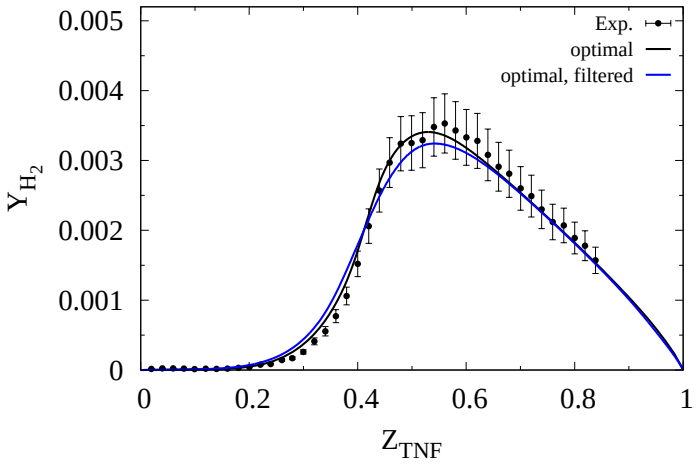

Figure 4.7: Comparison of H_2 mass fraction conditioned on Z_{TNF} for flame C at $x/d = 30$, against the optimal solution (black line), and the filtered optimal solution (blue line).

4.4.1 Experimental uncertainties

Figure 4.6 shows a comparison of the experimental conditional mean mass fractions of CO, H_2O, and H_2 for flame C at $x/d = 30$, against three flamelet solutions: the effective Lewis number solution which corresponds to γ^{opt} extracted with the error map analysis (Fig. 4.4b), the unity Lewis number case, and the laminar Lewis number solution. The χ_{st} value in all three flamelet solutions is set to χ_{st}^{opt}. As can be seen, for some of the measured scalars such as CO (Fig. 4.6a), it is difficult to conclude on the optimality of any solutions, due to the large experimental uncertainties (larger than the differences between the two extreme flamelet solutions). However, from Figs. 4.6b and 4.6c, it is evident that for other species, such as H_2O and H_2, the differences between the unity Lewis number and laminar Lewis number flamelets are larger than the experimental uncertainties. In an attempt to account for the uncertainties in the measured species mass fractions, the error map analysis was repeated using species-dependent weights. However, no significant improvement was obtained, and the results shown in this work were obtained without these weights.

In summary, while the experimental uncertainties are large (see Table 4.2), the impact of the effective Lewis numbers is still larger.

4.4.2 Spatial resolution

The reported spatial resolution of the mass fraction measurements is $\sigma = 0.75$ mm [46, 71]. The effect of this resolution can be reproduced by filtering the flamelet

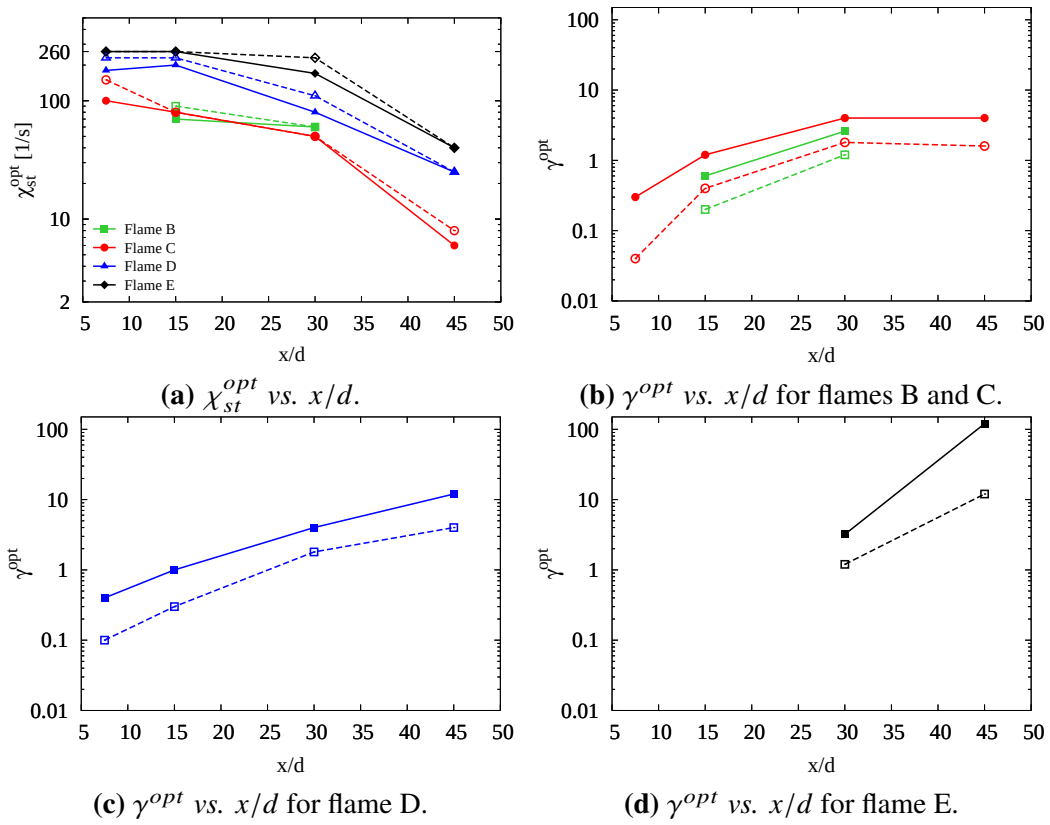

(a) χ_{st}^{opt} *vs.* x/d.

(b) γ^{opt} *vs.* x/d for flames B and C.

(c) γ^{opt} *vs.* x/d for flame D.

(d) γ^{opt} *vs.* x/d for flame E.

Figure 4.8: Optimal scalar dissipation rate, χ_{st}^{opt} (top left), and γ^{opt} (top right, bottom left, and bottom right), as a function of the downstream direction x/d for flames B, C, D, and E. The solid lines were obtained using GRIMech3.0 [135] without the nitrogen chemistry; the dashed lines were obtained using CaltechMech2.4 [111].

solution in mixture fraction space using a filter of width

$$\Delta Z = |\nabla Z|\sigma, \tag{4.10}$$

where $|\nabla Z|$ is evaluated from $\chi(Z)$, *i.e.*,

$$|\nabla Z|(Z) = \sqrt{\frac{\chi(Z)}{2\alpha(Z)}}. \tag{4.11}$$

Equation (4.10) can then be used to filter the flamelet solution using a top hat filter. The blue line in Fig. 4.7 shows the effect of averaging on the H_2 mass fraction for the optimal flamelet solution for flame C at $x/d = 30$. H_2 is used as a "worst case scenario" for this comparison, because of its large sensitivity to molecular/turbulent transport. As can be seen, spatial averaging has only a small effect on the flamelet solution.

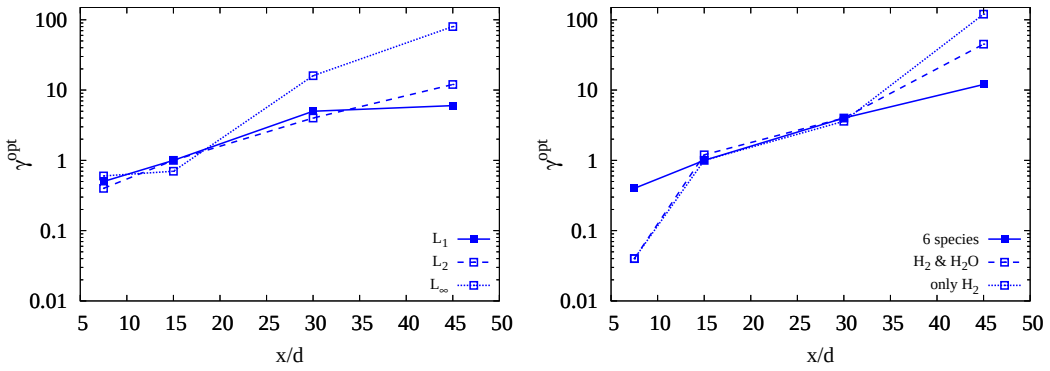

(a) Impact of different norms. **(b)** Impact of different species.

Figure 4.9: Comparison of γ^{opt} as a function of the downstream direction x/d for flame D, using different norms (left), and species (right). Left: the solid, dashed and dotted lines correspond to the L_1, L_2, L_∞ norms, respectively; right: the solid, dashed and dotted lines correspond to Eq. (4.8) using all 6 species, H_2 and H_2O, and only H_2, respectively.

4.4.3 Chemical model

An additional potential source of bias is given by the choice of the chemical model, which may affect the optimal solutions extracted using the error map analysis. To investigate this possibility, the analysis is repeated using CaltechMech2.4 [111]. The effect on the optimal flamelets is shown in Fig. 4.8. As can be seen, the same trends are observed for χ_{st}^{opt} and γ^{opt} with downstream distance. The differences between the χ_{st}^{opt} values are small, while larger differences between the γ^{opt} values are observed. That being said, the γ^{opt} profiles are almost uniformly shifted downwards, which does not affect the discussion in Secs. 4.5 and 4.6, and the results discussed in the following sections are obtained using GRIMech3.0 [135].

4.4.4 Choice of error norms

To investigate the effect of the choice of the error metric on the present analysis, the following L_1 and L_∞ norms were considered in addition to Eq. (4.8)

$$L_1(\chi_{st},\gamma) = \frac{1}{N_s N_p}\sum_{j,i}^{N_p,N_s}\frac{\left|Y_i(\chi_{st},\gamma,Z_{\mathrm{TNF},j}) - Y_i^{\mathrm{exp}}(Z_{\mathrm{TNF},j})\right|}{\max\limits_j\{Y_i^{\mathrm{exp}}(Z_{\mathrm{TNF},j})\}}, \tag{4.12}$$

and

$$L_\infty(\chi_{st},\gamma) = \max_{i,j}\left\{\frac{\left|Y_i(\chi_{st},\gamma,Z_{\mathrm{TNF},j}) - Y_i^{\mathrm{exp}}(Z_{\mathrm{TNF},j})\right|}{Y_i^{\mathrm{exp}}(Z_{\mathrm{TNF},j})}\right\}. \tag{4.13}$$

A comparison of γ^{opt} values for flame D, obtained using Eqs. (4.8), (4.12) and (4.13) is shown in Fig. 4.9a.

The optimal parameters obtained using the L_1 and L_2 norms are generally close for x/d = 7.5, 15 and 30. The γ^{opt} values for those stations differ by no more than 30%. Yet, large differences are found for x/d = 45: the χ_{st}^{opt} values differ by 60%, while the γ^{opt} values differ by a factor of 10. Once again, this large sensitivity/variation is not surprising as this location is close to the stoichiometric flame tip.

Finally, using the L_∞ norm, the largest differences with respect to the L_2 norm are found in flame D at x/d = 45, where the χ_{st}^{opt} values differ by a factor of 1.6 and the γ^{opt} values differ by a factor of 6.7. Based on the more erratic profiles obtained using the L_∞ norm, it is concluded that the high sensitivity of this norm on experimental uncertainties makes it unsuitable for the present analysis, and is not considered hereafter.

4.4.5 Choice of species for the error norm

As discussed in Sec. 4.2, mass fraction measurements used in this work include the six species O_2, CH_4, CO, CO_2, H_2O, and H_2. To reduce the influence of experimental outliers, the optimization problem given by Eq. (4.9) was solved considering all 6 species. These species have different measurement uncertainties [71], and might be affected differently by differential diffusion.

A comparison of γ^{opt} values for flame D, obtained considering the L_2 norm with different combinations of species, is shown in Fig. 4.9b. As can be seen, the γ^{opt} profiles show similar trends, and the values are close for $x/d = 15$ and $x/d = 30$. Once again, the largest differences are found close to the burner exit ($x/d = 7.5$), where the influence of the pilot may be felt, and close to the stoichiometric flame tip ($x/d = 45$): at the first location, the values differ by a factor of 10 with respect to the 6-species case; at the second, the γ^{opt} values obtained using one and two species differ by a factor of 10 and 2.7 with respect to the 6-species case, respectively. As can be seen, the use of only H_2 leads to the "saturation" of γ^{opt} at $x/d = 45$. The addition of H_2O reduces this effect; including all species reduces this even further, while producing a smoother behavior (γ^{opt} increases almost linearly with x/d).

4.4.6 Additional biases

Additional effects could bias the present analysis, such as radiative heat losses and thermo-diffusion (Soret and Dufour effects). Unfortunately, the importance of these effects could not be assessed in the present work.

4.5 Review of scaling based on the Reynolds number

A straightforward approach to estimate the coefficient α_T in Eq. (1.10), is simply to use a k-ε model, as was done in the work of Savard & Blanquart [47] for turbulent premixed flames, and that of Wang [75] for turbulent non-premixed flames. This approach is reviewed in this section, and applied to the Sandia flames.

4.5.1 Scaling based on the Reynolds number

The coefficient α_T can be expressed as $\alpha_T = \nu_T/Pr_T$, where ν_T is the turbulent viscosity, and Pr_T is the turbulent Prandtl number. Using a k-ε model for ν_T, α_T can be written as

$$\alpha_T = \frac{\nu_T}{Pr_T} = \frac{C_\mu k^2}{\varepsilon Pr_T} = \frac{C_\mu}{Pr_T}\frac{9}{4}\alpha Pr Re_T, \tag{4.14}$$

where $k = 3u'^2/2$ is the turbulent kinetic energy, $\varepsilon = u'^3/l$ is the energy dissipation rate, C_μ is the k-ε model constant, $Pr = \nu/\alpha$ is the Prandtl number, Re_T is the turbulent Reynolds number, defined as $u'l/\nu$, u' is the rms velocity fluctuation and l is the integral length scale. Hence, a possible scaling for γ is

$$\gamma = \frac{\alpha_T}{\alpha} = a^{Re_T} Re_T, \tag{4.15}$$

where a^{Re_T} is a scaling coefficient.

An estimate for this coefficient can be provided. The k-ε model constant C_μ can be set to 0.09 [146]. The Prandtl number Pr can be estimated from flamelet computations. For the present flames, $Pr \approx 0.6$-0.7. Next, an estimate for the turbulent Prandtl number Pr_T must be provided. For self-similar free-shear flows, a constant value of 0.7 has been shown to be a good approximation [147]. However, consistently with the assumption that $D_T = \alpha_T$, a value of 1 is also considered. With these values, the coefficient a^{Re_T} is estimated to vary in the range 0.1-0.2.

4.5.2 Estimating turbulent quantities

The evaluation of Eq. (4.15) requires estimates for u' and l at the radial flame location r_F (defined as $<Z>(x, r_F) = Z_{st}$). Figure 4.10a shows the r_F values for the experimental data [72, 129] and the LES data of Mueller *et al.* [148]. As can be seen, the r_F values for the different flames remain close to each other for the length of the flame, with minor differences at the tip. Further, the LES data shows a good agreement with the experiments. Other LES data, such as those of Jones & Prasad [149] and Ihme & Pitsch [150] for flames D and E (not shown here), also suggest a flame-independence of r_F. Figure 4.10b shows the jet half-width r_{12}, defined as $<U>(x, r_{12}) = 0.5<U_0(x)>$, where $<U_0(x)>$ is the mean centerline velocity.

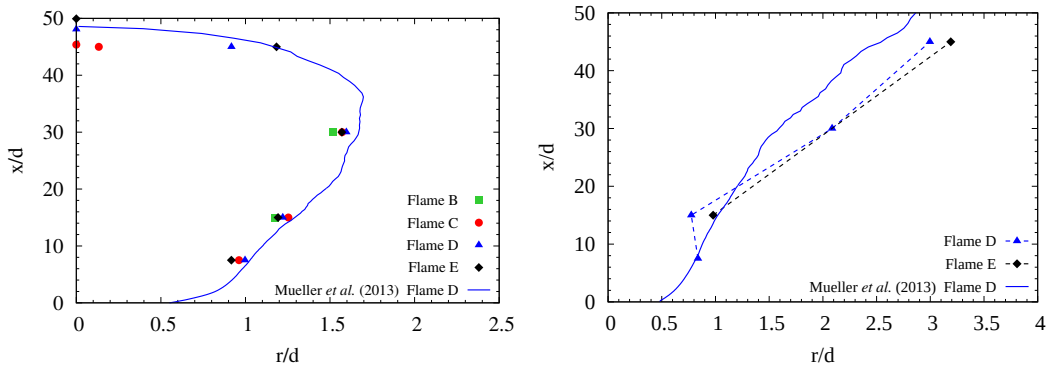

(a) Radial flame location r_F.

(b) Jet half-width r_{12}.

Figure 4.10: Radial flame location r_F (left) for flames B through E (green, red, blue, and black lines, respectively), and jet half-width r_{12} (right) for flames D and E (blue and black lines, respectively). The experimental data [72, 129] is represented by the full symbols and dashed lines; the LES data of Mueller *et al.* [148] is given by the lines without symbols.

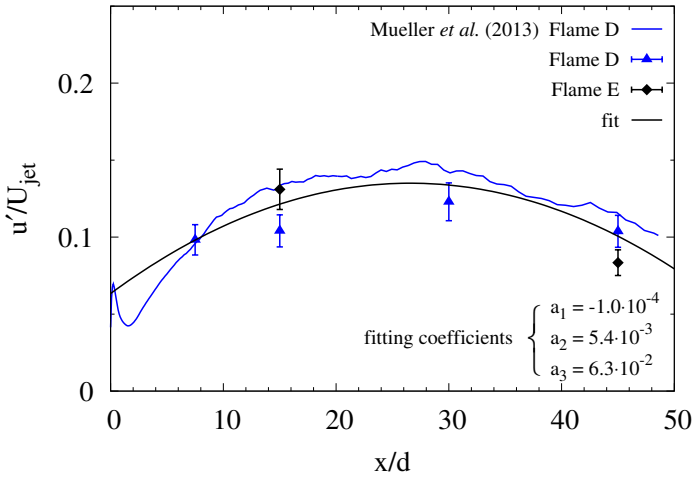

Figure 4.11: Rms velocity for flames D (blue) and E (black), at the radial flame location r_F, normalized by the bulk velocity of the respective jet. The experimental data of Schneider *et al.* [129] is represented by the symbols with error bars, while the LES data of Mueller *et al.* [148] is shown by the blue line. The solid black line represents the fit given by Eq. (4.18).

As can be seen, r_{12} is about the same for both flames D and E. Further, the LES data of Mueller *et al.* [148] are in good agreement with the experimental r_{12} values. This flame-independence of the r_{12} values is also supported by the LES data of Jones & Prasad [149], which is not shown here, for flames D and E. To summarize, Fig. 4.10 shows that, both r_F and r_{12} behave very similarly across flames.

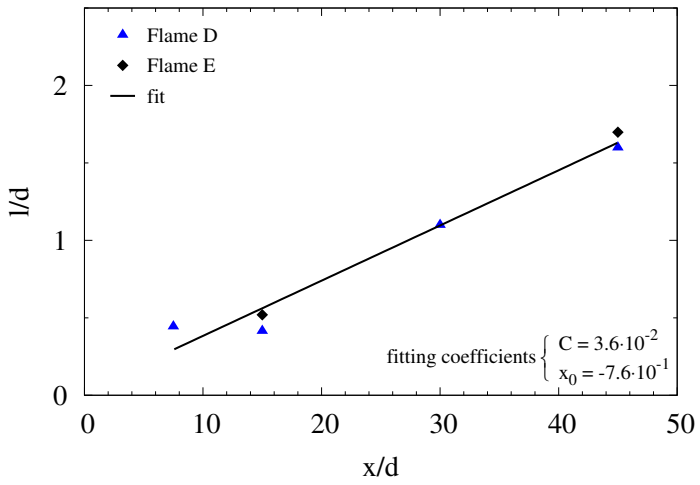

Figure 4.12: Estimated integral length scale for flames D (blue) and E (black) at the radial flame location. The line is the fit given by Eq. (4.22).

With this observation, the values of u' and l at the radial flame location, are assumed to follow the relations

$$\frac{u'}{U_{\text{jet}}} = f\left(\frac{x}{d}\right), \tag{4.16}$$

and

$$\frac{l}{d} = m\left(\frac{x}{d}\right), \tag{4.17}$$

where the functions f and m are considered to be the same for flames B through E.

Figure 4.11 shows u'/U_{jet} at the average radial flame location for flames D and E, normalized by the bulk velocity of the respective jet [129, 148]. Given the previous observations, a collapse of the normalized velocities for all flames is expected. As discussed in Sec. 4.2, velocity data is available only for flames D and E. To overcome this limitation, and using the previous observation, the following approximation is assumed in this work

$$\frac{u'}{U_{\text{jet}}} = a_1\left(\frac{x}{d}\right)^2 + a_2\left(\frac{x}{d}\right) + a_3. \tag{4.18}$$

In Eq. (4.18), u' is computed from the available data as

$$u' = \sqrt{\frac{u_{\text{rms}}^2 + 2v_{\text{rms}}^2}{3}}, \tag{4.19}$$

and the fitting coefficients a_i, shown in Fig. 4.11, are computed by using a nonlinear least square package applied to the experimental [129] and LES [148] data at stations $x/d = 7.5$, 15, 30 and 45. Equation (4.18) is then used for all flames.

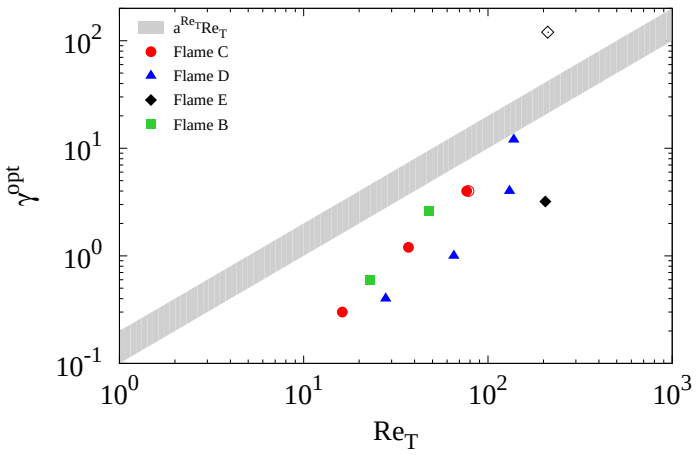

Figure 4.13: Evolution of γ^{opt} with Reynolds number. The gray band represents Eq. (4.15) with the estimates for a^{Re_T} discussed in Sec. 4.5.1. The first two stations of flame E are not shown, as their γ^{opt} values are 0. The open red symbol represents flame C at $x/d = 45$, for which the average stoichiometric flame length is 45.4 diameters downstream of the burner exit (see Sec. 4.3.4); flame E at $x/d = 45$ has also been marked with an open symbol to highlight the large difference in γ^{opt} values obtained with the L_1 and L_2 norms (see Sec. 4.4.4).

The integral length scale, l, defined as

$$l \equiv \frac{u'^3}{\varepsilon}, \tag{4.20}$$

is computed at the average radial flame location, r_F, using

$$\frac{l}{r_{12}} = g\left(\frac{r}{r_{12}}\right), \tag{4.21}$$

where g is computed using self-similar profiles for isothermal round jets [151, 152]. It should be noted that g is almost constant for $0 < r < r_{12}$. First, l is estimated for flames D and E, for which r_{12} can be computed from the available velocity data (see Fig. 4.10b). The data points are then fitted using the relation

$$\frac{l}{d} = C\frac{x - x_0}{d}, \tag{4.22}$$

where C and x_0 are fitting constants (shown in Fig. 4.12). The fit given by Eq. (4.22), which is shown in Fig. 4.12, is then used for all flames.

4.5.3 Assessment of the scaling based on the Reynolds number

Figure 4.13 shows a comparison of γ^{opt} against the model given by Eq. (4.15). The extracted γ^{opt} values are found to transition from a laminar mixing regime towards unity, and this transition is positively correlated with a local Re_T. However, as can

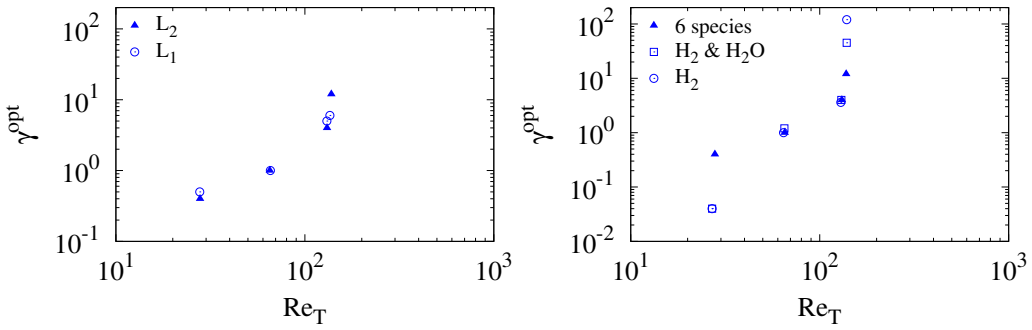

(a) Impact of different norms.

(b) Impact of different species.

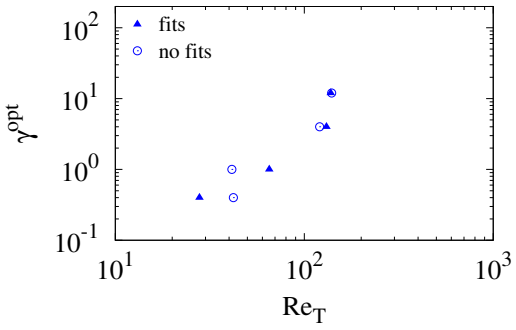

(c) Impact of uncertainties on Re_T.

Figure 4.14: Evolution of γ^{opt} with Reynolds number for flame D, showing the differences between the L_2 and L_1 norms (Eqs. (4.8) and (4.12), respectively) (left), the effects of different species combinations on the L_2 norm (center), and differences between using Re_T values obtained with and without the fits given by Eqs. (4.18) and (4.22) (right).

be seen, the magnitude of the predicted γ^{opt} values using the $a^{Re_T} \approx 0.1$-0.2 range discussed in Sec. 4.5, overestimates the extracted values by an order of magnitude; and the transition from laminar to turbulent mixing occurs at much larger Re_T. Similar observations were made in [47] for turbulent premixed flames.

To better understand the effect of the uncertainties of the present analysis, Fig. 4.14 shows the extracted γ^{opt} values with the local Re_T, using the L_2 and L_1 norms (Fig. 4.14a), using Eq. (4.8) with different species combinations (Fig. 4.14b), and the effect of the fits given by Eqs. (4.18) and (4.22) on the local Re_T values. As can be seen, the L_1 and L_2 norms lead to similar γ^{opt} values, as discussed in Sec. 4.4.4. The use of different species combinations leads to large γ^{opt} differences in the jet near field ($x/d = 7.5$) and close to the flame tip ($x/d = 45$), as discussed in Sec. 4.4.5. Finally, Fig. 4.14c shows that, for flame D, the Re_T values with and without the fits (4.18), and (4.22), differ at the most by a factor of 1.3 at $x/d = 30$.

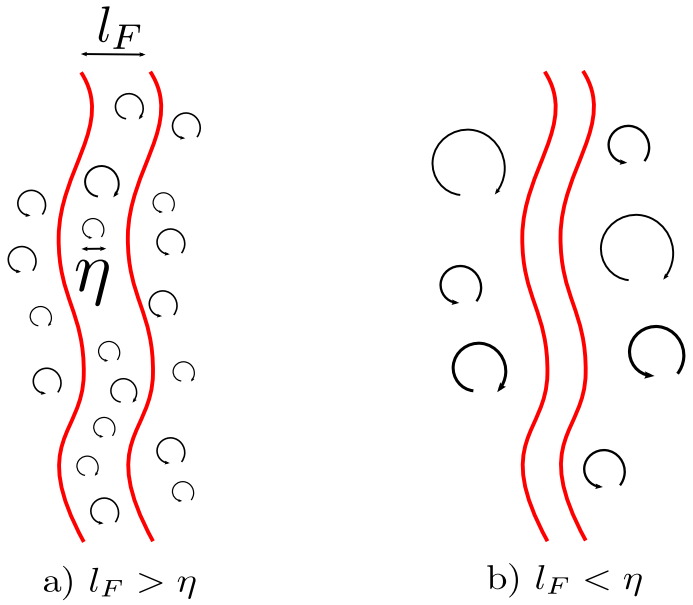

Figure 4.15: Sketch of turbulent non-premixed flames for a) $\eta < l_F$, and b) $\eta > l_F$.

4.6 Scalings based on the Karlovitz number

In this section, scalings based on flame characteristic scales are investigated.

4.6.1 Turbulent scales interacting with the flame

The k-ε approach discussed in Sec. 4.5 represents a simple way of computing a dimensionally correct coefficient α_T, yet it does not present any direct dependence on flame-relevant parameters. This is unexpected as turbulent mixing of a scalar should involve the "thickness" of that scalar. Here, this scalar thickness is computed as

$$l_F \equiv 4\frac{Z_{st}(1-Z_{st})}{|\nabla Z|_{st}}, \tag{4.23}$$

where $|\nabla Z|_{st}$ is computed as $[\chi_{st}^{opt}/(2\alpha)]^{1/2}$. A derivation is given in Appendix A. Depending on the relative magnitude of l_F, l, and the Kolmogorov length scale η, defined as

$$\eta \equiv \left(\frac{\nu^3}{\varepsilon}\right)^{\frac{1}{4}}, \tag{4.24}$$

the flame is affected differently by the turbulence, as is schematically shown in Fig. 4.15, where the two cases where $\eta < l_F$ and $\eta > l_F$ are represented. It should be noted that the ratios l_F/η, l/l_F and l/η, evaluated at the average radial flame location, vary with downstream distance.

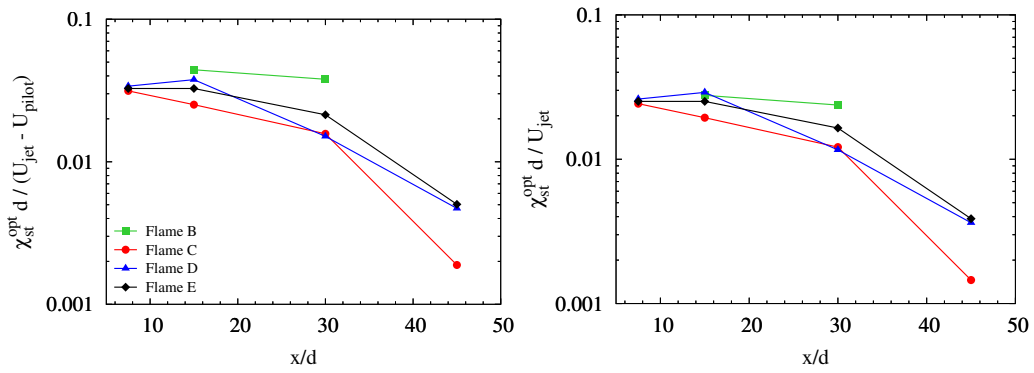

Figure 4.16: Optimal χ_{st} values normalized by $(U_{\text{jet}} - U_{\text{pilot}})/d$ (left) and U_{jet}/d (right), as a function of downstream direction for flames B, C, D, and E.

The ratio of the flame thickness l_F to the Kolmogorov length scale η, is related to the Karlovitz number through

$$Ka \equiv \left(\frac{l_F}{\eta}\right)^2, \tag{4.25}$$

where the quantities on the r.h.s. are evaluated at stoichiometric conditions. Using Eq. (4.23), the ratio l_F/η can be expressed as

$$\frac{l_F}{\eta} = 4\sqrt{2}Z_{st}(1 - Z_{st})Re_{\text{jet}}^{\frac{1}{4}}\left(\frac{f^3}{mh^2}\right)^{\frac{1}{4}}, \tag{4.26}$$

where the following expression has been used

$$\chi_{st} = \frac{U_{\text{jet}}}{d}h\left(\frac{x}{d}\right). \tag{4.27}$$

Figure 4.16 shows the χ_{st}^{opt} values normalized by by $(U_{\text{jet}} - U_{\text{pilot}})/d$ and U_{jet}/d[‡]. The normalization by U_{jet}/d is considered in Eq. (4.27), since a better collapse is obtained, as shown in Fig. 4.16. The function $h(x/d)$ can be taken to be an average of the profiles normalized by U_{jet}/d.

The ratio l/η can be expressed as

$$\frac{l}{\eta} = \frac{u'^3}{\varepsilon}\left(\frac{\varepsilon}{\nu^3}\right)^{\frac{1}{4}} = Re_T^{\frac{3}{4}}, \tag{4.29}$$

[‡]These normalizations are suggested through a simple dimensional argument, and by analogy with the planar counterflow diffusion flame [10], for which the scalar dissipation may be written as

$$\chi(Z) = \frac{a}{\pi}\exp\left(-2\left[\text{erfc}^{-1}(2Z)\right]^2\right), \tag{4.28}$$

where a is the strain-rate. For the present configuration, $a \approx U_{\text{jet}}/d$ or $a \approx (U_{\text{jet}} - U_{\text{pilot}})/d$.

which can be rewritten as

$$\frac{l}{\eta} = Re_{\text{jet}}^{\frac{3}{4}} (fm)^{\frac{3}{4}} . \tag{4.30}$$

From Eqs. (4.26) and (4.30), it can be seen that the local Ka is less sensitive to the jet Reynolds number than the local turbulent Reynolds number. This weak dependence on Re_{jet} is consistent with the weak dependence of γ on Re_{jet} (Fig. 4.4b) and suggests a possible scaling based on the Ka number.

Savard & Blanquart [47] proposed two scalings for turbulent premixed flames: one based on a length scale argument, the other on a time scale argument. An analogous approach may be followed also for turbulent non-premixed flames.

4.6.2 Flame length scale-based scaling

Assuming that α_T is controlled by eddies of the size of the flame, a possible scaling is

$$\alpha_T \sim u(l_F) l_F, \tag{4.31}$$

where l_F is given by Eq. (4.23), and $u(l_F)$ is the turnover velocity of eddies of size l_F. The velocity $u(l_F)$ can be related to l_F through

$$u(l_F) = (\varepsilon l_F)^{1/3}. \tag{4.32}$$

Using Eqs. (4.31) and (4.32), the following scaling for γ can be derived

$$\gamma \sim \frac{(\varepsilon l_F^4)^{\frac{1}{3}}}{\nu}, \tag{4.33}$$

or

$$\gamma = a^{l_F} \left(\frac{l_F}{\eta}\right)^{\frac{4}{3}} = a^{l_F} Ka^{\frac{2}{3}}, \tag{4.34}$$

where a^{l_F} is a scaling coefficient.

The result given by Eq. (4.34) is to be expected, as the Karlovitz number provides a simple mean of relating relevant flame parameters to turbulence parameters. It should be noted that Eqs. (4.14) and (4.31) are equivalent up to a constant multiplicative factor, if $l_F = l$ and Eq. (4.32) is used.

4.6.3 Flame time scale-based scaling

Alternatively, one can assume that in a turbulent non-premixed flame, the eddy diffusivity is controlled by eddies whose time scale is equal to the flame time scale,

τ_F. Using this argument, α_T, can be expressed as

$$\alpha_T \sim \frac{[l_m(\tau_F)]^2}{\tau_F}, \tag{4.35}$$

where $l_m(\tau_F)$ is the size of eddies of turnover time τ_F. Following Peters [10, 153], an expression for l_m can be obtained by equating the corresponding eddy turnover time to the flame time scale

$$l_m(\tau_F) = \sqrt{\varepsilon \tau_F^3}. \tag{4.36}$$

The flame time scale may be defined by considering the relaxation time of one of the species, but this would leave an ambiguity as to which species is best suited. Another approach is to define a general chemical time scale from Eq. (4.23) as

$$\tau_F \equiv \frac{l_F^2}{4\alpha} \propto \frac{Z_{st}^2(1 - Z_{st})^2}{\chi_{st}}, \tag{4.37}$$

where χ_{st}^{opt} is used as χ_{st}. It should be noted that Eq. (4.37) is equivalent to the expression derived by Peters [153] for a time scale at the extinction threshold using one-step asymptotics, up to the constant multiplicative factor of 8.

If, as a further approximation, α is taken to be proportional to ν, given a constant Prandtl number, then, combining Eqs. (4.35) and (4.36) yields the scaling

$$\gamma \sim \frac{\varepsilon}{\nu}\tau_F^2, \tag{4.38}$$

or

$$\gamma = a^{\tau_F}\frac{\tau_F^2}{\tau_\eta^2} \equiv a^{\tau_F} Ka^2, \tag{4.39}$$

where τ_η is the Kolmogorov time scale, a^{τ_F} is a scaling coefficient. The Kolmogorov time scale is defined as $\tau_\eta \equiv \sqrt{\nu/\varepsilon}$, where both ν and ε should be evaluated at stoichiometric conditions. The kinematic viscosity, ν, is computed from the optimal flamelet solution at the stoichiometric mixture fraction.

It should be noted that Eq. (4.25) and $Ka \equiv \tau_F/\tau_\eta$ are equivalent if Eqs. (4.23) and (4.37) are used, and $\alpha \approx \nu$ is assumed. It should also be noted that Eqs. (4.14) and (4.35) are equivalent up to a constant multiplicative factor, if $\tau_F = l/u'$ and Eq. (4.36) is used.

4.6.4 Assessment of the scalings based on the Karlovitz number

As can be seen from Fig. 4.17, the extracted γ^{opt} values show a transition from the laminar regime, towards unity, and the data points are generally positively correlated with the Karlovitz number, yet no clear trend is observed. The points corresponding to flame B are significantly shifted to the left. As will be discussed in

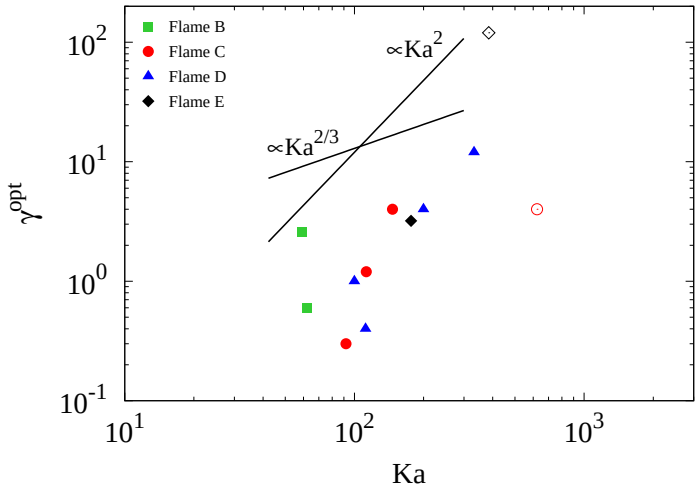

Figure 4.17: Evolution of γ^{opt} with Karlovitz number. The first two stations of flame E are not shown, as their γ^{opt} values are 0. The open red symbol represents flame C at $x/d = 45$, for which the average stoichiometric flame length is $x/d = 45.4$ (see Sec. 4.3.4); flame E at $x/d = 45$ has also been marked with an open symbol to highlight the large uncertainty of the γ^{opt} value at that location (see Sec. 4.6.4). The solid lines represent the scalings given by Eqs. (4.34) and (4.39).

Ch. 7, the approach used to estimate the flame thickness has a strong impact on the flame Karlovitz numbers, and needs to be more thoroughly examined. The last point of flame C is artificially shifted to the right. The cause for this shift is most likely a combination of low γ^{opt} and χ_{st}^{opt} values at this location. This is not surprising, as the stoichiometric flame tip for flame C is close to $x/d = 45$. Further, the last point for flame E is characterized by a large γ uncertainty. This can clearly be seen by the shape of the error contours shown in Fig. 4.3c, which is also likely caused by the proximity of that measurement station to the stoichiometric flame tip.

As can be seen, the trend followed by the data points is somewhat different from the two scalings discussed in Secs. 4.6.2 and 4.6.3. One possible reason that explains this difference, is the fact that the Ka number is too small. In other words, the flame thickness l_F might fall in the dissipation range, and not in the inertial subrange, from which the two scalings given by Eqs. (4.34) and (4.39) were derived. However, beyond the present work, the scalings discussed in Secs. 4.6.2 and 4.6.3 could be extended to include corrections for the dissipation range.

4.7 Summary

In this chapter, a new flamelet-based methodology to extract effective Lewis numbers from experimental and numerical data sets of turbulent diffusion flames has

been proposed. This technique has been applied to a set of experimental turbulent non-premixed methane/air jet flames (Sandia flames) by comparing measured species mass fractions with solutions of the non-unity Lewis number flamelet equations. For each flame and each downstream location, two *optimal* flamelet parameters were extracted, including a stoichiometric scalar dissipation rate, χ_{st}^{opt}, and the ratio $\gamma^{opt} \equiv \alpha_T/\alpha$. The effective Lewis numbers for each species are then computed using Eq. (1.11) with γ^{opt}.

For the four turbulent flames considered, the evaluated effective Lewis numbers (γ^{opt}) were found to transition from their laminar values at the burner exit plane ($\gamma^{opt} = 0$), towards unity further downstream ($\gamma^{opt} \to \infty$). Interestingly, these effective Lewis numbers were not found to increase with the jet Reynolds number. The χ_{st}^{opt} values were found to decrease with axial distance, and, with the exception of the lowest Reynolds number flame, to increase with jet Reynolds number.

The extracted $\chi_{\mathrm{TNF},st}^{opt}$ values were found to systematically over-estimate the measured $\langle \chi_{\mathrm{TNF},st} \rangle$ values of Karpetis & Barlow [132]. It is expected that multi-dimensional effects, including convective and diffusive transport along the mixture fraction iso-surfaces, are essentially lumped into the extracted χ_{st}^{opt} values. To investigate this effect, a budget analysis of the flamelet equations using DNS data of jets at increasing Reynolds numbers should be carried out. The computational cost of performing these DNS is extremely high, and is beyond the scope of the current work.

Previously-suggested correlations for the parameter γ with both Reynolds and Karlovitz numbers were compared to the extracted γ^{opt} values. However, large experimental uncertainties and the limited number of measured quantities prevented a conclusive assessment of these models.

The work discussed in this chapter represents a first step towards modeling of differential diffusion effects in turbulent non-premixed jet flames. More conclusive results should be obtained using DNS data. Unfortunately, carrying out DNS of non-premixed jet flames presents a prohibitive computational cost, and is limited to low Reynolds numbers. In the following sections, a series of DNS of Sandia flame B are discussed. This flame has the lowest jet Reynolds number among the Sandia flames ($\mathrm{Re}_{\mathrm{jet}} \approx 8200$), while still being turbulent.

Chapter 5

DIRECT NUMERICAL SIMULATION OF SANDIA FLAME B: GRID RESOLUTION REQUIREMENTS AND GRID INDEPENDENCE

In the previous chapter, a flamelet-based technique to extract effective Lewis numbers from experimental or numerical data of non-premixed turbulent flames was described. This technique was then applied to a well-characterized experimental database (the "Sandia flames"), and previously-suggested models for these effective Lewis numbers were assessed. Limitations of the experimental data base, including large uncertainties, few measured quantities and limited spatial resolution, prevented a conclusive assessment of the mechanisms associated with the evolution of the flame structure from a molecular diffusion-controlled regime, to a turbulence-dominated one.

For all these reasons, a campaign of DNS of Sandia flame B is carried out. Flame B has the lowest Reynolds number among the Sandia flames ($\mathrm{Re_{jet}} \approx 8200$), while still being turbulent. Further, flame B should be simulated for an additional reason. In Sec. 4.5.2 flame independence was assumed for several turbulence and flame parameters, including the radial flame location, r_F, the jet half-width, r_{12}, the normalized rms velocity at the flame location, $u'/\mathrm{U_{jet}}$, and the integral length scale l/r_{12} at r_F. While the assumption of flame independence for these quantities is expected to hold for the higher Reynolds number flames, that may not be the case for flame B. Fortunately, that flame is the easiest to simulate using DNS, and the validity of those assumptions can be investigated.

While performing DNS of flames C-E is also desirable, the computational cost remains prohibitive. For these laboratory-scale flames, the high cost associated with the fine grid resolution is compounded by the large number of scalars transported, and the necessity of converging statistics sufficiently to investigate phenomena that occur at the smallest scales, such as turbulence-chemistry interactions.

In the next sections, a detailed description of the grid design is carried out, followed by an *a posteriori* assessment of the chosen grid resolution. An extensive validation using available experimental data will be the subject of Ch. 6. The flamelet-based methodology discussed in Ch. 4 will then be applied to the DNS data base in Ch. 7.

5.1 Introduction

Direct numerical simulations have become an important tool in turbulent combustion research [11, 154], enabling detailed investigations of temporal and spatial structures that would be difficult to investigate experimentally [155]. Despite the high cost of DNS, the surge in computational resources over the past few decades has spurred a growing body of work on more realistic, laboratory-scale flames.

Some examples of the past decade are the following. Sankaran *et al.* [156] investigated the structure of a spatially developing lean methane-air Bunsen flame using 52 million grid points; Bell *et al.* [157] studied a slot flame with an effective resolution of about 98 million grid points; Grout *et al.* [158, 159] performed a DNS of a reactive fuel jet in cross-flow, using 1.6 billion grid points. Yoo *et al.* [50] investigated the stabilization mechanism of a turbulent lifted ethylene jet flame (Reynolds number of 10,000) using over 1.29 billion grid points. In Karami *et al.* [160], a DNS of a turbulent premixed jet burner with Reynolds number of 5280 was carried out using 256 million grid points. Recently, MacArt *et al.* [161] investigated a spatially-developing, planar, turbulent premixed flame with a Reynolds number of 5000, using up to 226.5 million grid points.

In DNS, the choice of the grid has a major impact on the computational cost. That is why it is important to ensure that an optimal distribution of grid points is chosen, such that the desired resolution is obtained at the minimum cost. For simple configurations, designing the grid can be straightforward: a uniform mesh may be used, where the mesh size can be easily estimated from criteria developed for homogeneous isotropic turbulence (HIT) [162] and chemistry resolution requirements [57]. However, designing grids for spatially developing flames is typically more challenging, due to the wide range of local aerodynamic effects and the strong anisotropy of the flow. For these flames, the use of a uniform mesh size would lead to prohibitive computational costs, and, therefore, it is common practice to add stretching to the grid.

An important question arises. What should the resolution be in non-uniform grids? One could ensure that HIT grid resolution criteria apply in each separate direction [161]. However, such a naive approach would lead to a large number of grid points without clear benefits. A typical approach for non-HIT applications is to rely on well-characterized benchmark cases to design the computational grid. Unfortunately, such studies may not be available for the configuration under investigation, or the parameters may be too different.

Inlet	Ø[mm]		Velocity	Composition	Temp. [K]
	inner	outer	profile, [m/s]		
main jet	7.2	7.7	file,[§] 18.2	Y_{N_2}=0.648 Y_{O_2}=0.196 Y_{CH_4}=0.156	294
pilot	18.2	18.9	top-hat, 6.8	[†]	[‡]
co-flow	none		top-hat, 0.9	Y_{N_2}=0.758 Y_{O_2}=0.236 Y_{H_2O}=0.006	291

[§] From an auxiliary turbulent pipe flow simulation.
[†,‡] Computed from the burnt side of a CH_4/air premixed flamelet at $\phi = 0.77$ [72].

Table 5.1: Inlet conditions used in this work.

For turbulent non-premixed jet flames, there is little work towards a systematic assessment of grid resolution requirements. DNS studies of this configuration with detailed descriptions of the grid, and assessments of grid independence, are missing. As a result, non-optimal grids are often adopted, with a large number of grid points used as a "safety margin".

Choosing an optimal grid in DNS of turbulent combustion is also important for another reason. These simulations are affected by multiple uncertainties, which are introduced by the choice of the combustion models, as well as uncertainties in the boundary conditions [163], and sampling errors associated with the limited run time of the simulations [164]. All these uncertainties may very well be dominating over discretization errors, and completely offset any benefit of using overly refined grids.

It is the objective of this work to perform a well-characterized DNS of Sandia flame B, with a detailed description of the grid set-up, and an *a posteriori* assessment of the chosen grid resolution with refined cases. As previously discussed, a detailed comparison with available experimental data will be the subject of Ch. 6. This chapter is organized as follows. Section 5.2 provides an overview of the boundary conditions. In Sec. 5.3, the grid resolution is discussed. The chosen test cases for the present thesis are discussed in Sec. 5.4. An *a posteriori* discussion of grid independence is carried out in Sec. 5.6, and a summary of the observations is given in Sec. 5.7.

5.2 Boundary conditions

A detailed overview of the inflow conditions is given in Table 5.1. The main jet issues at $U_{jet} = 18.2$ m/s, and is generated though an auxiliary turbulent pipe flow simulation at the same Reynolds number, $Re_{jet} = 8200$. The auxiliary simulation generates a total of 9500 two-dimensional slices of the u, v, w, and p fields, for a total running time t_{max} of $48d/U_{jet}$. The fuel pipe inflow is repeated every t_{max}, and the composition is taken directly from the reported values [72]. The fuel stream is a mixture of CH_4 and air at 25% and 75% by volume, respectively, whose equivalence ratio ($\phi \approx 3.19$) is beyond the burning limit ($\phi_R \approx 1.82$).

The main jet is surrounded by a pilot flame with a velocity of 6.8 m/s, for which a top-hat profile is used. The pilot flame burns a mixture of C_2H_2, H_2, air, CO_2, and N_2 with the same enthalpy and equilibrium composition as CH_4/air at an equivalence ratio of 0.77 [71]. The fuel and pilot streams are separated by a pipe with inner and outer diameters of $d = 7.2$ mm and $d_o = 7.7$ mm, respectively.

A co-flowing stream of air at 0.9 m/s is present, which is modeled through a top-hat velocity profile. The composition of the co-flow is the same as that given in [72]. The pipe separating the pilot and the air co-flow streams has inner and outer diameter of $d_{p,i} = 18.2$ mm and $d_{p,o} = 18.9$ mm, respectively. For the present work, the inflow is recessed by $1d$ from the burner exit plane, to allow the shear layers to develop correctly.

The remaining boundaries are modeled as follows. A Neumann condition is applied to the outer domain boundary to represent the free-stream co-flow. For the present work, cylindrical grids are used (see Sec. 5.3), and the centerline treatment follows the formulation of Desjardins *et al.* [78]. A convective condition is used at the outflow. Finally, no-slip and no-penetration conditions are used for the fuel pipe and pilot pipe walls.

5.3 *A priori* design of the grid

In this section, a detailed description of the baseline grid is provided. Here, the computational cost is reduced as much as possible through a careful design of the computational grid. First, an *a priori* analysis of the chosen radial and axial grid stretching is provided. Second, the overall grid is presented.

5.3.1 Resolving the turbulence

A ubiquitous grid resolution criterion is based on the popular work of Yeung & Pope on Homogeneous Isotropic Turbulence (HIT) [162]. To fix notation, $\Delta\xi$ is used to represent a uniform grid spacing. The Kolmogorov length scale, η, is computed using Eq. (4.24), where the average kinematic viscosity $\langle\nu\rangle$ is used, and the dissipation rate of turbulent kinetic energy, ε, is computed using [165]

$$\varepsilon \equiv \left\langle \sigma'_{ik} \frac{\partial u'_i}{\partial x_k} \right\rangle \langle\rho\rangle^{-1}, \tag{5.1}$$

where $\langle\cdot\rangle$ denotes averaging in time and in the statistically-homogeneous azimuthal direction, and $(\cdot)' = (\cdot) - \langle\cdot\rangle$. In Yeung & Pope [162], it is observed that the value

$$\Delta\xi/\eta \lessapprox 3, \tag{5.2}$$

is sufficient for low-order velocity statistics, and

$$\Delta\xi/\eta \lessapprox 2, \tag{5.3}$$

is needed for higher order quantities, such as dissipation, which is an example of a derivative statistic, and higher statistical moments. In HIT, Eq. (5.3) also ensures that the cumulative dissipation represents over 99% of the dissipation [147]. However, the extension of Eqs. (5.2) and (5.3) to non-HIT applications is not straightforward. For example, it is not clear if Eqs. (5.2) and (5.3) should apply to all three directions simultaneously, and doing so as a "precaution" would lead to a large number of grid points.

In the following sections, a detailed description of how the grid is designed will be provided. As a practical approach to overcome the difficulty of applying Eqs. (5.2) and (5.3) to non-HIT applications, an equivalent mesh size [166, 167] will be considered

$$\Delta = (r\Delta\theta\Delta x\Delta r)^{1/3}, \tag{5.4}$$

where Δx, Δr and $\Delta\theta$ represent the grid size in the axial, radial and azimuthal directions, respectively. To minimize the number of grid points, the *a priori* grid design discussed in the following sections will attempt to satisfy Eq. (5.2) using Eq. (5.4).

A convenient way to construct the grid for jet flames, is to consider two conceptual parts: a "pipe flow" region, which extends axially from the inlet to the burner exit plane and radially from the centerline to the fuel pipe inner diameter, and a "main jet" region, representing the rest of the computational domain. The former region, where the smallest turbulence scales are found, is much smaller than the latter.

Pipe flow region

Radial grid stretching is obtained through a hyperbolic tangent profiles [168] from the centerline to $d_{p,i}/2$, and linear stretching otherwise. For $r/d < 0.5$ (Sec. 5.3.2 will discuss the radial grid for $r > d/2$), the hyperbolic stretching coefficient is 2.4. In this region, the radial grid spacing is minimum at $r = d/2$, where $\Delta r^+ = 0.47$[§], and is maximum at the centerline, where $\Delta r^+ = 13.9$. The first location off the wall at which the axial velocity is computed is $r^+ = 0.24$, and the grid is such that there are 8 grid points within the viscous sublayer.

The grid in the azimuthal direction is uniform, with a total of 128 grid points. For $r < d/2$, the circumferential grid spacing is $(\frac{1}{2}\Delta r \Delta\theta)^+ \approx 0.34$ near the centerline and $(\frac{d}{2}\Delta\theta)^+ \approx 12.8$ at the pipe wall. As reference, for the uniform grid used by Eggels *et al.* [167] in their pipe flow DNS ($\mathrm{Re}_{\mathrm{jet}} = 5300$), the circumferential grid spacing varies from $(\frac{1}{2}\Delta r \Delta\theta)^+ \approx 0.05$ near the centerline, to a maximum value of $(\frac{d}{2}\Delta\theta)^+ \approx 8.84$ at the pipe wall.

A constant grid spacing of $\Delta x^+ = 7.03$ is used in the axial direction up to a distance of $1d$ downstream of the burner exit plane, the same as that used by Eggels *et al.* [167].

For Eggels *et al.* [167] the largest Δ^+ is 4.9, at the wall. However, with the present grid stretching, the range $3.2 < \Delta^+ < 7.9$ is obtained for $r < d/2$, where the maximum value $\Delta^+ = 7.9$ is found at $r/d = 0.29$, and $\Delta^+ = 3.2$ for the first cell off the centerline.

The present pipe flow grid is coarser than the well known pipe flow DNS of Wu & Moin [169]. However, the chosen resolution is deemed sufficient to resolve low order statistics, such as means and standard deviations of velocities and scalars.

Main jet region

For the present jet, a clear distinction between potential core, transition region and far field is not possible, due to the low Reynolds number and the effects of heat release; instead, a single "main jet region" extending from the burner exit plane up to the domain outflow is considered. For this region, a constant streamwise grid stretch factor is used. The determination of this factor requires an estimate for the axial growth of the smallest turbulence scales. In the absence of detailed velocity

[§]The superscript "+" indicates scaling in inner units [147], *e.g.*, $\Delta r^+ = \Delta r u_\tau / \nu$, where u_τ is the friction velocity and ν is the kinematic viscosity.

data, a simple conservative estimate can be obtained through the observed axial growth of η for isothermal round self-similar jets [170]

$$\eta = \left(48 Re_{\text{jet}}^3\right)^{-\frac{1}{4}} x, \quad x \gg d, \tag{5.5}$$

where x is the axial distance from the burner exit plane. The estimate given by Eq. (5.5) is conservative, since the fluid viscosity and diffusivities can increase dramatically with temperature, with an attendant reduction of the local Reynolds number [171]. If we assume that Δ^+ may grow at the same rate of Eq. (5.5), then the centerline Δ^+ can increase by a factor of 6 between the inflow and the outflow. However, that would result in extremely elongated grid cells towards the domain outflow, and does not take into account the presence of a potential core. Here, a constant axial grid stretching of 0.25% is used, *i.e.*, $\Delta x_i = 0.0025 \Delta x_{i-1}$, where Δx_i is the axial grid spacing for the ith cell. With this choice, the centerline Δ^+ and Δx at the outflow are 2.4 and 13 times their respective values at the burner exit plane. The chosen axial grid stretching is shown in Fig. 5.2a.

5.3.2 Resolving the chemistry

A priori grid resolution estimates for the chemistry are difficult to make in spatially-developing jet flames, due to the large variation of the local aerodynamic effects on the flame structure.

Several criteria are available in the literature. Lignell *et al.* [172] performed a three-dimensional DNS of a temporally evolving non-premixed ethylene jet flame; in their work, it was suggested to have at least 10 grid points across the thinnest radical species structures. In the DNS of Hawkes *et al.* [114], a temporally evolving plane jet flame was simulated. They suggested using at least 20 grid points across the OH layer. Both these studies suggest that one should (*i*) define a characteristic length scale for the smallest chemistry structures, and (*ii*) ensure that enough grid points are used across it.

Following this approach, here the reaction zone thickness is computed as

$$l_R \approx \frac{\Delta Z_i}{|\nabla Z|}, \tag{5.6}$$

where ΔZ_i can be taken to be the width in mixture fraction space of a radical species i, and where $|\nabla Z|$ can be computed at the mixture fraction location of peak species mass fraction as

$$|\nabla Z| = \sqrt{\frac{\chi}{2\alpha}}. \tag{5.7}$$

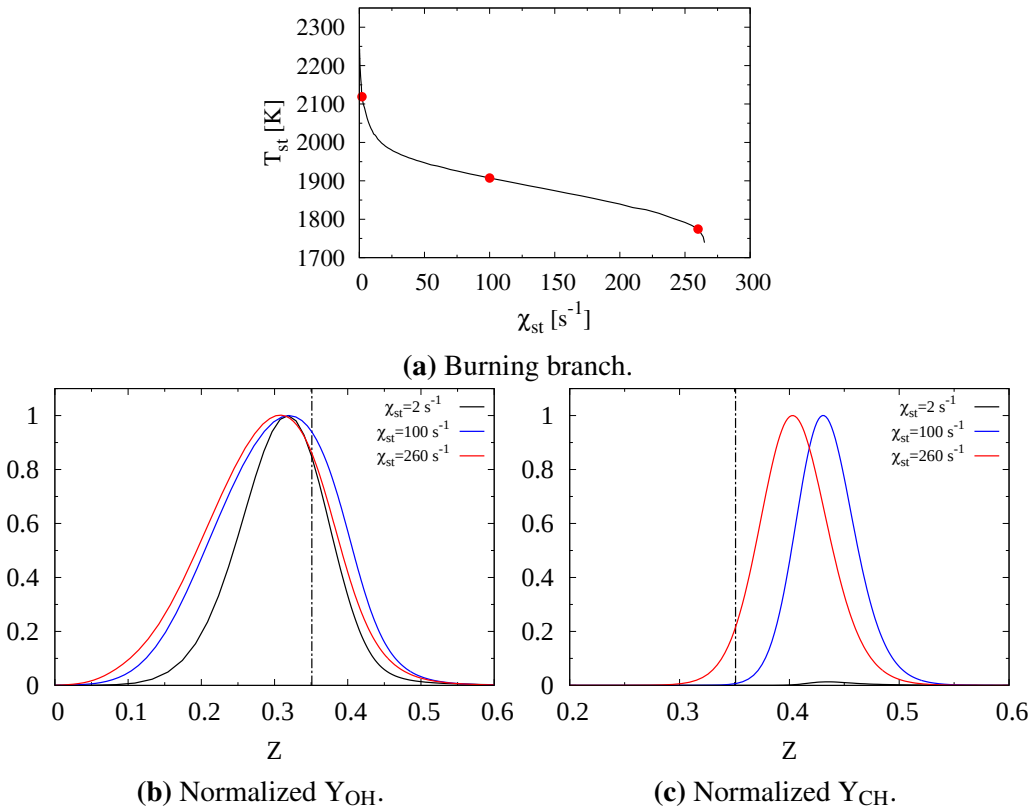

(a) Burning branch.

(b) Normalized Y_{OH}.

(c) Normalized Y_{CH}.

Figure 5.1: Top: burning branch of the S-shaped curve obtained solving flamelet equations [66] using the FlameMaster code [79] with the GRIMech3.0 chemical model [135]. Bottom: OH and CH layers for flamelet solutions corresponding to $\chi_{st} = 2\ s^{-1}$ (black) χ_{st}, $= 100\ s^{-1}$ (blue) and $\chi_{st} = 260\ s^{-1}$ (red). The vertical dot-dashed line represents the stoichiometric mixture fraction.

Equation (5.6) assumes that the radical layer is located around the stoichiometric mixture. Here, the OH and CH layers are considered. Figure 5.1 shows the OH and CH mass fractions in mixture fraction space obtained by solving the flamelet equations (see Ch. 2). Three values of χ_{st} are considered, spanning the entire burning branch of the S-shaped curve (see Fig. 5.1a). As can be seen, the thickness in mixture fraction space of both the OH and CH layers presents only small differences for a wide range of χ_{st} values, and can be considered to be constant, with $\Delta Z_{OH} = 0.5 \pm 0.05$ and $\Delta Z_{CH} = 0.2 \pm 0.05$.

First, l_R is estimated for the base of the jet, where χ_{st} is largest. In this region, the flame is likely located within a laminar mixing layer, and the normal to the stoichiometric surface is expected to remain close to the radial direction [132]. Considering the extinction scalar dissipation ($\chi_{st} = 265\ s^{-1}$), l_R is estimated to be $\approx 0.9 \pm 0.07$ mm and $\approx 0.4 \pm 0.1$ mm, for OH and CH, respectively. The maximum

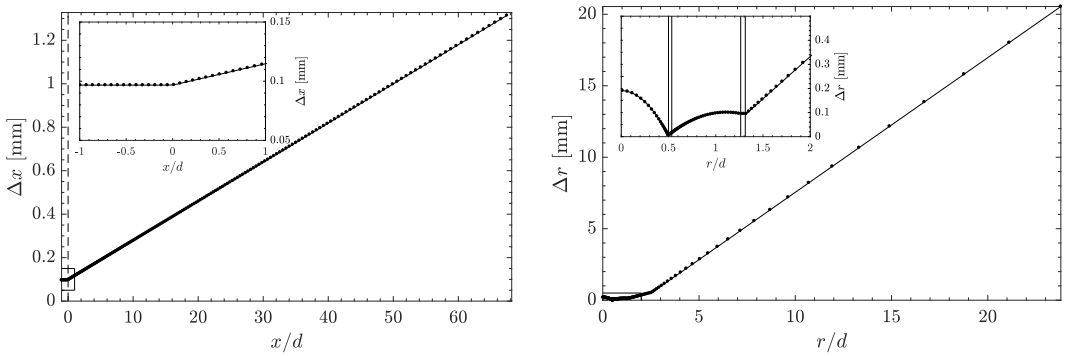

(a) Axial grid stretching. **(b)** Radial grid stretching.

Figure 5.2: Left: axial grid stretching for the baseline grid; vertical dashed line: burner exit plane; the insert represents a close-up of the axial grid for $-1 < x/d < 1$; symbols represent every fifth grid point. Right: radial grid stretching for the baseline grid; the insert represents a close-up for $r/d \leq 2$; solid vertical lines: radial location of the fuel pipe and pilot pipe walls; each symbol represents a grid point; only every other grid point is shown for the insert.

radial grid spacing for $d/2 < r < d_{p,o}/2$ is 0.1 mm, suggesting that, as a worst-case-scenario, the OH and CH radical layers are represented approximately by 10 and 4 grid points, respectively. An *a posteriori* analysis of the grid resolution for the chemistry will be carried out in Sec. 5.6.

Far downstream of the burner exit plane, the flame becomes corrugated, and cannot be considered parallel to any given direction. Thus, the mean grid size should be considered in place of Δr for an *a priori* assessment of the grid resolution for the chemistry. Since χ_{st} is expected to decay rapidly moving downstream [10], a value of $\chi_{st} = 2\,s^{-1}$ is assumed to estimate l_R. With this choice, $l_{R,\mathrm{OH}} \approx 10$ mm and $l_{R,\mathrm{CH}} \approx 5$ mm. Assuming that the flame is always located within $r \lessapprox 2d$, the maximum Δ is ≈ 0.7 mm.

5.3.3 Baseline grid

To conclude, the baseline grid consists of a cylindrical mesh with $1120 \times 224 \times 128$ ($\approx 32 \times 10^6$) grid points, in the axial, radial, and azimuthal directions, respectively. The grid extends for $\mathrm{Lx} = 69.3d$ axially, beyond the estimated stoichiometric flame tip [72], $\mathrm{Lr} = 23.8d$ radially, and $\mathrm{Lz} = 2\pi$ azimuthally.

Figure 5.2b shows the radial grid stretching for the entire domain, and the insert shows a close-up for $r/d \leq 2$, where the smallest turbulence and chemistry scales are located.

	Case					
	BL	Res-x	Res-r	Res-z	UL	RAD
grid points						
nx	1120	2240	1120	1120	1120	1120
nr	224	224	448	224	224	224
nz	128	128	128	256	128	128
domain size						
Lx [d]	69.3	69.3	69.3	69.3	69.3	69.3
Lr [d]	23.8	23.8	23.8	23.8	23.8	23.8
Lz [rad]	2π	2π	2π	2π	2π	2π
simulation time						
$[d/U_{\text{jet}}]$	243.0	45.5	45.5	45.5	126.4	200
$[\tau]$	3.05	0.58	0.58	0.58	1.60	2.52
data files	192	180	180	180	100	158
saving rate						
$[s]$	$5{\cdot}10^{-4}$	$1{\cdot}10^{-4}$	$1{\cdot}10^{-4}$	$1{\cdot}10^{-4}$	$5{\cdot}10^{-4}$	$5{\cdot}10^{-4}$
$[d/U_{\text{jet}}]$	1.26	0.25	0.25	0.25	1.26	1.26
transport properties	MA	MA	MA	MA	UL	MA

Table 5.2: Simulations carried out in this work: BL, baseline case; Res-x, twice the resolution in the axial direction; Res-r, twice the resolution in the radial direction; Res-z, twice the resolution in the azimuthal direction; UL, unity Lewis number case; RAD, case with radiation heat losses. nx, ny, nz represent the number of grid points in the axial, radial, and azimuthal directions, respectively. Lx, longitudinal length of the domain from the recessed inflow to the outflow; Lr, radial extension of the computational domain; Lz, azimuthal extension of the computational domain. The simulation time considered to compute the statistics is given in d/U_{jet} and τ units (τ is given by Eq. (5.8)). The data file saving rate is shown in seconds and d/U_{jet} units. The last row specifies the transport model for the species mass diffusion coefficients: MA, mixture-averaged; UL, unity Lewis numbers.

5.4 Test cases and total run time

A summary of the chosen test cases is given in Table 5.2. These include one case with the baseline grid (BL), and three cases with refined grids, which are used to assess grid independence (see Sec. 5.6). The refined grids are obtained from the baseline grid by doubling the resolution in the axial (case Res-x), radial (case Res-r), and azimuthal (case Res-z) directions. Two additional cases are considered. First, differential diffusion effects on the flame structure are systematically isolated by running a case with unity Lewis numbers (case UL). Comparisons against case UL will be discussed in Sec. 7. Second, a simulation with radiative heat losses is performed. Flame B is the lowest Reynolds number among the Sandia flames, and the temperature decrease caused by radiation heat loss is expected to have a non-

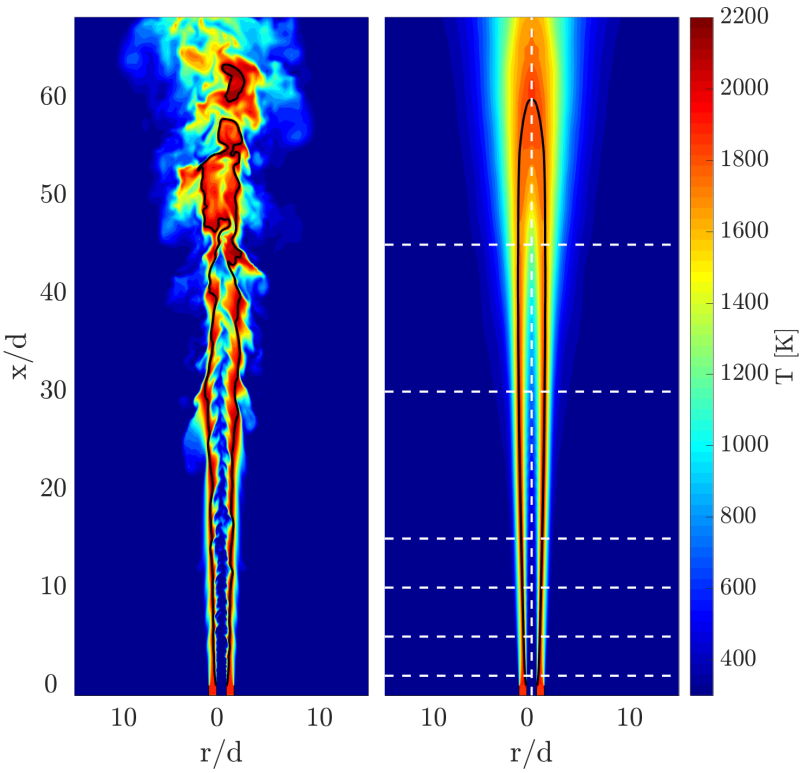

(a) Instantaneous T. **(b)** Averaged T.

Figure 5.3: Instantaneous (left) and averaged (right) temperature field for case BL. The averaging is carried out both in time and the azimuthal direction. Solid black line: stoichiometric iso-surface; dashed white lines: location of comparisons considered in this work, which include $x/d = 1,\ 5,\ 10,\ 15,\ 30,\ 45$ and the centerline.

negligible impact of the global mixing field and the flame structure. Case RAD will be discussed in Chs. 6 and 7.

The simulation times reported in Table 5.2 represent the total time considered to compute the statistics, and do not include initialization transients. More specifically, $243.0d/\mathrm{U_{jet}}$ units of simulation time are considered for case BL, while for each of the refined cases only $45.5d/\mathrm{U_{jet}}$ of simulation time are used, due to the much higher computational cost. For the three refined cases, the statistics are computed considering the approximately the same physical time interval. Data files were stored every 0.5ms ($\approx 1.26d/\mathrm{U_{jet}}$) for cases BL, UL and RAD, and every 0.1ms ($\approx 0.25d/\mathrm{U_{jet}}$) for each of the refined cases. Each data file obtained with the baseline grid is 11.3GB, while data files from each of the refined cases is twice that amount. The total DNS data corresponding to the cases reported in Table 5.2 is 17.3TB.

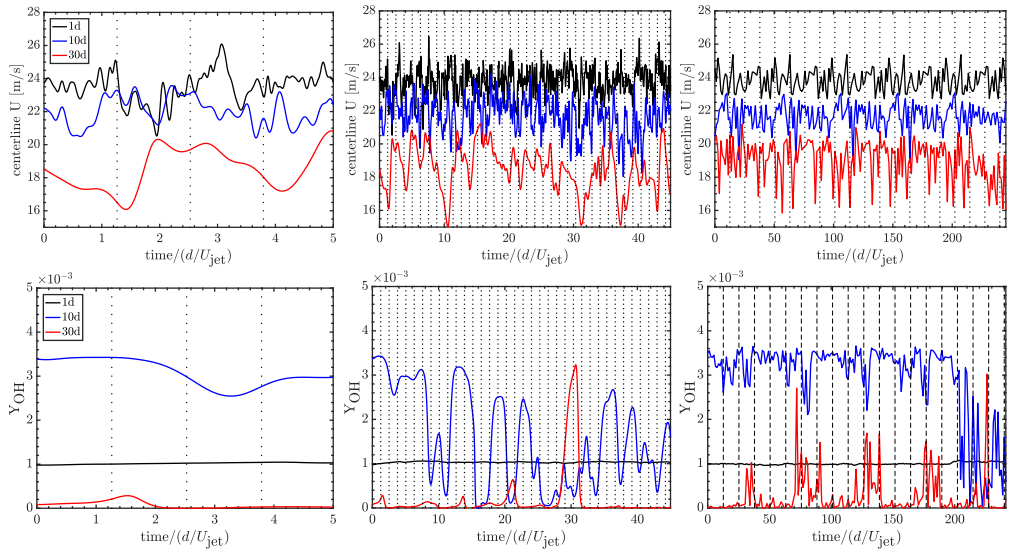

Figure 5.4: Time series over three time periods of centerline U velocity (top) and the OH mass fraction at $r/d = 1$ (bottom), for $x/d = 1$ (black), $x/d = 10$ (blue), and $x/d = 30$ (red), from case BL. Left and center: every time step is shown; the vertical dotted lines represent every data file. Right: entire simulation time; the vertical dotted lines represent every tenth data file.

A convective flow through time may be defined as

$$\tau \equiv \int_0^{Lx} \frac{dx}{\langle U(x) \rangle} \approx 79.1 \left(\frac{d}{\mathrm{U_{jet}}} \right) = 0.0313 \; s, \tag{5.8}$$

where $\langle U(x) \rangle$ is the mean centerline velocity, and Lx is the longitudinal domain length. The averaging time of each simulation in τ units is reported in Table 5.2.

In the analysis carried out in Ch. 3, it was shown that for small chemical models (tens of species and hundreds of reactions) and three dimensional DNS, the computational cost associated with mixture-averaged transport properties is only marginally greater than using constant Lewis numbers. That is why for all four cases considered in this chapter, mixture-averaged transport properties are considered.

The instantaneous and averaged temperature field for case BL is shown in Figs. 5.3a and 5.3b, respectively. All averages considered in this chapter are carried out both in time and in the azimuthal direction, which is statistically homogeneous. In the next sections, comparisons between case BL and the refined cases are carried out along the centerline, and the cross-stream planes shown in Fig. 5.3b.

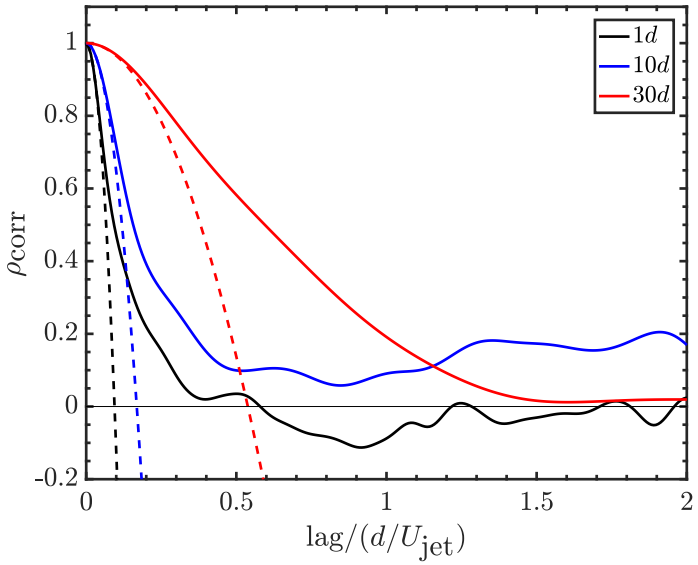

Figure 5.5: Solid lines: two-time auto-correlation for the centerline U for $x/d = 1$ (black), $x/d = 10$ (blue) and $x/d = 30$ (red). Dashed lines: osculating parabolas.

5.5 Convergence of statistics

The high cost of DNS often leads to relatively short running times, and as a result, sampling errors for the statistics may be of the same order as or even larger than discretization errors [164]. In this section, the estimation of sampling errors for sample means is discussed. Figure 5.4 shows time series of the centerline U and the OH mass fraction at $r/d = 1$, which is close to the radial location of its peak mass fraction, for several downstream stations. As can be seen, for the same downstream locations, the two quantities present significantly different fluctuation levels, and the oscillations occur with a much different frequency. Further, the behavior of each quantity changes qualitatively and quantitatively moving downstream. Thus, for different quantities at different locations, achieving the same sampling error will require different simulation running times.

5.5.1 Randomness and time-correlation

When assessing sampling errors, it is desirable to have independent samples, and a direct way to estimate the sample decorrelation distance is through the two-time autocorrelation function [147]

$$\rho_{\mathrm{corr}}(\mathrm{lag}) \equiv \frac{\langle X'(t)X'(t+\mathrm{lag})\rangle}{\langle X'(t)^2\rangle}, \tag{5.9}$$

where X is some quantity of interest, and $X' = X - \langle Z\rangle$. Figure 5.5 shows ρ_{corr} for U at three downstream locations along the centerline.

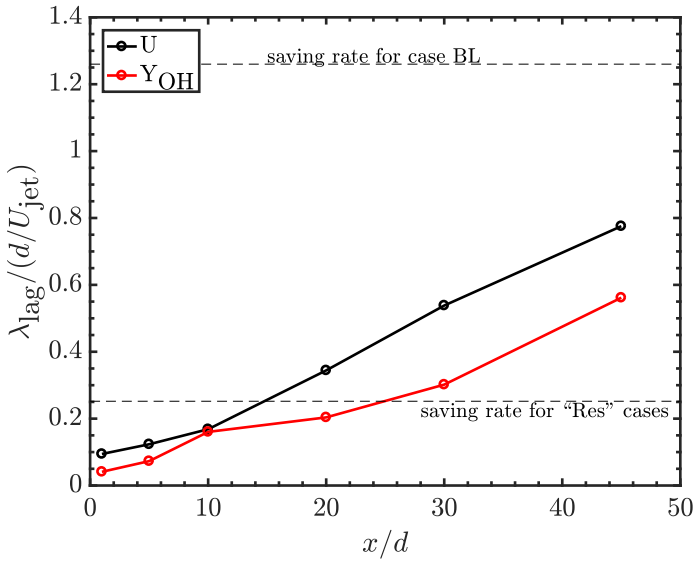

Figure 5.6: τ_{lag} for U (centerline) and Y_{OH} ($r/d = 1$) for several downstream stations up to $x/d = 45$.

From Eq. (5.9), an integral length scale may be computed as

$$\tau_{int} \equiv \int_0^\infty \rho_{corr}(\text{lag}) d\text{lag}. \tag{5.10}$$

Typically, samples are considered decorrelated if the separation time is at least τ_{int} [173]. However, directly computing ρ_{corr} through its definition tends to be noisy [174] due to the short running time of the simulations, which may lead to large errors when evaluating Eq. (5.10). As an alternative approach, one can extract a time scale from the curvature of ρ_{corr} for zero lag, since for small lag ρ_{corr} can be considered to be converged. More precisely, the time scale may be computed as the x-axis intercept of the osculating parabola

$$\rho(\text{lag}) \approx 1 - \frac{\text{lag}^2}{\lambda_{lag}^2}. \tag{5.11}$$

Osculating parabolas to ρ_{corr} are shown in Fig. 5.5, and Fig. 5.6 shows λ_{lag} for both U (at the centerline) and OH (at $r/d = 1$), for $x/d < 45$. As expected, λ_{lag} for both quantities is found to increase with axial distance. Figures 5.5 and 5.6 also show the data file saving rate for the baseline and refined cases. As can be seen, the chosen data file saving rate for the baseline case is larger than the largest λ_{lag} for both U and Y_{OH}, suggesting that the data files with that separation may be considered independent up to $x/d \approx 45$.

As an alternative approach to investigate sample independence for a quantity of interest X, one may consider the convergence of the sample standard deviation

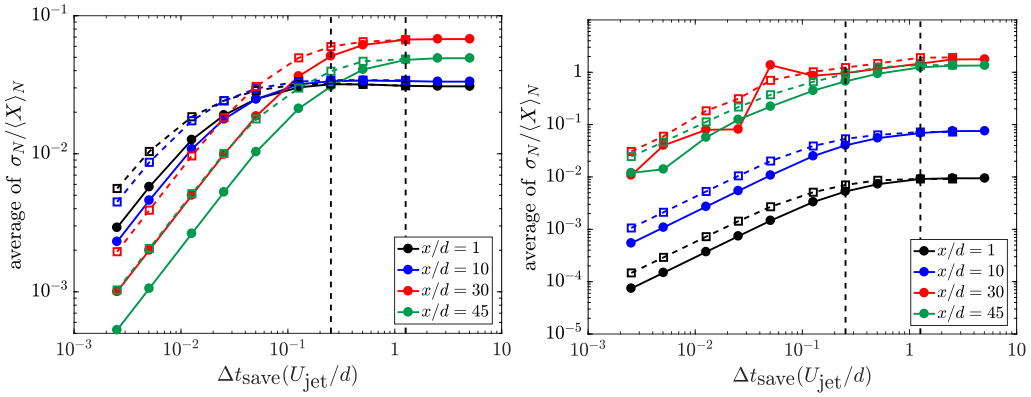

(a) Mean centerline streamwise velocity. **(b)** Mean OH at $r/d = 1$.

Figure 5.7: Average of $\sigma_N/\langle X\rangle_N$ with the normalized sample separation time, for the centerline U (left) and the OH mass fraction at $r/d = 1$ (right). Four downstream locations are considered: $x/d = 1$, black; $x/d = 15$, blue; $x/d = 30$, red; $x/d = 45$, green. Solid lines and full symbols: $N = 9$; dashed lines and empty symbols: $N = 18$. The vertical dashed line represents the separation time between data files.

relative to the sample average

$$\frac{\sigma_N}{\langle X\rangle_N} \equiv \frac{1}{\langle X\rangle_N}\sqrt{\frac{1}{N-1}\sum_{i=1}^{N}(X_i - \langle X\rangle)^2}, \tag{5.12}$$

where

$$\langle X\rangle_N \equiv \frac{1}{N}\sum_{i=1}^{N} X_i, \tag{5.13}$$

for increasing sample separation distances. In Eq. (5.12), the sum is carried out over N samples generated by the simulation. Here, two sample sizes are considered, including $N = 9$ and $N = 18$. Equation (5.12) is then computed for every set of 9 and 18 samples obtained with the given time separation distance, and then an average is plotted. This is shown in Fig. 5.7, for U and OH. For both quantities, the average of the ratio $\sigma_N/\langle X\rangle_N$ initially grows with the sample separation time, and then plateaus when the separation time is greater than the decorrelation time. As expected, for large sample separation times, the standard deviation becomes independent of the sample size and the separation distance. More specifically, for both the centerline U and OH at $r/d = 1$, data files stored at the baseline saving rate may be considered decorrelated for all downstream stations considered. In Fig. 5.7b, the average $\sigma_N/\langle X\rangle_N$ values for $x/d = 1$ and $x/d = 10$ are much lower than the other stations. That occurs because for these stations, the flame is likely to be embedded within a laminar mixing region, and the rms of Y_{OH} is much lower than further downstream (see Fig. 5.4).

5.5.2 Confidence intervals

The sampling error for the mean can be defined as

$$e_N \equiv \langle X \rangle_N - E[X], \tag{5.14}$$

where $E[X]$ is the true mean. For independent and identically distributed random variables (i.i.d.), the classical central limit theorem (CLT) states that the error e_N approaches a centered Gaussian distribution with variance σ^2/N, where σ is the standard deviation of the random variables $\{X_i\}$. In other words, the sampling error e_N is fully characterized by its variance. Hence, if N is the number of independent samples being considered, then the 95% confidence interval for $\langle X \rangle_N$ is

$$\left(\langle X \rangle_N - 1.96 \frac{\sigma_N}{\sqrt{N}}, \langle X \rangle_N + 1.96 \frac{\sigma_N}{\sqrt{N}} \right), \tag{5.15}$$

where σ_N is the sample standard deviation.

It is important to note however, that if the random variables $\{X_i\}$ are not independent, then correlations between the samples must be taken into account [164]. A large body of work exists to estimate the effect of such correlations, and extensions of the CLT for correlated data may be used. However, that is beyond the scope of the present work.

For the present configuration, the statistics are computed by averaging in time and in the statistically-homogeneous azimuthal correlation. For a cylindrical grid, the effect of azimuthal-averaging grows with distance from the centerline axis, and the statistics are expected to be the least converged at the axis. That is why in the following sections, 95% confidence intervals for the mean will be provided only along the centerline.

5.6 Grid independence

Comparing simulations with different levels of grid refinement is the ultimate *a posteriori* test for grid independence. Yet, this is rarely if ever done, when DNS of laboratory-scale flames are considered. In this section, an *a posteriori* analysis of the grid described in Sec. 5.3 is carried out. First, The chosen grid resolution for case BL is analyzed at the base of the jet, where the smallest scales are expected to be found. Then, comparisons between the baseline and refined grids will be carried out along the centerline and for the cross-stream planes shown in Fig. 5.3b. Both means and standard deviations of the streamwise velocity U and mass fractions of the two radical species, OH and CH, will be considered.

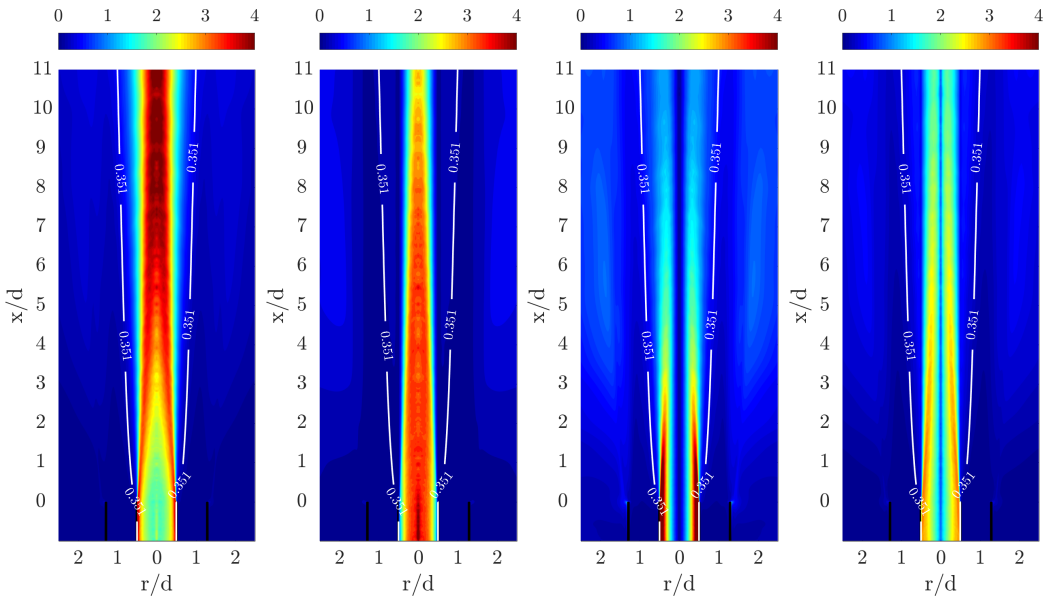

(a) $\Delta x/\eta$. **(b)** $\Delta r/\eta$. **(c)** $r\Delta\theta/\eta$. **(d)** Δ/η.

Figure 5.8: Contour maps of $\Delta x/\eta$ (a), $\Delta r/\eta$ (b), $r\Delta\theta/\eta$ (c), and Δ/η (d), for the base of the jet (case BL). White contour: stoichiometric iso-surface.

It should be noted that for the goal of the present thesis, the computational grid should be sufficiently refined to resolve low order statistics of velocities and scalar quantities.

5.6.1 *A posteriori* analysis of the base of the jet

As a first step towards the assessment of the chosen grid resolution for the baseline case, the base of the jet is considered. Ensuring that this region is adequately resolved is fundamental for the correct development of the jet. The axial, radial, azimuthal, and mean grid size are compared to the Kolmogorov length scale in the region $x/d < 11$. To assess if the chemistry is adequately resolved, the mass fractions of OH and CH are considered.

Figure 5.8 shows contour maps of $\Delta x/\eta$; $\Delta r/\eta$; $r\Delta\theta/\eta$; and Δ/η for the base of the jet. The Kolmogorov length scale is computed using Eqs. (4.24) and (5.1). The contour maps clearly show that there are regions for which Δx, Δr and $r\Delta\theta$ do not satisfy Eq. (5.3). More specifically, values of $\Delta x/\eta \approx 4.2$ are found around $x/d = 10$, $\Delta r/\eta \approx 4.0$ are found in the burner exit region along the centerline, and $r\Delta\theta/\eta \approx 7$ are found again in the burner exit region for $r/d \approx 0.5$. However, from Fig. 5.8d it can be seen that the largest values of Δ/η are around 3 and are located around the burner exit region, as estimated from the design of the grid. As will

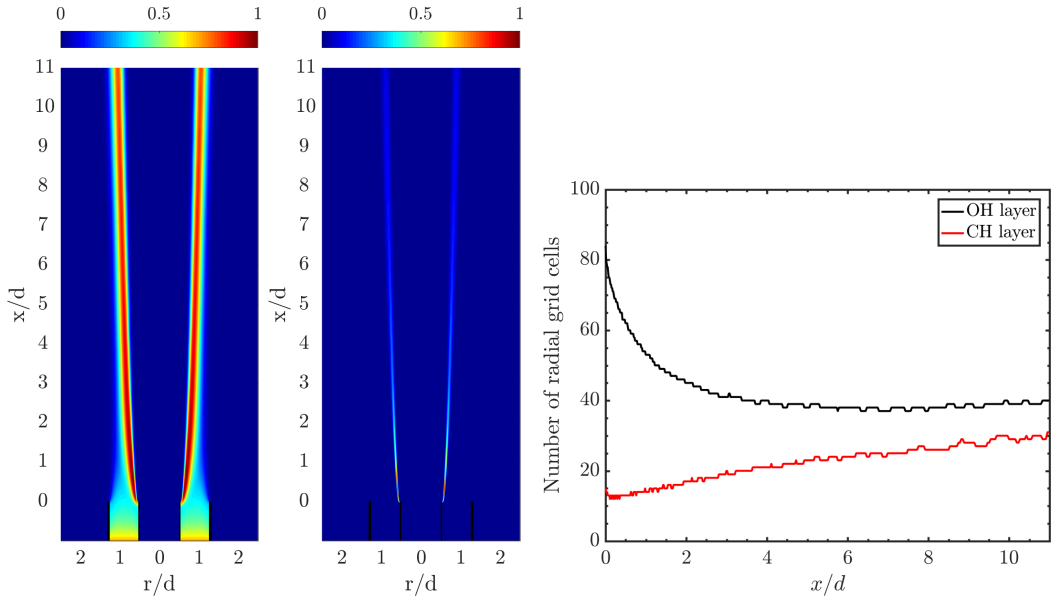

(a) Normalized Y_{OH}. **(b)** Normalized Y_{CH}. **(c)** Grid points through the radical layers.

Figure 5.9: Left and center: contour maps of Y_{OH} (a) and Y_{CH} (b) for the base of the jet (case BL). Black contour: stoichiometric iso-surface; horizontal white lines: downstream locations of the velocity and scalar comparisons shown in Figs. 5.10, 5.11 and 5.13. Right: number of radial grid cells through the OH and CH layers (black and red, respectively). A threshold of 10% of the peak value is considered.

be shown in the following sections, and in the following chapter, the chosen grid resolution is adequate for low order statistics. However, using the mean grid size Δ to satisfy Eq. (5.2), is neither necessary nor sufficient to design grids, and more work should be carried out to investigate the validity of this approach.

As mentioned previously, several grid resolution requirements for the chemistry are available in the literature. For example, Lignell *et al.* [172] reports that a minimum of 10 grid points are necessary across the thinnest radical species structures. Hawkes *et al.* [114] suggests to have at least 20 grid points per OH layer, defined through its source term. Figures 5.9a and 5.9b show the average OH and CH mass fractions for the base of the jet, normalized by their maximum value. More quantitatively, Fig. 5.9c shows the number of radial grid points through the OH and CH layers. Here, the layers are defined considering a threshold of 10% of the peak mass fraction at each downstream location. As can be seen, the number of grid points is always in excess of 10.

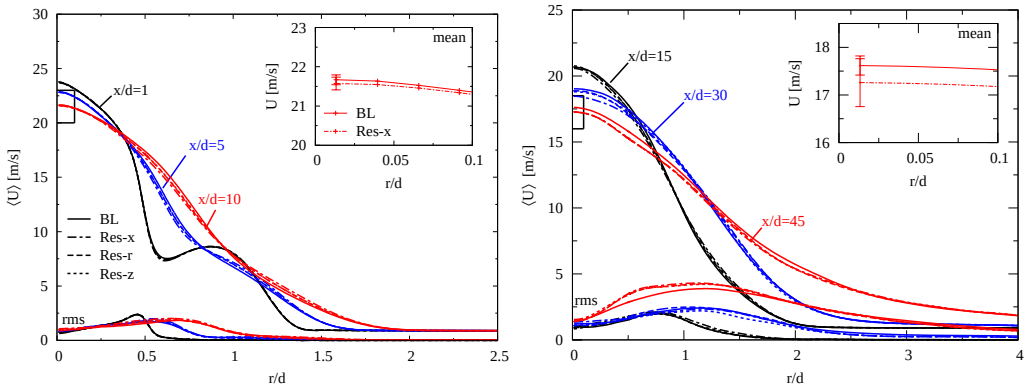

(a) $x/d = 1,\ 5,\ 10.$ **(b)** $x/d = 15,\ 30,\ 45.$

Figure 5.10: Radial profiles of mean axial velocity from case BL (solid line) and cases Res-x (dot-dashed line), Res-r (dashed line), and Res-z (dotted line) for $x/d = 1,\ 5,\ 10$ (left) and $x/d = 15,\ 30,\ 45$ (right) downstream of the burner exit plane. The insets show confidence intervals for the mean at the centerline, for cases BL and Res-x at $x/d = 10$ and $x/d, = 45$.

5.6.2 Unconditional statistics

In this section, unconditional statistics for the baseline and refined cases are compared. As discussed in Sec. 5.2, for case BL, 192 data files are considered, for a total time of $243d/U_{\text{jet}}$. For each of the refined cases, 180 data files are considered, which corresponds to a total time of $45.5d/U_{\text{jet}}$. It should be reminded that data files for the refined cases were stored five times more frequently than for the baseline case. Averaging for the three refined cases is carried out over the same physical time.

Radial profiles

Figure 5.10 shows radial profiles of the mean and the rms streamwise velocity component. Small differences are observed for the base of the jet ($x/d = 1,\ 5$ and 10), with practically no differences at $x/d = 1$, and small differences for $x/d = 5$ and $x/d = 10$. Moving downstream the velocity decays rapidly, and the mean and rms radial profiles for $x/d = 15,\ 30,\ 45$ show larger differences. Further, these differences are often largest near the centerline, since the effect of azimuthal averaging decreases moving towards the centerline. For example, at $x/d = 45$, the rms profiles for all three refined cases underestimate case BL near the centerline. This suggests that, for $x/d = 45$, the simulation time for the three refined cases may not be sufficient to have converged standard deviations at the centerline. 95% confidence intervals for the centerline mean are also provided for cases BL and Res-x, at $x/d = 10$ and $x/d = 45$. For case BL, the confidence intervals are estimated con-

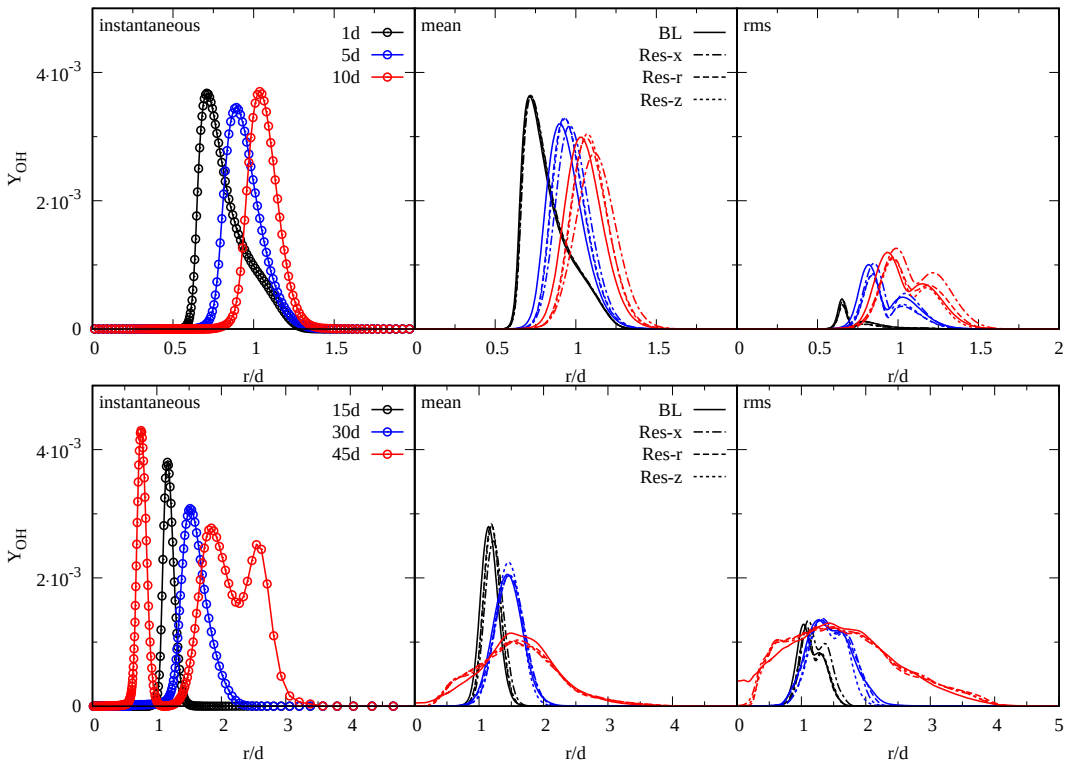

Figure 5.11: Instantaneous (left), mean (center), and rms (right) radial profiles of Y_{OH} for $x/d = 1,\ 5,\ 10$ (top) and $x/d = 15,\ 30,\ 45$ (bottom) downstream of the burner exit plane. Solid line, BL; dot-dashed, Res-x; dashed, Res-r; dotted, Res-z. The instantaneous profiles are taken from a slice of a single data file.

sidering $N = 192$ in Eq. (5.15), for both stations. For case Res-x, N is set to 180 for $x/d = 10$, but $N = 36$ is used for $x/d = 45$, as a conservative estimate (see Sec. 5.5). These confidence intervals suggest that most of the difference between case BL and Res-x at the centerline is due to sampling errors, as will be discussed below for centerline profiles.

Figure 5.11 shows instantaneous, mean, and rms radial profiles of the OH mass fraction. The instantaneous profiles are generally narrower than the averaged ones. Yet, there are always well over 20 grid points across the OH layer for all downstream stations, suggesting once more that the chosen grid is adequate to resolve the chemistry. At $x/d = 45$, two peaks for the instantaneous radial OH mass fraction profile are visible. The reason is self-evident from Fig. 5.12, from which the instantaneous radial profile is taken. Mean and rms values for the first station are in excellent agreement. However, some differences are found further downstream. More precisely, at $x/d = 5$ and $x/d = 10$, mean and rms profiles from the baseline and refined cases have a similar shape, yet a shift in the radial location and small

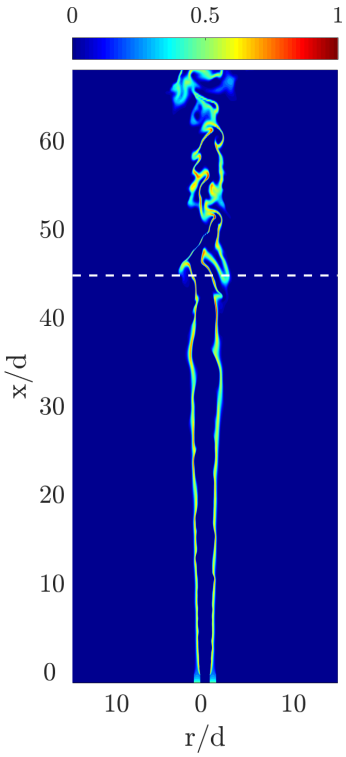

Figure 5.12: Instantaneous cross-section of normalized Y_{OH} (the max value is 0.0053), from which the instantaneous profiles in Fig. 5.11 are taken. The white dashed line represents the station at $x/d = 45$.

magnitude differences are also evident. The maximum shift is limited to about $0.15d$. Some differences are also evident for $x/d = 15$, 30, and 45. The centerline rms values are zero for the refined cases at $x/d = 45$, and non-zero for case BL. It should be reminded that the three refined cases were carried out for about the same physical time, and for a total time of about 1/5 of case BL. Thus, it is likely that the flame never intersects the centerline during the limited run time of the refined cases. To investigate if these differences are grid effects, the flame structure will be considered in Sec. 5.6.3.

Radial profiles for the CH mass fraction are shown in Fig. 5.13. As can be seen, the CH radical layer is significantly narrower than OH. Nonetheless, the instantaneous profiles show that there are always at least 10 grid points across the layer. While the mean profiles are in excellent agreement for $x/d = 1$, a shift is present for $x/d = 5$ and $x/d = 10$. Standard deviations for the first three stations show shape and magnitude differences. For the last three stations, the mean and rms values show somewhat larger differences. These differences may be the result of grid resolution effects as well as sampling errors associated with the limited run time of the

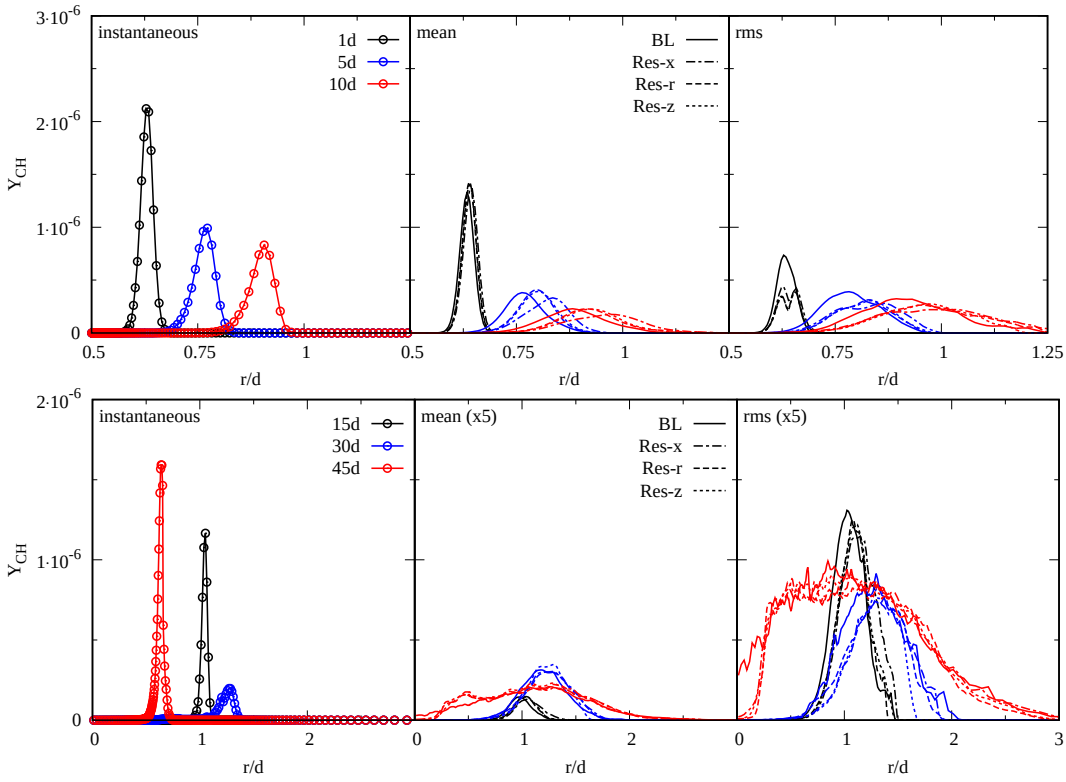

Figure 5.13: Instantaneous (left), mean (center), and rms (right) radial profiles of Y_{CH} for $x/d = 1,\ 5,\ 10$ (top) and $x/d = 15,\ 30,\ 45$ (bottom), downstream of the burner exit plane. Solid line, BL; dot-dashed, Res-x; dashed, Res-r; dotted, Res-z. The instantaneous profiles are taken from a slice of a single data file.

refined cases. In Sec. 5.6.3, conditional statistics will be considered in an attempt to decouple the two effects.

Centerline profiles

Centerline velocity and mixture fraction statistics for case BL and the three refined cases, are compared in Fig. 5.14. Unless otherwise stated, centerline profiles shown in this and the following chapters are computed at a distance $r/d = 1/20$ away from the axis, to take advantage of azimuthal averaging (for the baseline grid, $r/d = 1/20$ is located between the second and third row of cells). For both U and Z, both mean and rms profiles are in excellent agreement for $x/d \lessapprox 15$, while small differences are observed in the region $15 \lessapprox x/d \lessapprox 45$. 95% confidence intervals are shown for case BL and case Res-x, which show the greatest differences. Case Res-x presents a larger rms than the other cases, for $20 \lessapprox x/d \lessapprox 30$. While the confidence intervals account for most of the difference between these two cases, it cannot be concluded from these comparisons alone that grid effects are not present. Yet, as will be

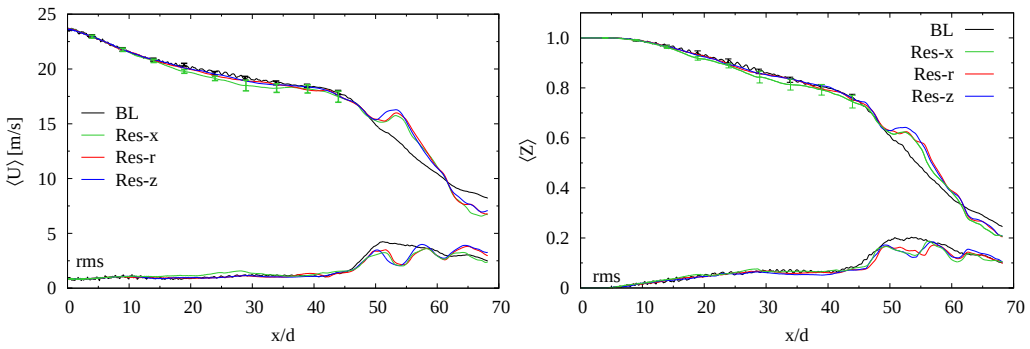

(a) Streamwise velocity. **(b)** Mixture fraction.

Figure 5.14: Centerline mean and rms velocity (left) and mixture fraction (right). Solid black, BL; green, Res-x; red, Res-r; blue, Res-z. 95% confidence intervals for the mean are shown for cases BL and Res-x.

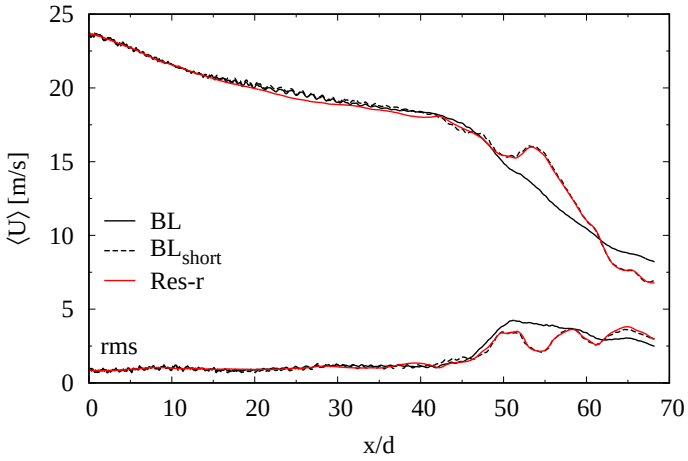

Figure 5.15: Effect of total averaging time on the centerline velocity statistics. Solid black, BL; dashed black, BL_{short}; red, Res-r.

discussed in the following sections, conditional species profiles from case BL and the refined cases show an almost perfect agreement, at least up to $x/d = 45$.

The centerline rms profiles are in good agreement up to $x/d \approx 40$, after which case BL departs from the three refined cases, which remain close up to the domain outflow. Beyond $x/d \approx 45$, the centerline mean and rms profiles show significant differences between the baseline and the refined cases. That is not surprising, since statistics for the refined cases were computed averaging only for $45.5d/U_{jet}$, whereas $243.0d/U_{jet}$ units of simulation time were considered for the baseline case (see Sec. 5.4). The statistics for the three refined cases are computed over the same physical time, which explains why they agree so well for $x/d > 45$. To investigate this further, the statistics for case BL are recomputed considering the same physical time used for the refined cases (case "BL_{short}"). Unsurprisingly, both mean and rms

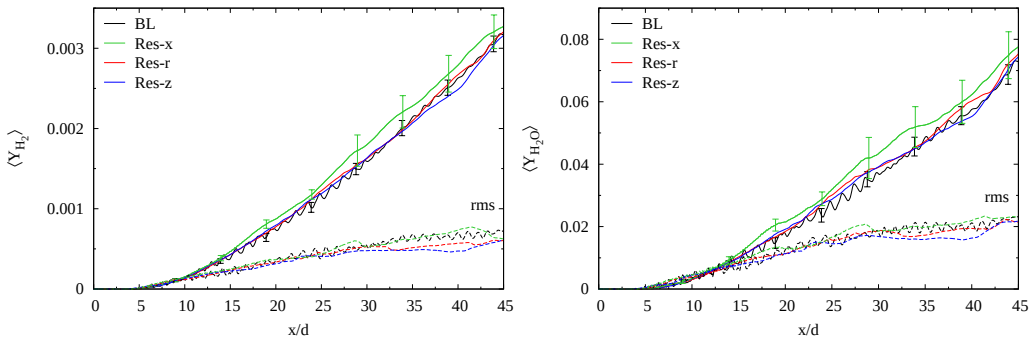

(a) Centerline H_2. **(b)** Centerline H_2O.

Figure 5.16: Centerline H_2 (left) and H_2O (right) mean (solid lines) and rms (dashed lines) mass fraction profiles. Black, BL; green, Res-x; red, Res-r; blue, Res-z.

profiles from case BL_{short} are found to be in excellent agreement with the refined cases up to the end of the computational domain, as shown in Fig. 5.15.

In Ch. 7, optimal flamelet parameters will be extracted from the DNS data by comparing flamelet solutions to conditional mean species profiles, computed for several downstream locations between $x/d = 7.5$ and $x/d = 45$, similarly to what was done for experimental data in Ch. 4. In Ch. 7, the only statistic considered beyond $x/d = 45$ is the stoichiometric flame tip location, x_F. Hence, it is important to ensure that the conditional mean species profiles up to $x/d = 45$ are statistically converged and grid independent. Grid independence will be assessed in Sec. 5.6.3 by comparing case BL with the refined cases. In the next chapter, the convergence of unconditional and conditional statistics for stations up to $x/d = 45$ will be investigated for the two cases RAD and UL.

Centerline oscillations

Small oscillations are visible for centerline statistics of all quantities stored in data files, namely the species mass fractions, the temperature, the velocity, the pressure, and the mixture fraction. This can be seen, for example, from the centerline velocity and mixture fraction statistics shown in Figs. 5.14 and 5.15, respectively, as well as from Fig. 5.16, which shows the H_2 and H_2O mass fractions up to $x/d = 45$. It is also observed that all quantities show similar oscillations, as is exemplified by the comparison of $\langle U \rangle$ and $\langle Z \rangle$ shown in Fig. 5.17.

While all simulations show these centerline oscillations, their amplitude and wavelength is observed to depend on the data file saving rate, as well as the local mean velocity. To investigate this further, Fig. 5.18 shows a close-up of the mean cen-

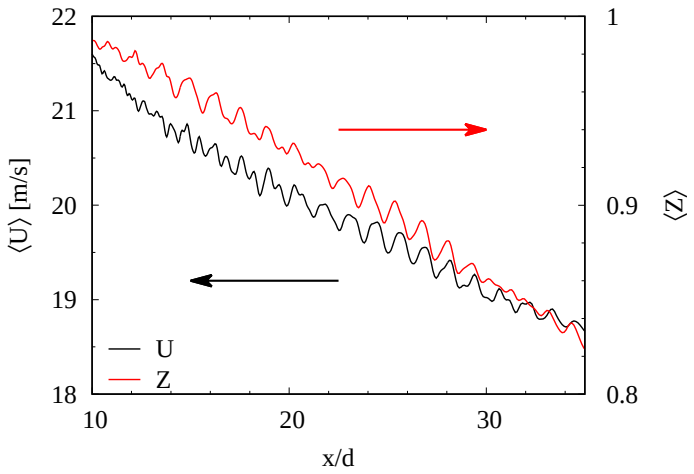

Figure 5.17: Comparison of centerline mean U and Z profiles.

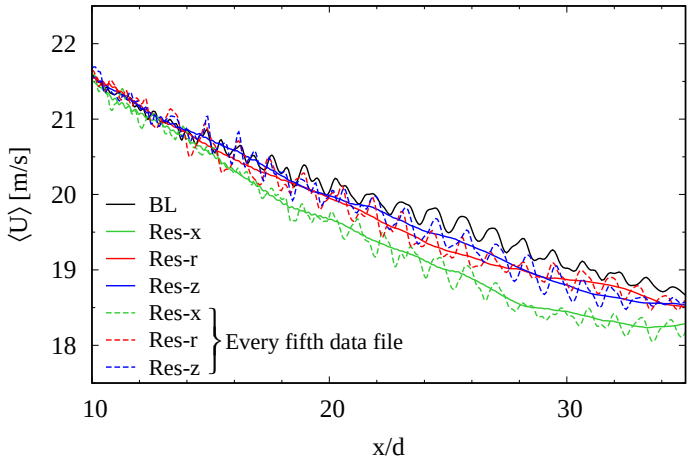

Figure 5.18: Comparison of mean centerline velocity profiles computed using different Δt_{save}. Solid lines: statistics computed using all available data files; dashed lines: statistics computed considering every fifth data file. The data file saving rate for the refined cases is five times that of the baseline case (see Sec. 5.4).

terline velocity profile for $10 \leq x/d \leq 35$. In that close-up, it can be seen that the oscillations from case BL are much larger (in both amplitude and wavelength) than for the refined cases. The refined cases are much smoother, yet oscillations at a wavelength approximately equal to 1/5 of the wavelength of case BL are visible. It should be reminded that for the baseline case, data files were stored every $1.26d/\text{U}_{\text{jet}}$, while five times that rate was considered for each of the refined cases. Thus, if every fifth data file from the refined cases is considered, the same oscillations should be evident from each of the refined cases. This is shown in Fig. 5.18, where it can be seen that the oscillations of case BL can be reproduced by all three refined cases, if the statistics are computed using every fifth data file. Since data

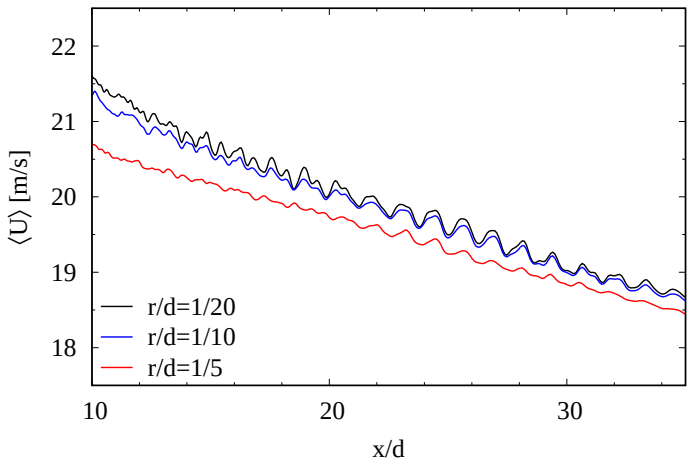

Figure 5.19: Radial decay of the oscillations for the mean streamwise velocity component from case BL, for three radial locations. Averaging is carried out in time and in the azimuthal direction.

files from cases RAD and UL were stored at the same rate of case BL, their centerline statistics show the same oscillations of case BL.

These oscillations show some independence from the total number of data files used to compute the statistics, as shown in Fig. 5.15. In this figure, $243d/U_{\text{jet}}$ units of simulation time are used for case BL, while only 45.5 for case BL_{short} (192 and 36 data files, respectively), with practically no differences on the centerline oscillations. Furthermore, Fig. 5.19 shows that the magnitude of these oscillations rapidly decays for increasing radial distance from the axis, which might be due to the effect of azimuthal averaging. For reference, at $x/d = 20$, the average radial location of the stoichiometric mixture fraction, $r_F/d \approx 1.3$ (see Ch. 7). It is suggested here that these oscillations are a result of the relatively large data file saving rate (especially for cases BL, RAD, and UL). More specifically, a link is observed between the saving rate for the data files which are used to compute the statistics, and the spatial wavelength of these oscillations. It is observed that at the downstream location x, the wavelength $\lambda_{os}(x)$ of these oscillations is approximately

$$\lambda_{os}(x) \approx \langle U(x) \rangle \Delta t_{\text{save}}, \tag{5.16}$$

where $\langle U(x) \rangle$ is the mean centerline velocity, and Δt_{save} is the data file saving period.

Based on the previous observations, these oscillations should be removed by decreasing Δt_{save}, which is not possible, unless the simulations are re-run. However, to investigate if these oscillations have any impact on the analysis discussed in Ch. 7,

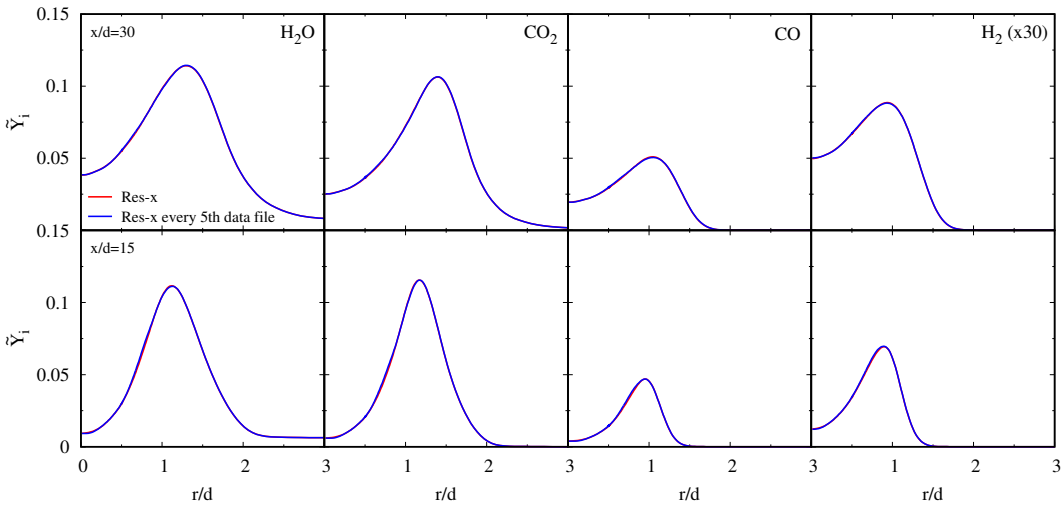

Figure 5.20: Comparison of Favre-average radial profiles of species mass fractions for $x/d = 30$ (top) and $x/d = 15$ (bottom). Red, Res-x; blue, Res-x every 5^{th} data file.

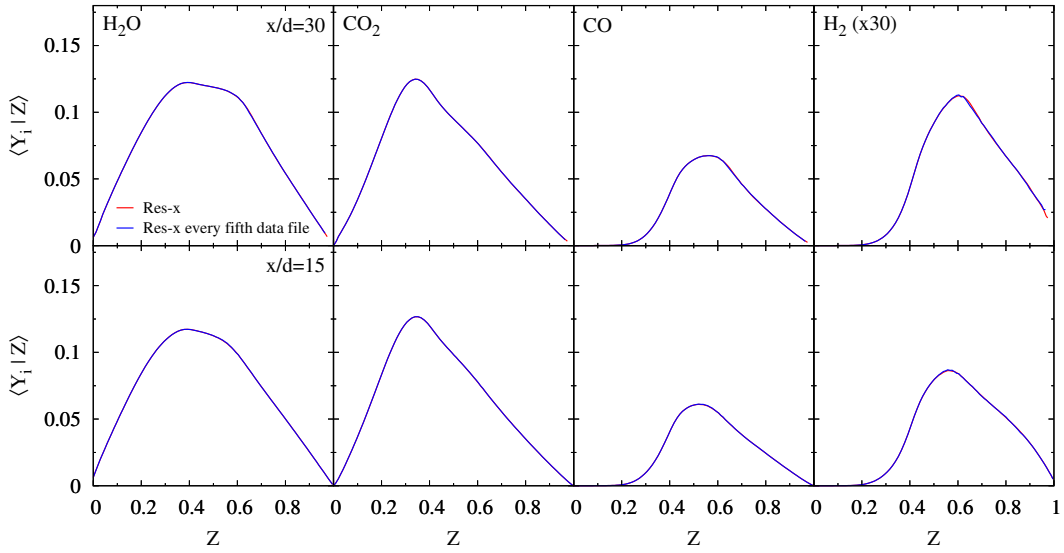

Figure 5.21: Comparison of conditional species mass fractions for $x/d = 30$ (top) and $x/d = 15$ (bottom). Red, Res-x; blue, Res-x every 5^{th} data file.

the refined cases may be used. More specifically, centerline oscillations for the refined cases were observed to be practically absent, compared to cases BL, RAD, and UL. Yet, it was shown that each of the refined cases can reproduce the same oscillations of these three cases, when only every fifth data file is used to compute the statistics. This observation can be used to assess the impact of these oscillations. Unconditional and conditional species profiles from cross-stream planes are computed from the refined cases using every data file and every fifth data file. This is shown in Figs. 5.20 and 5.21, respectively, for $x/d = 15$ and $x/d = 30$, which is

within the downstream region where centerline oscillations are more evident. For both figures, both sets of profiles are virtually indistinguishable, suggesting that these oscillations have no impact on the present analysis.

5.6.3 Flame structure

Assessing grid independence using unconditional statistics requires that the simulations be carried out long enough to "average-out" even the relatively slow, large scale structures. That can be extremely expensive, making the comparison with refined simulations impractical. One approach to avoid this difficulty is to compare conditional statistics. More precisely, scalar profiles may be compared in mixture fraction space instead of physical space. With this approach, large scale structures are effectively decoupled from the flame structure. The assumption of this approach is that the large scale structures do not impact the small-scale dynamics.

In this chapter and in the following, conditional means,

$$\langle \phi | \psi \rangle, \tag{5.17}$$

and conditional standard deviations,

$$\langle (\phi - \langle \phi | \psi \rangle)^2 \, | \psi \rangle^{\frac{1}{2}} = \left(\langle \phi^2 | \psi \rangle - \langle \phi | \psi \rangle^2 \right)^{\frac{1}{2}}, \tag{5.18}$$

are computed from the DNS data base, where ϕ is either the temperature or a species, and ψ is either Z or Z_{TNF}. For a given downstream location, conditional means and standard deviations of the quantity of interest are computed considering the entire cross-stream plane. Conditional mean and standard deviations shown in the present and following chapters are computed using 101 bins.

Centerline

To investigate if the differences between case BL and the refined cases shown in Fig. 5.16 are grid resolution effects, centerline conditional mean and rms profiles for the same species are considered in Fig. 5.22. These centerline conditional statistics are computed considering $x/d \leq 60$. As can be seen, the conditional mean and rms profiles are in very good agreement.

Cross-stream

In Ch. 7, optimal flamelet parameters are extracted from conditional mean species profiles computed from cross-stream planes between $x/d = 7.5$ and $x/d = 45$. Thus,

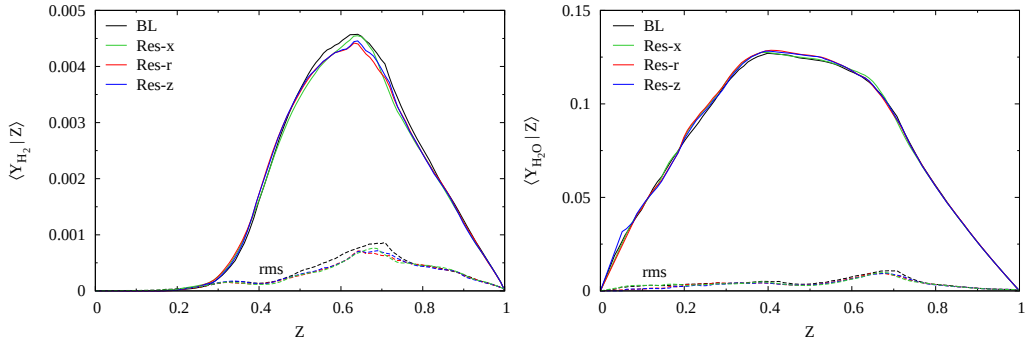

Figure 5.22: Centerline conditional mean (solid lines) and rms (dashed lines) H_2 (left) and H_2O (right) mass fraction profiles. Black, BL; green, Res-x; red, Res-r; blue, Res-z.

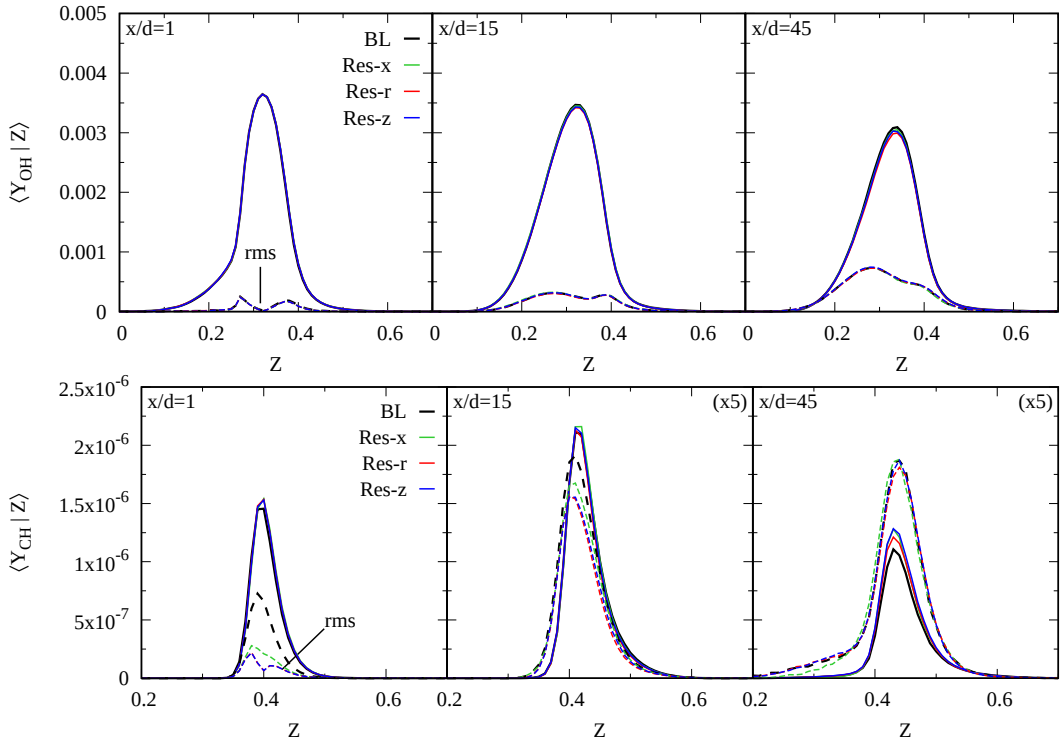

Figure 5.23: Conditional mean (solid lines) and standard deviation (dashed lines) of Y_{OH} (top) and Y_{CH} (bottom), for $x/d = 1,\ 15,\ 45$, downstream of the burner exit plane. Black, BL; green, Res-x; red, Res-r; blue, Res-z.

it is important to ensure that grid independence is achieved for cross-stream conditional mean profiles. In this section, conditional statistics are considered for several species and downstream locations. More specifically, the OH and CH radicals are considered, as well as H_2 and H_2O, which are two of the species used in the error map analysis discussed in Ch. 4. In Fig. 5.23, the OH and CH mean and rms mass fractions are shown, for the three downstream locations $x/d = 1,\ 15$, and 45. As can be seen, the conditional means are in excellent agreement for all downstream sta-

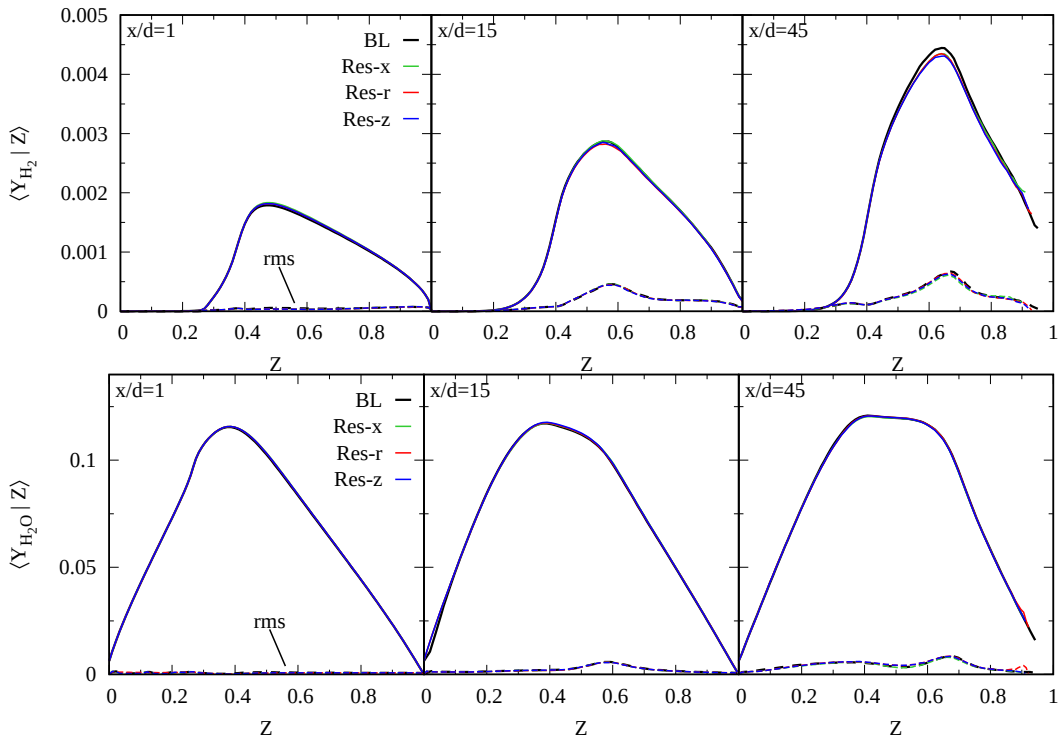

Figure 5.24: Conditional mean (solid lines) and standard deviation (dashed lines) of Y_{H_2} (top) and Y_{H_2O} (bottom), for $x/d = 1$, 15, 45, downstream of the burner exit plane. Black, BL; green, Res-x; red, Res-r; blue, Res-z.

tions, for both OH and CH. The rms profiles for OH are in excellent agreement for all stations. For the rms CH mass fraction profiles, some differences are observed for $x/d = 1$ and $x/d = 15$, while the agreement is very good for all cases at $x/d = 45$. Figure 5.24 shows the conditional mean and standard deviation of the H_2 and H_2O mass fractions, for the three downstream locations $x/d = 1$, 15, and 45. For both quantities, both the mean and rms profiles show an excellent agreement between case BL and each of the refined cases.

These observations suggest that the differences for the unconditional profiles discussed in Sec. 5.6.2 may be simply due to the limited running time of the refined cases, which is not be sufficient to "average-out" the relatively slow, large scale structures of the jet. The only quantity that may be show some grid effects is the rms of CH, for which some differences between case BL and the refined cases were observed even when considering mixture fraction-conditioned profiles. Regardless, the comparisons shown above suggest that the conditional mean species profiles for stations up to $x/d = 45$ are virtually grid-independent. That is important for the analysis carried out in Ch. 7.

5.7 Summary

In this work, a campaign of DNS of Sandia flames B was carried out. The chosen test cases include a baseline case, three cases with twice the grid resolution is the axial, radial or azimuthal directions, respectively, a case with unity Lewis numbers, and a case with radiation heat losses. The last two cases will be discussed in the following chapters.

The computational grid was designed to ensure that the ratio Δ/η is at most equal to three. An posteriori analysis for the base of the jet, where the grid resolution requirements are the most stringent, showed that this criterion is satisfied, and that enough grid points were used to represent layers of the radical species OH and CH, following suggestions from the literature.

Unconditional means and standard deviations along the centerline and for the downstream planes at $x/d = 1,\ 5,\ 10,\ 15,\ 30$, and 45, were considered. For the streamwise velocity component, an excellent agreement with the refined cases was found at the base of the jet ($x/d \lessapprox 15$). However, small differences were observed moving downstream up to $x/d \approx 45$, and large differences between case BL and the refined cases were observed beyond that location. For $x/d < 45$, where radial profiles are considered, differences were found to be largest at the centerline, where the effect of azimuthal averaging is absent. The largest differences were observed between cases BL and Res-x. While the estimated 95% confidence intervals for the sampling errors account for most of these differences, small grid effects cannot be excluded. To assess this further, conditional statistics were considered, as discussed below. To assess if the large differences observed beyond $x/d \approx 45$ are due to the limited run time of the refined cases, the mean and rms centerline velocity from case BL was recomputed using only $45.5d/U_{\text{jet}}$ units of simulation time (case "BL_{short}"), the same averaging time as for the refined cases, spanning approximately the same physical time. As expected, case BL_{short} was found to be in excellent agreement with case Res-x up to the end of the computational domain, confirming that the refined cases were not run for long enough to "average-out" the large scale structures beyond $x/d \approx 45$.

Centerline mean and rms profiles were observed to have oscillations. It was observed that the wavelength of these oscillations is approximately $\lambda_{os}(x) \approx \langle U(x) \rangle \Delta t_{\text{save}}$. For the refined cases, the data file saving rate is five times that of the baseline case, and oscillations are observed at a much reduced amplitude and with a wavelength of approximately $1/5$ of the baseline case. However, it was

shown that the same oscillations of the baseline case can be recovered from each of the refined cases, when every fifth data file is considered to compute the centerline statistics. These oscillations were found to rapidly decay with radial distance from the centerline, which may be due to the effect of azimuthal averaging. The comparison of unconditional and conditional species profiles for cross-stream planes from case Ref-x, using all data files and every fifth data file, showed no differences. Further, axial and cross-stream conditional statistics from case BL and the refined cases were found to be in excellent agreement. To conclude, all these test suggest that these centerline oscillations have no impact on the present analysis.

While the observations discussed in this chapter suggest that these oscillations are simply a result of the averaging procedure, and have no impact on the analysis discussed in Ch. 7, it is nonetheless important to ensure that they do not represent some unwanted forcing mechanism that changes the behavior of the jet to an unphysical state. In the following chapter, the DNS database will be extensively validated using available experimental data. As will be shown, a very good agreement with measurements is achieved, suggesting once more that these oscillations have no impact on the present analysis.

Radial comparisons of OH and CH, showed an excellent agreement for the first downstream location. However, further downstream, both the OH and CH layers showed some differences with the refined cases. More specifically, the mean OH and CH from the baseline and refined cases showed a lateral shift and similar magnitude. The comparison of the rms values for OH from the baseline and refined cases showed a similar profiles with a radial shift. Some shape and magnitude differences were observed for the rms CH.

To investigate if these differences were a result of the relatively short run time of the refined cases, conditional means and standard deviations of the two radicals OH and CH, as well as the two intermediates H_2 and H_2O (used for the error map analysis described in Chs. 4 and 7), were analyzed. The comparisons suggest that the conditional mean species profiles are grid-independent for the entire downstream region of interest for the analysis carried out in Ch. 7 ($7.5 < x/d < 45$).

Chapter 6

VALIDATION OF THE DNS WITH EXPERIMENTAL DATA

In this chapter, comparisons with available experimental data are carried out. The purpose is to validate the DNS database, and to isolate the effects of radiation heat loss and differential molecular diffusion. Towards these goals, cases BL, UL, and RAD are considered. In App. C, the effect of the choice of several additional parameters is investigated for flame A, which is laminar.

6.1 Assessment of the optically-thin assumption for case RAD

As was discussed in Ch. 2, for case RAD radiation heat transfer is considered by means of a radiation source term, $\dot{q}_{\text{rad}}/c_p$, which is added to the energy equation. The term $\dot{q}_{\text{rad}}$ is modeled using an optically-thin radiation assumption, where the radiative properties are based on the RADCAL model of Grosshandler [84]. RADCAL is the recommended radiation model for the target flames of the TNF Workshop [72], and is quite popular, due to the simplicity with which radiative heat transfer can be included in simulations. However, there is some evidence that this model over predicts radiative losses for the Sandia flames [72], due to strong absorption by the 4.3 μm wavelength of CO_2 [87–89]. Thus, it is expected that the correct radiative case is in "between" cases BL and RAD. Yet it will be shown in Ch. 7 that optimal flamelet parameters extracted from the two cases BL and RAD are close, and the same conclusions can be drawn from either simulation.

The validity of the optically-thin assumption may be assessed as follows. Here the gas is considered to be gray. Over an elemental distance ds, the spectral intensity I is attenuated through absorption by the amount

$$dI = -a_p I ds, \tag{6.1}$$

where a_p is the absorption coefficient. Similarly, attenuation by scattering is

$$dI = -\sigma_s I ds, \tag{6.2}$$

where σ_s is the scattering coefficient. The extinction coefficient is

$$\beta = a_p + \sigma_s. \tag{6.3}$$

The optical thickness τ_o is defined as

$$\tau_o = \int_0^s \beta ds, \tag{6.4}$$

so the ratio of transmitted and incident radiant intensities, can be estimated using

$$\frac{I}{I_0} = \exp(-\tau_o) \tag{6.5}$$

Thus, for $\tau_o \gg 1$, the optically-thin assumption is not valid.

For gaseous non-luminous flames, such as Sandia flame B, scattering can be neglected [89, 175]. The absorption coefficient can be computed as

$$a_p = \sum_i p_i a_{p,i}, \tag{6.6}$$

where the summation is carried out over the four species CH_4, H_2O, CO_2, and CO. The coefficients $a_{p,i}$ are curve fits for the Plank mean absorption coefficients for each of the four species. More details may be found on the TNF Workshop website [72]. Figure 6.1 shows a_p computed using a slice of a data file from case RAD, where it can be seen that the largest values are around 2[¶]. Consequently, the right hand side of Eq. (6.5) is far from unity only over distances that are comparable to the flame length. For example, taking $a_p = 2$ as a worst-case scenario, and either $l_p = d$ or $l_p = x_F$, Eq. (6.5) is approximately 0.99 or 0.43, respectively.

6.2 Unconditional statistics

A comparison of unconditional averages is useful to assess global flow-field effects. In this section, radial and centerline Favre-average profiles will be discussed. Here the emphasis is placed on the effects of radiation on the global flow-field, and only cases BL and RAD are considered. For a quantity ϕ, the Favre-mean is defined as

$$\widetilde{\phi} = \frac{\langle \rho\phi \rangle}{\langle \rho \rangle}, \tag{6.7}$$

and the rms of the Favre-fluctuation, $\phi'' = \phi - \widetilde{\phi}$, is

$$\sqrt{\widetilde{\phi''^2}} = \sqrt{\widetilde{\phi^2} - \widetilde{\phi}^2}. \tag{6.8}$$

In Eqs. (6.7) and (6.8), $\langle \cdot \rangle$ denotes Reynolds-averaging, which is carried out by averaging in time and in the statistically-homogeneous azimuthal direction.

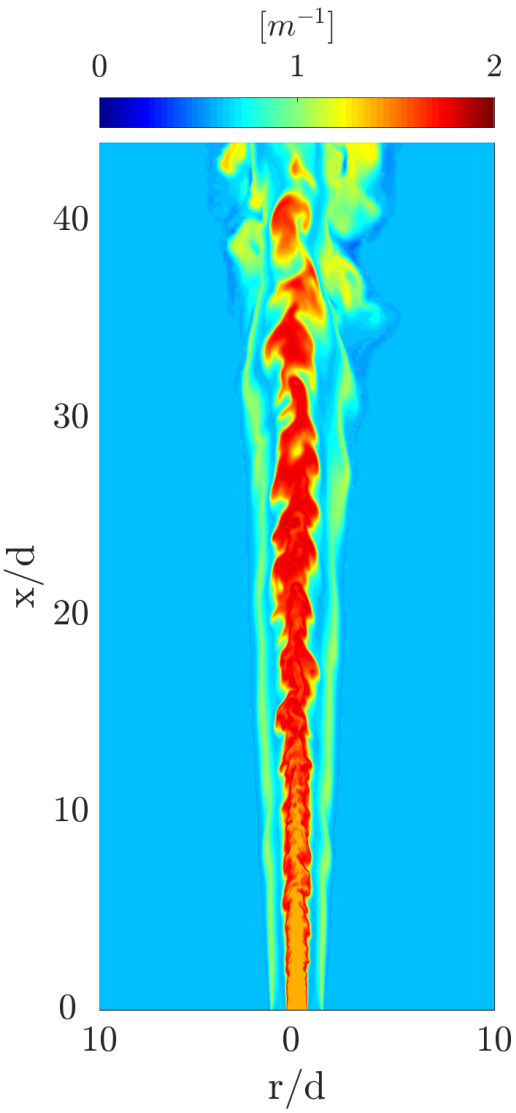

Figure 6.1: Plank mean absorption coefficient from RADCAL, computed from a slice of a single data file from case RAD.

6.2.1 Radial profiles

As mentioned in Ch. 5, due to the initialization transient for case RAD, only the last $200d/U_{\text{jet}}$ units of simulation time are considered. This initialization transient can be seen in Fig. 6.2, where the peak value of the azimuthally-averaged temperature is shown for the stations at $x/d = 1$, 5, 10, 15, 30, and 45. Case RAD is initialized from a data file from case BL. As expected, the peak temperature is found to decrease, before oscillating around a plateau. Periodic structures repeating every $48d/U_{\text{jet}}$ are visible up to $x/d = 15$. It should be reminded that this periodicity

¶It should be noted that $a_p \approx 0.6$ in the oxidizer stream, which is due to a small concentration of H_2O present in the coflow ($Y_{H_2O} = 0.006$, see Sec. 5.2).

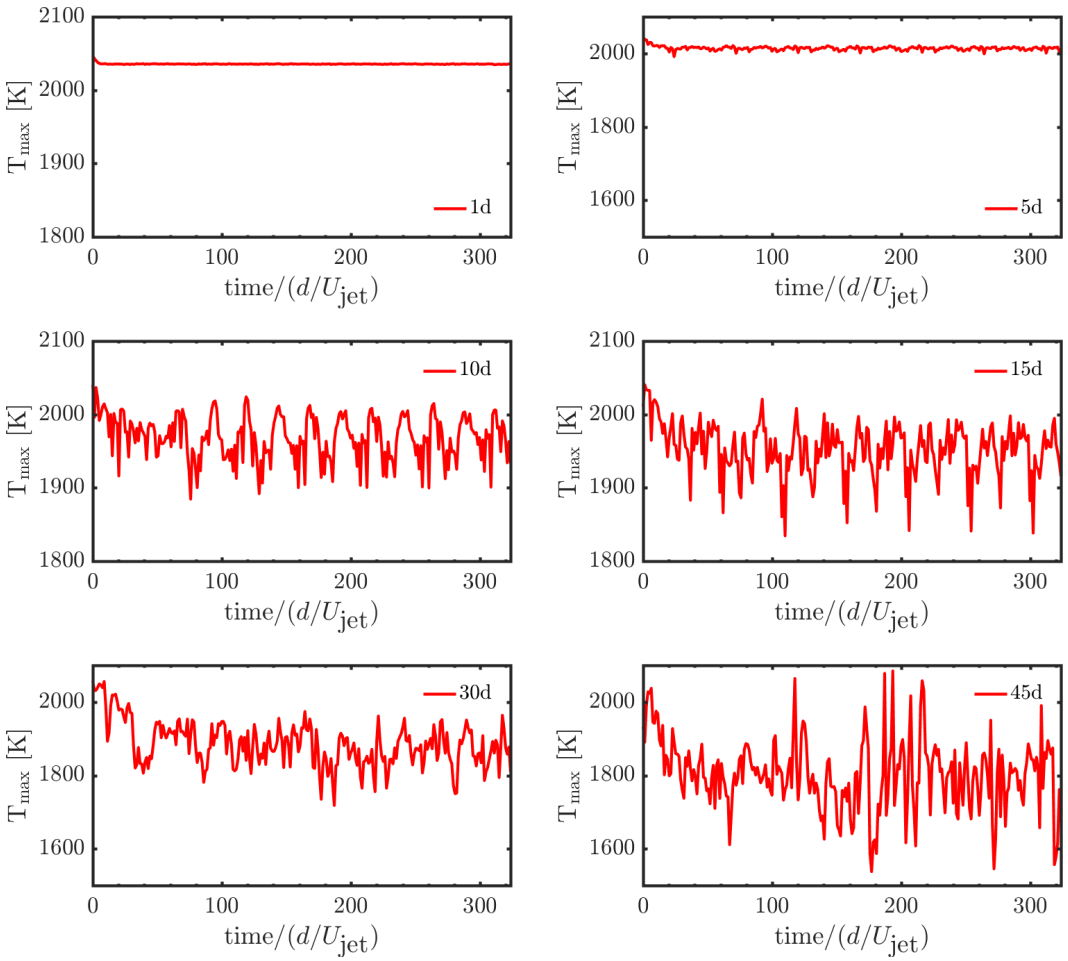

Figure 6.2: Peak temperature for $x/d = 1$, 5, 10, 15, 30, 45 from case RAD (data files are averaged in the azimuthal direction). The initial time represents a data file from case BL.

is caused by the fuel pipe inflow, which has a period of $48d/U_{jet}$, as discussed in Ch. 5. The plateau is reached faster for stations that are closer to the burner exit plane. The initialization transient, which is longest for the last station, is at most about $100d/U_{jet}$ units of simulation time. That is why, for the statistics considered in the present and following chapters, only the last $200d/U_{jet}$ (158 data files) are considered, to ensure that for all stations up to $x/d = 45$ the transient is not included.

To assess convergence of unconditional statistics for case RAD, radial and centerline mean and rms profiles are evaluated using two averaging intervals. Figure 6.3 shows Favre-average radial temperature mean and rms profiles at $x/d = 7.5$, 15, 30 and $x/d = 45$, computed using data files corresponding to the last $200d/U_{jet}$ and $100d/U_{jet}$ (158 and 79 data files, respectively). As can be seen, both mean and rms profiles show virtually no difference for the first three stations, and only small

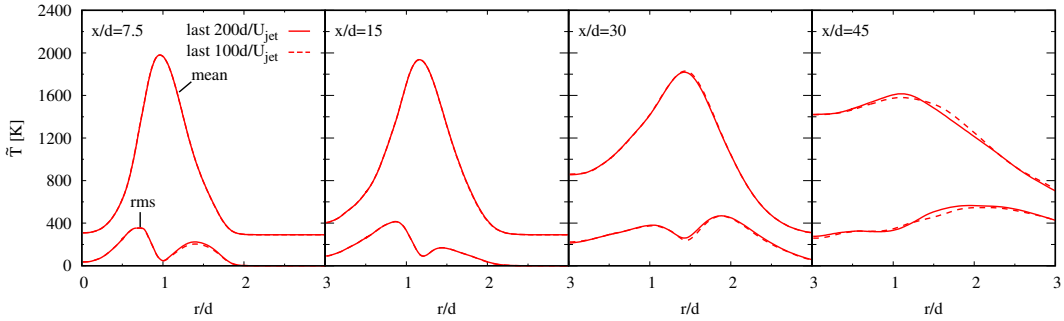

Figure 6.3: Comparison of Favre-average and rms radial temperature profiles for $x/d = 7.5$, 15, 30, 45. To assess convergence of the statistics, the mean and rms values are computed for the last $200d/U_{\text{jet}}$ (solid lines) and the last $100d/U_{\text{jet}}$ (dashed lines) units of simulation time.

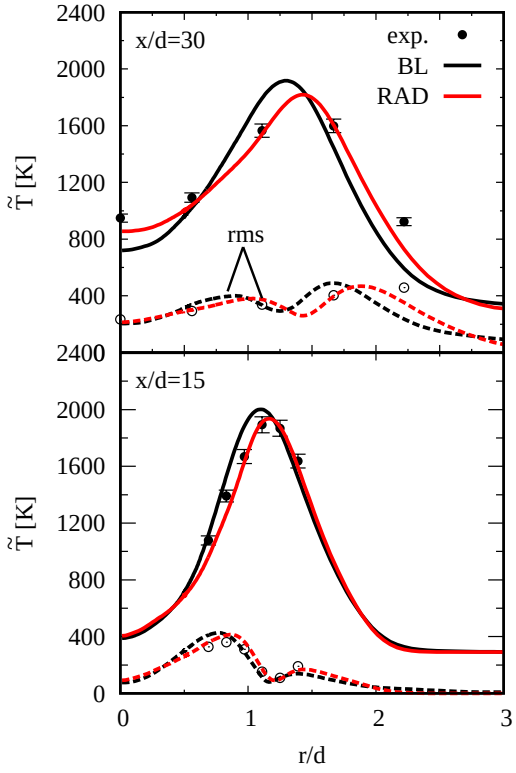

Figure 6.4: Comparison of Favre-average radial profiles of temperature for $x/d = 30$ (top) and $x/d = 15$ (bottom). Solid lines and full symbols: mean quantities; dashed lines and empty symbols: rms values. Black lines, BL; red lines, RAD; symbols, experiments. The vertical bars represent the estimated uncertainties for the temperature [46].

differences for $x/d = 45$. Thus, the last $200d/U_{\text{jet}}$ units of simulation time for case RAD will be considered in this and the following chapter.

Next, cases BL and RAD and the experiments are compared. Figures 6.4 and 6.5 show radial profiles of Favre-average temperature and species mass fractions, re-

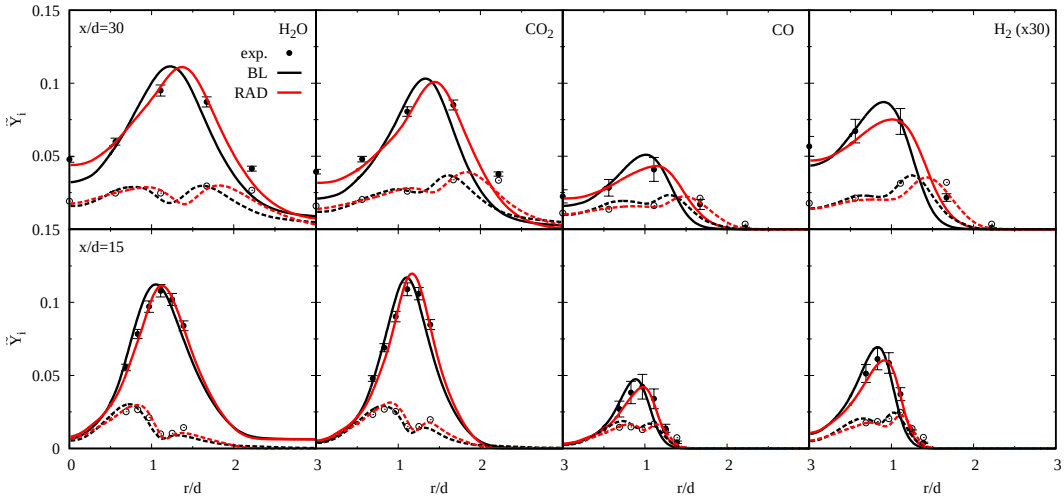

Figure 6.5: Comparison of Favre-average radial profiles of species mass fractions for $x/d = 30$ (top) and $x/d = 15$ (bottom). Solid lines and full symbols: mean quantities; dashed lines and empty symbols: rms values. Black lines, BL; red lines, RAD; symbols, experiments. The vertical bars represent the estimated uncertainties for the species [46].

spectively, for case BL, case RAD, and the experiments, for $x/d = 15$ and $x/d = 30$. The comparisons show that case RAD is in good agreement with the measured mean and rms values, at both locations. It is also evident that the temperature differences due to the radiative heat losses have a major impact on the mixing field for Sandia flame B. More specifically, the radial mean and rms temperature profiles for case RAD are shifted outwards compared to the non-radiating case. Further, at $x/d = 30$, case RAD shows a higher centerline temperature than case BL.

6.2.2 Centerline profiles

In this section, centerline mixture fraction profiles are analyzed. The purpose is to assess if the statistics are sufficiently converged up to $x/d = 45$, to assess the impact of radiation heat loss on the flame, and to carry out comparisons with experimental and LES data.

Figure 6.6 shows centerline mean mixture fraction profiles from case RAD. These profiles were computed using data files corresponding to the last $200d/U_{\text{jet}}$ and $100d/U_{\text{jet}}$ units of simulation time, to assess convergence. As can be seen, only small differences are visible starting from $x/d \approx 45$. The error bars represent 95% confidence intervals computed for the case with $100d/U_{\text{jet}}$ units of simulation time, where it is assumed that the data files are independent.

Regular oscillations along the centerline are visible, as was discussed in Ch. 5. It was shown in the previous chapter that the magnitude and wavelength of these

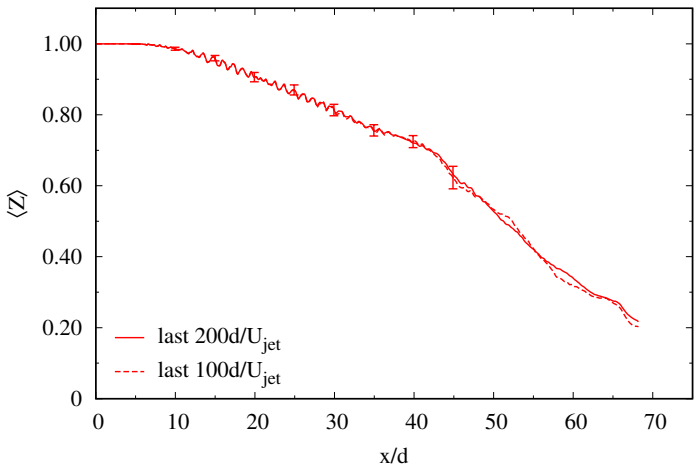

Figure 6.6: Centerline mixture fraction profiles from case RAD. To assess convergence, the Z profiles are computed using the last $200d/U_{\text{jet}}$ (solid lines) and the last $100d/U_{\text{jet}}$ (dashed lines) units of simulation time. The error bars are 95% confidence intervals computed considering the case with $100d/U_{\text{jet}}$ units of simulation time.

oscillations can be greatly reduced by reducing the data file saving period. Further, tests carried out in that chapter suggest that these oscillations have no impact on centerline and cross-stream conditional statistics.

Figure 6.7 shows centerline profiles of Favre-average $\widetilde{Z}_{\text{TNF}}$ from cases BL and RAD, compared to available measurements for flames B-E, and the LES of flame D from Mueller *et al.* [148]. The experimental measurements include flame B, for which a single data point at $x/d = 30$ is available (the centerline value at $x/d = 15$ is not available), and profiles for flames C, D, and E. As can be seen, case RAD presents an elongated structure compared to the higher Reynolds number flames. Differences between case RAD and flames C-E suggest that radiative heat losses only partially account for this elongated structure. The single centerline experimental data point existing for flame B is located between case RAD and the experimental profiles for the higher Reynolds number flames. The confidence intervals shown in Fig. 6.6 do not explain this difference.

Flame B is expected to have an elongated structure for several reasons. For flames C-E, the Reynolds number is large enough that some self-similarity is achieved. However, flame B is often referred to as transitional [71], and it is expected that the stoichiometric flame tip for this flame should be located further downstream than for the higher Reynolds number flames. As described by Hottel & Howthorne [176], by increasing the nozzle velocity of a jet flame, the flame height should initially increase almost linearly in the laminar regime; after the transition occurs, the flame

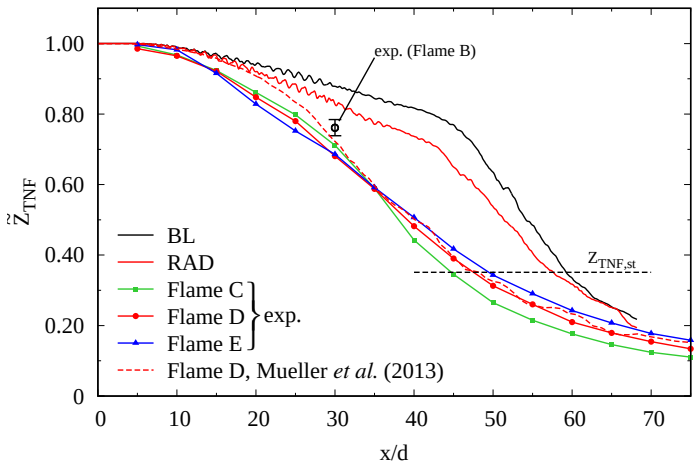

Figure 6.7: Centerline Favre-average measured mixture fraction profile. Black solid line, BL; solid red line, RAD; dashed red line, LES of Mueller *et al.* [148]; lines with symbols: measurements for flames C (green), D (red), and E (blue) [72]. Black empty circle: measured centerline Favre-average Z_{TNF} for flame B with the reported uncertainty [123].

height should then decrease, and eventually plateau once the jet is a fully developed turbulent flame. Flame B is also characterized by a higher pilot mass flow rate relative to the main jet. More precisely, the ratio U_{pilot}/U_{jet} ($\dot{m}_{pilot}/\dot{m}_{jet}$, where $\dot{m}$ is the mass flow rate) is about 37% (30%) in flame B, and only 23% (18%) for flames C-E. Hence, flame B has a larger effective momentum diameter.

The LES of Sandia flame D from Mueller *et al.* [148] is also shown. The centerline LES data is initially in good agreement with cases BL and RAD up to $x/d \approx 15$ and $x/d \approx 20$, respectively, and is then found to approach the centerline measurements for flame D. The good initial agreement between cases BL and RAD, and the LES, suggests that for these simulations the inlet conditions were modeled similarly. Unfortunately, inlet velocity data is not available for flame B (see App. B), and a better assessment of the impact of the inlet modeling cannot be carried out.

6.3 Conditional statistics

When comparing unconditional statistics from different simulations, one should ensure that the simulation time is sufficient to "average-out" the relatively slow, large spatial structures. That may be impractical when DNS are considered, due to the high computational cost. One approach to overcome this difficulty is simply to condition the statistics on a transported scalar, such as the mixture fraction. This effectively decouples the large scale hydrodynamic fluctuations from the flame structure. As discussed in Ch. 5, the assumption of this approach is that the large scale structures do not impact the small-scale dynamics.

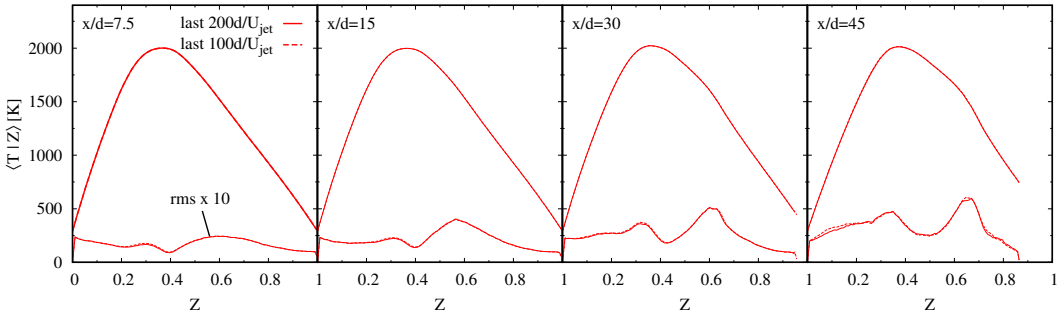

(a) Case RAD.

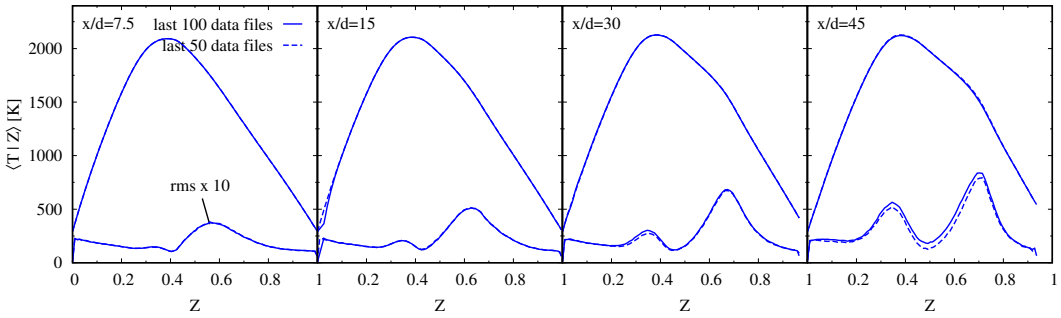

(b) Case UL.

Figure 6.8: Conditional mean and standard deviation temperature profiles from case RAD (top row) and case UL (bottom row), for $x/d = 7.5,\ 15,\ 30,\ 45$. Top row: comparison of statistics computed using the last $200d/U_{\text{jet}}$ (solid lines) and $100d/U_{\text{jet}}$ (dashed lines) units of simulation time. Bottom row: comparison of statistics computed using the last 100 data files (solid lines) and the last 50 data files (dashed lines).

Both radiation heat loss and differential molecular diffusion are expected to have an impact on the flame structure. That is why in this section, all three cases BL, RAD, and UL are considered. As was discussed in Ch. 5, for each of the downstream locations where comparisons are carried out, the entire cross-stream plane is considered to compute conditional statistics from the DNS.

It should be reminded that the conditional statistics are computed from the simulations considering 101 bins. For the experimental measurements, 50 bins are used.

6.3.1 Scalar profiles

Convergence of statistics

Before carrying out the comparisons with experiments and case BL, it is useful to assess the convergence of the conditional mean and rms profiles for the cases RAD and UL. Figure 6.8 shows the conditional mean and standard deviation temperature for cases RAD (Fig. 6.8a) and UL (Fig. 6.8b) at $x/d = 7.5,\ 15,\ 30$ and 45. It should

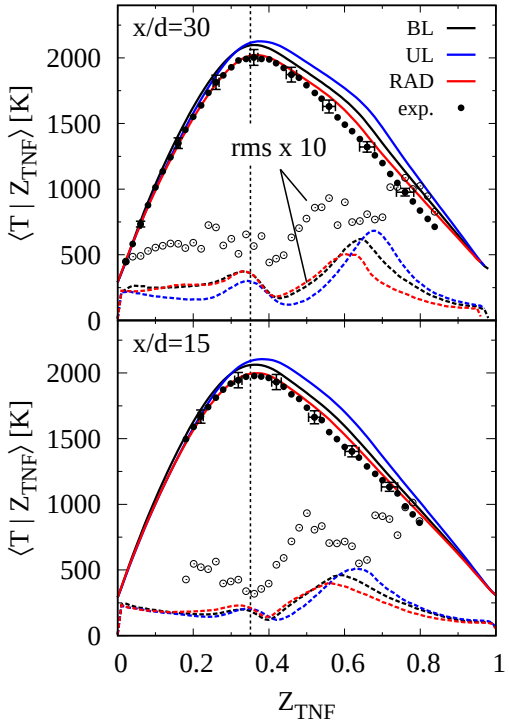

Figure 6.9: Comparison of temperature conditioned on Z_{TNF}, from case BL (black lines), case UL (blue lines), case RAD (red lines), and the measurements (symbols), for $x/d = 30$ (top) and $x/d = 15$ (bottom). Solid lines and the full symbols: conditional mean quantities; dashed lines and empty symbols: conditional rms values. The rms values are multiplied by a factor of 10 for clarity. The vertical dotted line represents the stoichiometric mixture fraction. The horizontal and vertical bars represent the reported uncertainties [46, 123].

be reminded that, with the exception of the stoichiometric flame tip location, only stations up to $x/d = 45$ will be considered in Ch. 7. For case RAD, the statistics are computed using the last $200d/U_{jet}$ and $100d/U_{jet}$ units of simulation time (158 and 79 data files, respectively). For case UL, a comparison is carried out between statistics computed using the last 100 and 50 data files. All profiles are in excellent agreement, showing that the statistics of interest are sufficiently converged.

Comparisons with experiments

Conditional mean and rms temperature profiles from cases BL, UL, and RAD, are compared to experiments in Fig. 6.9. For the conditional statistics, 50 bins are used for the experimental data, and 101 for the DNS data. As can be seen from the conditional mean profiles, case RAD is in excellent agreement the experiments. Significant differences between case BL and case RAD are observed on the rich side of the mixture. Further, the comparison with case UL shows that neglecting differential diffusion effects leads to an over-prediction of the temperature. Con-

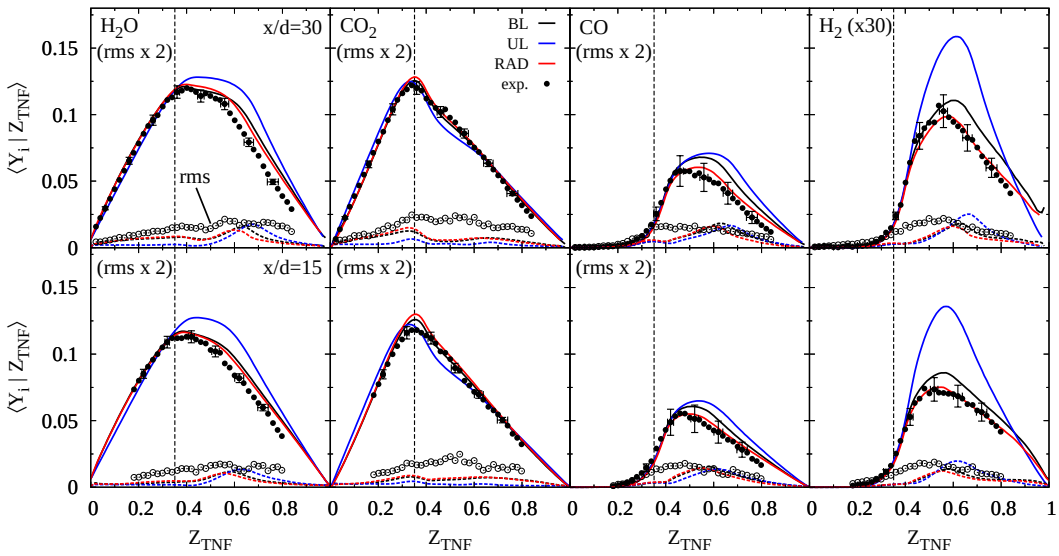

Figure 6.10: Comparison of species mass fractions conditioned on Z_{TNF}, from case BL (black lines), case UL (blue lines), case RAD (red lines) and the measurements (symbols), for $x/d = 30$ (top) and $x/d = 15$ (bottom). Solid lines and full symbols: conditional mean quantities; dashed lines and empty symbols: conditional standard deviations. Vertical dashed line: stoichiometric mixture fraction. The rms values for H_2O, CO_2, and CO are multiplied by a factor of 2, and both means and standard deviations of H_2 are multiplied by a factor of 30, for clarity. The horizontal and vertical bars represent the reported uncertainties [46, 123].

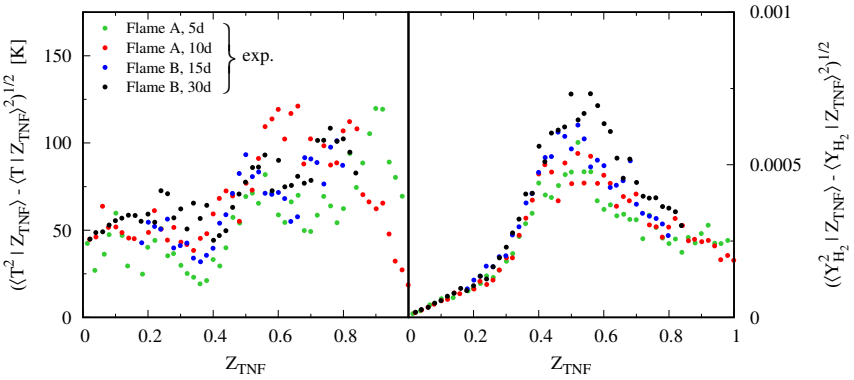

Figure 6.11: Conditional standard deviation for temperature (left) and Y_{H_2} (right), from experimental measurements [72]. Symbols: green, flame A at $x/d = 5$; red, flame A at $x/d = 10$; blue, flame B at $x/d = 15$; black, flame B at $x/d = 30$.

ditional temperature standard deviations from the DNS are found to systematically underestimate the experiments. The reason will be clarified below.

Comparisons of conditional mean species mass fractions are shown in Fig. 6.10. Two product species (H_2O and CO_2) and two intermediates (CO and H_2) are considered. For the two product species, there is little difference between cases RAD

and BL. However, for CO and H_2, which present a greater sensitivity to temperature variations, significant differences are observed between cases RAD and BL on the rich side of the mixture. More specifically, case RAD is in excellent agreement for both intermediates, while case BL is not. As expected, case UL greatly over-predicts the H_2 mass fraction. For unity Lewis numbers, the diffusivity of H_2 is much smaller than for the non-unity Lewis number case, and the diffusion of H_2 away from the fuel consumption region is greatly reduced, resulting in higher concentrations on the rich side of the mixture. Case UL is also found to over-predict the H_2O and CO mass fractions, while only modest changes are observed for CO_2.

Conditional standard deviations for the four considered species, are also found to generally underestimate the corresponding experimental profiles. The reason is likely to be the relatively high measurement noise [46]. More specifically, when conditional statistics are considered, the large flow-field fluctuations are effectively decoupled from the flame structure. As a result, conditional standard deviation are found to be generally smaller than unconditional ones, and measurement noise may very well be dominating over fluctuations of the flame structure, especially for low turbulence intensities, such as those found in flame B. This may be seen in Fig. 6.11, where the experimental conditional standard deviations from flame B are similar to the values found in flame A. Flame A is laminar, and the fluctuations in this flame are mainly caused by photon shot noise in the Raman measurements [46]. In the following section, the noise from flame A will be used to correct conditional probability density functions for several scalars.

6.3.2 Probability density functions

Conditional probability density functions (cpdf's) of temperature, and H_2 and H_2O mass fractions are shown in Fig. 6.12. The cpdf of each scalar is computed considering samples within a conditioning window around the peak conditional mean value of that scalar. The conditioning windows for the temperature, and the H_2 and H_2O mass fractions, are $0.33 < Z_{TNF} < 0.43$, $0.48 < Z_{TNF} < 0.58$ and $0.35 < Z_{TNF} < 0.45$, respectively. These conditioning windows are consistent with those used by Barlow & Frank [71]. Four downstream stations are considered, namely $7.5d$, $15d$, $30d$ and $45d$. For $x/d = 15$ and $x/d = 30$, experimental measurements are available.

As previously discussed, the conditional mean values for case RAD are in excellent agreement with experiments. Yet the conditional standard deviations generally underpredict the experimentally measured values. Here, case RAD is considered to

investigate if measurement noise can be taken into account to represent the experimental cpdf's [71].

For all scalars, the cpdf's from case RAD show a progressive broadening moving downstream. The most probable H_2 and H_2O values are found to increase with downstream distance.

The experimental profiles are found to be wider than case RAD: that is likely a consequence of the measurement noise discussed in Sec. 6.3.1. To take this effect into account, a noised radiative case, "RAD+noise", is considered using the following procedure. For each downstream station, only the points within the chosen conditioning window are considered. Samples are then assembled considering all data files from case RAD. Then, for each scalar, white Gaussian noise is added to the samples, and the cpdf is computed. This approach assumes that the measurement noise is decorrelated from the DNS data. The variance of this noise is taken from fits to the conditional mean variance found in flame A at $x/d = 5$ and $x/d = 10$, within the same conditioning window (the average of the fit across the conditioning window is considered). This choice is motivated by the assumption that all fluctuations for that flame at that location are a result of measurement noise only [46]. The fits, which are shown in Fig. 6.13, are obtained through local regression smoothing (LOESS), with a span $Z_{TNF} = 0.25$. As can be seen from Fig. 6.12, the width of the cpdf's corresponding to the noised cases is in good agreement with the experimental profiles, for all scalars.

6.3.3 Differential diffusion parameter

Following Barlow *et al.* [46], a differential diffusion parameter is computed as

$$z \equiv \frac{Y_H - Y_{H,2}}{Y_{H,1} - Y_{H,2}} - \frac{Y_C - Y_{C,2}}{Y_{C,1} - Y_{C,2}}, \tag{6.9}$$

where, as discussed in Ch. 4, the subscripts "1" and "2" refer to the fuel and oxidizer streams, respectively; Y_H and Y_C represent the hydrogen and carbon mass fractions, respectively, which are computed from the measured species only. The reported values for the fuel and oxidizer feeds are $Y_{C,1} = 0.1170$, $Y_{C,2} = 0.0$, $Y_{H,1} = 0.0393$, and $Y_{H,2} = 0.0007$ [72].

The conditional mean of Eq. (6.9), $\langle z|Z_{TNF}\rangle$, is compared to measurements in Fig. 6.14. Four downstream stations are considered, namely $x/d = 7.5$, 15, 30, and 45. Cases BL and UL are shown for all stations. Case RAD is shown for the two intermediate stations. As can be seen, cases BL and RAD are both in excellent

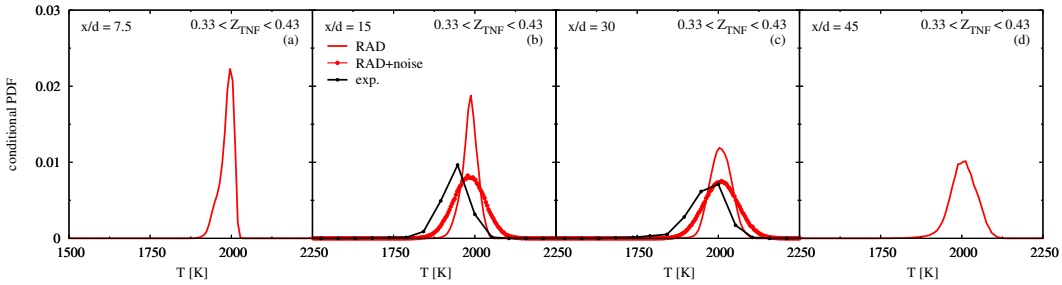

(a) Temperature.

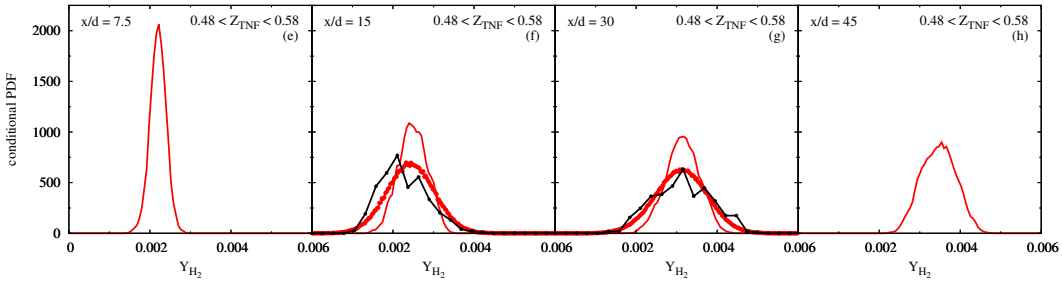

(b) Y_{H_2}.

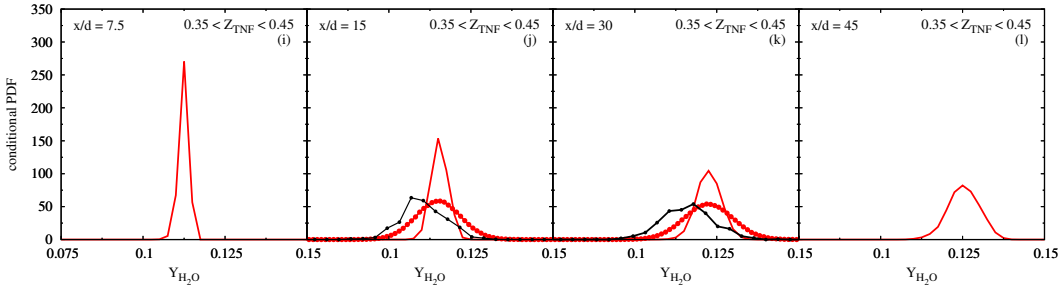

(c) Y_{H_2O}.

Figure 6.12: Conditional probability densities of temperature (top), Y_{H_2} (center), and Y_{H_2O} (bottom), for $x/d = 7.5$ (a, e, i), $x/d = 15$ (b, f, j), $x/d = 30$ (c, g, k), $x/d = 45$ (d, h, l). Solid red line: RAD; dashed red line with symbols, noised RAD case; black line with symbols: experiments [72].

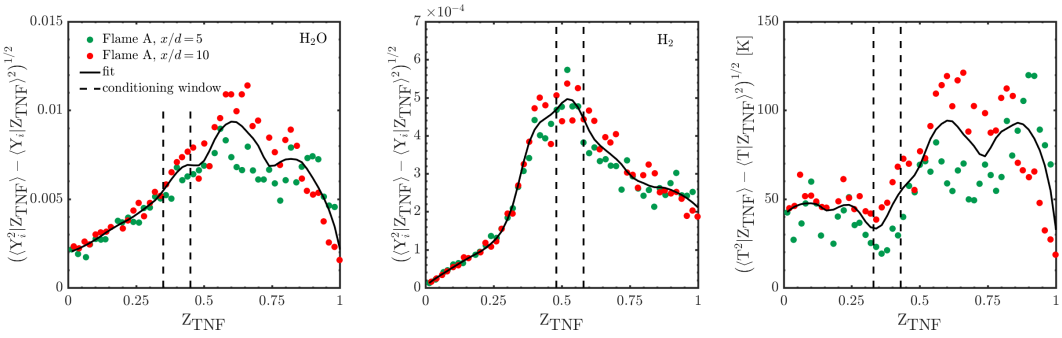

Figure 6.13: Conditional standard deviation for H_2O (left), Y_{H_2} (center), and temperature (right) from experimental measurements of flame A [72]. Symbols: green, flame A at $x/d = 5$; red, flame A at $x/d = 10$. Solid line: local regression smoothing (LOESS), with span $Z_{TNF} = 0.25$. Vertical dashed lines: scalar conditioning window.

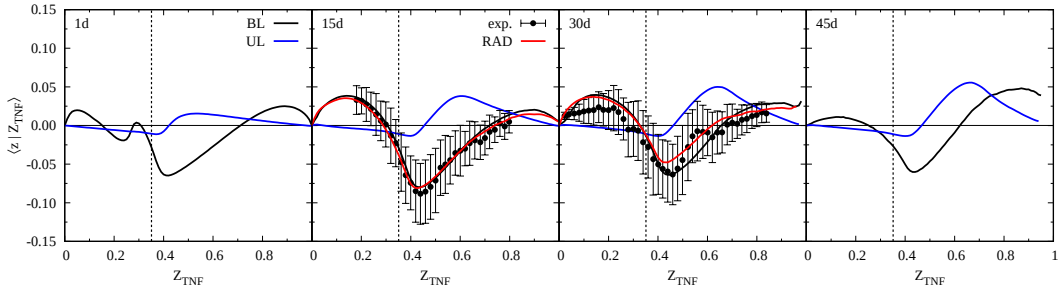

Figure 6.14: Conditional mean differential diffusion parameter z from the experiments [46, 72] (symbols) and the DNS (lines), at $x/d = 7.5,\ 15,\ 30$ and 45. Black, BL; blue, UL; red, RAD. Vertical bars: experimental conditional standard deviations, which include both noise and turbulent fluctuations. Vertical dashed line: stoichiometric mixture fraction.

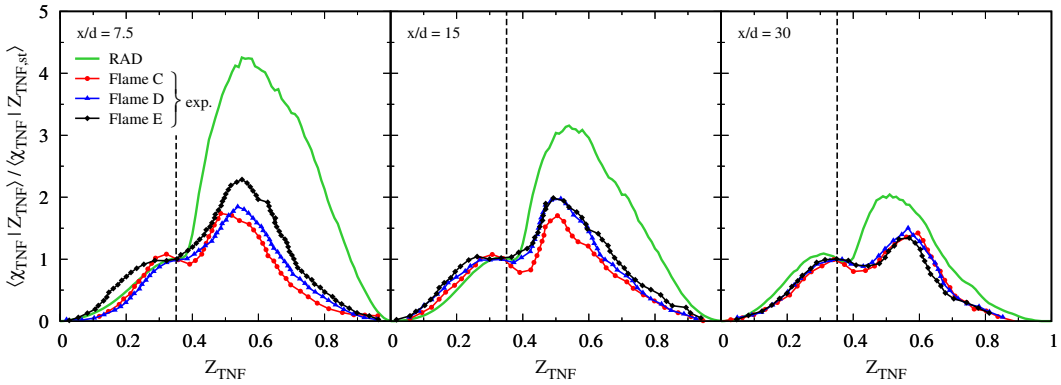

Figure 6.15: Conditional three-dimensional scalar dissipation rate normalized by its stoichiometric value, *vs.* x/d, for case RAD, and flames C, D, and E [132], for stations $x/d = 7.5,\ 15,\ 30$. Green, RAD; red, flame C; blue, flame D; black, flame E. Vertical dashed line: stoichiometric mixture.

agreement with the measurements for $x/d = 15$. A good agreement is also found for $x/d = 30$, where some differences between cases BL and RAD are evident on the rich side. As discussed above, z is computed only using the measured species, and is not strictly a measure of differential diffusion alone. The effect of the missing species on z can clearly be seen by comparison with case UL, which is nonzero.

6.3.4 Scalar dissipation

In this section, statistics of χ are discussed, and comparisons to measurements available for flames C-E are also provided.

Conditional means

Figure 6.15 shows profiles of χ_{TNF} conditioned on $\mathrm{Z_{TNF}}$ for case RAD, and the measurements for flames C, D, and E [132], for the three stations $x/d = 7.5,\ 15,\ 30,$

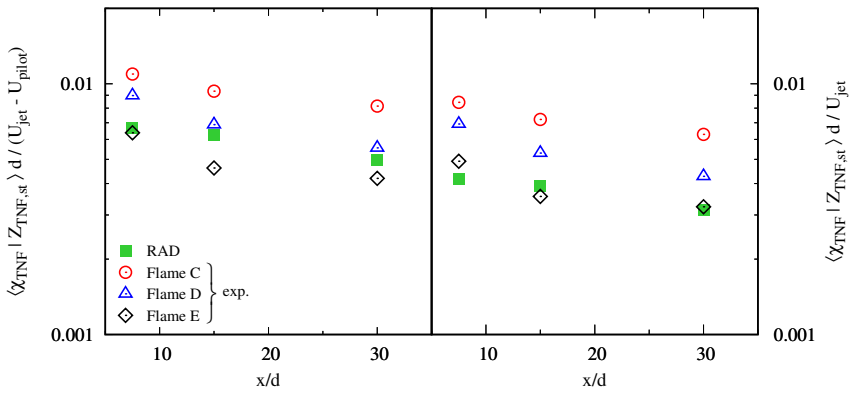

Figure 6.16: $\langle \chi_{\mathrm{TNF}} | Z_{\mathrm{TNF},st} \rangle$ normalized by $(\mathrm{U_{jet}} - \mathrm{U_{pilot}})/d$ (left) and $\mathrm{U_{jet}}/d$ (right), for case RAD (green), and flames C (red), D (blue), and E (black) [132], for stations $x/d = 7.5,\ 15,\ 30$.

for which measurements are available. All profiles in Fig. 6.15 are normalized by their stoichiometric value. The stoichiometric scalar dissipation rate is expected to scale approximately with the jet Reynolds number. Two different normalizations are considered, including $(U_{\mathrm{jet}} - U_{\mathrm{pilot}})/d$ and U_{jet}/d (see Ch. 4), which lead to qualitatively similar results, as can be seen in Fig. 6.16. For all three stations considered, flames C, D, and E have similar shapes for the $\langle \chi_{\mathrm{TNF}} | Z_{\mathrm{TNF}} \rangle$ profiles. The normalized profile from case RAD shows a more pronounced peak on the rich side of the mixture. The values of $\chi_{\mathrm{TNF,st}}$ shown in Fig. 6.16 are roughly within a factor of 2 of each other, which is the reported uncertainty associated with the experiments [132]. The two normalizations lead to qualitatively similar results.

In Karpetis & Barlow [132], the three-dimensional scalar dissipation profiles were constructed from the one-dimensional (radial) profiles, using knowledge of the flame orientation, which is computed from the OH signal. Unfortunately, this methodology is affected by a number of uncertainties, which make any comparison to simulations difficult. That is why Fig. 6.17 shows a comparison of one-dimensional (radial) scalar dissipation profiles. While the shape of the profiles is qualitatively similar to its three-dimensional counterpart, case RAD is generally closer to the higher Reynolds number flames. Figure 6.18 shows the normalized stoichiometric scalar dissipation rate with axial distance. While flames C and D are within a factor of 2 from case RAD, flame E is significantly lower than the corresponding three-dimensional values, which is consistent with significant extinction observed for this flame [46]. As explained by Karpetis & Barlow [132], the three-dimensional measurement technique relies on the presence of OH, and is consequently biased against flame extinction.

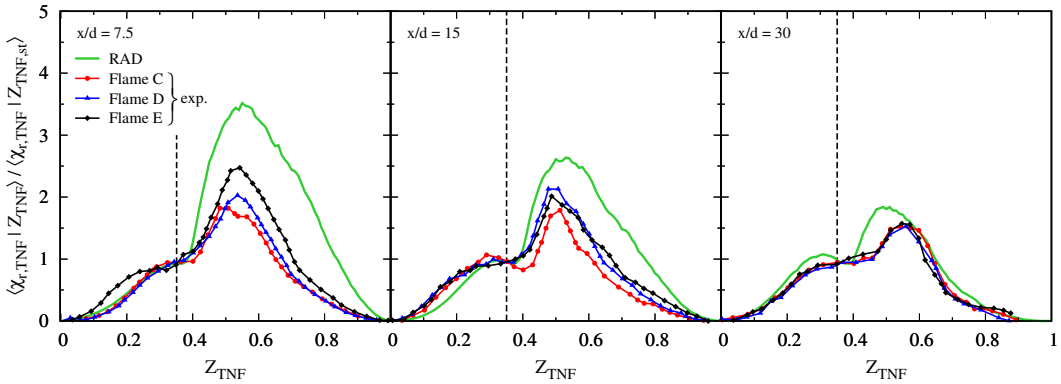

Figure 6.17: Conditional one-dimensional scalar dissipation rate normalized by its stoichiometric value, *vs.* x/d, for case RAD, and flames C, D, and E[132], for stations $x/d = 7.5,\ 15,\ 30$. Green, RAD; red, flame C; blue, flame D; black, flame E. Vertical dashed line: stoichiometric mixture.

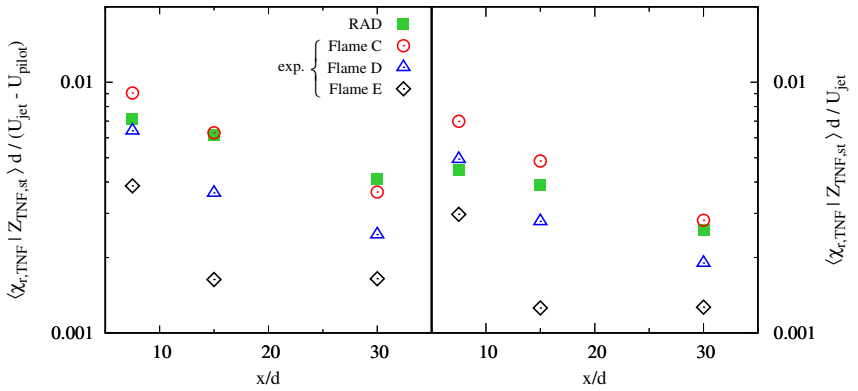

Figure 6.18: $\langle \chi_{r,\mathrm{TNF}} | Z_{\mathrm{TNF},st} \rangle$ normalized by $(\mathrm{U_{jet}} - \mathrm{U_{pilot}})/d$ (left) and $\mathrm{U_{jet}}/d$ (right), for case RAD (green), and flames C (red), D (blue), and E (black) [132], for stations $x/d = 7.5,\ 15,\ 30$.

Probability density functions

Figure 6.19 shows the probability density function of χ_{TNF} within the conditioning window $0.3 < \mathrm{Z_{TNF}} < 0.4$, the same as that used by Karpetis & Barlow [132]. Case RAD is compared to the measured values for flames C, D, and E [132]. To assess the impact of this conditioning window, a smaller one with half the range is also considered for case RAD, with negligible impact. The profiles show a reduction of peak height and increase in width with increasing jet Reynolds number. The three flames C, D, and E have roughly the same profile at $x/d = 30$, while flame B remains substantially narrower. The conditional standard deviations from Gaussian fits to the probability density functions are presented in Fig. 6.19 (d). These standard deviations are found to collapse when plotted against $\mathrm{Re_{jet}}(x/d)^{1/2}$, as shown in Fig. 6.20. The normalization that collapses the data is proposed based on the ob-

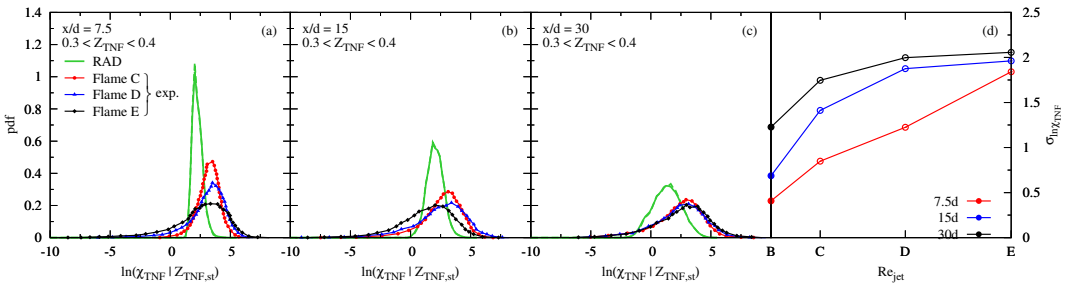

Figure 6.19: Probability densities of the logarithm of χ_{TNF} conditioned on the stoichiometric Z_{TNF} for $x/d = 7.5$ (a), $x/d = 15$ (b) and $x/d = 30$ (c). Experimental data from Karpetis & Barlow [132]. Two conditioning windows are considered for case RAD, including $0.3 < Z_{\mathrm{TNF}} < 0.4$ (solid green), which is consistent with the experiments, and $0.325 < Z_{\mathrm{TNF}} < 0.375$ (dashed green). (d): standard deviations of Gaussian fits to the probability density functions; full symbols: RAD; open symbols: experiments.

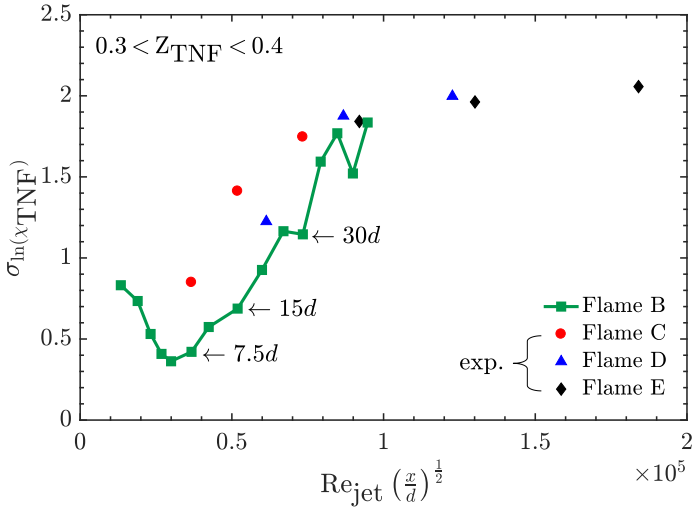

Figure 6.20: Standard deviation of the Gaussian fits to the profiles in Fig. 6.19, plotted with $\mathrm{Re}_{\mathrm{jet}}(x/d)^{1/2}$. Green, case RAD; red, flame C; blue, flame D; black, flame E.

servation that the standard deviations shown in Fig. 6.19 (d) increase monotonically both with the jet Reynolds number, and with downstream distance from the burner exit plane.

6.4 Summary

In this chapter, comparisons to available experimental data were carried out to validate the DNS database. The effects of radiation heat loss and differential diffusion were systematically isolated by comparing cases BL and RAD, and BL and UL, respectively.

Comparisons of Favre-mean and -rms of scalar quantities at $x/d = 15$ and $x/d = 30$ show an excellent agreement between case RAD and the experiments. This sug-

gests that the choice of the chemical model, the grid resolution, and the boundary conditions, are adequate. Differences between cases BL and RAD show that, for flame B, radiation heat loss has a non-negligible impact on the mixing field.

Centerline Favre-average mixture fraction profiles from cases RAD and BL were compared to experimental data for flames B-E (a single data point is available for flame B), and the LES data of Mueller *et al.* [177] for flame D. Compared to the higher Reynolds number flames, case BL was found to have an elongated structure, and this difference is only partly accounted for when radiation heat losses are included. For $x/d \lessapprox 15$, cases BL, RAD and the LES were found to be in good agreement, suggesting that the inlet conditions were modeled similarly. The LES profile was found to over-predict the measurement for flame D up to $x/d \approx 30$, and to be in excellent agreement downstream of that station.

Conditional mean temperature and species profiles at $x/d = 15$ and $x/d = 30$ showed an excellent agreement between case RAD and the experiments. Neglecting radiation heat losses was found to result in an increase of the peak temperature of about 70K, and over-prediction of the CO and H_2 mass fractions. Neglecting differential diffusion effects was found to result in higher temperatures (the peak temperature increased by about 110K with respect to the baseline case), and over-prediction of the H_2O, CO, and H_2 mass fractions. Differential diffusion was found to have a greater impact on the flame structure than radiation heat loss.

The comparison of conditional probability densities showed that case RAD is in excellent agreement with experimental measurements, once the effect of measurement noise is taken into account.

Following Barlow *et al.* [46], a differential diffusion parameter z was considered. The comparisons with experiments showed an excellent agreement for $x/d = 15$ and a good agreement for $x/d = 30$.

Scalar dissipation statistics from case RAD were compared to measurements available for the higher Reynolds number flames (flames C-E), showing significant shape differences on the rich side of the mixture. However, once normalized, the stoichiometric scalar dissipation rate was found to compare well with flames C-E. For the one-dimensional scalar dissipation rate profiles, case RAD was found to be generally closer to the measurements. The normalized stoichiometric one-dimensional scalar dissipation rate values from case RAD were found to be closer to flames C and D (the one-dimensional values for flame E are affected by extinction, and were

found to be significantly lower). Finally, probability density functions of the logarithm of the scalar dissipation rate from case RAD were compared to flames C-E. The scalar dissipation in flame B was found to be approximately log-normal, with a shape that remains more peaked than for flames C-E, as downstream distance is increased. Standard deviations from the log-normal fits to these pdf's were found to increase with downstream distance and Reynolds number. Further, these standard deviations are found to collapse when plotted against $\mathrm{Re}_{\mathrm{jet}}(x/d)^{1/2}$.

To conclude, the results presented in this chapter show that the choice of grid resolution, chemical model, and boundary conditions for the DNS is adequate to reproduce experimental measurements with high fidelity, once radiation heat losses and differential diffusion are included.

Chapter 7

ANALYSIS OF EFFECTIVE LEWIS NUMBERS FROM THE DNS OF SANDIA FLAME B

In Ch. 4, a methodology was introduced to extract effective Lewis numbers from experimental or numerical data of turbulent non-premixed flames. This methodology was applied to the Sandia flames, a set of well-characterized experimental measurements of non-premixed jet flames at varying jet Reynolds numbers. In that analysis, the effective Lewis numbers were shown to transition from their laminar values close to the burner exit plane, to unity further downstream. Previously-suggested scalings for γ were then analyzed.

However, limitations in the experimental data set, including large uncertainties and the relatively few measured quantities, were shown to introduce large biases and prevent a conclusive assessment of the transitioning behavior of the flame structure, as well as the correct modeling approach.

In Ch. 4, turbulence and flame parameters, including the radial flame location r_F, the jet half-width, r_{12}, the rms velocity, u', and the integral length scale, l, were estimated assuming independence across flames B-E. While expected to be valid for the higher Reynolds number jets, this approach may not hold for low turbulence intensities. In particular, flame B can be considered to be a worst-case scenario, since it has the lowest Reynolds number. Fortunately, flame B is also the easiest to simulate through DNS, as was discussed in the previous chapters. Here, the analysis carried out in Ch. 4 is extended to the DNS data of flame B. Flame independence for the turbulence and flame parameters is assessed, and the scalings for γ are recomputed for flame B using case RAD.

7.1 Extracting effective Lewis numbers

In this section, the steady-state non-unity Lewis number flamelet equations are applied to the DNS data to extract optimal χ_{st} and γ values, for several downstream locations.

7.1.1 Methodology

As was discussed in Chs. 2 and 4, the scalar dissipation rate, χ, is a parameter that must be specified when solving the flamelet equations. Here, for consistency with the approach used in Ch. 4, the same *a priori* model for χ is used. That is, the shape of χ in mixture fraction space is evaluated from the solution of the mixture fraction transport equation, Eq. (1.6), for counterflow diffusion flames [133, 134] and unsteady mixing layers [65]. Thus, the only free parameter for χ is its stoichiometric value, χ_{st}, which is used to scale the magnitude. In other words, the optimal χ_{st} is still computed as a solution to the two-dimensional minimization problem given by Eq. (4.9).

In the expression for the ith species effective Lewis number (introduced in Ch. 1)

$$\mathrm{Le}_{i,\mathrm{eff}} = \frac{1+\gamma}{\frac{1}{\mathrm{Le}_i}+\gamma}, \tag{7.1}$$

it is assumed that the Lewis number of species i, Le_i, is constant in mixture fraction space. This assumption is retained in the analysis of cases BL and RAD, since approximating mixture-averaged transport properties with a set of constant non-unity Lewis numbers was found to be a good approximation in Ch. 3. It should be reminded that the species' Lewis numbers in Eq. (7.1), are pre-computed from flamelet solutions, at the location of maximum temperature. A further assumption is to assume that γ is constant in mixture fraction space, as was done in Ch. 4.

7.1.2 Error maps

The optimal flamelet parameters represent the solution of the optimization problem given by Eq. (4.9). Given the low cost of obtaining a single steady-state solution, the flamelet equations (Eq. (4.4)) are solved for a range of χ_{st} and γ values. The pair (χ_{st}, γ) whose corresponding flamelet minimizes the error given by Eq. (4.8), is called optimal. The χ_{st} values theoretically span the range $[0, \chi_q]$, where χ_q is the extinction scalar dissipation rate. However, solving the flamelet equations for the entire range is not practical, and a discrete set of values in the range $[2, 260]$ is chosen instead ($\chi_q \approx 265\ s^{-1}$). This range represents most of the burning branch of the S-shaped curve for the laminar Lewis number limit ($\gamma = 0$). In Eq. (7.1), the parameter γ spans theoretically the range $[0, \infty)$. Practically, a discrete set of values is chosen, spanning the range $[0, 120]$. It should be reminded that Eq. (7.1) presents a small sensitivity to γ, for values much larger or much smaller than one. For example, considering the Lewis number of hydrogen, $\mathrm{Le}_{\mathrm{H_2}} \approx 0.3$, the difference between $\mathrm{Le}_{\mathrm{H_2,eff}}$ for $\gamma = 100$ and $\gamma = 1000$ is only approximately 0.02.

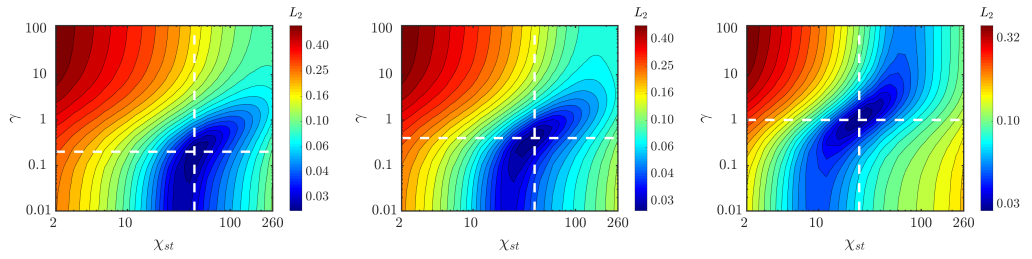

(a) $x/d = 7.5$. **(b)** $x/d = 15$. **(c)** $x/d = 30$.

Figure 7.1: Contour maps of the L_2 error, given by Eq. (4.8), for case RAD, at $x/d = 7.5$ (left), $x/d = 15$ (center), and $x/d = 30$ (right). The white dashed lines intersect at the optimal flamelet (minimum L_2 error).

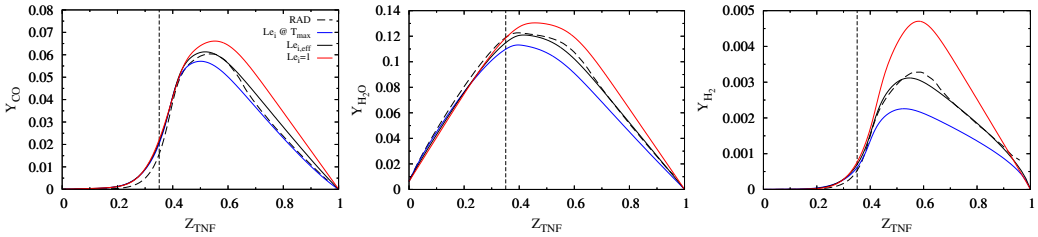

(a) CO mass fraction. **(b)** H_2O mass fraction. **(c)** H_2 mass fraction.

Figure 7.2: Comparison of conditional mean mass fractions of Y_{CO} (left), Y_{H_2O} (center), and Y_{H_2} (right), from case RAD at $x/d = 30$, with the flamelet solutions corresponding to effective Lewis numbers (black line), unity Lewis numbers (red line), and laminar Lewis numbers (blue line). The vertical dashed line represents the stoichiometric mixture fraction.

While all species in the chemical model may be used to compute the error maps, only the measured ones are used, for consistency with the analysis carried out in Ch. 4. More precisely, only the mass fractions of O_2, CH_4, CO, CO_2, H_2O, and H_2 are considered. Further, the same measured mixture fraction, Z_{TNF}, is computed, where the interference correction given by Eq. (4.2) is used.

Figure 7.1 shows error maps for case RAD at $x/d = 7.5$, 15, and 30. The white dashed lines intersect at the location of the optimal solution. As can be seen, the γ^{opt} values are found to increase with downstream distance, while the χ_{st}^{opt} values decrease. For the three stations considered, the effective Lewis number of H_2 is 0.34 at $x/d = 7.5$, 0.38 at $x/d = 15$, and 0.46 at $x/d = 30$.

7.1.3 Optimal flamelet parameters

Figure 7.2 shows a comparison of the conditional mean mass fractions of CO, H_2O, and H_2 from case RAD at $x/d = 30$, against three flamelet solutions: the effective

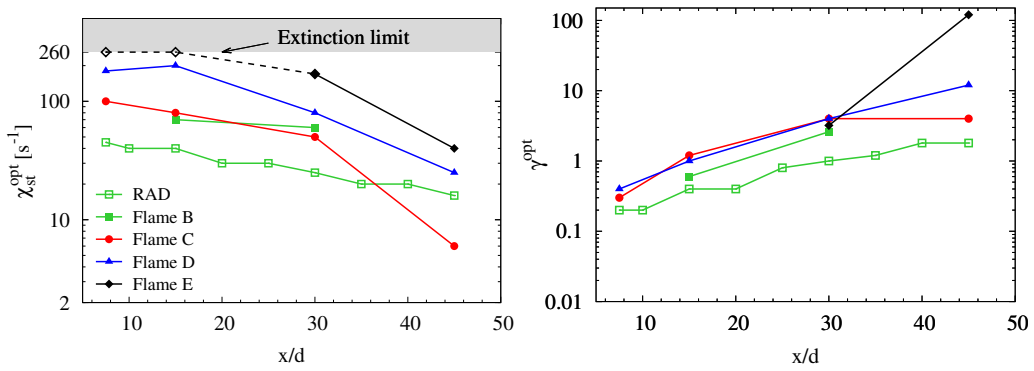

(a) χ_{st}^{opt} *vs.* x/d. **(b)** γ^{opt} *vs.* x/d.

Figure 7.3: χ_{st}^{opt} (left), and γ^{opt} (right) as a function of the downstream direction x/d. Green with open symbols, RAD; green with full symbols, flame B; red, flame C; blue, flame D; black, flame E. See caption of Fig. 4.4 for a more complete description.

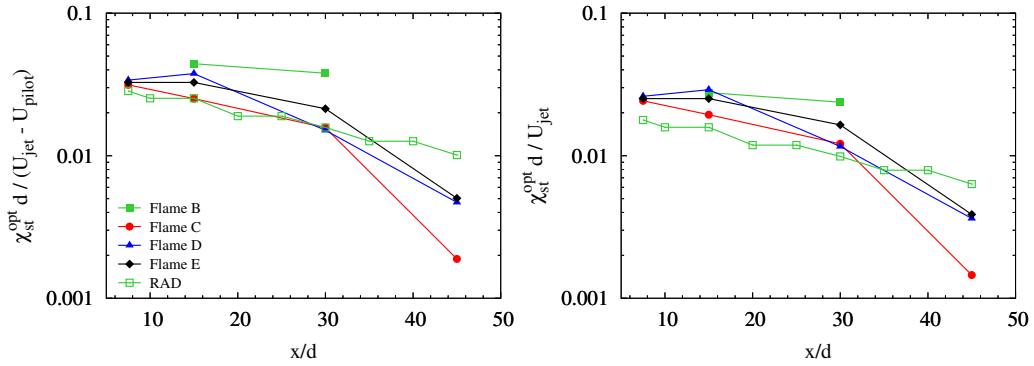

Figure 7.4: χ_{st}^{opt} normalized by $(U_{jet} - U_{pilot})/d$ (left) and U_{jet}/d (right), as a function of downstream direction for flames B, C, D, and E and case (RAD).

Lewis number solution ($\gamma = \gamma^{opt}$), the unity Lewis number case ($\gamma \to \infty$), and the laminar Lewis number solution ($\gamma = 0$). The χ_{st} value in all three flamelet solutions is set to χ_{st}^{opt}. The optimal flamelet is found to be generally in good agreement with the DNS. For CO, all three flamelets are found to over-estimate its concentration on the lean side; moving towards the richer mixture, case RAD is found to move from the optimal flamelet, to the laminar Lewis number one. For both H_2O and H_2, the optimal flamelet is generally well representative of case RAD.

These results show that the optimal flamelet can be well representative of the data, especially given the assumptions associated with representing the conditional mean flame structure with a single steady-state, constant non-unity Lewis number flamelet.

Comparison of case RAD and the experiments

In this chapter, the results discussed in Ch. 4 are compared to the DNS, with the goal of highlighting similarities and differences.

Figure 7.3 shows the optimal flamelet parameters from the experiments, compared to those from case RAD. The χ_{st}^{opt} values from case RAD are found to be generally decreasing, similarly to the profiles extracted from the measurement data of flames B-E. The values extracted from case RAD are lower than the values extracted from the measurements of flame B. More specifically, at the two downstream locations where experiments are available, *i.e.*, $x/d = 15$ and $x/d = 30$, the χ_{st}^{opt} values extracted from the experiments are $70s^{-1}$ and $60s^{-1}$, respectively, while the values found from case RAD are $40s^{-1}$ and $25s^{-1}$, respectively. It is interesting to note that, for $x/d < 30$, the values of χ_{st}^{opt} from case RAD and those extracted from flames C-E, are ordered according to their respective jet Reynolds numbers. To assess this further, Fig. 7.4 shows the χ_{st}^{opt} values normalized by $(\mathrm{U_{jet}} - \mathrm{U_{pilot}})/d$ and by $\mathrm{U_{jet}}/d$. While being close, the profiles do not show a perfect collapse, with either normalization. For both normalizations, the χ_{st}^{opt} values from the experiments of flame B are generally higher than those for flames C-E for $x/d > 30$. The slope of χ_{st}^{opt} from case RAD differs from flames C-E for $x/d > 30$. That may be caused by the elongated shape of flame B compared to the higher Reynolds number flames, as was discussed in Ch. 6.

Figure 7.3b shows that the γ_{st}^{opt} values from case RAD are generally increasing with downstream distance, similarly to the profiles extracted from the measurement data of flames B-E. The values extracted from case RAD are lower than those from the measurements of flame B. More specifically, the γ^{opt} values for flame B at $x/d = 15$ and $x/d = 30$ are 0.6 and 2.6, respectively, while the values computed from case RAD at the same locations are 0.4 and 1.0, respectively. Interestingly, while flames C and D have practically the same γ^{opt} values for $x/d < 30$, both case RAD and flame B are lower. As previously discussed, the stoichiometric flame tip for flames C-E is located at $x/d \approx 45$, and large differences are observed for the γ^{opt} values from those flames, at that location.

Multiple reasons could explain the discrepancies between the values of χ_{st}^{opt} from case RAD, and those from measurements of flame B, including experimental uncertainties, and biases introduced by the models used (*e.g.*, the chemical model). The fact that both the χ_{st}^{opt} values and the γ^{opt} values for case RAD are lower than those extracted from the measurements of flame B is consistent with the shape of the error maps shown in Fig. 7.1. The shape of the error contours around the optimal

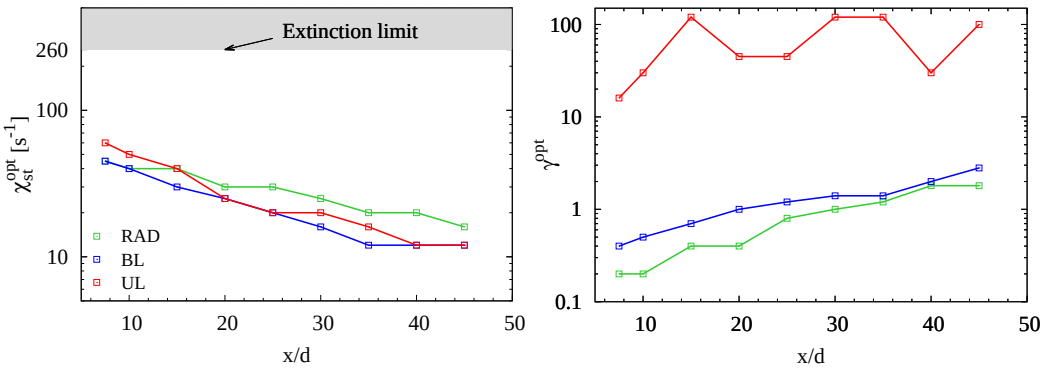

(a) χ_{st}^{opt} *vs.* x/d. **(b)** γ^{opt} *vs.* x/d.

Figure 7.5: χ_{st}^{opt} (left), and γ^{opt} (right) as a function of the downstream direction x/d. Green, RAD; blue, BL; red, UL. The shaded region corresponds to values of χ_{st} above the laminar Lewis number extinction limit.

solution is approximately oriented at 45^o. In other words, small error differences are associated with the simultaneous increase or decrease of χ_{st}^{opt} and γ^{opt}. That means that χ_{st} and γ generally have opposing effects, which tend to offset each other. For example, for the three species shown in Fig. 7.2, an increase in γ will result in higher mass fractions (the red lines are always above the blue lines). On the other hand, increasing χ_{st} values will cause the mass fractions to decrease.

Comparison of cases BL, RAD, and UL

Figure 7.5 shows a comparison of optimal flamelet parameters from cases BL, UL and RAD. Figure 7.5a shows that, for all three cases, the χ_{st}^{opt} profiles are generally decreasing with axial distance, *i.e.*, the qualitative behavior is the same. For $x/d < 10$, cases RAD and BL are partly overlapping, and lower than case UL. All three profiles remain within a factor of 2 of each other. Figure 7.5b shows that the γ^{opt} profiles for cases BL and RAD remain close for the entire range $7.5 < x/d < 45$. This suggest that not including radiation heat loss, and not considering the conditional temperature profiles in the error map analysis, has a small impact on γ^{opt}. As expected, the γ^{opt} values for case UL are much higher than the other two cases for the entire range $7.5 < x/d < 45$. As previously discussed for the optimization analysis presented in Ch. 4, the chosen range for γ was $[0, 120]$, where $\gamma = 120$ is considered a proxy for $\gamma \to \infty$. While the γ^{opt} values for case UL remain high for the entire range $7.5 < x/d < 45$, they are not always equal to 120. That is not surprising, since the expression for the effective Lewis numbers, Eq. (7.1), presents a small sensitivity to γ for large values of this parameter. For example, the effective

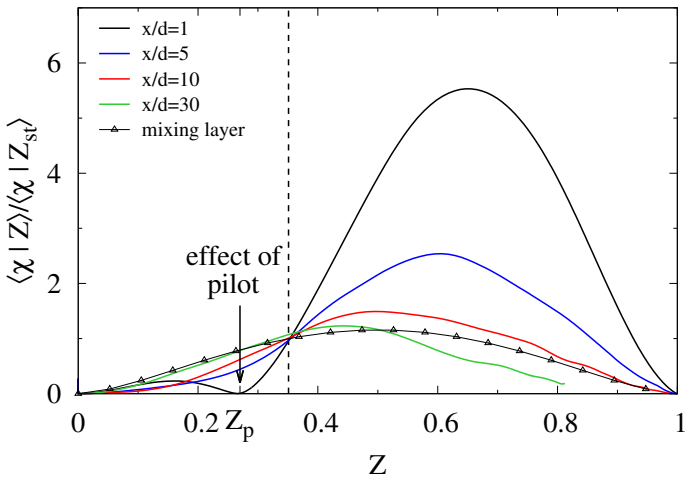

Figure 7.6: Comparison of $\langle\chi(Z)|Z\rangle/\langle\chi|Z_{st}\rangle$ computed from case RAD (no symbols), and Eq. (4.5) with Eq. (4.6) (symbols). The vertical line represents the stoichiometric mixture fraction. "Z_p" is the pilot feed mixture fraction.

Lewis number of H_2 is 0.98 for $\gamma = 120$ and 0.93 for $\gamma = 30$. The values of γ^{opt} close to the burner exit plane are likely affected by the pilot flame. The pilot strongly affects the scalar dissipation rate at the base of the jet, and acts as an additional feed (in the flamelet framework discussed in Ch. 4, non-premixed jet flames are modeled as a two-feed system). The effect of the pilot flame can be seen in Fig. 7.6, where the $\langle\chi(Z)|Z\rangle/\langle\chi|Z_{st}\rangle$ profiles from case RAD at several downstream locations, are compared to the shape of $\chi(Z)$ used to solve the flamelet equations (Eq. (4.6)).

One approach to include the effect of the pilot, could be to use the following closure for the scalar dissipation rate in the flamelet equations [23]

$$\chi(Z, \boldsymbol{x}) = \langle\chi|Z\rangle(\boldsymbol{x}), \tag{7.2}$$

where $\langle\chi|Z\rangle(\boldsymbol{x})$ is computed from available data. This approach is not pursued here.

Comparison of optimal parameters using Z and Z_{TNF}

In Ch. 4, the optimal parameters were extracted from the data through an error map analysis based on six measured species (including O_2, CH_4, H_2O, H_2, CO_2, and CO), as well as a measured mixture fraction, Z_{TNF}. Moreover, to take into account interference in the measured CH_4 signal, a correction was considered for this species (see Sec. 4.2). Figure 7.7 compares the optimal parameters χ_{st}^{opt} and γ^{opt} extracted by performing the error map analysis with either Z or Z_{TNF}. The

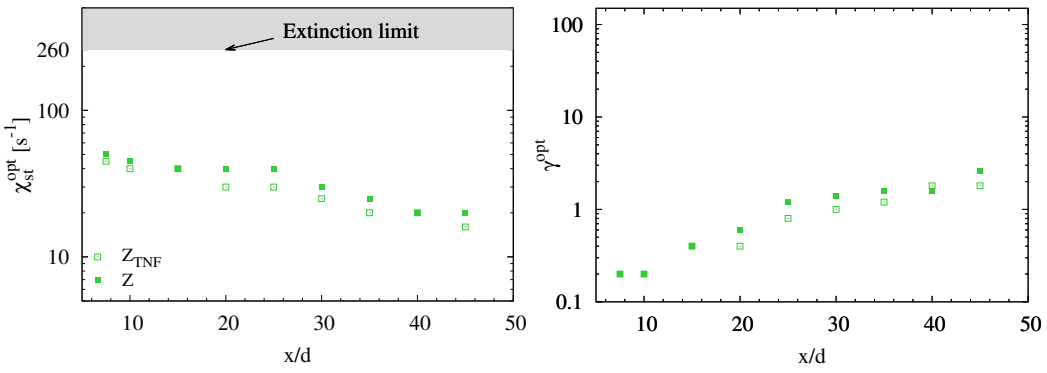

(a) χ_{st}^{opt} *vs.* x/d. **(b)** γ^{opt} *vs.* x/d.

Figure 7.7: χ_{st}^{opt} (left), and γ^{opt} (right) as a function of the downstream direction x/d, obtained from case RAD, with optimization carried out considering either Z_{TNF} (empty symbols) or Z (full symbols).

comparison shows that two approaches lead to qualitatively and quantitatively very similar results.

Comparison of χ_{st}^{opt} and $\langle\chi|Z_{st}\rangle$

Figure 7.8 compares the optimal χ_{st} values extracted from case RAD, with $\langle\chi|Z_{st}\rangle$ computed from the same simulation. Consistently with the observations discussed in Ch. 4, the optimal χ_{st} values are found to be systematically larger than the measured $\langle\chi|Z_{st}\rangle$. Once again, the two sets of values are not expected to be the same in a turbulent flame, since in the present approach, a single, one-dimensional, steady-state flamelet is used to represent the conditional mean flame structure. In other words, it is expected that both optimal parameters χ_{st} and γ^{opt} are also representative of any effect not adequately represented by this approximation. As previously suggested, it is likely that multi-dimensional effects, including convective and diffusive transport along the mixture fraction iso-surfaces, are essentially lumped into the χ_{st}^{opt} values.

7.2 Scalings for γ

In Ch. 4, previously-suggested scalings for γ were assessed. First, a standard k-ε argument was used to derive the Reynolds number-based scaling given by

$$\gamma = \frac{\alpha_T}{\alpha} = a^{Re_T} Re_T, \tag{7.3}$$

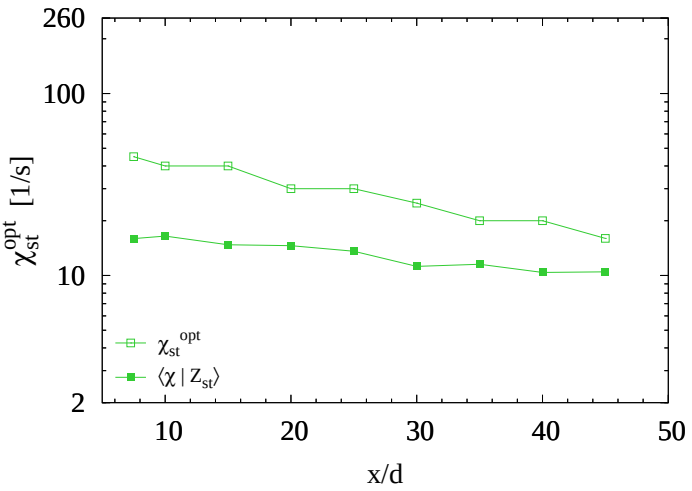

Figure 7.8: Comparison of the optimal scalar dissipation rate, χ_{st}^{opt} with the values $\langle \chi | Z_{st} \rangle$ from case RAD, as a function of the downstream direction x/d.

where a^{Re_T} is a scaling coefficient. Next, flame length and time scales were used to suggest the two Karlovitz number-based scalings given by

$$\gamma = a^{l_F} Ka^{\frac{2}{3}}, \tag{7.4}$$

and

$$\gamma = a^{\tau_F} Ka^{2}, \tag{7.5}$$

where a^{l_F} and a^{τ_F} are scaling coefficients. In the following sections, these scalings will be assessed for case RAD.

7.2.1 Turbulence and flame quantities

The evaluation of the local Reynolds number requires estimates for several turbulence and flame quantities, namely the rms velocity, u', the integral length scale, l, and the jet half-width, r_{12}. Further, these quantities should be computed at the radial flame location, r_F, for each downstream location.

In Secs. 4.5 and 4.6 it was assumed that the quantities r_F, r_{12}, and the ratios u'/U_{jet} and l/r_{12} are all flame-independent. While that is expected to be valid for the higher Reynolds number flames, significant uncertainties could be introduced for flame B, due to its low Reynolds number (in the original work of Barlow *et al.* [71], this flame was characterized as "transitional"). That is why the validity of these assumptions for flame B is analyzed here using case RAD.

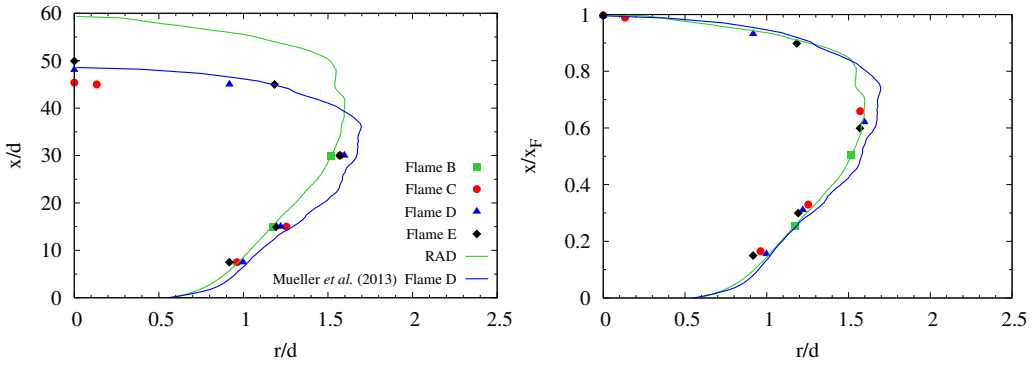

(a) r_F *vs.* x/d. **(b)** r_F *vs.* x/x_F.

Figure 7.9: Radial flame location r_F for flames B through E (green, red, blue, and black, respectively) with downstream distance in jet diameters (left) and normalized by the stoichiometric flame tip location (right). Symbols: measurements [72]. Solid lines: green, RAD; blue, LES of Mueller *et al.* [148]. In (b), the downstream location of the measured points for flame B is normalized by the stoichiometric flame tip location from case RAD ($x_F \approx 59.3d$).

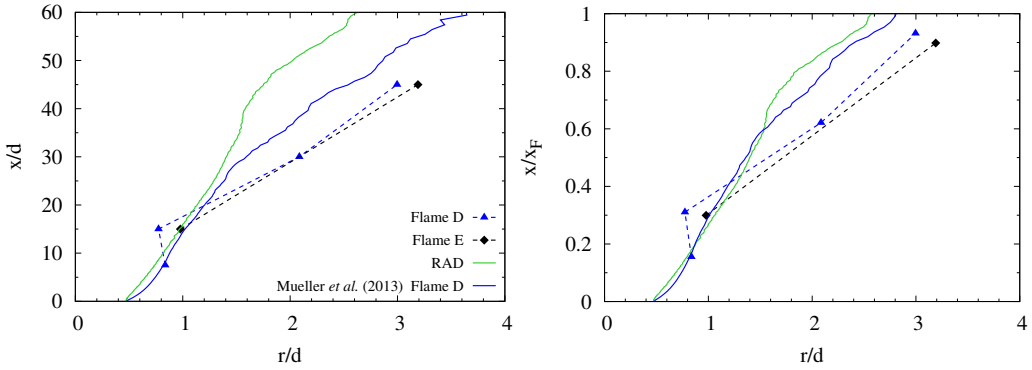

(a) r_{12} *vs.* x/d. **(b)** r_{12} *vs.* x/x_F.

Figure 7.10: Jet half-width r_{12} for flames B, D and E (green, blue and black, respectively) with downstream distance in jet diameters (left) and normalized by the stoichiometric flame tip location, x_F (right). Symbols: measurements of Schneider *et al.* [129]. Solid lines: green, RAD; blue, LES of Mueller *et al.* [148].

Radial flame location and jet half-width

Figure 7.9 shows the radial flame location r_F for the experimental data [72], the LES of Mueller *et al.* [148], and case RAD. The profiles are plotted with downstream distance in jet diameters (Fig. 7.9a), and relative to the stoichiometric flame tip location x_F (Fig. 7.9b), which is defined as $\langle Z \rangle(x_F, r = 0) = Z_{st}$. Figure 7.9a shows that case RAD is elongated, when compared to the measurements for flames C-E.

However, when normalized by the stoichiometric flame tip, the profiles are found to be in excellent agreement. Thus, the assumption of flame-independence for r_F in Secs. 4.5 and 4.6 is valid for flame B only after proper normalization of x.

Figure 7.10 shows the jet half-width, r_{12}, for the measurements of Schneider *et al.* [129], the LES [148], and case RAD. The downstream distance is shown both in jet diameters (Fig. 7.10a), and relative to the stoichiometric flame tip location x_F (Fig. 7.10b). Once again, the agreement between case RAD and the higher Reynolds number flames improves once the downstream distance is normalized by the flame tip location. The quality of the agreement is good, considering the relatively low Reynolds number of flame B. Case RAD and the LES are practically identical up to about 60% of the flame tip location, after which the differences remain small. These results suggest that the assumption of flame independence for r_{12} is valid in flame B, once the flame tip location is taken into account.

Velocity fluctuations and integral length scale

Given the flame-independence of r_F and r_{12}, in Ch. 4 the same was assumed for u'/U_{jet} and l/r_{12}, both evaluated at the radial flame location. More precisely, if the jet Reynolds number is sufficiently high, and both r_F and r_{12} are Reynolds number-independent, then, at each downstream location, u' should depend only on the jet Reynolds number, and l/r_{12} should asymptotically approach some constant

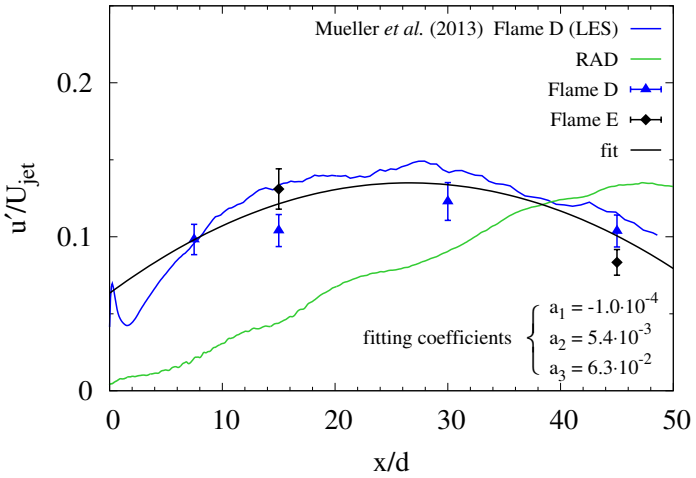

Figure 7.11: Rms velocity for flames B, D and E (green, blue and black, respectively), at the radial flame location r_F, normalized by the bulk velocity of the respective jet. Full symbols, experimental data [72, 129]; green line, case RAD; blue line, LES [148]; solid black line, fit given by Eq. (4.18), which only considers the experimental data for flames D and E, and the LES.

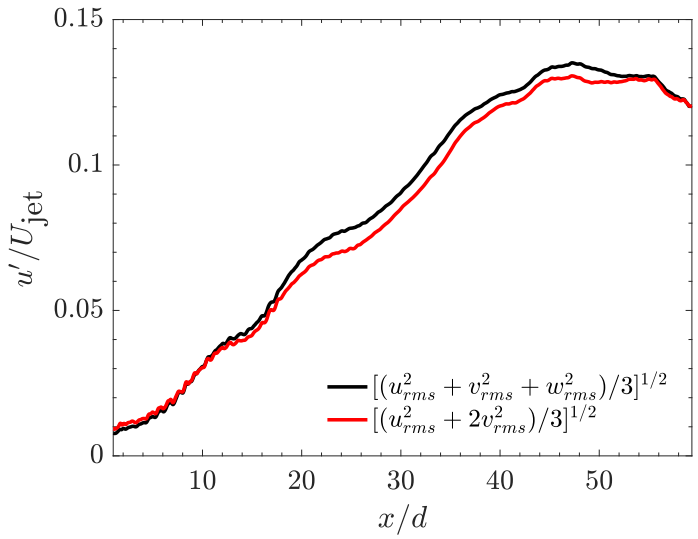

Figure 7.12: Comparison of u' at the radial flame location for case RAD, computed using either $u' = [(u^2_{\mathrm{rms}} + v^2_{\mathrm{rms}} + w^2_{\mathrm{rms}})/3]^{1/2}$ (black) or $u' = [(u^2_{\mathrm{rms}} + 2v^2_{\mathrm{rms}})/3]^{1/2}$ (red).

value [147]. It should be reminded that this assumption was necessary to estimate u' and l at the radial flame location for all flames, since velocity data is only available for a subset of the flames and downstream locations (see App. B). However, two issues can be identified. First, the validity of this assumption could not be tested for flames B and C, due to the missing velocity data. For flame B in particular, this assumption will be shown to not be valid, due to its relatively low Reynolds number. Second, the base of all jets is strongly affected by the presence of the pilot flame, and the flame is likely located within a low-$\mathrm{Re_T}$ region. That is why in the following sections, the analysis is carried out considering only stations beyond $x/d = 7.5$. Figure 7.11 compares the ratio u'/U_{jet} at r_F from case RAD, the experimental measurements [69, 72] (flames D and E) and the LES of Mueller *et al.* [148] (flame D). The rms velocity from case RAD is computed as

$$u' = \left[\frac{u^2_{\mathrm{rms}} + v^2_{\mathrm{rms}} + w^2_{\mathrm{rms}}}{3}\right]^{\frac{1}{2}}, \tag{7.6}$$

while

$$v^2_{\mathrm{rms}} + w^2_{\mathrm{rms}} \approx 2v^2_{\mathrm{rms}} \tag{7.7}$$

is assumed for the experiments, as was done in Ch. 4. This approximation is quite good, as shown in Fig. 7.12, where u' is computed at the radial flame location for case RAD, using either Eq. (7.6), or the approximation given by Eq. (7.7). As shown in Fig. 7.11, case RAD presents much lower u'/U_{jet} values than flames D

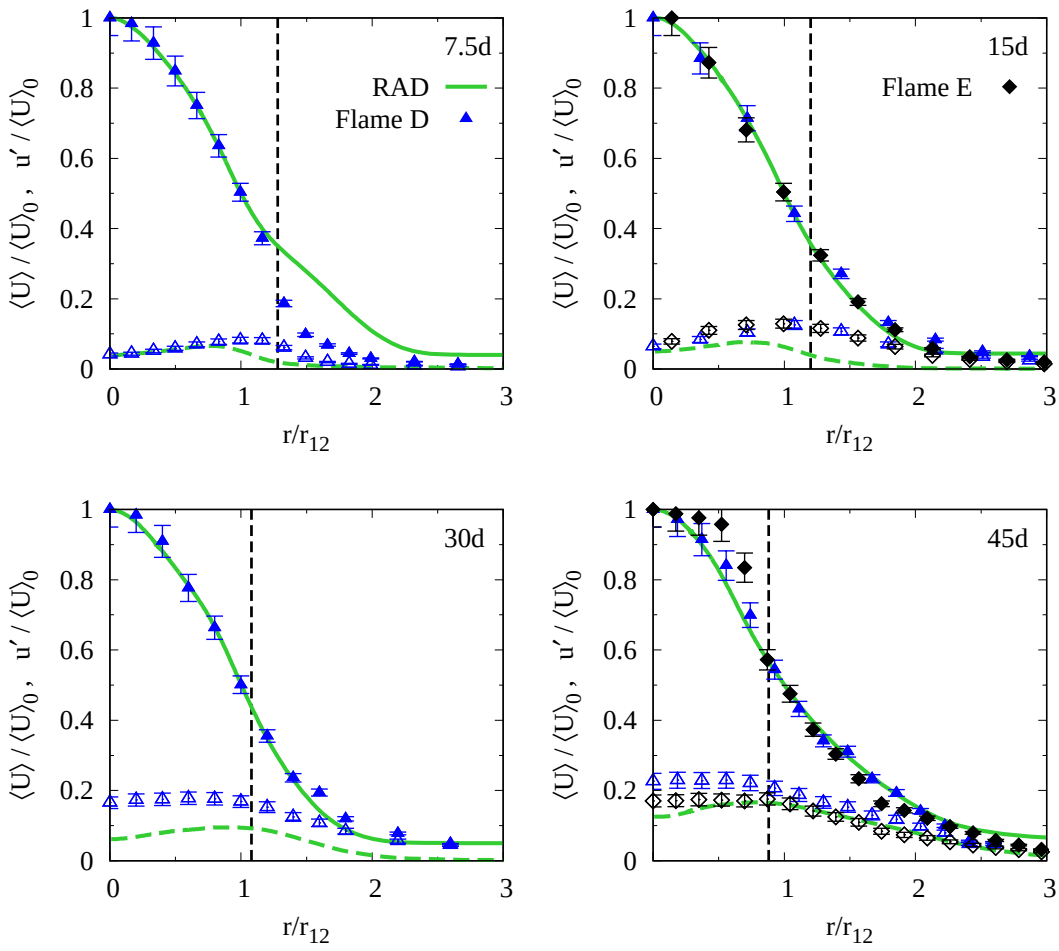

Figure 7.13: Normalized radial profiles of mean streamwise velocity (solid line and full symbols), and rms velocity (dashed line and empty symbols), for $x/d = 7.5$, 15, 30, 45. The profiles are normalized by the centerline mean velocity. Green, case RAD; blue, flame D; black, flame E [129]. The vertical dashed line is the radial flame location from case RAD. The vertical bars represent the reported uncertainties [129].

and E, for $x/d < 40$. That is consistent with the much lower Reynolds number for flame B, and suggests that the flame may initially lie within a laminar mixing layer.

Figure 7.13 shows a comparison of radial profiles of the mean streamwise velocity and the rms velocity for case RAD and the measurements for flames D and E. The location of r_F is also shown. From this figure, it can be seen that for the first two stations, u' at r_F from case RAD is much lower than the peak value, suggesting once again that for those stations the flame lies within a laminar region.

Figure 7.14 shows the estimated integral length scale at r_F. Values from case RAD are computed using the definition used in Ch. 4 directly

$$l \equiv \frac{u'^3}{\varepsilon}, \tag{7.8}$$

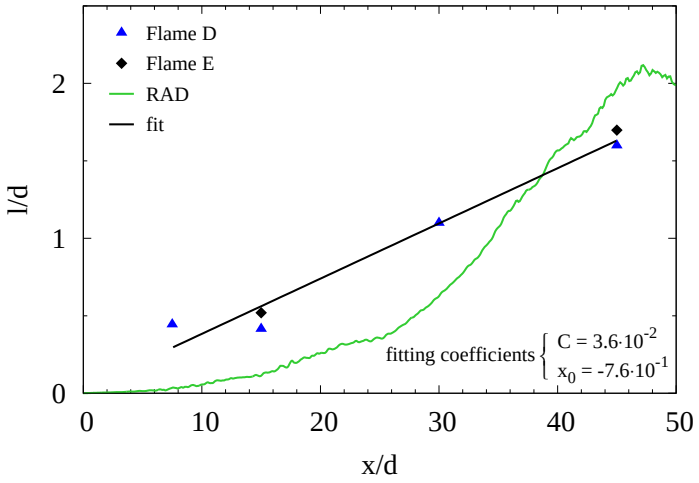

Figure 7.14: Estimated integral length scale at the radial flame location. Blue symbols, flame D; black symbols, flame E; green line, RAD; black line, fit given by Eq. (4.22). For case RAD, l is computed from the definition, Eq. (7.8), directly. However, for the experiments, scalings from self-similar round jets are used [151, 152].

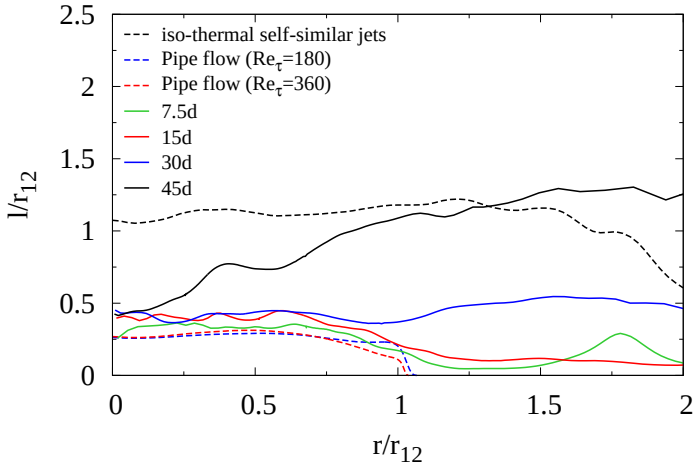

Figure 7.15: Integral length scale $l \equiv u'^3/\varepsilon$, normalized by r_{12}, for case RAD at $x/d = 7.5$ (green), $x/d = 15$ (red), $x/d = 30$ (blue), and $x/d = 45$ (solid black). The black dashed line is computed using fits from measurements of iso-thermal self-similar round jets [151, 152]. The blue and red dashed lines represent Eq. (7.8) computed from the turbulent pipe flow DNS data of El Khoury *et al.* [178].

while experimental values are estimated using scalings from self-similar iso-thermal round jets [151, 152] in Eq. (7.8). As expected, a significant difference is observed. While using scalings for self-similar jets is expected to be valid for the higher Reynolds number flames, that might not be the case for flame B, due to its relatively low Reynolds number. To investigate this further, Fig. 7.15 shows a comparison of Eq. (7.8) computed from case RAD, compared to the expected scaling for self-similar iso-thermal jets [151], and the scaling for turbulent pipe

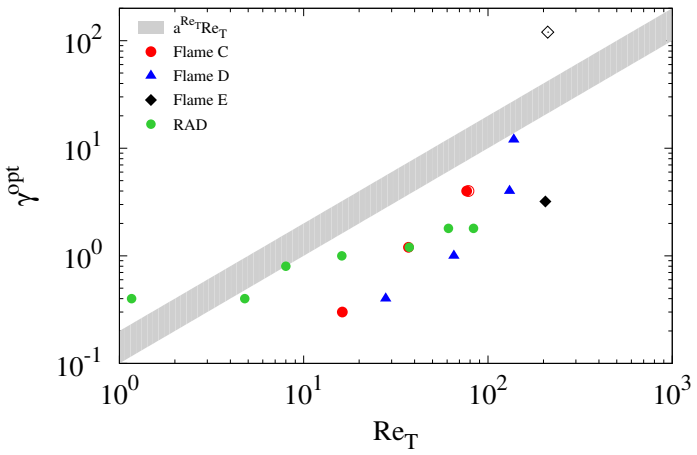

Figure 7.16: Evolution of γ^{opt} with Reynolds number. The gray band represents $a^{\text{Re}_\text{T}}\text{Re}_\text{T}$ with the estimates for a^{Re_T} discussed in Sec. 4.5.1. The first two stations of flame E are not shown, as their γ^{opt} values are 0. The open red symbol represents flame C at $x/d = 45$, for which the average stoichiometric flame length is 45.4 diameters downstream of the burner exit (see Sec. 4.3.4); flame E at $x/d = 45$ has also been marked with an open symbol to highlight the large difference in γ^{opt} values obtained with the L_1 and L_2 norms (see Sec. 4.4.4). The green symbols represent case RAD between $x/d = 7.5$ and $x/d = 45$.

flows. For the pipe flows, the data of El Khoury *et al.* [178] is used for two DNS at $\text{Re}_\tau \equiv (u_\tau d)/(2\nu)$ of 180 and 360 (for the present configuration, the Re_τ for the fuel pipe flow is approximately 267. Unsurprisingly, for the four stations considered, the profiles are found to be between the scalings for pipe flows and the profile for self-similar jets. More specifically, the first three stations are found to be relatively close to the pipe flow scalings, with $x/d = 7.5$ being the closest, while the l/r_{12} profile at $x/d = 45$ is found to be closer to the jet scaling.

These observations will be used in the following sections to recompute the local Reynolds and Karlovitz numbers for flame B using case RAD.

7.2.2 Scaling based on the Reynolds number

Having computed u' and l, Re_T for case RAD can be calculated directly, *i.e.*, without the fits given by Eqs. (4.18) and (4.22). The γ^{opt} and Re_T values computed for case RAD, are compared to those estimated from the experiments in Fig. 7.16. As previously discussed, optimal parameters from case RAD are extracted between $x/d = 7.5$ and $x/d = 45$, which is the same range used for experimental measurements. It should be reminded that stations before $x/d = 7.5$ are not considered due to the influence of the pilot flame, and stations beyond $x/d = 45$ are not considered due to the limited convergence of the statistics, as was discussed in Ch. 5. Similar

to the data points extracted from the experiments, a positive correlation is found between the γ^{opt} values and Re_T. The slope of the points computed from case RAD is less than what is observed for the experiments. That is not surprising, given the differences between flame B (case RAD) and the higher Reynolds number flames, concerning u' and l. Finally, similar to the points extracted from the experiments, the values computed for case RAD do not fall within the range estimated from the coefficient of Eq. (7.3). That is expected, since the turbulent Reynolds number does not take into account directly any flame length scale, and is not expected to adequately represent turbulence-chemistry interaction, as was discussed in Ch. 4.

7.2.3 Scaling based on the Karlovitz number

In this section, the optimal γ values are plotted against a local Karlovitz number computed from case RAD.

Estimating the flame thickness for case RAD

First, the flame thickness l_F should be computed. Considering the self-similar solution of a laminar unsteady mixing layer, the following definition of flame thickness may be derived (see App. A)

$$l_F \equiv 4\frac{Z(1-Z)}{|\nabla Z|}. \tag{7.9}$$

Equation (7.9) may be applied to the turbulent non-premixed jet flames considered in this work following several approaches. In Ch. 4, Eq. 7.9 was estimated at the stoichiometric mixture using the following approximation

$$|\nabla Z| = \left(\frac{\chi_{st}^{opt}}{2\alpha_{st}}\right)^{1/2}. \tag{7.10}$$

Here, this estimate will be referred to as l_F^{exp}. However, for case RAD, l_F may be computed without the assumption given by Eq. (7.10). One approach to compute l_F, is to consider the thickness of the averaged mixture-fraction profile,

$$l_{F,1} = 4\frac{\langle Z\rangle(1-\langle Z\rangle)}{|\nabla\langle Z\rangle|}. \tag{7.11}$$

This expression may be interpreted as the thickness of the turbulent flame brush. One could also consider the average of the instantaneous flame thickness,

$$l_{F,2} = 4\left\langle\frac{Z(1-Z)}{|\nabla Z|}\right\rangle. \tag{7.12}$$

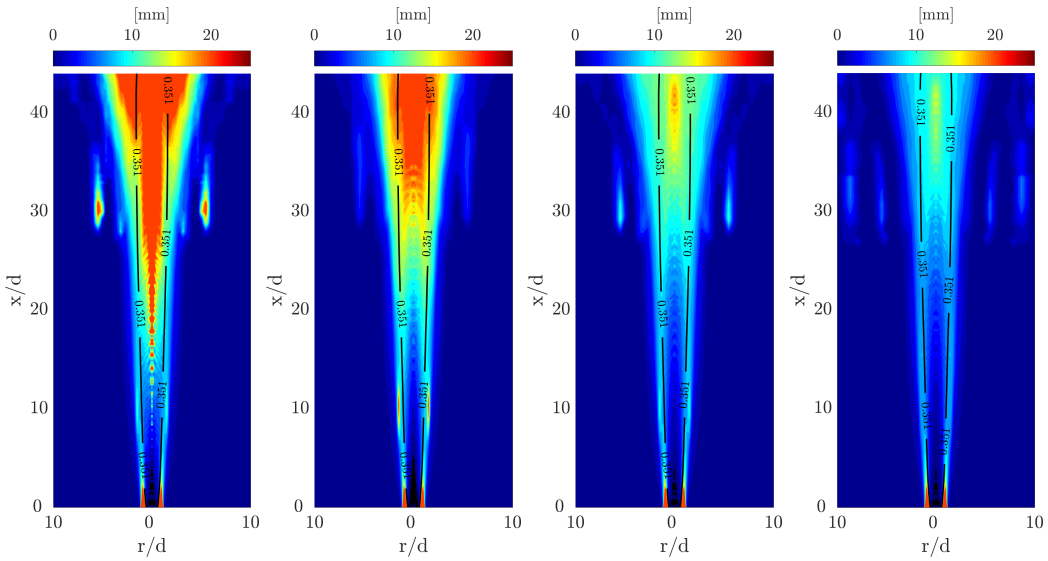

(a) $l_{F,1}$. **(b)** $l_{F,2}$. **(c)** $l_{F,3}$. **(d)** $l_{F,4}$.

Figure 7.17: Two-dimensional field of l_F computed using Eq. (7.11) (a), Eq. (7.12) (b), Eq. (7.13) (c), and Eq. (7.14) (d). The solid black line represents the stoichiometric mixture fraction.

As an intermediate expression, one may also evaluate

$$l_{F,3} = 4\frac{\langle Z\rangle(1-\langle Z\rangle)}{\langle|\nabla Z|\rangle}. \tag{7.13}$$

Finally, the following expression can also be considered

$$l_{F,4} = 4\frac{\langle Z\rangle(1-\langle Z\rangle)}{\langle|\nabla Z|^2\rangle^{1/2}}. \tag{7.14}$$

Equation (7.14) evaluated at the stoichiometric mixture fraction is the closest to l_F^{exp}. More specifically, if $\langle|\nabla Z|^2\rangle_{st}^{1/2}$ is replaced by $\chi_{st}^{opt}/(2\alpha_{st})$, then l_F^{exp} is recovered. It should be reminded that $\langle\cdot\rangle$ represents averaging carried out in time and in the azimuthal direction. In this section, these expressions are compared and used to compute the local Karlovitz number, $Ka \equiv (l_F/\eta)^2$.

In Fig. 7.17, two-dimensional maps of Eqs. (7.11), (7.12), (7.13), and (7.14) are shown, where it can be seen that the four expressions lead to qualitatively similar estimates for l_F. More quantitatively, the values of l_F^{exp}, $l_{F,1}$, $l_{F,2}$, $l_{F,3}$, and $l_{F,4}$, evaluated at the stoichiometric mixture fraction, are shown in Fig. 7.18. As expected, all five expressions show that the flame thickness increases with downstream distance, which is consistent with the progressive spreading of the jet. The profiles for $l_{F,1}$, $l_{F,2}$, $l_{F,3}$, and $l_{F,4}$, are found to be essentially the same up to $x/d \approx 10$. That is

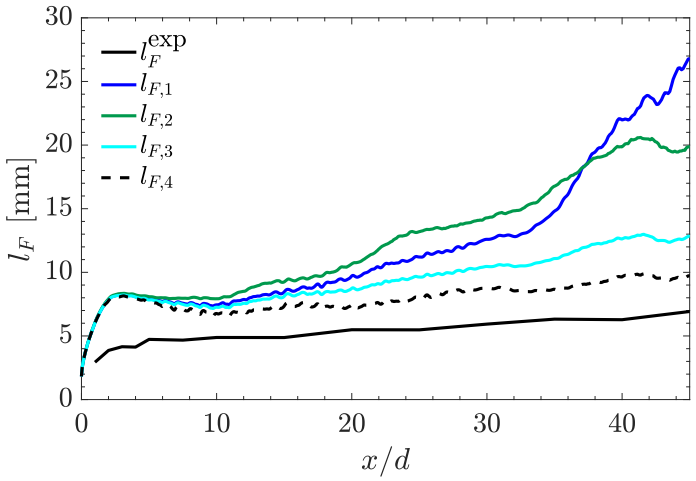

Figure 7.18: Comparison of different expressions for l_F evaluated at the stoichiometric mixture fraction. Solid black, l_F^{exp}; blue, $l_{F,1}$, green, $l_{F,2}$; cyan, $l_{F,3}$; dashed black, $l_{F,4}$.

consistent with the low fluctuation levels found at the stoichiometric mixture fraction close to the burner exit plane. Moving downstream, the four expressions are found to progressively diverge. The values of l_F^{exp} are much smaller than the those computed from the other expressions. That is expected since for each downstream location, the extracted χ_{st}^{opt} parameters are larger than the corresponding $\langle\chi|_{Z_{st}}\rangle$ values, as discussed in Secs. 4.3.4 and 7.1.3.

To evaluate the quality of the previous expressions for l_F, normalized cross-stream cuts of $\langle Z\rangle$ are considered for several downstream locations in Fig. 7.19. These profiles are compared to the hyperbolic tangent approximation to the self-similar solution of the one-dimensional unsteady laminar mixing layer, Eq. (A.2)

$$\frac{\langle Z\rangle(x,r)}{\langle Z\rangle(x,0)} \approx \frac{1}{2}\left[1-\tanh\left(\frac{r-r_{Z12}}{h}\right)\right], \tag{7.15}$$

where

$$h = \frac{l_F}{2}, \tag{7.16}$$

l_F is computed using the five previous expressions, and r_{Z12} is defined as

$$\frac{\langle Z\rangle(x,r_{Z12})}{\langle Z\rangle(x,0)} = 0.5. \tag{7.17}$$

As expected, $l_{F,1}$, $l_{F,2}$, $l_{F,3}$, and $l_{F,4}$, are close up to $x/d \approx 30$, and only deviate for the last station considered. The profile obtained using l_F^{exp} if found to be in relatively good agreement with the normalized $\langle Z\rangle$ shape for the first two stations, but performs poorly for the last two stations. Given these observations, $l_{F,2}$ appears to be the best expression.

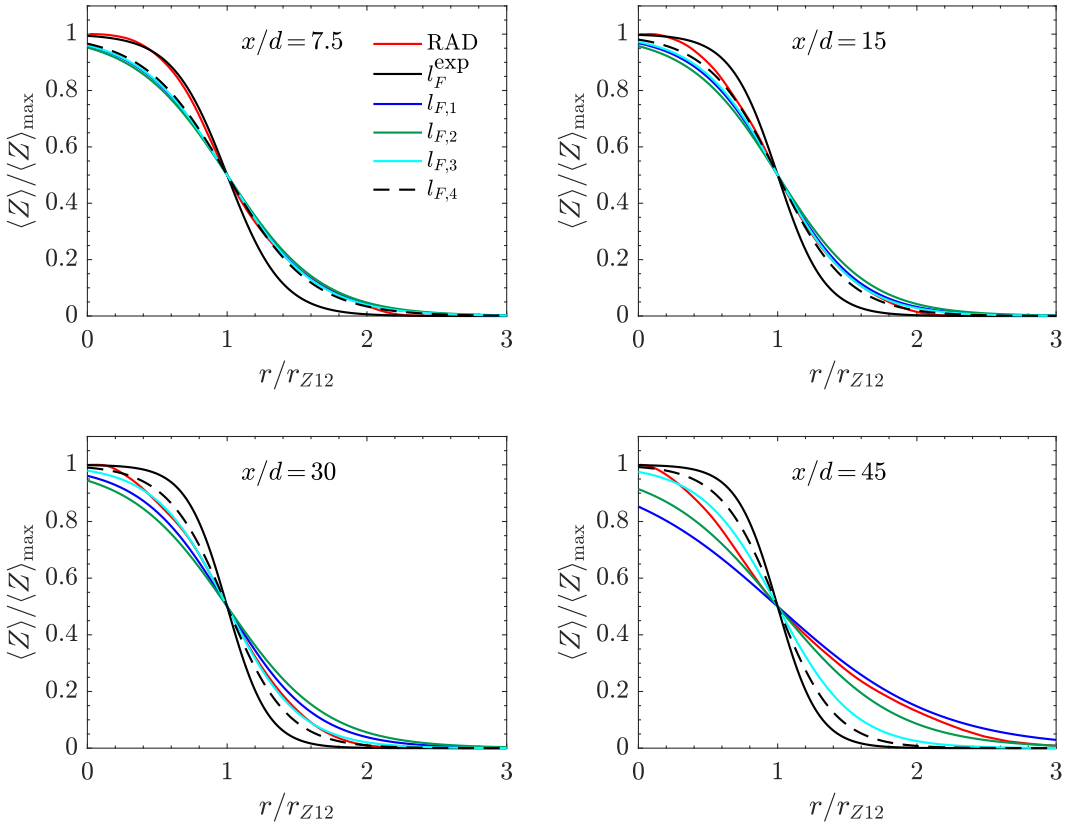

Figure 7.19: Comparison of radial profiles of normalized $\langle Z \rangle$ (solid black), at $x/d = 7.5$ (top left), $x/d = 15$ (top right), $x/d = 30$ (bottom left), and $x/d = 45$ (bottom right), with Eq. (7.9) (dashed black), Eq. (7.11) (red), Eq. (7.12) (blue), and Eq. (7.13) (green).

Estimating the Kolmogorov length scale for case RAD

Next, the Kolmogorov length scale is computed at r_F using Eq. (4.24), *i.e.*, $\eta \equiv (\nu^3/\varepsilon)^{1/4}$, where the average kinematic viscosity $\langle \nu \rangle$ is used, and the dissipation rate of turbulent kinetic energy, ε, is computed using the definition introduced in Ch. 5 (Eq. (5.1))

$$\varepsilon \equiv \left\langle \sigma'_{ik} \frac{\partial u'_i}{\partial x_k} \right\rangle \langle \rho \rangle^{-1}. \tag{7.18}$$

With l_F and η known, the Karlovitz number at r_F may be computed for case RAD.

γ^{opt} and the local Karlovitz number

Figure 7.20 shows the γ^{opt} values with the Karlovitz number at the flame location. It should be reminded that only stations in the range $7.5 \leq x/d \leq 45$ are considered. The two points estimated for flame B in Ch. 4, have now been replaced by case RAD. The Karlovitz numbers for case RAD are computed using all five expressions discussed above. While the profile from case RAD with $l_F^{\exp}$ presents

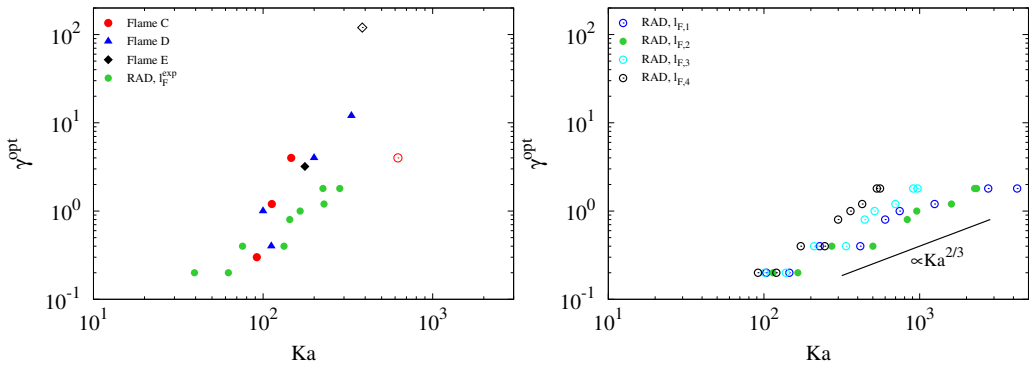

(a) Case RAD using l_F^{exp}. **(b)** Case RAD using $l_{F,1\text{-}4}$.

Figure 7.20: Evolution of γ^{opt} with Karlovitz number. The first two stations of flame E are not shown, as their γ^{opt} values are 0. The open red symbol represents flame C at $x/d = 45$, for which the average stoichiometric flame length is $x/d = 45.4$ (see Sec. 4.3.4); flame E at $x/d = 45$ has also been marked with an open symbol to highlight the large uncertainty of the γ^{opt} value at that location (see Sec. 4.6.4). Left: case RAD computed using l_F^{exp}; Right: case RAD computed using $l_{F,1}$ (blue), $l_{F,2}$ (green), $l_{F,3}$ (cyan), and $l_{F,4}$ (black). The solid black line represents the scaling given by Eq. (4.34).

a similar trend to the higher Reynolds number flames, significant differences are observed when the four expressions $l_{F,1}$, $l_{F,2}$, $l_{F,3}$, and $l_{F,4}$ are considered. More specifically, for all four expressions, the observed slope is much closer to the scaling $\gamma \propto Ka^{2/3}$, obtained from the flame length scale-based model for γ (see Ch. 4), with $l_{F,2}$ potentially being the closest. The reasons for this agreement should be investigated further using additional numerical data sets spanning a wide range of conditions.

7.3 Summary

In this chapter, the flamelet-based methodology to extract effective Lewis numbers discussed in Ch. 4, was applied to the DNS data base discussed in Chs. 5 and 6, and optimal flamelet parameters were extracted from cases BL, UL, and RAD.

The χ_{st}^{opt} and γ^{opt} values extracted from case RAD were found to follow the same trends observed for the parameters extracted from experimental data. Both the χ_{st}^{opt} and γ^{opt} values were found to under-estimate the corresponding experimental ones. Interestingly, the χ_{st}^{opt} values extracted from case RAD and flames C-E, were found to be ordered according to their respective jet Reynolds numbers.

The optimal χ_{st} values extracted from cases BL, UL, and RAD, were found to be all decreasing with axial distance, and to have a similar behavior. For the optimal γ values, cases BL and RAD were found to remain generally close. Unsurprisingly,

the γ^{opt} values for case UL were much larger than those for the other two cases. More specifically, γ^{opt} was found to increase rapidly from $x/d = 5$, and to reach its maximum value at $x/d = 15$, after which γ^{opt} remains large (it should be reminded that only discrete values in the range [0, 120] were considered for γ).

Next, the radial flame location, r_F, and the jet half-width, r_{12}, were analyzed for case RAD. While the r_F values for flames C-E can be considered to be flame-independent, the comparison with case RAD shows that this assumption is valid in flame B, only after normalization with respect to the stoichiometric flame tip. For r_{12}, case RAD, flames D and E, and the LES of Mueller *et al.* [148] (flame D), show once again that flame independence may be assumed in flame B if the downstream distance is normalized by the stoichiometric flame tip. While no velocity data is available for flame C, flame independence of r_{12} may be assumed, since its Reynolds number is intermediate between flame B and flames D and E.

Significant differences were found for u'/U_{jet} from case RAD, when compared to flames D and E (experiments and LES of Mueller *et al.* [148]). That is unsurprising, given the low Reynolds number in flame B. To assess this further, radial profiles of the mean and rms velocity from case RAD were compared to available measurements for flames D and E. The radial profiles of mean velocity from case RAD were found to be close to flames D and E, once normalized by the centerline value. However, the comparison of the radial profiles of rms velocity, showed that the fluctuation levels in case RAD at r_F are substantially lower than in flames D and E, up to $x/d = 30$.

In Ch. 4, the integral length scale, $l \equiv u'^3/\varepsilon$, was computed at r_F for all flames from a linear fit to values estimated for flames D and E, using scalings for self-similar jets. These values were then used for flames B-E. To investigate the validity of this assumption for flame B, the integral length scale was computed for case RAD, using directly its definition. A comparison of l/r_{12} at r_F from case RAD with the fit showed substantial differences, especially for $x/d \lessapprox 30$. To investigate this further, radial profiles of l/r_{12} were computed from case RAD for several downstream stations. As reference, the l/r_{12} values expected for fully developed turbulent pipe flows and self-similar round jets, were considered. The first three stations were found to be relatively close to the pipe flow scalings, with $x/d = 7.5$ being the closest, while the l/r_{12} profile at $x/d = 45$ was found to be closer to the jet scaling.

Given the differences between case RAD and the higher Reynolds number flames, the local Reynolds number was re-computed for flame B using case RAD. The γ^{opt}

values from case RAD were plotted with the Re_T values, at the radial flame location r_F. As a result of the differences for the u' and l values from case RAD compared to the fits for the higher Reynolds number flames, the slope of γ^{opt} was found to be lower than that of flames C-E. Similarly to the trends from the experiments, these values were found to not fall within the range estimated from the coefficient of Eq. (4.15).

Several approaches were considered to compute the flame thickness. While the γ^{opt} *vs.* Ka profile obtained from case RAD using l_F^{exp} was found to present a similar trend to the higher Reynolds number flames, significant differences were observed when the four expressions $l_{F,1}$, $l_{F,2}$, $l_{F,3}$, and $l_{F,4}$ were considered. For all four expressions, the observed slope was much closer to the scaling $\gamma \propto Ka^{2/3}$ (see Ch. 4), with $l_{F,2}$ potentially being the closest. The reasons for this agreement should be investigated further using additional DNS data sets spanning a wide range of conditions.

Chapter 8

CONCLUSIONS AND OUTLOOK

In this work, progress was made towards the correct modeling of differential diffusion, both for resolved simulations, and for reduced-order combustion models.

8.1 Assessment of the constant Lewis number assumption

The validity of the constant non-unity Lewis number assumption in chemically reacting flows was investigated by considering three different flames, spanning a wide range of conditions and displaying strong differential diffusion effects. The chosen flames were the following. First, a thermo-diffusively unstable, premixed H_2/air flame with an equivalence ratio $\phi = 0.4$ was considered. The fuel Lewis number for this flame is less than one. Two geometries were investigated, including a laminar two-dimensional flame and a moderately turbulent three-dimensional one. Second, a highly turbulent, premixed n-C_7H_{16}/air flame, with a fuel Lewis number larger than one was investigated. Finally, a laminar N_2-diluted C_2H_4/air-coflow pressurized diffusion flame was selected, with the goal of investigating the effect of the constant non-unity Lewis number approximation on the formation and evolution of key soot precursor species. For this flame, the fuel Lewis number is close to one.

For all flames, four cases were considered, including one with unity Lewis numbers, two with constant non-unity Lewis numbers, and a benchmark case with mixture-averaged properties. For the two constant non-unity Lewis number cases, the Lewis numbers were pre-computed using the solutions to the flamelet equations. Two methods were suggested to pre-compute the constant Lewis numbers from flamelets, including the peak species mass fraction location, and the peak temperature location.

For all configurations, it was shown that a good agreement with mixture-averaged transport properties can be achieved by using a set of constant non-unity Lewis numbers. For the chosen flames and the numerical framework, using a set of pre-computed constant Lewis numbers was found to have a minimal impact on the computational cost. Finally, the two constant non-unity Lewis number methods were shown to perform well, with neither consistently better than the other.

8.2 Effective Lewis numbers in turbulent non-premixed flames

A flamelet-based methodology was proposed to extract effective Lewis numbers from experimental and numerical data sets of turbulent non-premixed flames. This technique was applied to the "Sandia flames", a set of turbulent non-premixed methane/air jet flames of varying jet Reynolds numbers, with the exception of Sandia flame B. Effective Lewis numbers were extracted by comparing measured species mass fractions with solutions of the non-unity Lewis number flamelet equations. For each flame and each downstream location, two *optimal* flamelet parameters were extracted, including a stoichiometric scalar dissipation rate, χ_{st}^{opt}, and the ratio $\gamma^{opt} \equiv \alpha_T/\alpha$. The effective Lewis numbers for all species were computed using $\mathrm{Le}_{i,\mathrm{eff}} = (1 + \gamma^{opt})/(1/\mathrm{Le}_i + \gamma^{opt})$.

For the four turbulent flames considered, the χ_{st}^{opt} values were found to decrease with axial distance, and to increase with jet Reynolds number. The optimal χ_{st} values were found to be systematically larger than the available measured values. The effective Lewis numbers (γ^{opt}) were found to transition from their laminar values at the burner exit plane ($\gamma^{opt} \approx 0$), towards unity further downstream ($\gamma^{opt} \to \infty$).

Previously-suggested correlations for the parameter γ with both Reynolds and Karlovitz numbers were then compared to the extracted γ^{opt} values. However, large experimental uncertainties and the limited number of measured quantities prevented a conclusive assessment of these models.

8.3 Direct Numerical Simulation of Sandia flame B

A campaign of DNS of Sandia flame B ($\mathrm{Re}_{\mathrm{jet}} \approx 8200$) was carried out. The choice of Sandia flame B was motivated by three reasons. First, Sandia flame B has the lowest Reynolds number among the Sandia flames, while still being turbulent. Second, fewer measurements are available for this flame than the higher Reynolds number flames. Third, in Ch. 4, flame independence was assumed for several parameters, for the four flames B-E. The validity of this assumption could not be assessed for flames B and C, due to the limited data. This is particularly important for flame B, due to its relatively low Reynolds number.

To design the baseline computational grid, consisting of a cylindrical mesh with $1120 \times 224 \times 128$ ($\approx 32 \times 10^6$) grid points, both turbulence and the chemistry resolution requirements were considered. For the former, the jet was divided in a "pipe flow region" and a "main jet region". The grid was designed to satisfy $\Delta/\eta \lessapprox 3$, where $\Delta \equiv (r\Delta x \Delta r \Delta\theta)^{\frac{1}{3}}$ is a mean grid size. For the latter, a reaction zone thickness

based on the OH and CH radicals was defined, and chemistry resolution criteria available in the literature were considered.

A total of six simulations were carried out, including a baseline case (BL), three cases where the grid was refined twice in the axial (Res-x), radial (Res-r), and azimuthal (Res-z) directions, respectively, a unity-Lewis number case (UL) and a radiating case (RAD). The latter two cases were considered to isolate differential diffusion and radiation effects, respectively.

An *a posteriori* assessment for the base of the jet, where the smallest scales are expected to be found, showed that the ratio Δ/η is approximately less than 3. For the same region, the number of grid points through the averaged OH and CH layers (defined using a 10% of the peak value) was found to satisfy criteria suggested in the literature.

Comparisons of radial velocity profiles from the baseline and refined cases, showed a good agreement for the base of the jet. Moving downstream, some differences in the centerline region were observed. 95% confidence intervals for the mean values at the centerline, suggest that most of these differences can be attributed to the limited run time of the refined cases compared to the baseline case ($45.5d/U_{\text{jet}}$ and $243.0d/U_{\text{jet}}$ units of simulation time, respectively).

A comparison of the radial profiles of the OH and CH mass fractions was also carried out. For all downstream locations considered, the instantaneous profiles suggest that a sufficient number of grid points was used. Comparisons of mean and rms profiles of OH from case BL and the refined cases showed an excellent agreement for $x/d = 1$. Moving downstream, small shape and magnitude differences were observed, for both mean and rms profiles. The largest differences were observed near the centerline for the last station considered, $x/d = 45$. While the mean CH profiles are in excellent agreement for the first station, some shape and magnitude differences were observed for the other stations. The rms profiles for the CH mass fraction showed some differences for all stations considered.

Centerline velocity and mixture fraction statistics for case BL and the refined cases were considered. The mean profiles were found to be in good agreement at the base of the jet ($x/d \lessapprox 15$), and small differences were observed moving downstream up to $x/d \approx 45$. Beyond that location, large differences between case BL and the refined cases were observed. For $x/d < 45$, the largest differences were observed between cases BL and Res-x. While the estimated 95% confidence intervals for

the sampling errors were observed to include most of these differences, small grid effects could not be ruled out. To assess this further, conditional statistics were considered, as discussed below. The large differences observed beyond $x/d \approx 45$ were found to be due to the limited run time of the refined cases, compared to case BL.

To assess if the differences between case BL and refined cases observed for the unconditional statistics are caused by grid effects, conditional means and standard deviations for several species were considered along the centerline and for cross-stream planes. These include the radicals OH and CH, and two of the species considered in the error map analysis discussed in Ch. 4. The conditional mean statistics from case BL and the refined cases, were found to be in excellent agreement for all stations considered. Small differences were visible only for the CH conditional standard deviations from case Ref-x, compared to the other cases. These comparisons suggest that the chosen grid resolution is adequate for the analysis carried out in Ch. 7.

Centerline statistics for all quantities stored in data files were observed to have oscillations whose wavelength was found to be approximately $\lambda_{os}(x) \approx \langle U(x) \rangle \Delta t_{\text{save}}$. For the refined cases, whose Δt_{save} was set to be $1/5$ of that used for cases BL, RAD, and UL, centerline oscillations at a much reduced amplitude and wavelength were observed. More precisely, $\lambda_{os}(x)$ for the refined cases was found to be approximately $1/5$ of $\lambda_{os}(x)$ for case BL ($\lambda_{os}(x)$ for all three cases BL, RAD, and UL was found to approximately the same). However, it was shown that the same oscillations of the baseline case can be recovered from each of the refined cases, if every fifth data file is considered to compute the statistics. These oscillations were found to rapidly decay with radial distance from the centerline, which was ascribed to the effect of azimuthal averaging. Finally, conditional statistics from the refined cases, computed using every data file and every fifth data file, showed not differences, suggesting that these centerline oscillations have no impact on the analysis carried out in Ch. 7.

8.4 Validation with experimental data

The DNS data was then validated using available experimental data. The impacts of radiation heat loss and differential diffusion were systematically isolated by comparing cases BL and RAD, and BL and UL, respectively.

Favre mean and rms scalars from case RAD at $x/d = 15$ and $x/d = 30$ were found to be in very good agreement with the experiments, suggesting that the boundary conditions are correct, and that the modeling of the pilot flame through a top-hat velocity profile is adequate. Further, differences between cases BL and RAD showed that, for flame B, radiation heat loss impacts the mixing field.

The centerline Favre-average mixture fraction from cases RAD and BL was compared to experimental data for flames B-F (a single data point is available for flame B), and the LES data of Mueller *et al.* [177] for flame D. Compared to the higher Reynolds number flames, flame B was found to have an elongated structure. The effects of radiation heat loss were not sufficient to explain this elongated structure.

Comparisons of cases BL, RAD, and UL, and the experiments were carried out for $x/d = 15$ and $x/d = 30$. Both both stations, case RAD was found to be in very good agreement with the experiments. Neglecting radiation heat losses was found to result in an increase of the peak temperature of about 70K, and over-prediction of the CO and H_2 mass fractions. Neglecting differential diffusion effects was found to result in an increase of the peak temperature of about 110K, and over-prediction of the H_2O, CO, and H_2 mass fractions. Differential diffusion was found to have a greater impact on the flame structure than radiation heat loss.

The comparison of conditional probability densities showed that case RAD was found to be in good agreement with experimental measurements, once the effect of measurement noise is taken into account.

Following Barlow *et al.* [46], a differential diffusion parameter z was computed for the four downstream locations $x/d = 7.5,\ 15,\ 30,\ 45$. For the sake of comparison to experiments, the same species mass fractions were considered, including the interference correction discussed in Ch. 4. The comparisons with experiments showed an excellent agreement for $x/d = 15$ and a good agreement for $x/d = 30$. Cases BL and RAD were found to have negligible differences at $x/d = 15$, and small differences at $x/d = 30$. Due to the effect of the missing species, case UL was found to be non-zero at all four downstream locations.

Scalar dissipation statistics were also compared to measurements available for the higher Reynolds number flames (flames C-E). Significant shape differences were found between case RAD and flames C-E. However, once normalized by the fuel pipe inner diameter and jet bulk velocity, the stoichiometric scalar dissipation rate was found to compare well with flames C-E. The one-dimensional scalar dissipation

rate profiles were found to be generally closer to flames C-E. Finally, conditional probability densities of the logarithm of the scalar dissipation from case RAD were compared to flames C-E. The scalar dissipation in case RAD was found to be approximately log-normal, with a shape that remains more peaked than for flames C-E, as downstream distance is increased. Standard deviations from the log-normal fits to these cpdf's were found to increase with downstream distance and Reynolds number. Further, these standard deviations were found to approximately collapse onto a single curve, when plotted with $\mathrm{Re}_{\mathrm{jet}}(x/d)^{1/2}$.

To conclude, the choice of grid resolution, chemical model, and boundary conditions for the DNS was found to be adequate to reproduce experimental measurements with high fidelity, once radiation heat losses and differential diffusion were included.

8.5 Analysis of effective Lewis numbers for the DNS of Sandia flame B

The flamelet-based methodology to extract effective Lewis numbers discussed in Ch. 4 was applied to the DNS data base. Optimal flamelet parameters were extracted from cases BL, UL, and RAD, and compared to those extracted from the experimental data of flames B-E.

The χ_{st}^{opt} and γ^{opt} values extracted from case RAD, were found to follow the same trends observed for the optimal parameters computed from the experimental data. More specifically, the χ_{st}^{opt} values were found to decrease with downstream distance, and the γ^{opt} values were found to increase. A comparison between the optimal flamelet solution and case RAD at $x/d = 30$ was found to generally be in good agreement with the flame structure. Both optimal parameters from case RAD were found to under-estimate the corresponding values computed from the experimental data of Sandia flame B. Interestingly, the χ_{st}^{opt} values from case RAD and flames C-E, were found to be ordered according to the respective jet Reynolds number.

The comparison of the optimal χ_{st} extracted from cases BL, UL, and RAD shows the same behavior across all three cases. For the optimal γ values, cases BL and RAD were found to remain generally close, suggesting that radiation heat losses have a secondary effect. Unsurprisingly, the γ^{opt} values for case UL were much larger than those for the other two cases.

In Ch. 4, flame-independence was assumed for both the radial flame location r_F and the jet half-width r_{12}, across all four flames B-E. However, the validity of this assumption could not be investigated for flame B, for which scalar measurements

are available only for $x/d = 15$ and $x/d = 30$, and no velocity data is available. To assess the validity of this assumption for flame B, case RAD was compared to experimental and LES data for the higher Reynolds number flames. The comparisons showed that flame independence for both r_F and r_{12} may be assumed in flame B only after normalization by the stoichiometric flame tip.

Flame independence was also assumed for $u'/\mathrm{U_{jet}}$ and l/r_{12}, both evaluated at r_F. The $u'/\mathrm{U_{jet}}$ profile from case RAD was found to differ significantly from the values for flames D and E (measurements of Schneider *et al.* [129] and LES of Mueller *et al.* [148]). That is surprising, given the low Reynolds number of flame B. While the mean radial velocity profiles from case RAD were found to be close to flames D and E, once normalized by the centerline value, the normalized rms velocity profiles were found to be significantly different for the first three stations considered ($x/d = 7.5,\ 15,\ 30$). More specifically, the rms values in case RAD at r_F were substantially lower than in flames D and E, up to $x/d = 30$.

In Ch. 4, the $l \equiv u'^3/\varepsilon$ values at r_F were estimated for flames B-E using scalings for self-similar isothermal jets. In Ch. 7, the validity of this assumption for flame B was assessed by computing l directly from its definition, using data from case RAD. As expected, the comparison showed substantial differences, especially for $x/d \lessapprox 30$. Radial profiles of l/r_{12} from case RAD were found to be significantly different from the reported scalings for self-similar round jets.

Given these observations, the local Reynolds number was re-computed for flame B using case RAD directly, instead of the fits for u'/U_{jet} and l/r_{12} discussed in Ch. 4. Similarly to the values extracted from experiments, the γ^{opt} values from case RAD were found to be positively correlated with the local Reynolds number. Yet, a collapse within the range of values estimated from the $\gamma = a^{\mathrm{Re_T}}\mathrm{Re_T}$ scaling was not observed.

Several approaches were considered to compute the flame thickness. In Ch. 4, the flame thickness was estimated for all flames using the extracted χ_{st}^{opt} values. This estimate for the flame thickness, referred to as l_F^{exp}, was found to significantly underestimate the values computed using the four expressions $l_{F,1}$, $l_{F,2}$, $l_{F,3}$, and $l_{F,4}$, which were observed to be generally more representative of the normalized $\langle Z \rangle$ radial profiles found in the jet flame.

While the γ^{opt} *vs.* Ka profile obtained from case RAD using l_F^{exp} was found to present a similar trend to the profiles for the higher Reynolds number flames, sig-

nificant differences were observed when the Karlovtiz number for case RAD was recomputed using the four expressions $l_{F,1}$, $l_{F,2}$, $l_{F,3}$, and $l_{F,4}$. For all four expressions, the observed slope was much closer to the scaling $\gamma \propto Ka^{2/3}$ (see Ch. 4), with $l_{F,2}$ potentially being the closest. While encouraging, the reasons for this observation should be investigated further using additional numerical data sets spanning a wide range of conditions.

8.6 Limitations and directions for future work

In this section, directions for future work are proposed.

8.6.1 Direct Numerical Simulations of Sandia flame B

In Chs. 5 and 6 a campaign of DNS of Sandia flame B was discussed. The analysis revealed several difficulties associated with the grid design process. First, there is a lack of DNS studies of jet flames with detailed *a priori* discussions of the grid design, combined with extensive *a posteriori* assessments. Second, there is limited work towards the development of general grid resolution criteria which can be applied to the present configuration.

The *a posteriori* tests carried out in Ch. 5 suggest that satisfying the criterion $\Delta/\eta < 3$ is sufficient for the goals of the present work. However, it is not suggested here that this approach is valid in general. For instance, a potential issue of using the mean grid size Δ to design non-uniform grids, is that it masks the aspect ratio of the cells. This issue should be investigated as part of future work. The impact of the Δ/η criterion on statistics of interest should also be analyzed, and alternative definitions for the mean grid size should be considered, such as $\Delta \equiv [\Delta x^2 + \Delta r^2 + (r\Delta\theta)^2]^{1/2}$.

8.6.2 Assessment of the flamelet assumptions

The flamelet-based methodology developed in Ch. 4 relies on several important assumptions. In that framework, it is assumed that a single one-dimensional, flat, steady-state, adiabatic, non-unity Lewis number flamelet can represent the conditional mean flame structure of a turbulent non-premixed flame, provided that the two parameters χ_{st} and γ are chosen properly. These assumptions are briefly reviewed, and directions for future work are proposed.

Mixture fraction-dependence of the optimal flamelet parameters

The cross-stream dependence of the optimal flamelet parameters is prescribed *a priori*. Two issues can be identified. First, γ and $\mathrm{Le}_{i,\mathrm{eff}}$ are assumed to be constant in mixture fraction space, and only vary with downstream distance for a given flame. While this may be valid as a first approximation, significantly different turbulence levels are expected to be found across the mixture fraction range at any downstream location of a turbulent non-premixed jet flame. Consequently, γ and $\mathrm{Le}_{i,\mathrm{eff}}$ should be representative of this. Analogously, the shape of the scalar dissipation rate $\chi(Z)$ was prescribed *a priori* in Eq. (4.4), and only its stoichiometric value was allowed to vary with downstream distance. While this approach should be intended as a first approximation for the present analysis, common expressions used for the $\chi(Z)$ profiles are not fully representative of piloted jet flames [23, 179]. Thus, future work should investigate this issue further. As a possible next step in the analysis, the conditional mean Favre scalar dissipation rate profiles from experimental or numerical data should be used.

Species-dependence of the optimal flamelet parameters

In Ch. 4, six measured species were considered to extract the optimal flamelet parameters. These same species were also considered when analyzing the DNS data in Ch. 7, for consistency. As part of future work, the effect of the choice of the species on the error map analysis should be investigated further.

In this work, as a first step, it is assumed that the γ^{opt} values are species-independent. In other terms, for each flame and each downstream location, a single γ^{opt} value is used to determine the effective Lewis numbers for all species. The validity of this assumption should be assessed as part of future work.

Multi-dimensional terms in the flamelet equations

The optimal χ_{st} parameters were found to be systematically larger than the $\langle\chi|\mathrm{Z}_{\mathrm{TNF},st}\rangle$ values (see Ch. 4). While multiple reasons could explain this difference, it should be reminded that, in the present approach, a single, one-dimensional, steady-state flamelet is used to represent the conditional mean flame structure. Thus, it is expected that both optimal parameters χ_{st} and γ^{opt} are also representative of any effect not adequately represented by this approximation. For instance, it is expected that multi-dimensional effects, including convective and diffusive transport along the mixture fraction iso-surfaces, are essentially lumped into the effec-

tive χ^{opt}. These multi-dimensional effects should be systematically characterized through a budget analysis using DNS data.

Representing the conditional mean flame structure

Even without considering multi-dimensional effects, there remains the issue of representing the conditional mean flame structure using a single flamelet. If χ is parameterized by χ_{st}, then an average of flamelet solutions corresponding to a distribution of χ_{st} values should be compared to the conditional mean flame structure. As discussed by Peters [10], an alternative approach is to replace this distribution with a delta function at the Favre mean value $\widetilde{\chi}$. The validity of this assumption should also be systematically assessed through a budget analysis using DNS data.

Flamelet modeling of radiation effects

In the present flamelet formulation, radiation heat losses are not included. While Fig. 7.5 suggests that the impact of radiation on the present analysis is secondary, it should nonetheless be quantified more systematically.

8.6.3 *A posteriori* assessment of models for γ

The purpose of the analysis carried out in Chs. 4, 5, 6, and 7, is to make progress towards the correct *a priori* modeling of differential diffusion effects in turbulent non-premixed flames. As part of future work, these models should be assessed *a posteriori* in several steps. First, tabulated chemistry DNS of the same flames used to develop these *a priori* models, should be carried out. The flamelet tables should contain an additional dimension to account for γ. Next LES of flames at varying Reynolds numbers should also be considered.

Appendix A

FLAME THICKNESS AND TIME SCALE

To define a flame thickness, l_F, a one-dimensional unsteady laminar mixing layer is considered, where infinite amounts of fuel and oxidizer, initially separated, are allowed to diffuse [10]. The corresponding similarity solution is

$$Z(\xi) = \frac{1}{2}\,\mathrm{erfc}\,(\xi)\,, \tag{A.1}$$

where ξ is the similarity variable. The profile given by Eq. (A.1) can be approximated as

$$Z(y) \approx \frac{1}{2}\left[1 - \tanh\left(\frac{y}{h}\right)\right], \tag{A.2}$$

where y is a flame-normal coordinate and h is a scaling length such that Eq. (A.2) approximates Eq. (A.1). A flame thickness may be defined as

$$l_F \equiv 2h, \tag{A.3}$$

which can be rewritten as

$$l_F = 4\frac{Z(1-Z)}{|\nabla Z|}. \tag{A.4}$$

A flame time scale, τ_F, is defined such that $l_F = \sqrt{4\alpha\tau_F}$, which leads to the following expression

$$\tau_F = 8\frac{Z^2(1-Z)^2}{\chi(Z)}. \tag{A.5}$$

It should be noted that Eqs. (A.4) and (A.5) are independent of Z.

Appendix B

OVERVIEW OF MEASUREMENT DATA FOR THE SANDIA FLAMES

B.1 The TNF Workshop

The International Workshop on Measurement and Computation of Turbulent Non-premixed Flames (TNF) has been established to better coordinate research efforts in turbulent non-premixed and partially premixed combustion [72], with an emphasis on turbulence-chemistry interaction [180]. As such, a growing set of burners and flames with well defined boundary and operating conditions has been developed and organized within the framework of the Workshop.

One of the more popular datasets is represented by the so-called "Sandia flames", a set of six non-premixed piloted CH_4/air jet flames of increasing Reynolds number (labeled A-F), from laminar to turbulent [71]. The burner was developed by

Flame	A		B		C		D		E		F	
Re_{jet}	~1100 (laminar)		~8200 (transitional)		~13400 (turbulent)		~22400 (turbulent)		~33600 (turbulent)		~44800 (turbulent)	
type / x/d	scal.	vel.	scal.	vel.	scal.	vel.	scal.	vel.	scal.	vel.	scal.	vel.
1/7.2	✗	✗	✗	✗	✗	✗	✗	✓	✗	✓	✗	✓
1	✗	✗	✗	✗	✓	✗	✓	✓	✓	✗	✓	✓
2	✗	✗	✗	✗	✓	✗	✓	✓	✓	✗	✓	✓
3	✗	✗	✗	✗	✓	✗	✓	✓	✓	✗	✓	✓
5	✓	✗	✗	✗	✗	✗	✗	✗	✗	✗	✗	✗
7.5	✗	✗	✗	✗	✓	✗	✓	✓	✓	✗	✓	✓
10	✓	✗	✗	✗	✗	✗	✗	✗	✗	✗	✗	✗
15	✗	✗	✓	✗	✓	✗	✓	✓	✓	✓	✓	✓
30	✗	✗	✓	✗	✓	✗	✓	✓	✓	✗	✓	✓
45	✗	✗	✗	✗	✓	✗	✓	✓	✓	✓	✓	✓
60	✗	✗	✗	✗	✓	✗	✓	✓	✓	✗	✓	✓
75	✗	✗	✗	✗	✓	✗	✓	✗	✓	✗	✓	✗
centerline	✗	✗	✗	✗	✓	✗	✓	✓	✓	✓	✓	✓

Table B.1: Synoptic table of scalar and velocity experimental data for the Sandia flames [72]. Available data: ✓; missing data: ✗. It should be noted that the same velocity measurements are reported for flames D-F [129], but only the ones shown above are available.

Bilger and co-workers at Sydney University [126, 127] with the intent of isolating turbulence-chemistry interaction effects [180], using a simple geometry and chemistry. This well-characterized dataset is often the target of choice in modeling studies, as it spans a wide range of jet Reynolds numbers, and has well-defined boundary and operating conditions [61].

Model development has typically focused on the higher Reynolds number flames (D-F), for which neglecting differential diffusion effects was found to be a reasonable approximation [23, 46, 180]. As a result, a richer set of experimental data exists for these flames, while fewer measurements are available for flames A-C [72].

B.2 Scalar and velocity measurements

Scalar and velocity measurements available for the Sandia flames [72] are listed in Table B.1. As can be seen, velocity data [129] is available for the higher Reynolds number flames (D-F), but not for flames (A-C). Further, most scalar measurements are available for flames (C-F). The measured scalars and the respective uncertainties are shown in Table 4.2.

Appendix C

SANDIA FLAME A

Sandia flame A is laminar and steady, and can be easily simulated. It has the same chemistry and the same burner geometry of the higher Reynolds number flames, and can be used to investigate the effect of modeling choices. In this appendix, Sandia flame A is considered to investigate the effects of radiation heat loss, thermal diffusion, and an alternative choice for the chemical model. For this flame, experimental measurements are available for $x/d = 5$ and $x/d = 10$ only [71]. For each plot the reported scalar uncertainties are shown [46, 123].

C.1 Chosen test cases

The chosen test cases are listed in Table C.1. These include a baseline case, ABL, a radiating case, ARAD, a case with the CaltechMech2.4 [111] chemical model, ACM, a case with thermal diffusion, ATD, and a case with both radiation and thermal diffusion, ARAD+TD.

In the following sections, each of the cases ARAD, ACM, ATD and ARAD+TD will be compared to the baseline case. The comparisons will include the temperature, two product species, H_2O and CO_2, and two intermediates, CO and H_2. Favre-average profiles will be considered to investigate the effect on the hydrodynamic field, and conditional averages will be used to assess the effect on the flame structure.

	Case				
Model	ABL	ARAD	ACM	ATD	ARAD+TD
GRIMech3.0	✓	✓	✓	✗	✓
Radiation	✗	✓	✗	✗	✓
CaltechMech2.4	✗	✗	✓	✗	✗
Soret & Dufour	✗	✗	✗	✓	✓
Mix.-av. transp. prop.	✓	✓	✓	✓	✓

Table C.1: Sandia flame A test cases: ABL, baseline case; ARAD, radiation case; ACM, CaltechMech2.4 case; ATD, thermo-diffusion case; ARAD+TD, radiation and thermo-diffusion case.

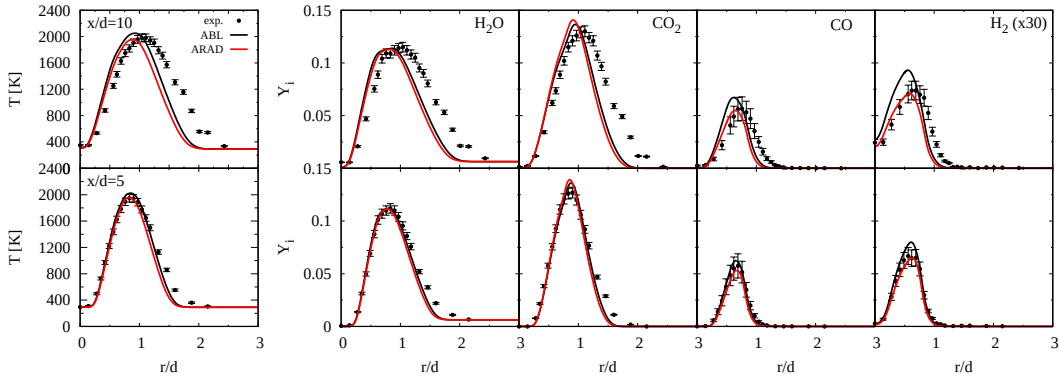

Figure C.1: Comparison of Favre-average temperature (left) and species mass fractions (right). Symbols: experiments; black line, ABL; red line, ARAD.

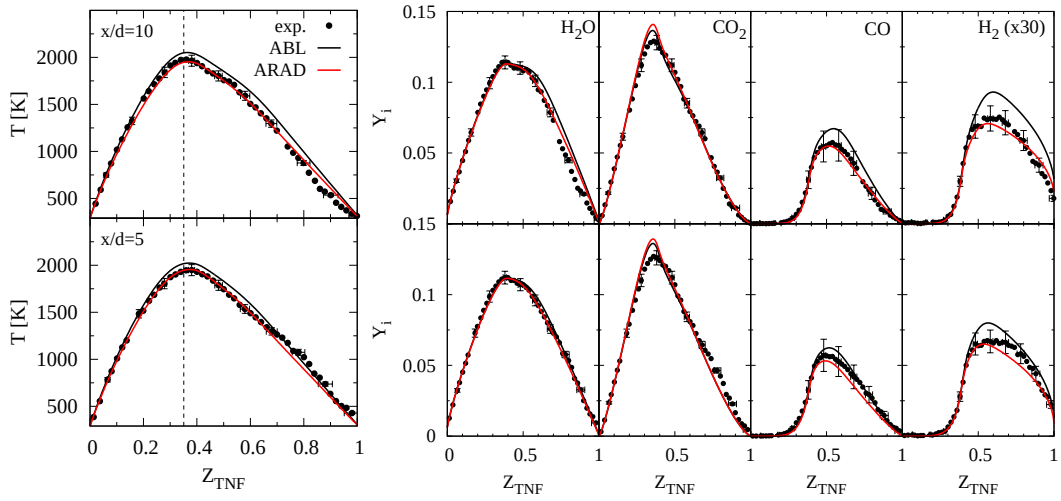

Figure C.2: Comparison of temperature (left) and species mass fractions (right), conditioned on the measured mixture fraction, Z_{TNF}. Symbols: experiments; black line, ABL; red line, ARAD. The vertical dashed line represents the stoichiometric mixture.

C.2 Effect of radiation heat loss

In this section, the effect of radiation is isolated by comparing case ARAD to case ABL. Figure C.1 compares Favre-average radial profiles of temperature and species mass fractions at $x/d = 5$ and $x/d = 10$. For the first station, both cases predict the radial location of the flame, with case ARAD generally in better agreement with the experiments than case ABL. At $x/d = 10$, both cases predict a narrower flame than the experiments. Case ARAD better predicts the peak mass fractions of CO and H_2. Figure C.2 shows comparisons of conditional mean temperature and species mass fraction profiles. As can be seen, the temperature from case ARAD is in excellent agreement with the experiments. Including radiation also improves the prediction of the conditional species profiles, at both downstream stations.

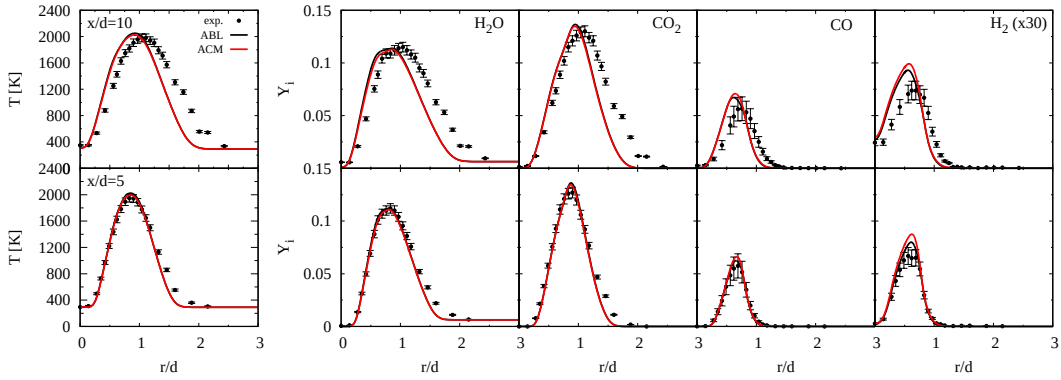

Figure C.3: Comparison of Favre-average temperature (left) and species mass fractions (right). Symbols: experiments; black line, ABL; red line, ACM.

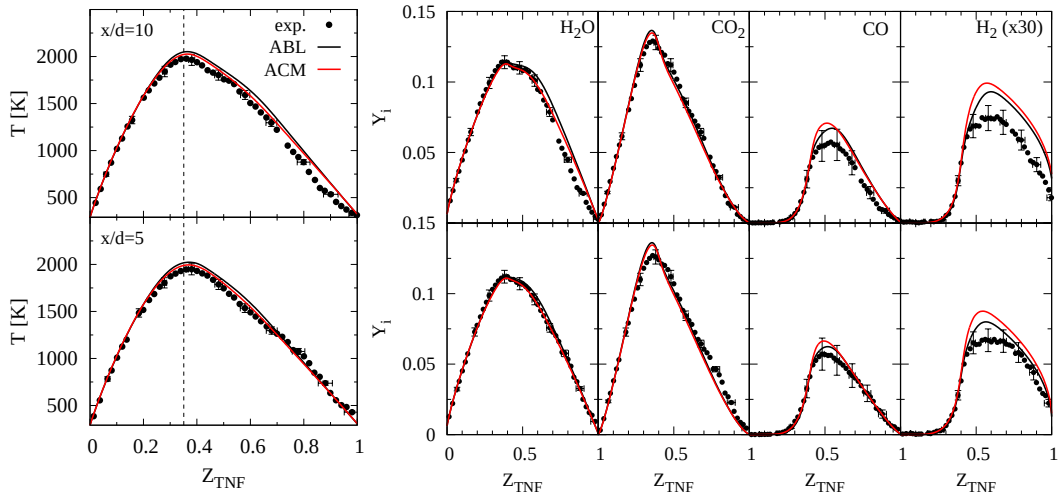

Figure C.4: Comparison of temperature (left) and species mass fractions (right), conditioned on the measured mixture fraction. Symbols: experiments; black line: ABL; red line: ACM.

C.3 Comparison of chemical models

To investigate the effect of the choice of the chemical model, Sandia flame A is simulated both using GRIMech3.0 [135] and a version of the CaltechMech2.4 [111] chemical model without the soot chemistry, which includes a total of 171 species and 1894 reactions (forward and backward reaction counted separately). From Figs. C.3 and C.4 it can be seen that the two chemical models lead to very similar results, with only minor differences.

C.4 Effect of thermal diffusion

Thermal diffusion includes the species flux due to temperature gradients (Soret effect), and the energy flux due to species gradients (Dufour effect). In simulations of

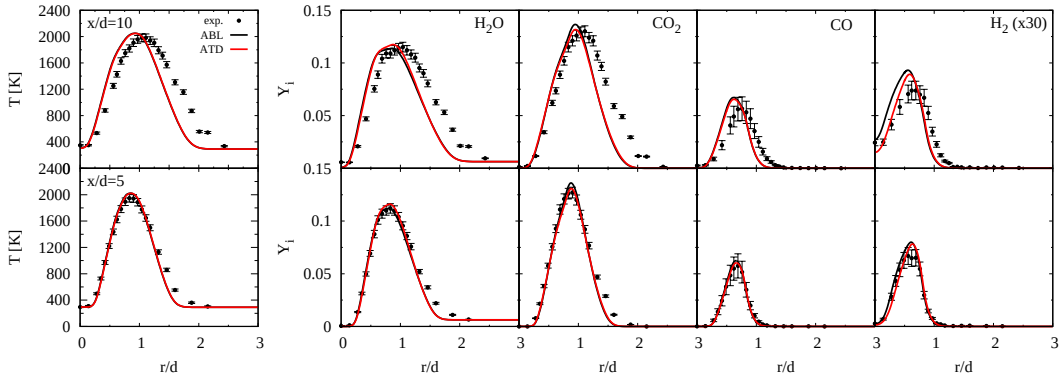

Figure C.5: Comparison of Favre-average temperature (left) and species mass fractions (right). Symbols: experiments; black line, ABL; red line, ATD.

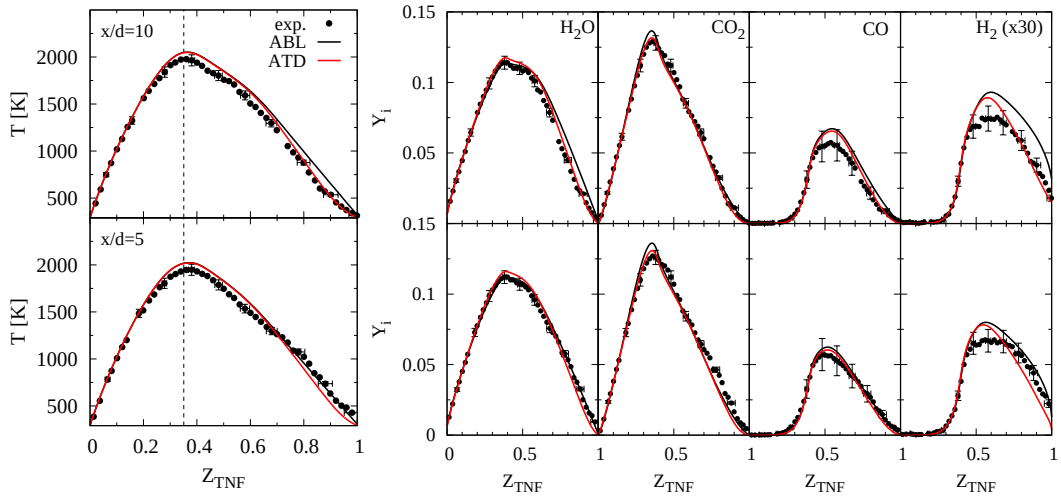

Figure C.6: Comparison of temperature (left) and species mass fractions (right), conditioned on the measured mixture fraction. Symbols: experiments; black line, ABL; red line, ATD.

hydrocarbon flames, it is common practice to neglect thermal diffusion. Here, the impact of this assumption is assessed for flame A.

C.4.1 Modeling of thermal diffusion

Using the mixture-averaged model of Chapman and Cowling [181], thermal diffusion is included by means of an additional term to the species diffusion flux $\boldsymbol{j}_i$

$$- D_i^T \frac{\nabla T}{T}, \tag{C.1}$$

where the D_i^T are the species thermal diffusion coefficients. Following Paul and Warnatz [182], the coefficients D_i^T can be rewritten as

$$D_i^T = \rho \frac{W_i}{W} D_{i,m} k_{Ti}, \tag{C.2}$$

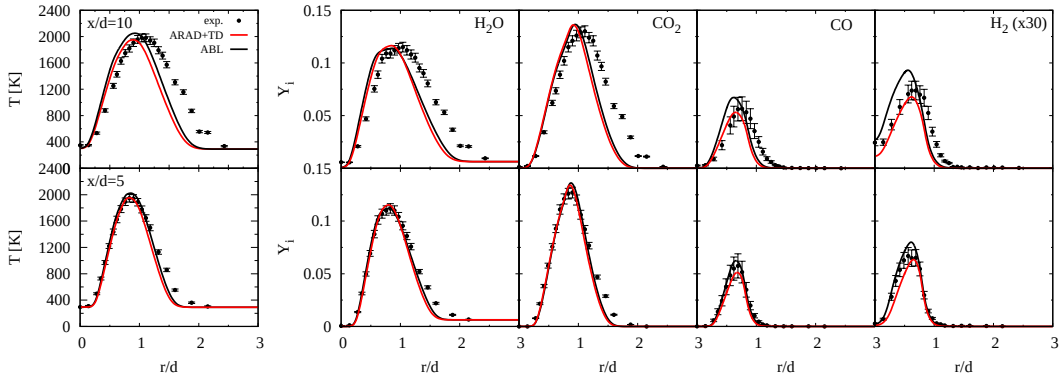

Figure C.7: Comparison of Favre-average temperature (left) and species mass fractions (right). Symbols: experiments; black line, ABL; red line, ARAD+TD.

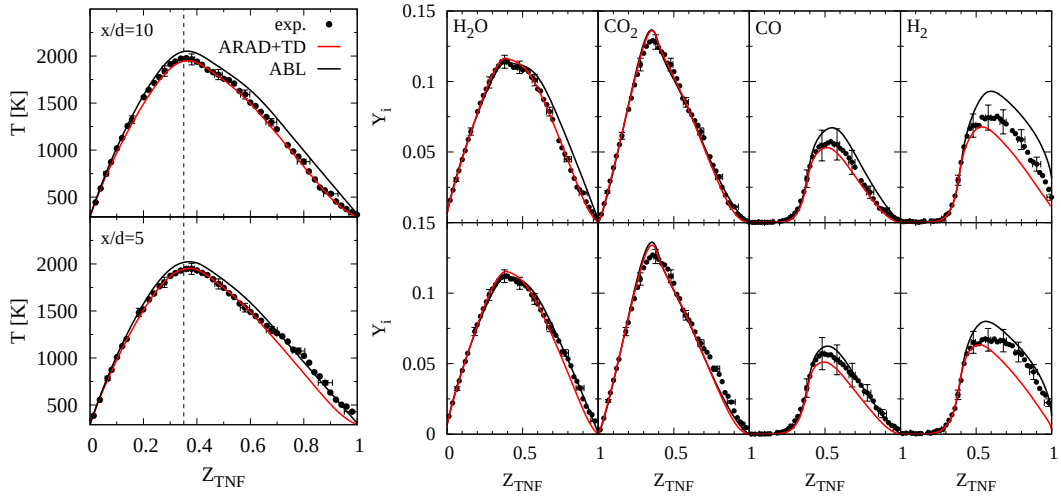

Figure C.8: Comparison of temperature (left) and species mass fractions (right), conditioned on the measured mixture fraction. Symbols: experiments; black line, ABL; red line, ARAD+TD.

where k_{Ti} is the ith species thermal diffusion ratio [181]. A more detailed description of the coefficients k_{Ti} may be found in Schlup & Blanquart [183]. With the extra flux given by Eq. (C.2), an additional term must be considered for the correction velocity given by Eq. (1.4) [183]

$$\boldsymbol{u}_c^T = \frac{1}{\rho}\frac{\nabla T}{T}\sum_i D_i^T . \tag{C.3}$$

C.4.2 Comparisons

Figure C.5 shows Favre-average radial profiles, where it can be seen that thermal diffusion has only a small impact on the scalars. As excepted, the largest effect is on the rich side of the mixture, where H_2 has the largest concentration. This can be seen more clearly from the conditional averages shown in Fig. C.6. The scalar

profiles in cases ABL and ATD differ for $Z_{\mathrm{TNF}} \gtrapprox 0.7$, and the largest impact is for H_2.

C.5 Effect of radiation and thermal diffusion

In this section, the combined effects of radiation and thermal diffusion are investigated. Figure C.7 shows a comparison of Favre-average scalar profiles, and Fig. C.8 shows the same quantities conditioned on the measured mixture fraction. As can be seen, including radiation and thermal diffusion generally improves comparisons with experiments. The H_2 mass fraction from case ARAD+TD significantly underestimates the experimental measurements for $Z_{\mathrm{TNF}} \gtrapprox 0.5$.

Appendix D

QUASI STEADY STATE ASSUMPTION

For DNS on turbulent jet flames, it is common to reduce the cost associated with the chemistry thorough various mechanism dimension reduction techniques [8], such as skeletal reduction [184], lumping of chemical species, reaction pathways and species diffusivities [185], quasi-steady-state (QSS) and partial equilibrium reaction (PE) approximations [186], to name a few. However, these techniques require some form of error propagation control, and were not adopted in this work.

In Ch. 5, the OH and CH layers are considered to assess the grid resolution. However, for many species with small chemical timescales (such as radicals), the Quasi Steady State Assumption (QSSA) proves to be a valid approximation [187]. For these species, which typically are present only in thin layers, transport equations need not be solved. This removes stiffness from the integration of the chemical source term [8], and allows the use of coarser meshes. For all these reasons, the QSSA is a common mechanism reduction technique for DNS of turbulent flames [172].

With the QSSA, algebraic expressions can be found for the species. In Fig. D.1 the expression for the OH mass fraction is compared to the values from case BL

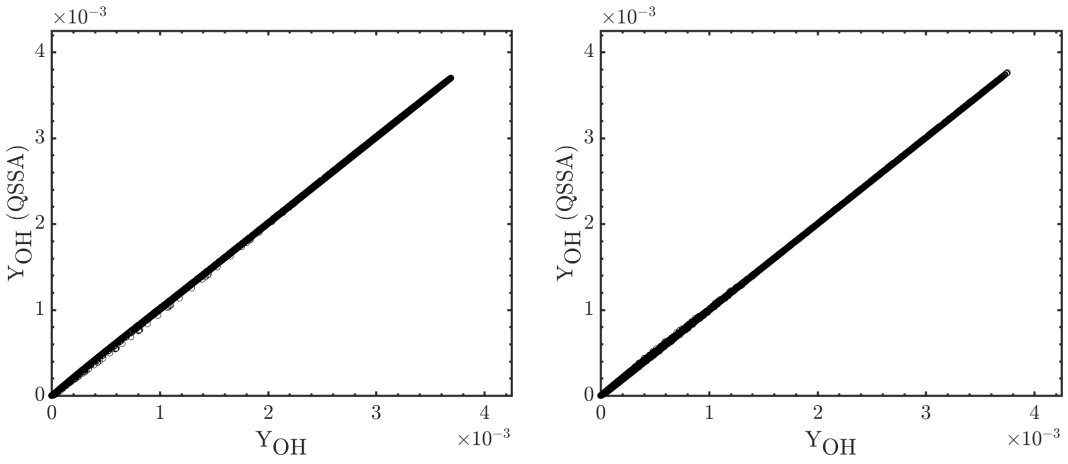

(a) $x/d = 1$. **(b)** $x/d = 10$.

Figure D.1: Scatter plots of OH mass fraction computed using the QSSA against its value from case BL. Species for which the QSSA is valid are expected to collapse onto the line $y = x$.

for the two stations $x/d = 1$ and $x/d = 10$. The base of the jet, where diffusion and convective time scales are expected to be the smallest, can be considered as a worst-case-scenario to test the QSSA. As can be seen, this approximation is valid for OH (that is also the case for CH).

BIBLIOGRAPHY

[1] World Energy Model. https://www.shell.com/energy-and-innovation/the-energy-future/scenarios/shell-scenarios-energy-models/world-energy-model/. 2017.

[2] J. Conti et al. International Energy Outlook 2016 With Projections to 2040. Tech. rep. USDOE Energy Information Administration (EIA), Washington, DC (United States). Office of Energy Analysis, 2016.

[3] J. Tollefson. Atmospheric science: Climate's smoky spectre. *Nature* 460.7251 (2009), pp. 29–32.

[4] Heath and Environment. https://www.epa.gov/pm-pollution.

[5] T. Nicolai et al. Urban traffic and pollutant exposure related to respiratory outcomes and atopy in a large sample of children. *Eur. Respir. J.* 21.6 (2003), pp. 956–963.

[6] T. R. Skopek et al. Mutation of human cells by kerosene soot. *J. Nat. Cancer Inst.* 63.2 (1979), pp. 309–312.

[7] P. Wilkinson et al. A global perspective on energy: health effects and injustices. *Lancet* 370.9591 (2007), pp. 965–978.

[8] T. Lu et al. Dynamic stiffness removal for direct numerical simulations. *Combust. Flame* 156.8 (2009), pp. 1542–1551.

[9] K. N. C. Bray. The challenge of turbulent combustion. *Proc. Combust. Inst.* 26.1 (1996), pp. 1–26.

[10] N. Peters. Turbulent Combustion. Cambridge University Press, 2000.

[11] L. Vervisch and T. Poinsot. Direct numerical simulation of non-premixed turbulent flames. *Annu. Rev. Fluid Mech.* 30.1 (1998), pp. 655–691.

[12] R.W. Bilger. Turbulent jet diffusion flames. *Prog. Energy Combust. Sci.* 1.2-3 (1976), pp. 87–109.

[13] R. W. Bilger. Turbulent diffusion flames. *Annu. Rev. Fluid Mech.* 21.1 (1989), pp. 101–135.

[14] N. Peters. Laminar flamelet concepts in turbulent combustion. *Proc. Combust. Inst.* 21.1 (1988), pp. 1231–1250.

[15] A. Violi et al. Experimental formulation and kinetic model for JP-8 surrogate mixtures. *Combust. Sci. Technol.* 174.11-12 (2002), pp. 399–417.

[16] F. Bisetti et al. On the formation and early evolution of soot in turbulent nonpremixed flames. *Combust. Flame* 159.1 (2012), pp. 317–335.

[17] V. Nilsen and G. Kosály. Differential diffusion in turbulent reacting flows. *Combust. Flame* 117.3 (1999), pp. 493–513.

[18] F. Bisetti, A. Attili, and H. Pitsch. Advancing predictive models for particulate formation in turbulent flames via massively parallel direct numerical simulations. *Phil. Trans. R. Soc. A* 372.2022 (2014), p. 20130324.

[19] H. Pitsch. Unsteady flamelet modeling of differential diffusion in turbulent jet diffusion flames. *Combust. Flame* 123.3 (2000), pp. 358–374.

[20] C. D. Pierce and P. Moin. Progress-variable approach for large-eddy simulation of non-premixed turbulent combustion. *J. Fluid Mech.* 504 (2004), pp. 73–97.

[21] J. C. Ferreira. Flamelet modelling of stabilization in turbulent non-premixed combustion. PhD thesis. Diss. Techn. Wiss. ETH Zürich, Nr. 11984, 1996.

[22] A. W. Cook and J. J. Riley. Subgrid-scale modeling for turbulent reacting flows. *Combust. Flame* 112.4 (1998), pp. 593–606.

[23] H. Pitsch and H. Steiner. Large-eddy simulation of a turbulent piloted methane/air diffusion flame (Sandia flame D). *Phys. Fluids* 12.10 (2000), pp. 2541–2554.

[24] M. Ihme and H. Pitsch. Prediction of extinction and reignition in non-premixed turbulent flames using a flamelet/progress variable model: 1. A priori study and presumed PDF closure. *Combust. Flame* 155.1 (2008), pp. 70–89.

[25] A. Kempf et al. Large Eddy Simulations of Swirling Non-premixed Flames With Flamelet Models: A Comparison of Numerical Methods. *Flow Turbul. Combust.* 81.4 (2008), pp. 523–561.

[26] N. Burali et al. Assessment of the constant non-unity Lewis number assumption in chemically-reacting flows. *Combust. Theor. Model.* 20.4 (2016), pp. 1–26.

[27] International Sooting Flame (ISF) Workshop, July 30th - July 31st 2016, Seoul, South Korea. https://www.adelaide.edu.au/cet/isfworkshop/. 2016.

[28] A. D'Anna. Combustion-formed nanoparticles. *Proc. Combust. Inst.* 32.1 (2009), pp. 593–613.

[29] J. Appel, H. Bockhorn, and M. Frenklach. Kinetic Modeling of Soot Formation with Detailed Chemistry and Physics: Laminar Premixed Flames of C_2 Hydrocarbons. *Combust. Flame* 121.1 (2000), pp. 122–136.

[30] G. Blanquart and H. Pitsch. Analyzing the effects of temperature on soot formation with a joint volume-surface-hydrogen model. *Combust. Flame* 156.8 (2009), pp. 1614–1626.

[31] C. K. Westbrook et al. Computational combustion. *Proc. Combust. Inst.* 30.1 (2005), pp. 125–157.

[32] C. K. Law. Combustion at a crossroads: Status and prospects. *Proc. Combust. Inst.* 31.1 (2007), pp. 1–29.

[33] S. B. Pope. Small scales, many species and the manifold challenges of turbulent combustion. *Proc. Combust. Inst.* 34.1 (2013), pp. 1–31.

[34] V. Giovangigli. Multicomponent transport in laminar flames. *Proc. Combust. Inst.* 35.1 (2015), pp. 625–637.

[35] A. Ern and V. Giovangigli. EGLIB: A general-purpose Fortran library for multicomponent transport property evaluation. *Manual of EGlib version* 3 (2004), p. 12.

[36] S. B. Dworkin, M. D. Smooke, and V. Giovangigli. The impact of detailed multicomponent transport and thermal diffusion effects on soot formation in ethylene/air flames. *Proc. Combust. Inst.* 32.1 (2009), pp. 1165–1172.

[37] J. F. Grcar, J. B. Bell, and M. S. Day. The Soret effect in naturally propagating, premixed, lean, hydrogen–air flames. *Proc. Combust. Inst.* 32.1 (2009), pp. 1173–1180.

[38] D. Valiev et al. Numerical study of interaction between Darrieus-Landau instability and spatially periodic shear flow. *25th International Colloquium on the Dynamics of Explosions and Reactive Systems*. 2015.

[39] M. D. Smooke et al. Computational and experimental study of soot formation in a coflow, laminar diffusion flame. *Combust. Flame* 117.1 (1999), pp. 117–139.

[40] R. B. Bird, W. E. Stewart, and E. N. Lightfoot. Transport phenomena. John Wiley & Sons, 2007.

[41] J. O. Hirschfelder et al. Molecular theory of gases and liquids. Vol. 26. Wiley New York, 1954.

[42] S. Mathur, P. K. Tondon, and S. C. Saxena. Thermal conductivity of binary, ternary and quaternary mixtures of rare gases. *Mol. Phys.* 12.6 (1967), pp. 569–579.

[43] S. Lapointe, B. Savard, and G. Blanquart. Differential diffusion effects, distributed burning, and local extinctions in high Karlovitz premixed flames. *Combust. Flame* 162.9 (2015), pp. 3341–3355.

[44] H. Wang et al. A high temperature chemical kinetic model of *n*-alkane (up to *n*-dodecane), cyclohexane, and methyl-, ethyl-, *n*-propyl and *n*-butyl-cyclohexane oxidation at high temperatures, JetSurF version 2.0; September 19, 2010. http://web.stanford.edu/group/haiwanglab/JetSurF/JetSurF2.0/index.html. 2010.

[45] G. Blanquart, P. Pepiot-Desjardins, and H. Pitsch. Chemical mechanism for high temperature combustion of engine relevant fuels with emphasis on soot precursors. *Combust. Flame* 156.3 (2009), pp. 588–607.

[46] R. S. Barlow et al. Piloted methane/air jet flames: Transport effects and aspects of scalar structure. *Combust. Flame* 143.4 (2005), pp. 433–449.

[47] B. Savard and G. Blanquart. An *a priori* model for the effective species Lewis numbers in premixed turbulent flames. *Combust. Flame* 161.6 (2014), pp. 1547–1557.

[48] B. Savard, B. Bobbitt, and G. Blanquart. Structure of a high Karlovitz n-C_7H_{16} premixed turbulent flame. *Proc. Combust. Inst.* 35.2 (2015), pp. 1377–1384.

[49] D. O. Lignell et al. The effect of flame structure on soot formation and transport in turbulent nonpremixed flames using direct numerical simulation. *Combust. Flame* 151.1 (2007), pp. 2–28.

[50] C. S. Yoo et al. Direct numerical simulations of ignition of a lean n-heptane/air mixture with temperature inhomogeneities at constant volume: Parametric study. *Combust. Flame* 158.9 (2011), pp. 1727–1741.

[51] P. Pepiot-Desjardins and H. Pitsch. An efficient error-propagation-based reduction method for large chemical kinetic mechanisms. *Combust. Flame* 154.1 (2008), pp. 67–81.

[52] D. A. Goussis and U. Maas. Model reduction for combustion chemistry. *Turbulent Combustion Modeling*. Springer, 2011, pp. 193–220.

[53] D. A. Schwer, P. Lu, and W. H. Green. An adaptive chemistry approach to modeling complex kinetics in reacting flows. *Combust. Flame* 133.4 (2003), pp. 451–465.

[54] L. Liang, J. G. Stevens, and J. T. Farrell. A dynamic adaptive chemistry scheme for reactive flow computations. *Proc. Combust. Inst.* 32.1 (2009), pp. 527–534.

[55] T. Poinsot and D. Veynante. Theoretical and Numerical Combustion. 2nd ed. RT Edwards Inc., 2005.

[56] H. Pitsch, M. Chen, and N. Peters. Unsteady flamelet modeling of turbulent hydrogen-air diffusion flames. *Proc. Combust. Inst.* 27.1 (1998), pp. 1057–1064.

[57] E. R. Hawkes and J.-H. Chen. Direct numerical simulation of hydrogen-enriched lean premixed methane–air flames. *Combust. Flame* 138.3 (2004), pp. 242–258.

[58] E. Giacomazzi, F. R. Picchia, and N. Arcidiacono. A review of chemical diffusion: Criticism and limits of simplified methods for diffusion coefficient calculation. *Combust. Theor. Model.* 12.1 (2008), pp. 135–158.

[59] E. R. Hawkes and J.-H. Chen. Comparison of direct numerical simulation of lean premixed methane–air flames with strained laminar flame calculations. *Combust. Flame* 144.1 (2006), pp. 112–125.

[60] R. Sankaran et al. Response of flame thickness and propagation speed under intense turbulence in spatially developing lean premixed methane–air jet flames. *Combust. Flame* 162.9 (2015), pp. 3294–3306.

[61] H. Pitsch. Large-eddy simulation of turbulent combustion. *Annu. Rev. Fluid Mech.* 38 (2006), pp. 453–482.

[62] R. S. Rogallo and P. Moin. Numerical Simulation of Turbulent Flows. *Ann. Rev. Fluid Mech.* 16.1 (1984), pp. 99–137.

[63] M. Lesieur and O. Metais. New Trends in Large-Eddy Simulations of Turbulence. *Ann. Rev. Fluid Mech.* 28.1 (1996), pp. 45–82.

[64] C. Meneveau and J. Katz. Scale-Invariance and Turbulence Models for Large-Eddy Simulation. *Ann. Rev. Fluid Mech.* 32.1 (2000), pp. 1–32.

[65] N. Peters. Laminar diffusion flamelet models in non-premixed turbulent combustion. *Prog. Energy Combust. Sci.* 10.3 (1984), pp. 319–339.

[66] H. Pitsch and N. Peters. A consistent flamelet formulation for non-premixed combustion considering differential diffusion effects. *Combust. Flame* 114.1 (1998), pp. 26–40.

[67] M. Ihme and H. Pitsch. Modeling of radiation and nitric oxide formation in turbulent nonpremixed flames using a flamelet/progress variable formulation. *Phys. Fluids* 20.5 (2008), p. 055110.

[68] M. Ihme, C. M. Cha, and H. Pitsch. Prediction of local extinction and re-ignition effects in non-premixed turbulent combustion using a flamelet/progress variable approach. *Proc. Combust. Inst.* 30.1 (2005), pp. 793–800.

[69] M. C. Drake et al. Measurements of temperature and concentration fluctuations in turbulent diffusion flames using pulsed Raman spectroscopy. *Proc. Combust. Inst.* 18.1 (1981), pp. 1521–1531.

[70] M. C. Drake, R. W. Pitz, and M. Lapp. Laser Measurements on Nonpremixed H_2-Air Flames for Assessment of Turbulent Combustion Models. *AIAA J.* 24.6 (1986), pp. 905–917.

[71] R. S. Barlow and J. H. Frank. Effects of turbulence on species mass fractions in methane/air jet flames. *Proc. Combust. Inst.* 27.1 (1998), pp. 1087–1095.

[72] R. S. Barlow. International Workshop on Measurement and Computation of Turbulent Non-Premixed Flames (TNF). http://www.sandia.gov/TNF/. 2003.

[73] R. S. Barlow and A. N. Karpetis. Scalar length scales and spatial averaging effects in turbulent piloted methane/air jet flames. *Proc. Combust. Inst.* 30.1 (2005), pp. 673–680.

[74] B. Savard. Characterization and modeling of premixed turbulent *n*-heptane flames in the thin reaction zone regime. PhD thesis. California Institute of Technology, 2015.

[75] H. Wang. Consistent flamelet modeling of differential molecular diffusion for turbulent non-premixed flames. *Phys. Fluids* 28.3 (2016), p. 035102.

[76] D. Veynante and L. Vervisch. Turbulent combustion modeling. *Prog. Energy Combust. Sci.* 28.3 (2002), pp. 193–266.

[77] C. Han et al. Examination of the effect of differential molecular diffusion in DNS of turbulent non-premixed flames. *Int. J. Hydrogen Energy* 42.16 (2017), pp. 11879–11892.

[78] O. Desjardins et al. High order conservative finite difference scheme for variable density low Mach number turbulent flows. *J. Comput. Phys.* 227.15 (2008), pp. 7125–7159.

[79] H. Pitsch. FlameMaster, a C++ computer program for 0D combustion and 1D laminar flame calculations. http://www.itv.rwth-aachen.de/downloads/flamemaster/. 1998.

[80] A. Majda. Compressible Fluid Flow and Systems of Conservation Laws in Several Space Variables. Springer-Verlag Berlin Heidelberg, 1984.

[81] A. Majda and J. Sethian. The derivation and numerical solution of the equations for zero Mach number combustion. *Combust. Sci. Technol.* 42.3-4 (1985), pp. 185–205.

[82] Y. Xuan. Progress in numerical modeling of non-premixed combustion. PhD thesis. California Institute of Technology, 2014.

[83] J. H. Ferziger and H. G. Kaper. Mathematical Theory of Transport Processes in Gases. Amsterdam: North-Holland, 1972.

[84] W. L. Grosshandler. RADCAL: A Narrow-Band Model for Radiation. *Calculations in a Combustion Environment, NIST Technical Note* 1402 (1993).

[85] International Sooting Flame (ISF) Workshop, August 2nd - August 3rd 2014, Pleasanton Hilton, Pleasanton, California. https://www.adelaide.edu.au/cet/isfworkshop/. 2014.

[86] International Sooting Flame (ISF) Workshop, July 27th - July 28thst 2018, Trinity College Dublin, Ireland. https://www.adelaide.edu.au/cet/isfworkshop/. 2018.

[87] J. H. Frank, R. S. Barlow, and C. Lundquist. Radiation and nitric oxide formation in turbulent non-premixed jet flames. *Proc. Combust. Inst.* 28.1 (2000), pp. 447–454.

[88] X. L. Zhu et al. The effects of self-absorption of radiation on an opposed flow partially premixed flame. *Combust. Flame* 129.3 (2002), pp. 342–345.

[89] P. J. Coelho, O. J. Teerling, and D. Roekaerts. Spectral radiative effects and turbulence/radiation interaction in a non-luminous turbulent jet diffusion flame. *Combust. Flame* 133.1-2 (2003), pp. 75–91.

[90] S. R. Turns and F. H. Myhr. Oxides of nitrogen emissions from turbulent jet flames: Part I–Fuel effects and flame radiation. *Combust. Flame* 87.3-4 (1991), pp. 319–335.

[91] S. R. Turns. Understanding NOx formation in nonpremixed flames: experiments and modeling. *Prog. Energy Combust. Sci.* 21.5 (1995), pp. 361–385.

[92] N. S. A. Smith et al. A comparison of CMC and PDF modelling predictions with experimental nitric oxide LIF/Raman measurements in a turbulent H_2 jet flame. *Combust. Sci. Technol.* 105.4-6 (1995), pp. 357–375.

[93] R. S. Barlow et al. Nitric oxide formation in dilute hydrogen jet flames: isolation of the effects of radiation and turbulence-chemistry submodels. *Combust. Flame* 117.1-2 (1999), pp. 4–31.

[94] J. Kim and P. Moin. Application of a fractional-step method to incompressible Navier-Stokes equations. *J. Comput. Phys.* 59.2 (1985), pp. 308–323.

[95] B. Savard et al. A computationally-efficient, semi-implicit, iterative method for the time-integration of reacting flows with stiff chemistry. *J. Comput. Phys.* 295 (2015), pp. 740–769.

[96] R. D. Falgout and U. M. Yang. hypre: A library of high performance preconditioners. *ICCS*. Springer. 2002, pp. 632–641.

[97] M. Herrmann, G. Blanquart, and V.t Raman. Flux corrected finite volume scheme for preserving scalar boundedness in reacting large-eddy simulations. *AIAA J.* 44.12 (2006), pp. 2879–2886.

[98] M. Herrmann, G. Blanquart, and V. Raman. Flux corrected finite volume scheme for preserving scalar boundedness in reacting large-eddy simulations. *AIAA J.* 44.12 (2006), pp. 2879–2886.

[99] R. J. Kee et al. CHEMKIN-III: A Fortran Chemical Kinetics Package for the Analysis of Gas Phase Chemical and Plasma Kinetics," Sandia National Laboratories Report (1996).

[100] D. G. Goodwin, H. K. Moffat, and R. L. Speth. Cantera: An Object-Oriented Software Toolkit for Chemical Kinetics, Thermodynamics, and Transport Processes. http://www.cantera.org. Version 2.3.0. 2017. DOI: 10.5281/zenodo.170284.

[101] Y. Xuan, G. Blanquart, and M. E. Mueller. Modeling curvature effects in diffusion flames using a laminar flamelet model. *Combust. Flame* 161.5 (2014), pp. 1294–1309.

[102] N. Peters. Local quenching due to flame stretch and non-premixed turbulent combustion. *Combust. Sci. Technol.* 30.1-6 (1983), pp. 1–17.

[103] R. S. Barlow and J.-Y. Chen. On transient flamelets and their relationship to turbulent methane-air jet flames. Vol. 24. 1. Elsevier. 1992, pp. 231–237.

[104] R. W. Bilger. Molecular Transport Effects in Turbulent Diffusion Flames at Moderate Reynolds Number. *AIAA J.* 20.7 (1982), pp. 962–970.

[105] W. Bilger and R. W. Dibble. Differential molecular diffusion effects in turbulent mixing. *Combust. Sci. Technol.* 28.3-4 (1982), pp. 161–172.

[106] L. L. Smith et al. Laser Raman scattering measurements of differential molecular diffusion in turbulent nonpremixed jet flames of H_2/CO_2 fuel. *Combust. Flame* 100.1 (1995), pp. 153–160.

[107] E. R. Hawkes et al. Direct numerical simulation of turbulent combustion: fundamental insights towards predictive models. *J. Phys.: Conf. Ser.* 16.1 (2005), pp. 65–79.

[108] J. S. Kim and F. A. Williams. Structures of flow and mixture-fraction fields for counterflow diffusion flames with small stoichiometric mixture fractions. *SIAM J. Appl. Math.* 53.6 (1993), pp. 1551–1566.

[109] S. B. Pope. PDF methods for turbulent reactive flows. *Prog. Energy Combust. Sci.* 11.2 (1985), pp. 119–192.

[110] Z. Hong, D. F. Davidson, and R. K. Hanson. An improved H_2/O_2 mechanism based on recent shock tube/laser absorption measurements. *Combust. Flame* 158.4 (2011), pp. 633–644.

[111] G. Blanquart. CaltechMech, version 2.4. http://www.theforce.caltech.edu/CaltechMech. 2017.

[112] M. S. Day et al. Cellular burning in lean premixed turbulent hydrogen-air flames: Coupling experimental and computational analysis at the laboratory scale. *J. Phys. Conf. Ser.* Vol. 180. 1. IOP Publishing. 2009, p. 012031.

[113] M. Day et al. A combined computational and experimental characterization of lean premixed turbulent low swirl laboratory flames II. Hydrogen flames. *Combust. Flame* 162.5 (2015), pp. 2148–2165.

[114] E. R. Hawkes et al. Scalar mixing in direct numerical simulations of temporally evolving plane jet flames with skeletal CO/H_2 kinetics. *Proc. Combust. Inst.* 31.1 (2007), pp. 1633–1640.

[115] C. Altantzis et al. Hydrodynamic and thermodiffusive instability effects on the evolution of laminar planar lean premixed hydrogen flames. *J. Fluid Mech.* 700 (2012), pp. 329–361.

[116] A. J. Aspden, M. S. Day, and J. B. Bell. Turbulence-chemistry interaction in lean premixed hydrogen combustion. *Proc. Combust. Inst.* 35.2 (2015), pp. 1321–1329.

[117] B. Savard and G. Blanquart. Broken reaction zone and differential diffusion effects in high Karlovitz n-C_7H_{16} premixed turbulent flames. *Combust. Flame* 162.5 (2015), pp. 2020–2033.

[118] P. L. Carroll and G. Blanquart. A proposed modification to Lundgren's physical space velocity forcing method for isotropic turbulence. *Phys. Fluids* 25.10 (2013), pp. 105–114.

[119] B. Bobbitt, S. Lapointe, and G. Blanquart. Vorticity transformation in high Karlovitz number premixed flames. *Phys. Fluids* 28.1 (2016), p. 015101.

[120] H. Pitsch. Improved pollutant predictions in large-eddy simulations of turbulent non-premixed combustion by considering scalar dissipation rate fluctuations. *Proc. Combust. Inst.* 29.2 (2002), pp. 1971–1978.

[121] R. K. A. Kailasanathan et al. Effect of diluents on soot precursor formation and temperature in ethylene laminar diffusion flames. *Combust. Flame* 160.3 (2013), pp. 656–670.

[122] R. K. A. Kailasanathan et al. Hydrocarbon species concentrations in nitrogen diluted ethylene-air laminar jet diffusion flames at elevated pressures. *Proc. Combust. Inst.* 34.1 (2013), pp. 1035–1043.

[123] R. S. Barlow et al. Scalar profiles and NO formation in laminar opposed-flow partially premixed methane/air flames. *Combust. Flame* 127.3 (2001), pp. 2102–2118.

[124] Y. Xuan and G. Blanquart. Numerical modeling of sooting tendencies in a laminar co-flow diffusion flame. *Combust. Flame* 160.9 (2013), pp. 1657–1666.

[125] V. Gururajan, F. N. Egolfopoulos, and K. Kohse-Höinghaus. Direct numerical simulations of probe effects in low-pressure flame sampling. *Proc. Combust. Inst.* 35.1 (2015), pp. 821–829.

[126] S.H. Stårner and R.W. Bilger. Characteristics of a piloted diffusion flame designed for study of combustion turbulence interactions. *Combust. Flame* 61.1 (1985), pp. 29–38.

[127] A.R. Masri, R.W. Dibble, and R.S. Barlow. The structure of turbulent non-premixed flames revealed by Raman-Rayleigh-LIF measurements. *Prog. Energy Combust. Sci.* 22.4 (1996), pp. 307–362.

[128] R. W. Bilger, S. H. Stårner, and R. J. Kee. On reduced mechanisms for methane-air combustion in nonpremixed flames. *Combust. Flame* 80.2 (1990), pp. 135–149.

[129] C. Schneider et al. Flow field measurements of stable and locally extinguishing hydrocarbon-fuelled jet flames. *Combust. Flame* 135.1 (2003), pp. 185–190.

[130] A. Sevault et al. On the structure of the near field of oxy-fuel jet flames using Raman/Rayleigh laser diagnostics. *Combust. Flame* 159.11 (2012), pp. 3342–3352.

[131] J. C. Sutherland, P.J. Smith, and J.H. Chen. Quantification of differential diffusion in nonpremixed systems. *Combust. Theor. Model.* 9.2 (2005), pp. 365–383.

[132] A. N. Karpetis and R. S. Barlow. Measurements of flame orientation and scalar dissipation in turbulent partially premixed methane flames. *Proc. Combust. Inst.* 30.1 (2005), pp. 665–672.

[133] A. Liñán. The asymptotic structure of counterflow diffusion flames for large activation energies. *Acta Astronaut.* 1.7 (1974), pp. 1007–1039.

[134] N. Peters and F. A. Williams. Liftoff characteristics of turbulent jet diffusion flames. *AIAA J.* 21.3 (1983), pp. 423–429.

[135] G. P. Smith et al. GRI-Mech 3.0. http://combustion.berkeley.edu/gri-mech/. 1999.

[136] F. C. Lockwood and H. A. Moneib. Fluctuating temperature measurements in a heated round free jet. *Combust. Sci. Technol.* 22.1-2 (1980), pp. 63–81.

[137] E. Effelsberg and N. Peters. Scalar dissipation rates in turbulent jets and jet diffusion flames. *Proc. Combust. Inst.* 22.1 (1989), pp. 693–700.

[138] A. Scholtissek et al. A multi-scale asymptotic scaling and regime analysis of flamelet equations including tangential diffusion effects for laminar and turbulent flames. *Combust. Flame* 162.4 (2015), pp. 1507–1529.

[139] A. J. Yule et al. Combustion-Transition Interaction in a Jet Flame. *AIAA J.* 19.6 (1981), pp. 752–760.

[140] L.-D. Chen et al. Vorticity generation in jet diffusion flames. *Combust. Sci. Tech.* 77.1-3 (1991), pp. 41–57.

[141] R. W. Schefer et al. Temporal evolution of turbulence/chemistry interactions in lifted, turbulent-jet flames. *Proc. Combust. Inst.* 25.1 (1994), pp. 1223–1231.

[142] N. T. Clemens and P. H. Paul. Effects of heat release on the near field flow structure of hydrogen jet diffusion flames. *Combust. Flame* 102.3 (1995), pp. 271–284.

[143] M. C. Soteriou. Flow-combustion interactions in the near field of high Damköhler number non-premixed exothermic jets. *Proc. Combust. Inst.* 27.1 (1998), pp. 1213–1219.

[144] V. Bergmann et al. Application of spontaneous Raman and Rayleigh scattering and 2D LIF for the characterization of a turbulent $CH_4/H_2/N_2$ jet diffusion flame. *Appl. Phys. B* 66.4 (1998), pp. 489–502.

[145] W. Meier et al. Raman/Rayleigh/LIF Measurements in a Turbulent $CH_4/H_2/N_2$ Jet Diffusion Flame: Experimental Techniques and Turbulence-Chemistry Interaction. *Combust. Flame* 123.3 (2000), pp. 326–343.

[146] D. C Wilcox. Turbulence Modeling for CFD. 3rd ed. DCW industries, Inc., 2006.

[147] S. B. Pope. Turbulent Flows. Cambridge University Press, 2000.

[148] M. E. Mueller, G. Iaccarino, and H. Pitsch. Chemical kinetic uncertainty quantification for Large Eddy Simulation of turbulent nonpremixed combustion. *Proc. Combust. Inst.* 34.1 (2013), pp. 1299–1306.

[149] W. P. Jones and V. N. Prasad. Large Eddy Simulation of the Sandia Flame Series (D-F) using the Eulerian stochastic field method. *Combust. Flame* 157.9 (2010), pp. 1621–1636.

[150] M. Ihme and H. Pitsch. Prediction of extinction and reignition in nonpremixed turbulent flames using a flamelet/progress variable model: 2. Application in LES of Sandia flames D and E. *Combust. Flame* 155.1 (2008), pp. 90–107.

[151] N. R. Panchapakesan and J. L. Lumley. Turbulence measurements in axisymmetric jets of air and helium. Part 1. Air jet. *J. Fluid Mech.* 246 (1993), pp. 197–223.

[152] H. J. Hussein, S. P. Capp, and W. K. George. Velocity measurements in a high-Reynolds-number, momentum-conserving, axisymmetric, turbulent jet. *J. Fluid Mech.* 258 (1994), pp. 31–75.

[153] N. Peters. Length scales in laminar and turbulent flames. *Numerical approaches to combustion modeling*. Ed. by E. S. Oran and J. P. Boris. Vol. 135. Washington, DC (US): AIAA, 1991. Chap. 6, pp. 155–182.

[154] J.-H. Chen et al. Terascale direct numerical simulations of turbulent combustion using S3D. *Comput. Sci. Disc.* 2.1 (2009), p. 015001.

[155] D. O. Lignell, J. H. Chen, and H. A. Schmutz. Effects of Damköhler number on flame extinction and reignition in turbulent non-premixed flames using DNS. *Combust. Flame* 158.5 (2011), pp. 949–963.

[156] R. Sankaran et al. Structure of a spatially developing turbulent lean methane–air Bunsen flame. *Proc. Combust. Inst.* 31.1 (2007), pp. 1291–1298.

[157] J. B. Bell et al. Numerical simulation of a laboratory-scale turbulent slot flame. *Proc. Combust. Inst.* 31.1 (2007), pp. 1299–1307.

[158] R. W. Grout et al. Direct numerical simulation of flame stabilization downstream of a transverse fuel jet in cross-flow. *Proc. Combust. Inst.* 33.1 (2011), pp. 1629–1637.

[159] R. W. Grout et al. A direct numerical simulation study of turbulence and flame structure in transverse jets analysed in jet-trajectory based coordinates. *J. Fluid Mech.* 706 (2012), pp. 351–383.

[160] S. Karami et al. Edge flame structure in a turbulent lifted flame: A direct numerical simulation study. *Combust. Flame* 169 (2016), pp. 110–128.

[161] J. F. MacArt, T. Grenga, and M. E. Mueller. Effects of combustion heat release on velocity and scalar statistics in turbulent premixed jet flames at low and high Karlovitz numbers. *Combust. Flame* 191 (2018), pp. 468–485.

[162] P. K. Yeung and S. B. Pope. Lagrangian statistics from direct numerical simulations of isotropic turbulence. *J. Fluid Mech.* 207 (1989), pp. 531–586.

[163] M. E. Mueller and V. Raman. Model form uncertainty quantification in turbulent combustion simulations: Peer models. *Combust. Flame* 187 (2018), pp. 137–146.

[164] T. A. Oliver et al. Estimating uncertainties in statistics computed from direct numerical simulation. *Phys. Fluids* 26.3 (2014), p. 035101.

[165] P. G. Huang, G. N. Coleman, and P. Bradshaw. Compressible turbulent channel flows: DNS results and modelling. *J. Fluid Mech.* 305 (1995), pp. 185–218.

[166] G. Grötzbach. Spatial resolution requirements for direct numerical simulation of the Rayleigh-Bénard convection. *J. Comput. Phys.* 49.2 (1983), pp. 241–264.

[167] J. G. M. Eggels et al. Fully developed turbulent pipe flow: a comparison between direct numerical simulation and experiment. *J. Fluid Mech.* 268 (1994), pp. 175–210.

[168] M. Vinokur. On one-dimensional stretching functions for finite-difference calculations. *J. Comput. Phys.* 50.2 (1983), pp. 215–234.

[169] X. Wu and P. Moin. A direct numerical simulation study on the mean velocity characteristics in turbulent pipe flow. *J. Fluid Mech.* 608 (2008), pp. 81–112.

[170] C. A. Friehe, C. W. Van Atta, and C. H. Gibson. Turbulent shear flows. *AGARD conferences*. 93. 1972.

[171] K. M. Tacina and W. J. A. Dahm. Effects of heat release on turbulent shear flows. Part 1. A general equivalence principle for non-buoyant flows and its application to turbulent jet flames. *J. Fluid Mech.* 415 (2000), pp. 23–44.

[172] D. O. Lignell, J. H. Chen, and P. J. Smith. Three-dimensional direct numerical simulation of soot formation and transport in a temporally evolving nonpremixed ethylene jet flame. *Combust. flame* 155.1-2 (2008), pp. 316–333.

[173] H. Tennekes and J. L. Lumley. A first course in turbulence. MIT press, 1972.

[174] D. B. Percival. Three curious properties of the sample variance and autocovariance for stationary processes with unknown mean. *Am. Stat.* 47.4 (1993), pp. 274–276.

[175] M. F. Modest and D. C. Haworth. Radiative heat transfer in turbulent combustion systems: theory and applications. Springer, 2016.

[176] H. C. Hottel and W. R. Hawthorne. Diffusion in laminar flame jets. *Proc. Combust. Inst.* 3.1 (1948), pp. 254–266.

[177] M. E. Mueller and H. Pitsch. LES model for sooting turbulent nonpremixed flames. *Combust. Flame* 159.6 (2012), pp. 2166–2180.

[178] G. K. El Khoury et al. Direct numerical simulation of turbulent pipe flow at moderately high Reynolds numbers. *Flow Turbul. Combust.* 91.3 (2013), pp. 475–495.

[179] H. Pitsch and H. Steiner. Scalar mixing and dissipation rate in large-eddy simulations of non-premixed turbulent combustion. *Proc. Combust. Inst.* 28.1 (2000), pp. 41–49.

[180] R. S. Barlow. Laser diagnostics and their interplay with computations to understand turbulent combustion. *Proc. Combust. Inst.* 31.1 (2007), pp. 49–75.

[181] S. Chapman and T. G. Cowling. The Mathematical Theory of Non–Uniform Gases. 3rd ed. Cambridge: Cambridge University Press, 1970. ISBN: 052140844.

[182] P. Paul and J. Warnatz. A re-evaluation of the means used to calculate transport properties of reacting flows. 27.1 (1998), pp. 495–504.

[183] J. Schlup and G. Blanquart. Validation of a mixture-averaged thermal diffusion model for premixed lean hydrogen flames. *Combust. Theor. Model.* (2017), pp. 1–27.

[184] H. Wang and M. Frenklach. Detailed reduction of reaction mechanisms for flame modeling. *Combust. Flame* 87.3 (1991), pp. 365–370.

[185] G. Li and H. Rabitz. A general analysis of exact lumping in chemical kinetics. *Chem. Eng. Sci.* 44.6 (1989), pp. 1413–1430.

[186] M. Bodenstein. Eine theorie der photochemischen reaktionsgeschwindigkeiten. *Z. Phys. Chem.* 85.1 (1913), pp. 329–397.

[187] T. Lu and C. K. Law. A criterion based on computational singular perturbation for the identification of quasi steady state species: A reduced mechanism for methane oxidation with NO chemistry. *Combust. Flame* 154.4 (2008), pp. 761–774.